Solvation and Extraction Mechanism of Aromatic Solutes and Asphaltene utilizing Deep Eutectic Solvents: Experimental and Atomistic Simulation Studies

A Thesis Submitted in Partial Fulfilment of the Requirements for the Degree of

DOCTOR OF PHILOSOPHY

By

NIKHIL KUMAR

DEPARTMENT OF CHEMICAL ENGINEERING
INDIAN INSTITUTE OF TECHNOLOGY
GUWAHATI-781039, Assam, India
December, 2022

Dedicated to My Late Grandparents, Parents, Wife, Teachers, and Friends

Indian Institute of Technology Guwahati
Department of Chemical Engineering

Statement

I hereby declare that the content embodied in this thesis entitled **"Solvation and Extraction Mechanism of Aromatic Solutes and Asphaltene utilizing Deep Eutectic Solvents: Experimental and Atomistic Simulation Studies"** is the result of investigations carried out by me at the Department of Chemical Engineering, Indian Institute of Technology Guwahati, Guwahati, India, under the supervision of **Prof. Tamal Banerjee**.

In keeping with the general practice of reporting scientific observations, due acknowledgements have been made wherever the work described is based on the findings of other investigators.

Guwahati,
December 2022 **Nikhil Kumar**

Indian Institute of Technology Guwahati

Department of Chemical Engineering

Certificate

It is certified that the work presented in the thesis entitled **"Solvation and Extraction Mechanism of Aromatic Solutes and Asphaltene utilizing Deep Eutectic Solvents: Experimental and Atomistic Simulation Studies"** is a bonafide work of **Mr. Nikhil Kumar (Roll No. 176107105),** has been carried out in the Department of Chemical Engineering, Indian Institute of Technology Guwahati, under my supervision and this work has not been submitted elsewhere for any other degree.

Dr. Tamal Banerjee
Professor
Department of Chemical Engineering
IIT Guwahati, Guwahati-781039
Assam, India

ACKNOWLEDGEMENTS

My doctoral dissertation would not have come to successful completion without the help of several people. I take this opportunity to express my sincere gratitude to all of them.

To begin, I would like to express my gratitude to my thesis supervisor, **Prof. Tamal Banerjee**, from the **Department of Chemical Engineering**, for motivating and building my confidence, as well as for their insightful suggestions, astute thinking, and coherent and logical counsel throughout the research period. His constant support, constructive criticism, and meticulous planning have contributed significantly to the development of the dissertation. His true scientific zeal, autonomy, and self-reliance have aided considerably in improving the quality of my research. This feat was only achieved as a result of their unwavering support. I shall be eternally grateful to them for granting me the freedom to explore many research possibilities without worrying about achieving a successful conclusion as a result of my efforts. He encouraged me to visit many organizations as part of my research, which aided my maturation as a newbie in the research fraternity. I have always been confident that God has endowed me with the opportunity to pursue a doctoral degree under their supervision. To be very candid, whatever knowledge I got during my research period was entirely due to them. It was an absolute privilege to work alongside them. Many thanks, sir, for your fantastic assistance and support.

I would like to extend my sincere gratitude to my doctoral committee members, **Prof. Ramagopal V. S. Uppaluri**, **Prof. Partho Sarathi Gooh Pattader**, and **Prof. Manas Das**, for their incisive ideas and comments throughout the Ph.D. program's evaluation process. I would also like to extend my thanks to **Prof. Partho Sarathi Gooh Pattader**, **Prof. S Senthilmurugan**, and **Prof. Vaibhav Vasant Goud**, members of my comprehensive exam committee. I also thank **Prof. Bishnupada Mandal**, **Prof. Anugrah Singh**, Ex-Head, and **Prof. Kaustubha Mohanty,** Head of the Department of Chemical Engineering, for their administrative support. Furthermore, I would like to thank other faculty members, research scholars, and support staff of the Department of Chemical Engineering, IIT Guwahati, for their kind cooperation.

I take this time to express my sincere gratitude to our collaborators, **Dr. Blake Simmons** (Chief Science & Technology Officer and Vice President for the Deconstruction Division) and **Dr. Seema Singh** (Director of Biomass Pre-treatment and Process Development

and Deputy VP of the Deconstruction Division) of *Joint BioEnergy Institute* (JBEI), California (U.S). I would also like to thank **Dr. Mood Mohan** (Postdoctoral Research Fellow, Oak Ridge National Lab**)** for his valuable and constructive discussions on various topics, which helped me apply them in my thesis work.

I would also like to thank Central Instruments Facility (CIF) IIT Guwahati for providing NMR Analysis. Computational time from the *PARAM-ISHAN* supercomputer (162 nodes and 3024 cores in each node), and Karplus (3 nodes, 12 cores in each node), facility of Institute, and Department of Chemical Engineering, IIT Guwahati is highly acknowledged. I acknowledge the Ministry of Human Resource Development (MHRD) and our institute for providing fellowship throughout the Ph.D. program.

I sincerely acknowledge my research group members **Mr. Nabendu Paul**, **Mr. Arindam Dutta**, **Mr. Nipu Kumar Das**, **Mr. Raghibul Hussain**, **Mr. Harish G**, **Mr. Harsh Thakur**, **Mr. Uday, and Ms. Anuska** for providing a cooperative research environment.

I would like to express my profound gratitude to my previous group members, **Dr. Dhirendra Kumar Mishra, Dr. Papu Kumar Naik**, **Dr. Mood Mohan**, **Dr. Basudhrity Banerjee**, **Dr. Pyarimohan Dehury**, **Dr. Upasana Mahanta**, **Dr. Debashis Kundu**, **Dr. Rima Biswas**, **Mr. Janardan Singh**, **Mr. Ashvini Upadhayay**, **Mr. Harish Bhupathi**, **Mr. Sai Dileep Kumar Seera**, **Ms. Sambita Choudhary** for their immense support, encouragement, and help.

My sincere thanks to IIT Guwahati friends **Mr. Rahul Kumar, Mr. Nilesh Khalse, Mr. Ramanujan Pandey, Mr. Shubham and Ms. Purnima Madu,** and many more for making my stay at IIT Guwahati memorable.

Finally, but certainly not least, I want to convey my sincere gratitude to my parents and family members for their sustained help and encouragement in all my personal and academic ventures. I feel proud and blessed to have such parents as my mother, **Mrs. Kamla Devi,** and my father, **Mr. Ajab Singh Yadav**, uncle and aunt. Special thanks to my loving brothers and sisters, **Mr. Akhilesh, Mr. Ashish, Mrs. Richa, and Mrs. Sandhya,** who always strengthened my morale by standing by me in all situations. I want to express my heartfelt thanks to all the family members who have encouraged me for several months and taught me to remain focused on my work daily.

I will be forever indebted to the courage, understanding, and dedicated support shown by my wife, **Mrs. Diksha Yadav.** The timing of the Ph.D. tenure made me happy that another member joined us in life's journey. He is none other than my son **Shivay Yadav**.

I wish to thank many other people whose names are not mentioned here, but this does not mean I have forgotten their help. Above all, I am thankful to GOD for giving me a wonderful and healthy life.

Nikhil Kumar

Thesis Abstract

Deep eutectic solvents (DES) have emerged over the last two decades as a novel class of ionic liquids (ILs). In their broadest sense, DESs are usually formed by mixing a quaternary ammonium salt (typically choline chloride and derivatives) with hydrogen bond donor molecules such as amines, amides, alcohols, carboxylic acids, sugars, or polyols. The mixing of these two components upon gentle heating and in a specific molar ratio leads to a depression of the melting point, resulting in most of the cases in a liquid at room temperature, where no waste is produced, and no further purification steps are needed. Furthermore, DES's components are often biodegradable and non-toxic.

The first part of this Ph.D. thesis focusses on the study of the liquid structure of DESs so as to understand the application of these solvents in solvation and extraction. Here, the atomistic Molecular Dynamics (MD) simulations provide the structural properties of these solvents by combining them with aromatic and aliphatic solutes. The aromatic components such as benzene and thiophene were found to be hydrogen-bonded to the DES entity. Here, the precursor of the DES, namely monoethanolamine (MEA), had a higher hydrogen bond affinity than its counterpart HBA (choline chloride). According to the present study results, the aliphatic portion in DES components is less encouraged, as their solubility for aliphatic compounds rises with an increase in the chain length of alkyl groups. We chose methyltriphenylphosphonium bromide (MTPB)-based solvents for the separation of the aromatic portion as they had minimal solubility for the aliphatic fraction. The selected DESs are considered the most promising solvents due to their higher extraction efficiency and distribution coefficient for the hydrocarbon stream.

After understanding DES liquid structure and specific solute-solvent interaction, the DES, comprising of hydrogen bond acceptor (HBA), namely methyltriphenylphosphonium bromide (MTPB), along with ethylene glycol (EG) as a hydrogen bond donor (HBD), was formulated with a molar ratio of 1:4. The DES was then used to extract benzene and benzothiophene from representative diesel fuel components, namely a mixture of *n*-decane, *n*-dodecane, and *n*-hexadecane. The extraction efficiency achieved for benzene and benzothiophene using the (MTPB+EG) was in the range of 80–83% for a single stage and more than 98% for three stages or more. The cluster chemistry study studied through DFT calculations revealed that the aromatic compound interacts favourably with the MTP cation

and EG of the DES through multiple non-covalent interactions (e.g., C−H···π, Br^{-}···O−H, Br^{-}···C−H and O−H···π) but does not interact directly with the bromide (Br^{-}) ion. In addition, the atomistic molecular dynamics (MD) simulation technique was then employed to investigate the equilibrium interphase behaviour of the DES + benzene + *n*-hexane ternary system with respect to its DES-rich and hydrocarbon-rich phases. In summary, HBA and HBD both play a predominant role in benzene extraction from hydrocarbon streams. Consequently, this study offers new findings for the computational MD simulation of benzene extraction from hexane, which becomes helpful in the absence of experimental data.

The second part of this Ph.D. thesis focuses on the dispersion of asphaltene in DESs. It aims to investigate the inhibition of petroleum asphaltene aggregation using a novel combination of deep eutectic solvents. Further, the COSMO-RS (Conductor-like Screening Model for Real Solvents) model was performed to screen possible combinations of DESs for asphaltene. Among the studied DES, the DES with thymol and diphenyl ether gave a higher solubility of asphaltene. An excellent agreement was obtained between the experimental and COSMO-RS predicted excess enthalpies and activity coefficients. It gives the best performance for asphaltene solubility, reaching a value of 42.10 ± 0.58 mg/ml at 298.15 K and atmospheric pressure compared to the other conventional solvents. The Density Functional Theory (DFT), Baders theory of QTAIM (Quantum Theory of Atom in Molecules), and NCI (Non-Covalent Interaction) analysis suggest the formation of the DES-asphaltene complex via a combined effect of hydrogen bonding linkage with van der Waals and dispersion interaction, as supported by the electron density at BCP (ρ_{BCP}) and the positive sign of the Laplacian of electron density ($\nabla\rho_{BCP}^{2}$). The present study has paved the way forward to rationally design and understand the impact of structural variation of DESs for their interaction with asphaltene.

Table of Contents

List of Figures

List of Tables

List of Abbreviations

AIM	Atoms in Molecules
BCP	Bond Critical Point
B3LYP	Becke three-parameter, Lee-Yang-Parr
B3LYP-D3 (BJ)	Dispersion corrected density functional theory (Becke Johnson)
BP86	Becke 1988 exchange functional and the Perdew 86 correlation
BSSE	Basis Set Superposition Error
CCSD(T)	Coupled Cluster Single-Double and Triple
ChCl	Choline Chloride
CHELPG	CHarges from Electrostatic Potentials using a Grid-based method
COSMO-RS	COnductor like Screening MOdel for Real Solvents
COSMO-SAC	COnductor like Screening MOdel for segment activity coefficient
DES	Deep Eutectic Solvents
DFT	Density Functional Theory
DGA1	Density Gradient Approximation
FMO	Frontier Molecular Orbital
FTIR	Fourier transform spectroscopy
HBA	Hydrogen Bond Acceptor
HBD	Hydrogen Bond Donor

HF	Hartree Fock Theory
HOMO	Higher Occupied Molecular Orbital
IL	Ionic Liquid
IEFPCM	Integral Equation Formalism Polarizable Continuum Model
IE	Interaction Energy
IP	Ionization Potential
LUMO	Lower Unoccupied Molecular Orbital
MD	Molecular Dynamics Simulation
NBO	Natural Bonding Orbitals
NCI	Non-Covalent Interaction
NMR	Nuclear Magnetic Resonance
NPA	Natural Population Analysis
QC	Quantum Chemical
RDG	Reduced Density Gradient
RESP	Restrained Electrostatic Potential
SCRF	Self-Consistent Reaction Field
TGA	Thermo-Gravimetric Analysis
TZVP	Triple Zeta Valence Potential
QAS	Quaternary Ammonium Salt

QTAIM	Quantum Theory of Atoms in Molecules
VMD	Visual Molecular Dynamics

List of Symbols

a_{eff}	Effective contact surface area of a segment in Å^2
C_{hb}	Effective contact surface area of a segment in Å^2
E_{misfit}	Misfit interaction energy
E_{vdW}	Van der Waals (vdW) interaction energy
$p_s(\sigma)$	Probabilistic surface charge distribution for mixture (S)
p^{Xi} (σ)	Sigma profile of the pure component *i*
r_{n}	Radius of the nth segment
r_{eff}	Radius of the standard surface segment (a_{eff}) in Å
r	Pure component volume
q	Pure component area
r_{avg}	Average radius in Å
R	Universal gas constant in (kcal mol^{-1} K^{-1})
T	Temperature in K
Q	Normalized area parameter
x_i	Mole fraction of species '*i*'
d_{mn}	Distance between the *m*th and *n*th segment
A^{PCM}	Molecular surface area in Polarizable Continuum Model, in^2
A_{ws}	Standard segment area, cm^2 mol^{-1}
V^{PCM}	Molecular surface volume in Polarizable Continuum Model, in^3
V_{ws}	Standard segment volume, cm^3 mol^{-1}

Greek Symbols

$\Gamma_s(\sigma)$	Segment activity coefficient for the mixture (S)
$\Gamma_i(\sigma)$	Segment activity coefficient for pure component (i)
γ_i/s	Component activity coefficient in the mixture (S)
Φ_i	Fugacity coefficient of the component in mixture
A	Non-randomness parameter
α'	Misfit constant in kJ mol^{-1} Å^{-2}
σ, σ'	Screening charge density in e Å^{-2}
σ_{don}	Screening charge density for hydrogen-bond donor in e Å^{-2}
σ_{acc}	Screening charge density for hydrogen-bond acceptor in e Å^{-2}
σ_{hb}	Screening charge density for hydrogen-bond in e Å^{-2}
τ_{vdW}	Dispersion coefficient in kJ mol^{-1} Å^{-2}
$\mu_s(\sigma)$	Sigma potential in kJ mol^{-1} Å^{-2} for a surface segment in solution S

CHAPTER 1

Introduction and Literature Review for the Dearomatisation and Asphaltene Dispersion in Deep Eutectic Solvents

1.1. Outlook

The solutes are dissolved in the solvent to create a macroscopically uniform mixture. Solvents are widely used in industrial and laboratory settings [1]. Hence, this sector is crucial to the contemporary global supply chain. The raw material processing (such as mineral separation and extraction) and product manufacture (oil, gas, plastics, and pharmaceuticals) require the use of solvents [2].

1.2 Molecular Liquids

A class of solvents is known as molecular liquids (MLs). The liquid phase MLs can be either polar or non-polar substances that have no formal charge. Typical MLs include water, alcohols (such as methanol), hydrocarbons (such as cyclohexane), fluorocarbons (such as perfluorooctane), carboxylic acids (such as acetic acid), amines (such as octylamine), tetrahydrofuran, and several amides. While strong short-range hydrogen bonding and van der Waals interactions dominate their structures, MLs are often accessible in liquid form under normal ambient conditions [3]. Most industrial chemical processes presently utilise MLs and will likely continue to do so for the foreseeable future. Although processing provides an undeniably helpful answer, it is not without substantial threats to ecological balance, human health, and public safety. If discharged into the environment, non-aqueous MLs can bioaccumulate and are generally toxic if consumed. Due to their high volatility, such solvents can substantially threaten the environment and human health during handling, shipment, and utilization. In addition, many commercially available solvents require significant energy inputs for both their manufacturing and proper disposal, and they are often made from either low petrochemical feedstock or freshwater [2].

An effort is currently underway to replace MLs with solvent-free conditions or with green solvents [4] and supercritical fluids like CO_2 to lessen these unintended environmental

effects [5]. The sc-CO_2 chemistry introduction, on the other hand, may need the construction of costly new facilities[5]. As a result, there is a push to find an alternative to traditional solvents [6, 7]. Therefore, scientists are developing environmentally friendly future solvents known as "green solvents" [6-8].

1.3 Ionic Liquids

By convention, molten salts that are liquid at temperatures below 100°C are classified as ionic liquids (ILs) [9]. In a few publications, there is a further distinction between ordinary ILs and room-temperature ionic liquids (RTILs). In 1914, Paul Walden reportedly created the first ionic liquid by melting ethylammonium nitrate (EAN) [10]. When Arrhenius first discovered the existence of ions in solution, the revelation of an ionic liquid with characteristics so close to the water was a significant breakthrough [2]. Another variant, Deep Eutectic Solvents (DES), is under the larger category of solvents known as the analogue of Ionic Liquids (ILs).

There has been a significant increase in research on ILs for use in industries such as processing, chemical synthesis, and self-assembly [11]. The chemical structure determines its properties, including its low melting point, for which ILs were primarily considered. To favour the less ordered liquid phase, the anisotropy and asymmetry of the cation and anion are used to destabilise the solid. 1, 3-alkyl-imidazolium cations with various anions provide the backbone of most "contemporary" ILs. The vast number of ILs that may be constructed is shown in figure 1.1. The desirable physical properties of ILs can be achieved by striking a balance between the ion-ion interactions and the choice of cation and anion. Intriguing ILs characteristics may be traced back to the solvent's strong nanostructure. To describe this structure, different interaction models have been proposed to explain, such as hydrogen bond networks, ion clusters, and self-assembled nanostructures. However, it is challenging to specify a specific set of 'rules' that

describe the structure of an IL due to the wide variety of ILs studied and the various techniques used to study them.

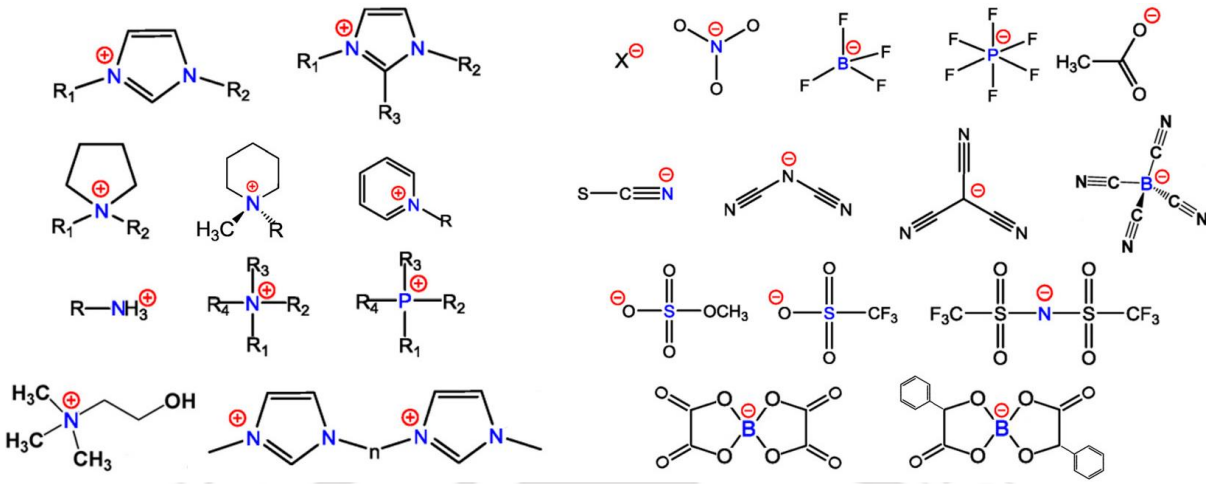

Figure 1.1. The chemical structures of typical cations and anions of ionic liquids.

ILs may be further subdivided into (poly)ionic liquids, surfactant ILs, switchable ILs, and IL mixtures [12]. Solvated Ionic Liquids (SILs) are one such 'sub-class' of ILs that was proposed by Angell and formalised by Mandai et al. [13]. Many ILs are made up of highly coordinating anions like Cl^- or big, non-coordinating ions that do not usually form complexes with metal ions. On the other hand, SILs consist entirely of coordinated ions [14]. Lithium salts are well-known complexes formed with strong, chelating Lewis acidic groups and a wide range of minute, complex inorganic cations [14-16]. The earliest SILs discovered were molten inorganic hydrate salts, but now most common SILs are stoichiometric mixtures of oligoethers (glymes) with metal salts [13].

Based on the strength of the counterion's interaction with the ions to produce the required solvate complexes, these SILs are further categorised as either "excellent" or "poor"[17]. Accordingly, SILs pose a problem for the conventional wisdom on ILs and DESs. While many DESs are based on metal ions or hydrated metal ions that are stoichiometrically combined with chelating Lewis acid molecules [18]. Hence there is likely to be a substantial

overlap between the structural properties of these systems [19]. Our present study focuses on a subset of ionic liquids (ILs) known as deep eutectic solvents.

1.4 Deep Eutectic Solvents

Ionic liquids (ILs), or salts with melting points below 100°C, have been studied for a long time. Their attributes, such as tunable solubility, low vapour pressures, and inflammability, have made them widely regarded as preferable solvents to volatile organic compounds (VOCs)[20]. In 2003, Abbott et al. found that a mixture of choline chloride and urea (both solids at room temperature) exhibits a significantly lower eutectic melting point than the individual melting points of components, thus forming a liquid phase at room temperature. This mixture was called a 'deep eutectic solvent' (DES)[21]. A significant step forward in green chemistry was taken with the discovery of the neoteric solvents known as Deep Eutectic Solvents (DESs). These solvents are typically characterized as combinations of two or more constituents that can mainly interact through intermolecular hydrogen bonding. All these mixtures could be either binary or ternary.

To develop a eutectic mixture, these substances must be introduced at a specific molar ratio [22]. The phrase "eutectic" derives from the Ancient Greek εὔτηκτος or *eútēktos*, meaning "conveniently liquefied". A eutectic point is the chemical composition and temperature at which a mixture of two solids melts entirely at the lowest melting temperature. Even though all mixtures of immiscible solid compounds have a eutectic point and many different compounds can form hydrogen bonds when taken in conjunction, the precise nature of what constitutes a DES remains a matter of debate, and several reported definitions fail to distinguish DES from other mixtures [23]. That is because the presence of a eutectic point or hydrogen bonding between components is an inadequate condition to define a "deep eutectic solvent." Martins et al. recently defined DES as "a mixture of two or more pure compounds for which

the eutectic point temperature is below that of an ideal liquid mixture, presentingsignificant negative deviations from ideality ($\Delta T_2 > 0$)". Here ΔT stands for the temperature depression, which is the difference between the ideal and the real eutectic point [23]. According to the same authors, temperature depression must lead to a liquid mixture at operating temperature. Since their composition is not predetermined, these systems are considerably more adaptable to modification.

There has been an incredible uptick in the research study of DES over the past decade, yet very little is understood about their background or defining features. Almost twenty years ago, Abbott et al. started the ball rolling by attempting to find liquids that could avoid the high cost and sensitivity to the moisture of some conventional ionic liquids [24]. This investigation tried many combinations based on various quaternary ammonium and metal salts. The combination of choline chloride (ChCl) and zinc chloride ($ZnCl_2$) in a 1:2 molar ratio was found to have the lowest freezing point (23-25°C). The same group of researchers later studied "deep eutectic solvents," which are eutectic mixtures of quaternary ammonium salts and hydrogen bond donors (HBD)[25]. The freezing point was reduced to 12°C by mixing the 1:2 molar ratio of ChCl: urea. As demonstrated by nuclear magnetic resonance (NMR) spectroscopy, hydrogen bonding between urea and chloride ion significantly lowers the freezing point (12°C) in comparison to that of individual melting points of ChCl (302°C) or urea (133°C). These solvents are not only liquefied at room temperature but can also be tuned to specific properties and have a high capacity for dissolving different compounds. The ChCl and carboxylic acid-based DES were then studied, showing that they also possessed a significant solubilizing capacity for certain metal oxides [25]. Chlorine hydrochloride and hydrated metal salts, such as chromium (III) chloride hexahydrate produced additional liquids [26]. Metal salts and HBD were later reported to produce an additional class of ambient temperature solvents, including amides (urea and acetamide) and diols (ethylene glycol and 1,

6-hexanediol). However, it was found that only a minor set of metal salts and HBD are capable of forming these compounds [27].

Later, Choi et al. coined the phrase "natural deep eutectic solvents" (NADESs) [28]. Another central feature for designing, developing, and applying green solvents is the origin and ecotoxicological properties of DES components. Thus, HBAs and HBDs of natural origin may be produced, leading to the so-called Natural DESs (NADESs). This group uses primary metabolites to synthesize DES [28, 29]. Aside from that, water can be a component of NADESs. They were initially hypothesized to account for the seemingly ubiquitous nature of metabolites in cells. It has been proposed that NADESs, together with water and lipids, may be regarded as a new cellular phase since different combinations of these candidates constituted liquids that efficiently solubilized diverse naturally occurring compounds. These mixtures might be engaged in the biosynthesis, storage, and transport of poorly water-soluble compounds and some processes like dehydration, drought resistance, and cryoprotection. Their environmental and economic benefits make them a top choice for consideration.

1.5 Classification of DESs

To classify the various eutectic mixtures, DES was divided into five groups according to the formula $Cat^+ X^- z Y$, where Cat^+ is, in principle, any ammonium, phosphonium, or sulfonium cation, and X is a Lewis base, generally a halide anion. The complex anionic species are formed between X^- and either a Lewis or Brønsted acid Y (*z* refers to the number of Y molecules interacting with the anion)[27, 30]. Type III eutectics, often based on ChCl and different HBD, have been lately in consideration. ChCl is the primary building block for the first synthesized type III DES. Since then, there has been a proliferation of chemicals utilised effectively in DES synthesis. While amides, alcohols, and carboxylic acids predominate as hydrogen bond donors

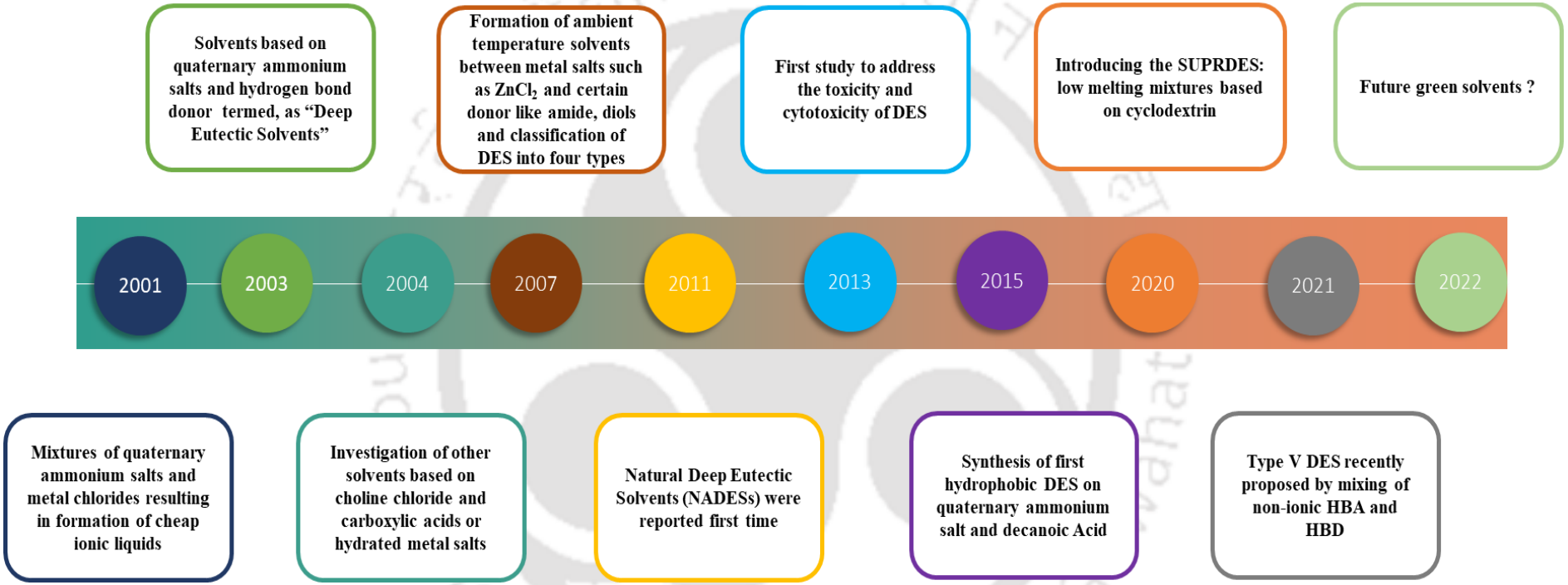

Figure 1.2. Major events marked the development of deep eutectic solvents throughout the years

(HBD), quaternary ammonium and phosphonium salts also predominate as hydrogen bond acceptors (HBA).

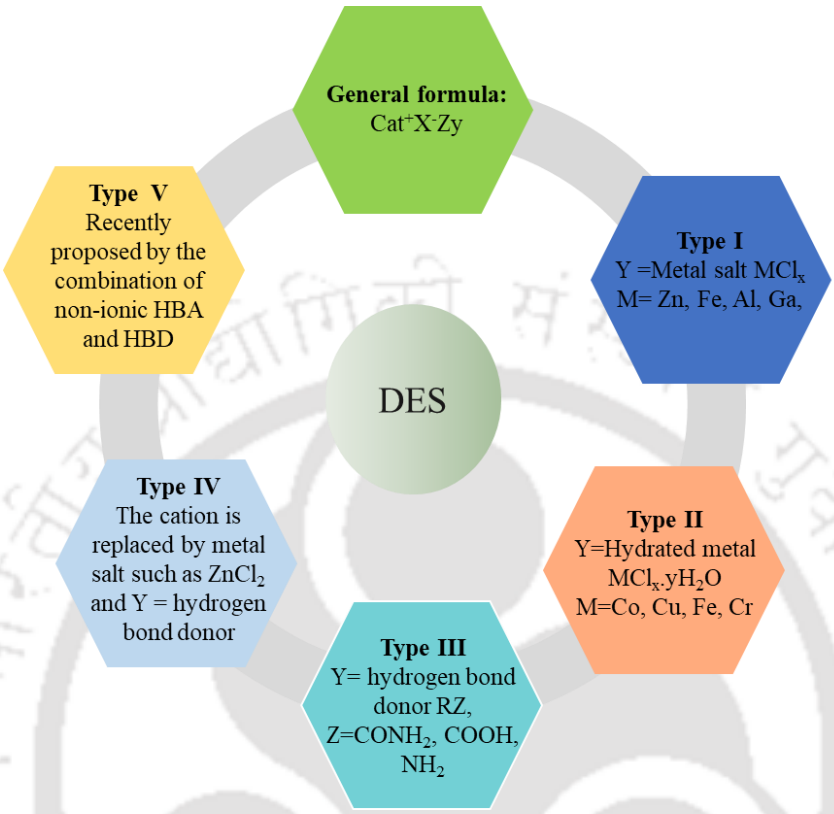

Figure 1.3. The five types of deep eutectic solvents are based on the general formula $Cat^{+}\ X^{-}\ z\ Y$.

The compounds, including sugars, sugar alcohols, and amino acids, are also considered for the formulation of NADES [29]. Hydrophobic DES has been studied recently. The chemicals such as tetrabutylammonium bromide (TBABr), menthol, thymol, and fatty acids as hydrogen bond acceptors are used with long alkyl chain alcohols and carboxylic acids such as HBD [31, 32]. In addition, ibuprofen, lidocaine, and phenylacetic acid are all examples of APIs that can be used to form DES. We refer to these solvents as THEDES (therapeutic deep eutectic solvents) when they have therapeutic use [33, 34]. Figure 1.4 depicts some more common HBA and HBD documented in the literature to prepare DESs.

Conversely, while NADES may sometimes qualify as a type V DES, this is not always the case. However, NADES were recently categorized into five primary classes [29, 35];

- Ionic liquids are made of an acid and a base;
- Neutral, made of only sugars or sugars and other polyalcohols;
- Neutral with acids, made of sugar/polyalcohols and organic acids;
- Neutral with bases, made of sugar/polyalcohols and organic bases;
- Amino acids-containing NADESs made of amino acids and sugars/ organic acids.

Due to their adaptability and the variety of possible precursor chemicals, the described type V DESs cannot be definitively placed in any of the categories mentioned above. Therefore, Countinho and colleagues presented a non-ionic type V DES. Their research demonstrated that a potent interplay between thymol and menthol produced significant, unfavourable departures from ideality. Resonance effects associated with the structure of phenolic chemicals, which served as potent hydrogen bonding, are responsible for the latter [36]. Additionally, two recent investigations described the use of cyclodextrins, which are non-toxic cyclic oligosaccharides, as hydrogen bond acceptors, resulting in the creation of liquid supramolecular mixtures at room temperature [36-38]. Figure 1.2 shows the significant milestones in the history of such green solvents.

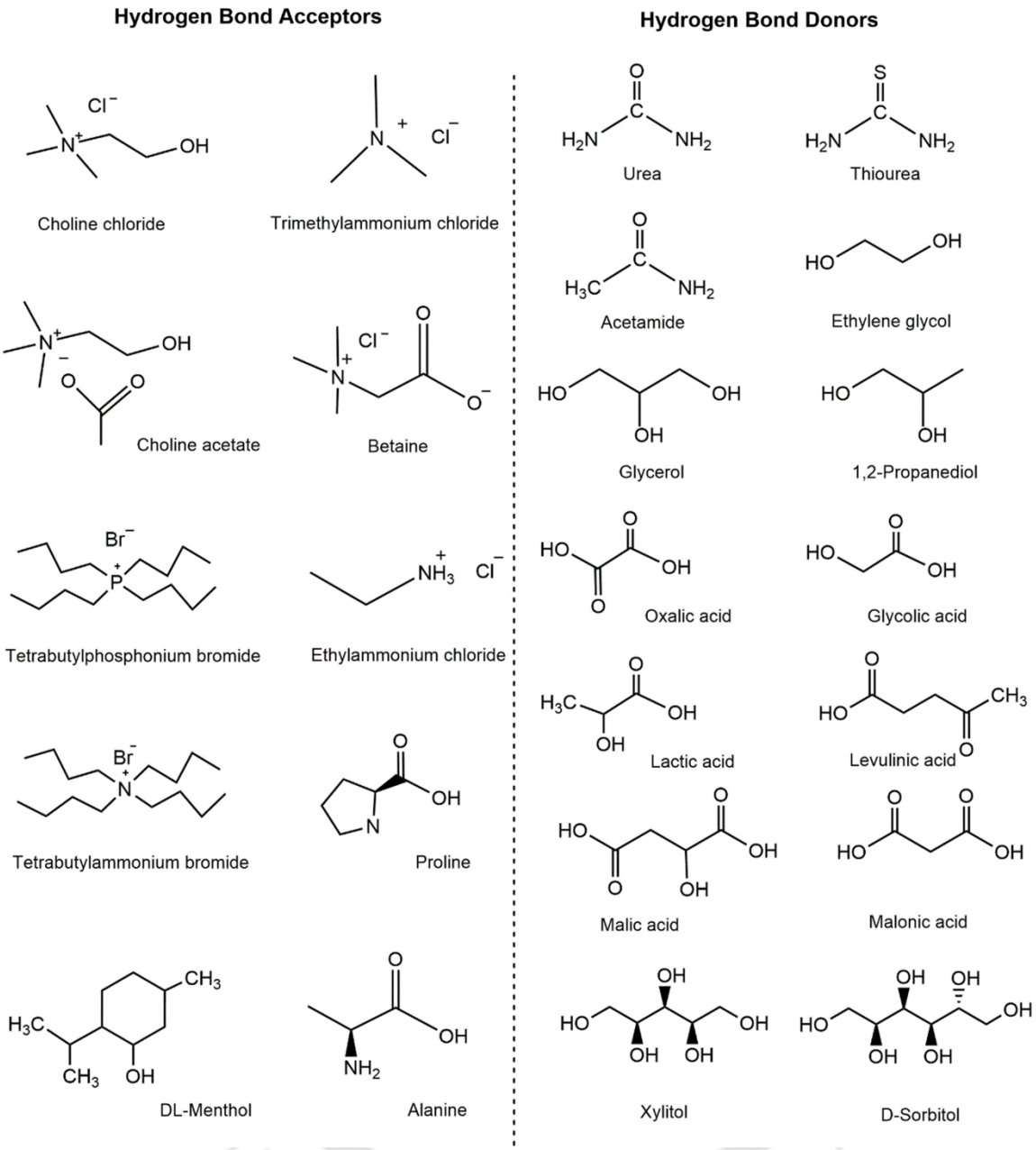

Figure 1.4. Commonly used HBA and HBD compounds in the synthesis of deep eutectic solvents.

1.6 Synthesis of DESs

The DESs are formed by combining two or more chemicals that can associate with strong hydrogen bonds to produce a deep eutectic mixture at a specific molar ratio. The two most common methods for preparing DES are heating and mixing until they form a transparent liquid [25]. There is typically a 100°C difference between the lowest and highest melting temperature. For solvents based on ChCl and carboxylic acids, however, as stated by Rodriguez et al., high

temperatures can cause a deterioration of the deep eutectic solvent due to an esterification reaction[39]. Mixing the compounds at room temperature and crushing them in a mortar with a pestle is the basis of the grinding procedure, which is repeated until a transparent liquid is produced [39]. In addition, Gutierrez et al.[40] revealed a technique that involves freeze-drying aqueous solutions of DES's constituents. Indeed, separate aqueous solutions of ChCl and urea (or thiourea) were mixed to form an aqueous solution of 1:2 ChCl: U (or ChCl: thiourea), having 5 wt.% solute concentration. The obtained solutions were then frozen and freeze-dried, resulting in the formation of transparent and viscous liquids. However, the water was found in the freeze-dried combination, which is known to interact with DES components and become a member of the DES network.

Dai et al. also disclosed an evaporation approach, which entails dissolving DESs components in water and then evaporating the solution at 50°C. The liquid produced is dehydrated using silica gel in a desiccator [29]. An eco-friendlier microwave-assisted method was described for the rapid synthesis of NADES that uses less time and energy[41]. Finally, a new method for synthesizing NADES using ultrasound has been developed [42]. The various application of deep eutectic solvents shown in figure 1.5.

1.7 ILs vs. DESs

Ionic liquids (ILs) were initially thought to be pure salts or eutectic salts in a molten state. They are ideal for engineering physical and analytical chemistry, electrochemistry, and biochemistry because of their excellent temperature stability and large electrochemical windows. Many IL's physical properties may be tuned by altering the anions and cations in the mixtures, depending on the application.

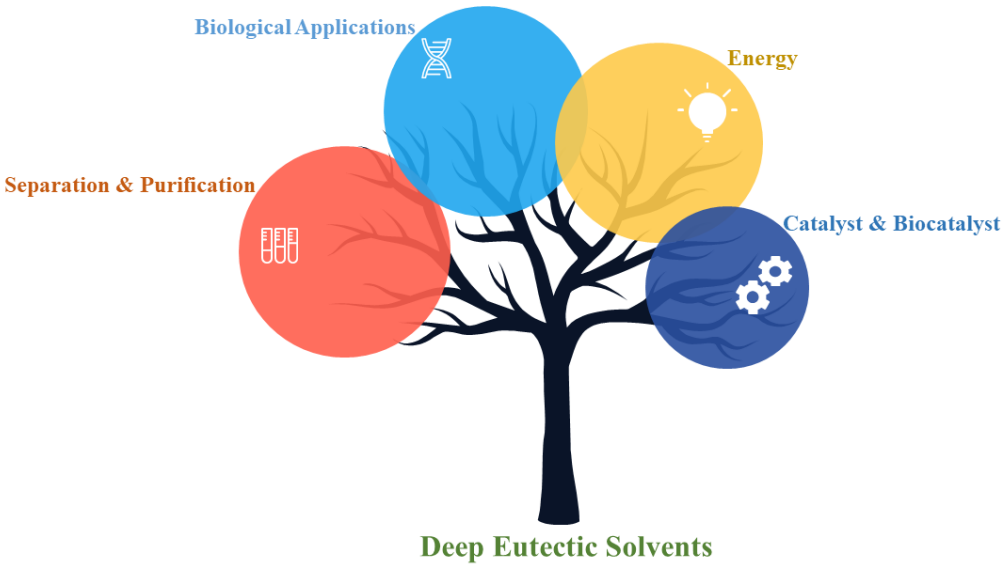

Figure 1.5. Various applications of deep eutectic solvents.

Furthermore, chemically modifying ions (typically cations) increases their effectiveness as task-specific solvents. The melting point of a cation is thought to be lowered by having a longer alkyl chain. ILs with long side chains have a bicontinuous shape, with apolar moieties in one area and polar alkyl tails in the other (Figure 1.6). In the nanoscale, DESs, like RTILS, have apolar and polar domains. In several fields, studies have demonstrated that the applications of DESs virtually completely cover those of ILs. Furthermore, the preparation of DESs is considerably more manageable than the preparation of ILs. As a result, these solvents can be considered a step forward in creating eutectic solvents.

1.8 Physiochemical Properties

The rising interest in DES can be attributed to the physicochemical aspects of these solvents. Given the diversity of compounds that can form DESs, they can be chemically tuned to meet the needs of a wide range of applications owing to their low volatility, non-flammability, low vapour pressure, chemical stability, and thermal stability. The subsequent sections discuss the physicochemical features of DESs, including their phase behaviour, density, viscosity, ionic conductivity, surface tension, and polarity.

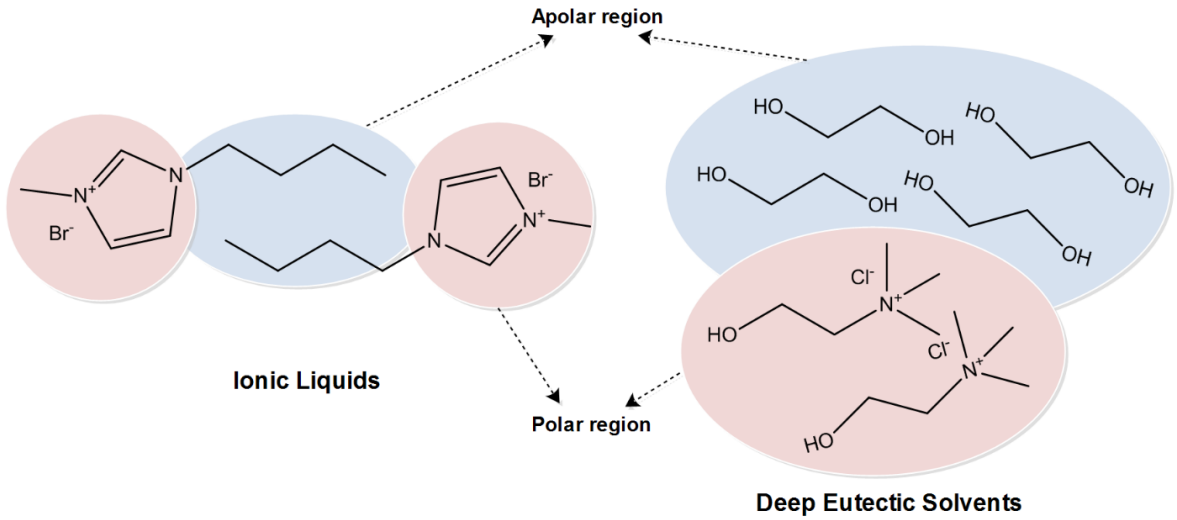

Figure 1.6. Comparison of ionic liquid and DESs.

(i) Phase Behaviour

A solid-liquid phase diagram for a DES system shows the melting temperature vs. eutectic composition. Let us consider a binary mixture of pure compounds such as A and B. The eutectic point is the chemical composition and minimum melting temperature (T_E) at which the melting curves of both compounds intersect (Figure 1.7)

Martins et al. argue that the DESs should be called for combinations having a melting point below the optimum eutectic temperature [23]. Moreover, they said a DES had to be liquid at operational temperature, even if it means a different composition than the eutectic composition. Therefore, it is crucial to have a phase diagram and to know the pure compounds melting properties to determine the optimal solubility curve.

The DESs have melting values from −69 to −149°C[22]. In a 2015 review article, Garcia et al. [43] compiled a list of DES with a melting point below 60°C. The freezing point of a mixture can be affected by several factors, including the HBD used for DESs, the organic salt and anion used, and the molar ratio of organic salt to HBD. The preparation can also affect

the freezing point value, albeit the eutectic composition must stay constant regardless of preparation.

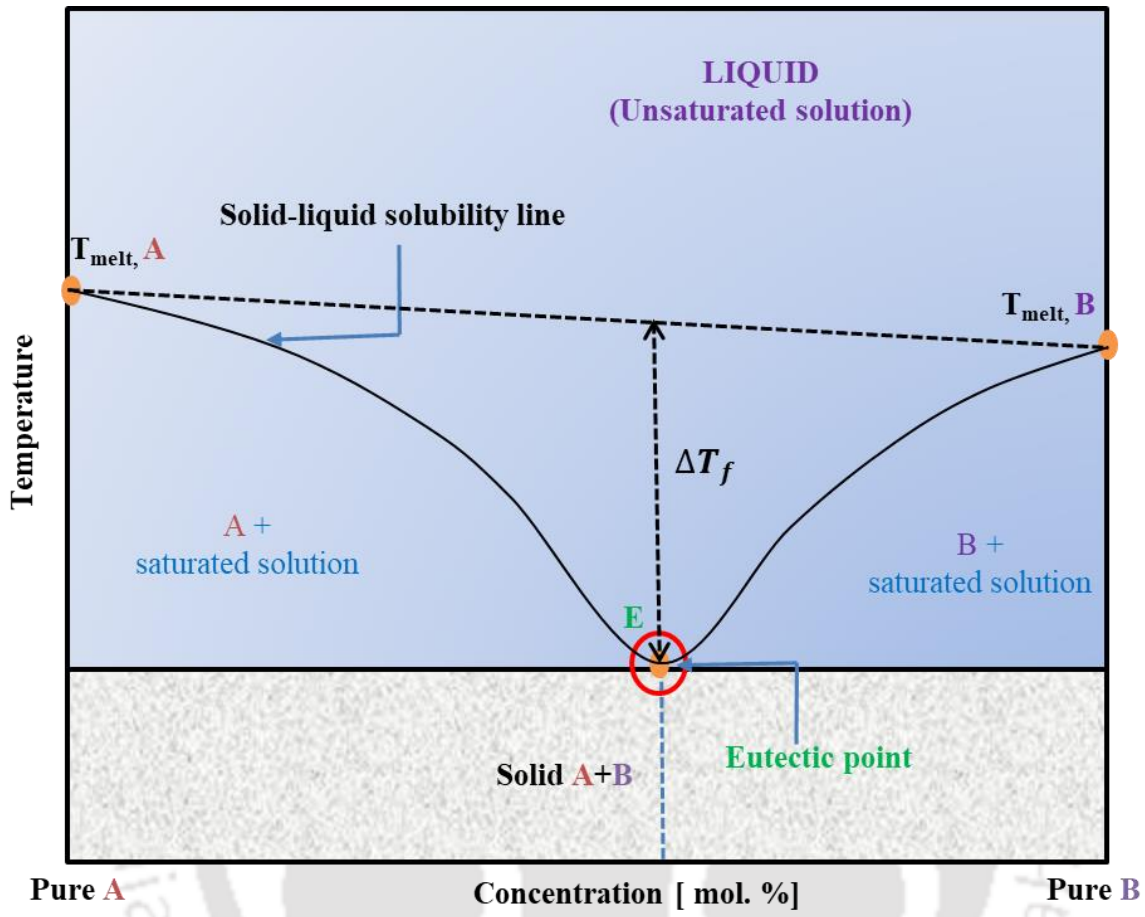

Figure 1.7. A schematic solid-liquid phase equilibrium diagram for a binary (deep) eutectic mixture (composed of components A and B), in terms of temperature as a function of the mole fraction of component B, at constant pressure. The eutectic point of the mixture and the melting points of pure A and pure B components are denoted by 'E', $T_{melt\ A}$, and $T_{melt\ B}$, respectively. The below solid texture areas indicate the regions where solid phases (A or B) are formed. As an example, for choline chloride-urea DES, the values of T_m, ChCl ('ChCl' denotes choline chloride), T_m, urea T_m, T_E, X_E, and urea at 1 atm are 302°C, 133°C, 12°C, and 0.67, respectively [25].

However, no relation was discovered between the melting points of pure components and the freezing point of solvents. Abbott et al. observed that the reduction in freezing point is proportional to the molecular weight of the HBD; therefore, lower molecular weight HBDs had

a more significant effect on freezing temperatures [25]. Abbott and co-workers originally defined temperature depression as the difference between the linear combination of the melting points of the pure components and the real eutectic point (T_1). Still, Martin that it would be more precise to define the temperature depression as the difference between the ideal and the real eutectic point (T_2), as otherwise, any mixture of compounds would be called a DES (Figure 1.8).

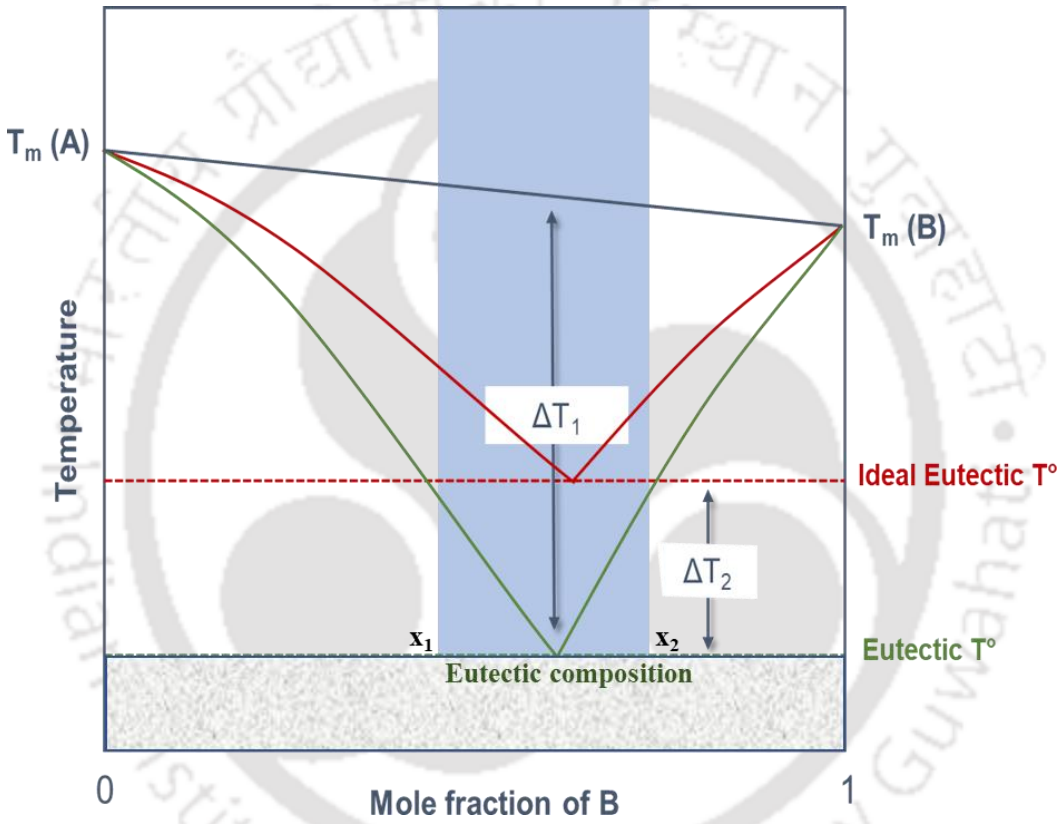

Figure 1.8. Solid-liquid phase diagram representing a simple ideal eutectic mixture (red line) and a deep eutectic mixture (green line).

(ii) Density

One of the most fundamental physicochemical properties of deep eutectic solvents is their density. Most of the reported DESs have densities greater than water, between the ranges of 1.0-1.3 g/cm³ at 25 °C, while DESs based on metal salts have densities in the range of 1.3-1.6 g/cm³[44]. The densities lower than water are achieved for hydrophobic deep eutectics

solvents[31]. The density of DESs exhibits temperature dependence; it decreases linearly as the temperature rises [22, 39, 45, 46]. Additionally, the density is affected by the eutectic mixture's molar ratio and the HBD of choice [39, 45, 47]. When the density of the HBD is less than that of the corresponding DESs, a higher mole percentage of HBD results in a lower density of DES, as stated by Shahbaz et al. [48].

Further, when hydroxyl groups are present in the HBD, the density of the ChCl-based DESs grows with the higher number of hydroxyl groups but reduces when aromatic groups are present. In addition, when the DES is made of acid, its density decreases when the chain length increases [39, 43, 49]. The variation in density of ChCl-based DESs among studies as a function of HBD type. These findings agree with those of Yusof et al. as they demonstrated that TBABr displays a more significant density: alcohol mixture formed DES when an HBD that possess a higher number of hydroxyl groups. The same group further ascertained that the density of HBD chains decreased with increasing length [50].

Chen and coworkers reported that the density of DESs barely responds to variations in ammonium salt alkyl chain length [51]. However, it is evident from the several experiments reviewed by Garcia et al. that the organic salt and its anion affect the density of DES. The phosphonium and bromide salts produce denser DESs than the ammonium and chloride salts[43]. Furthermore, Florindo et al. demonstrated that the density values of DESs prepared by either the heating approach or the grinding method are statistically indistinguishable [39]. Still, the density of the most researched 1:2 ChCl: U-based DES was shown to vary by as much as 4% amongst literature sources: Mjalli et al. undertook a series of research using various theoretical techniques to forecast the density of DES more accurately[52]. The density of type III DES as a function of temperature could be predicted with a high degree of accuracy using mass connectivity index-based correlation that took into account the molecular structures of DES-forming chemicals.

(iii) Viscosity

Another significant and extensively investigated physicochemical characteristic of green solvents has been their viscosity. Most of the reported DES have a high viscosity (> 100 m Pas) at room temperature and ambient pressure, which is mainly attributable to the vast hydrogen bond network between the components. In reality, the viscosity of ChCl: EG (1:2) is extremely low (only 37 mPas at 25°C). In comparison, the viscosities of sugar-based DES are substantial (12730 mPas for 1:1 ChCl: sorbitol at 30°C and 34400 mPas for 1:1 ChCl-glucose at 50°C), and even higher viscosities were reported for metal salts-based DES[22]. However, the hydrophobic DES based on DL-menthol has extremely low viscosities (7.61 mPas at 25°C for 1:3 DL-menthol: octanoic acid)[53, 54]. The viscosity of a eutectic mixture can be affected by many factors, including the components, temperature, and shear stress[27], the molar ratio between the components [55], and the temperature [21].

In addition to the intermolecular forces between the HBD and the ion, the steric effects, with the hole theory, can also contribute to the viscosity. The latter considers the liquid viscosity and ionic conductivity, which are affected by the presence of holes or voids in the fluid[56]. The HBD and the salt can affect the distribution of holes with a specific radius. It has also been suggested that the big pores in DESs contribute to the material's reduced viscosity by facilitating a certain degree of ionic mobility[43]. Notably, different viscosity values were reported by different studies for the same DES (e.g., 152 mPas vs. 527.28 mPas for 1:2 ChCl: Urea at 30°C; and 202 mPas vs. 2142 mPas for 1:1 ChCl: oxalic acid at 40°C; [52]. As Florindo et al.[39] mentioned, these main discrepancies could be related to the preparation technique, the experimental method, and the contaminants.

(iv) Ionic Conductivity

Most DES have weak ionic conductivities (k^2m S cm^{-1} at room temperature), as viscosity is the primary determinant of conductivity. As a result, as the temperature rises, the viscosity decreases, and the conductivity increases [22, 57]. The type of the organic salt, the HBD, the salt's anion, the molar ratio of the two [25], and the addition of water all influence these properties [58].

(v) Surface Tension

Compared to research on other physicochemical aspects, the surface tension of DESs has received insufficient attention. The strength of the intermolecular interactions between the HBD and the HBA as salt strongly influences this feature, making it a critical one. Despite this, very viscous liquids have high surface tensions. According to Garcia et al.[43] and Ibrahim et al.[46], the values concerning the reported DES typically range between 35 and 75 mN m^{-1} at 25 °C. The relatively high values were again observed for sugar-based DES, such as ChCl: D-glucose [59] and ChCl: D fructose, demonstrating their extensive hydrogen-bond network [57]. In addition, the cation type and salt mole fraction impact surface tension since quaternary ammonium salts with more hydroxyl groups or longer alkyl chains have a more significant impact. In addition, the surface tension linearly decreases with increasing temperature [43, 53, 57].

(vi) Polarity

Polarity is essential since it indicates a DESs overall solvation capacity. Despite its significance, the polarity of the DESs was not studied extensively or even addressed until recently. The solvatochromic parameters are used to make an approximation of this property, and they take into account the hypsochromic (blue) or bathochromic (red) shift of UV-vis bands for the negatively solvatochromic dyes (like Reichardt's betaine dye) or the positively

solvatochromic dyes (like the Nile red) [60]. Both the Dimroth and Reichardt polarity scales (ET and ETN)[60, 61]and the Kamlet and Taft multiparameter scale (the hydrogen bond donating ability, the hydrogen bond accepting ability, and the dipolarity/polarizability") are widely employed [62, 63]. Nile red and Reichardt's betaine dyes are two of the most often used probes in calibrating the Dimroth and Reichardt's scale. Kamlet and Taft's multiparameter scale uses chemicals like 4-nitroaniline and N, N-diethyl 4-nitroaniline to determine the parameters. It is important to note that the polarity scales are not standardized and instead rely on the specific solvatochromic probe [64].

1.8 Effect of Water in DESs

Although water is ubiquitous and some DESs and their forming components have a hygroscopic nature, the eutectic solvents will inevitably contain water [39, 65]. While water is generally considered a problem in DESs, numerous studies have intentionally added water to their solvents to tweak their properties to match the requirements of specific applications. In many of these cases, adding water improved the DESs performance. However, because DESs are synthesized in various working environments, the introduction of water alters the physicochemical properties and may compromise their stability[66]. This highlights the critical relevance of investigating the impact of water on eutectic systems. Water's effect on the physicochemical properties of DESs and the features of their supramolecular organizations are discussed in this section.

It is now apparent that the physicochemical properties of DES, at both small and large levels, are affected by the existence of water. Since binary mixtures of DES and water are already widely used, studying their interactions is vital. The increasing research of DES-water mixtures over the past few years can be attributed to the fact that they can mitigate the drawbacks of DES, such as their relatively high viscosity, without sacrificing any of the

compound's other desirable qualities. Due to water's strong polarity and propensity to interact with the hygroscopic components of the eutectic system, it is crucial to investigate if and how water influences the intra- and intermolecular interactions underlying the supramolecular network of DES. Investigations into water's impact on the DES system are few, despite its importance, but recently, the primary focus was on eutectics based on ChCl as an HBA. Different analytical techniques, including nuclear magnetic resonance (NMR), Brillouin spectroscopy (BS), total neutron scattering (NTS), along with molecular dynamics (MD) simulations, were used to investigate structural changes in DESs due to water. Some research has claimed that as water is added to DES, the system changes from "water-in-DES" to "DES-in-water." In contrast, other research has suggested that at a particular hydration level, DES changes into an aqueous solution after a particular concentration of water in DESs. In the former, water is considered another HBD [67-69], allowing it to join the DES's network and augment the HBA and HBD's hydrogen bonds even at low water contents[70, 71].

Water has a natural propensity to interact with the molecules that make up DES; however, this reduces the interactions that generally prevail in a DES supramolecular structure as the concentration of water increases. Multiple studies on ChCl-based DES (such as ChCl: U. ChCl: G, ChCl: EG, and ChCl: LA) have revealed that chloride anions preferentially hydrate. This is supported by several studies [72-75]. Nonetheless, the hydration level at which the changeover occurs for a given DES can vary with the water concentration in Solvents. For ChCl: U, the critical concentration ranged from 15% to 51%. Not enough studies are performed to reliably compare the onset and offset of different DESs. The structure of DES-water mixtures has not been shown to change with temperature in a small number of investigations [71, 76]. However, this transformation is anticipated to occur in all DES aqueous mixtures. Further, research on additional DES is necessary because the water content of the transition varies depending on the HBA and HBD types and their molar ratio [83]. In addition, the scope of

what may be achieved in fine-tuning DES water combinations for specific applications can only be increased with a thorough comprehension of water's impact on the structural arrangement of DES.

1.9 DESs as Solvents in a Multitude of Applications

Most of the studies focus on 'Type III' DES, and they are used in familiar places where they have been used in metal electrodeposition [77] and separation-extraction applications, Including fuel purification[78] and carbon dioxide sequestration[43]. DESs have also been used in inorganic synthesis and as an alternate organic reaction medium for classical and metal-catalyzed reactions[43, 47]. Among Type III DESs, ChCl: urea (reline), ChCl: glycerol (glyceline), and ChCl: ethylene glycol (ethaline) is the most commonly used green solvents[30]. These DESs are considered the most practical systems since they are based on relatively inexpensive and widespread HBDs like urea, the most widely used nitrogenous fertilizer globally, and have amenable physical features.

Similarly, the choline cation (usually as the choline chloride salt ChCl) is created as a megaton-scale supplement for animal feed by a one-step, gas-phase reaction involving HCl, trimethylamine, and ethylene oxide. Although the DES, as mentioned above, are typically benign, biodegradable, and non-cytotoxic [59, 79], they are not entirely green solvents, and the petrochemical feedstock must be noted. Among the first of these was the 2011 coinage of the term "natural deep eutectic solvent" (NADESs) by Choi et al.[28]; NADES are solvents that are derived totally from natural ingredients. Type III DESs were reportedly synthesized from over 30 combinations of naturally occurring carboxylic and amino acids, sugars, and water. In 2013, this same team presented further NADESs and showed their usefulness in specific extraction-separation applications [29]. Interestingly, Choi et al. postulated that plants would produce similar DESs in desiccating circumstances, where they would serve as a

cryoprotectant; subsequent work by Francisco et al. demonstrated the synthesis of many NADESs from sugar-amino acid mixtures[80]. It has been suggested that NADESs are the ideal environmentally friendly solvent thanks to their 'drinkable' components and renewable feedstock. However, there are drawbacks to using NADES; for example, the biofuel industry has discovered that using arable land to produce sugars for fuel and solvents can be problematic. Second, due to Maillard and caramelization processes and pyrolysis, NADESs have low thermal stability since they are a combination of natural acids and sugars.

Finally, the high water content of many NADESs raises an important question: are these systems indeed DES, or just aqueous dilutions of the separate DES components? Abbott et al. have presented innovative and more economically feasible DESs built around sodium salts with inexpensive and widely accessible HBD molecules. They hypothesize that a type IV DES combination of NaCl and glycerol would be the most cost-effective, rather than the more often used cholinium as HBD in DESs [81]. The suggested DES of NaCl and glycerol was proven unfeasible. Still, it was discovered that group 1 metal salts, in particular sodium acetate, may create liquids with DES-like physical features but with no real eutectic point. Whether or not these systems constitute DES is a semantic matter; what would be noteworthy and beneficial is the discovery of a DES or IL-analogue that can be produced cheaply and sustainably from bulk commodity chemicals.

1.9.1 Extraction of Aromatic Compounds using the Deep Eutectic Solvents

It is critical to create novel methods for efficiently separating these challenging 'hard to separate' liquid systems based on their physical characteristics. In recent years, researchers across the globe have focused more on a separation strategy that uses innovative solvents, including ionic liquids and deep eutectic solvents (DESs). The generated DESs structure and properties are sensitive to the type of HBA and HBD used and the molar ratio. DESs can fulfill

the separation needs of a wide range of systems due to their tunable nature. Here we elaborated on the application of DESs in non-polar solutes, mildly polar solutes, and polar solutes, all of which are examples of difficult-to-separate liquids.

1.9.2. Hard to Separate Liquid Systems

Liquid systems that are 'hard to separate' are ones in which individual components can not be extracted using conventional methods. Separation systems can be classified into three broad classes based on the polarity of the solutes, mainly non-polar, mildly polar, and polar solutes. Screening charge density distributions, also known as σ-profiles[82], are used to characterise the charge-related and molecule-specific features of the three common solutes, whose polarity depends on their molecular structure (Figure 1.9). The σ-profile is the probability distribution of molecular surface segments with a specific charge density. This is derived from a quantum chemical calculation performed within the conductor-like screening model (COSMO) solvation model {Klamt, 1995 #176}.

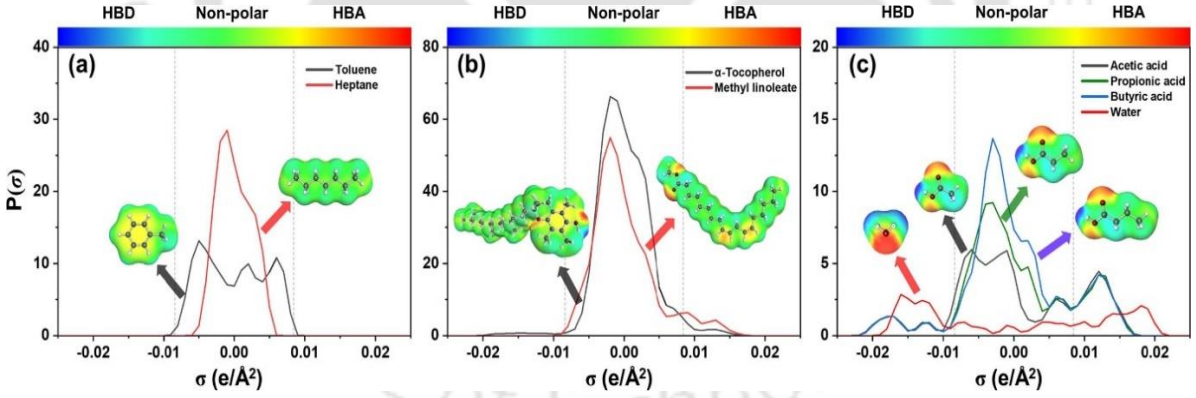

Figure 1.9 Three types of separation systems can be classified based on solute polarity. (a) Typical non-polar solute separation system: separation of aromatic and non-aromatic compounds. (b) Typical mildly polar solute separation system: recovery of vitamin E from deodorizer distillate. (c) Typical polar-solute separation system: recovery of volatile fatty acid from aqueous solution.

A non-polar solute is a molecule whose σ-profile is predominately located in the nonpolar region. Aromatic compounds are the most common type of nonpolar solute. There is

a significant need in the petrochemical and coal-chemical sectors for the separation of aromatic and non-aromatic hydrocarbons. However, separation is difficult since their boiling temperatures are so close together that they form azeotropes [83, 84].

The σ-profile of any given mildly polar solute would then exhibit a prominent peak distributed in the non-polar region, in addition to narrower peaks in the hydrogen bond donor (HBD) and hydrogen bond acceptor (HBA) regions, because all such solutes will have a non-polar backbone with functional groups (such as hydroxyl, carboxyl, or amino group). For example, vitamin E is typically sourced from deodorizer distillates of vegetable oils [85, 86]. Vitamin E has low selectivity and recovery efficiency because of the comprehensive non-polar backbone of many other property-similar components, such as fatty acid methyl esters.

Polar solutes are functional groups in hydrophilic substances interacting strongly with water via hydrogen bonds. The HBD and HBA areas both show prominent peaks in their σ-profiles. For instance, short-chain fatty acids, which are used as intermediates in synthesizing value-added chemicals, can be produced by the fermentation of organic waste streams [87]. However, due to their strong interactions with water and low concentrations, volatile fatty acids are difficult to extract from diluted aqueous solutions.

1.9.3. Application of DESs for Non-polar Aromatic Solute Extraction

Aromatic chemicals include aromatic hydrocarbons and heterocyclic sulphur-containing compounds, which are excellent examples of non-polar solutes. Obtaining aromatic hydrocarbons, vital compounds, is often done by distilling petrochemical products that already contain aromatics and alkane hydrocarbon mixtures. Due to their similar boiling points and propensity to form azeotropes, it is not easy to separate effectively, and this process is highly energy-intensive. Several environmental regulations impose severe limits on the amount of heterocyclic sulphur-containing compounds and aromatics present in the fuel. However, conventional hydrotreating is ineffective at low concentrations for deep desulfurization [88].

Therefore, the separation of aromatics and heterocyclic sulphur-containing compounds has been studied extensively using liquid-liquid extraction with DESs as extracting agent.

The concentration of aromatic compounds in a system lower than 20 wt.% is typically extracted using liquid-liquid extraction[89]. When the aromatic concentration is less than 20 wt.%, no feasible approach has been developed. The liquid-liquid extraction is more preferable due to its cheap energy cost and lack of change in physical characteristics and chemical structures[90]. In LLE, the selection of a suitable solvent is of utmost importance. Organic solvents such sulfolane, N-methylpyrrolidone, ethylene glycols, furfuryl alcohol, and N-formylmorpholine were frequently employed as organic solvents [83]. However, their high toxicity, flammability, and volatility could lead to issues such as volatile organic compound emissions and environmental pollution. Alternatively, DESs have emerged to separate aromatics from aliphatic compounds.

To separate mixtures of light aromatics and alkanes, several DESs have been explored as extracting agents [84, 91, 92], where the HBA ranged from choline salt to quaternary ammonium/phosphonium salt. Typically, HBD includes glycols, alkane diols, sugars, and organic acids. For this reason, a solvent with a high selectivity and distribution coefficient is always preferred. Therefore, the selectivity and distribution coefficient were studied to understand how varying the HBA/HBD ratio, solvent-to-feed ratio, initial aromatic concentration, extraction temperature, and other variables. It was discovered that DES structure and components affected aromatics removal efficiency. Toluene was isolated from a toluene/n-heptane mixture using DESs (Wang et al., [93]). Selectivity of toluene extraction was enhanced by the combination of HBA containing a large anion, a short chain, and a tiny central atom in the cation, and HBD containing appropriate functional groups and alkyl chain position. Choline or tetraethylammonium salt (e.g., ChCl, ChBr, TEAB, and TEAC) as HBA generated DES with higher selectivity to toluene but a lower distribution coefficient than sulfolane.

Comparatively, the TBPB-based DES showed a higher distribution coefficient but lower selectivity than sulfolane.

The separation of aromatics and non-aromatic components in diesel is just as crucial as the extraction of light aromatics (benzene, toluene, ethylbenzene, and xylene) from alkanes. After separation, non-aromatic components can be used as blending components to enhance the quality of diesel. In contrast, aromatics can be used as raw materials for hydrocracking to produce light aromatics, maximizing the benefits of catalytic cracking of diesel. To extract tetralin from a model light cycle oil, Wu et al. [94] developed several DESs using TBPB as the HBA and carboxylic acids as the HBD. Different HBDs and mole ratios of HBA to HBDs were investigated for potential impacts on extraction efficiency. Extraction performance was found to be good and stable with TBPB: LA (1:4) throughout the extraction and regeneration operations.

1.9.4 Extraction of Heterocyclic Sulphur Containing Compounds from Diesel Fuels

Deep desulfurization is essential for extracting trace sulphur-containing molecules from fuels because their presence could lead to environmental damage during combustion. Due to their high steric hindrance and limited reactivity, heterocyclic sulphur compounds are difficult to remove using standard hydrotreating methods. Extensive research on liquid-liquid extraction with DESs for desulfurization has shown outstanding performance [95-97].

For the extractive desulfurization of model fuel (a mixture of benzothiophene and *n*-octane), Li et al. [95] developed a variety of ammonium-based DESs. As shown in figure 1.10, the results showed that the HBA and HBD structures significantly affect the desulfurization efficiency. Compared to ChCl-based DES, the efficiency of TBAC-based DES, which has a longer chain length, is much greater. The TBAC: PEG (1:2) single-stage desulfurization efficiency is as high as 82.83% when polyethylene glycol is employed as HBD. Deep desulfurization was achieved by reducing the sulphur level of the model fuel to less than 8.5

ppm via a five-stage extraction process. The desulfurization efficiency can even reach as high as 89.53% in just one cycle, as discovered by Li et al. [96], who supplemented the DES with a three-component metal chloride.

DESs showed good desulfurization efficiency for various sulphur compounds. Thiophene, benzothiophene, and dibenzothiophene each had a 72%, 81.75%, and 80.47 % single-stage desulfurization efficiency for the DES TBPB: FA (1:1)[98]. Desulfurization efficiency was studied concerning oxidative desulfurization, with olefins and aromatics representing the composition of real fuel [99]. Extractive desulfurization is superior to the actual fuel despite a slight decline in efficiency compared to oxidative desulfurization.

Fuels were simultaneously dearomatized and desulfurized using DESs as an extracting agent due to the DESs high efficiency in extracting aromatic hydrocarbons and sulphur compounds from fuels. Toluene, thiophene, and quinoline were extracted using the DES MTPPB:TrEG (1:4) by Warrag et al.[100]. Based on the calculated distribution coefficient and selectivity, MTPPB:TrEG (1:4) exhibited exceptional quinoline extraction potential but comparatively poor performance for thiophene and, especially, toluene. Furthermore, several DESs reported that denitrification performed better than desulfurization and dearomatization, indicating that the two processes are, in fact, complex to isolate.

In conclusion, several DESs showed promising extraction efficiency while extracting aromatic compounds from fuel oil. It should be noted that in addition to evaluating the extraction efficiency for dearomatization and desulfurization, the solubility of the DES in fuel should also be taken into account, as the clean fuel is sensitive to solvent contamination. It is helpful that DES is less soluble in fuel and can be easily separated out of raffinate after production. In this study, we developed solvents that can extract the aromatic or sulphur compounds at ppm level.

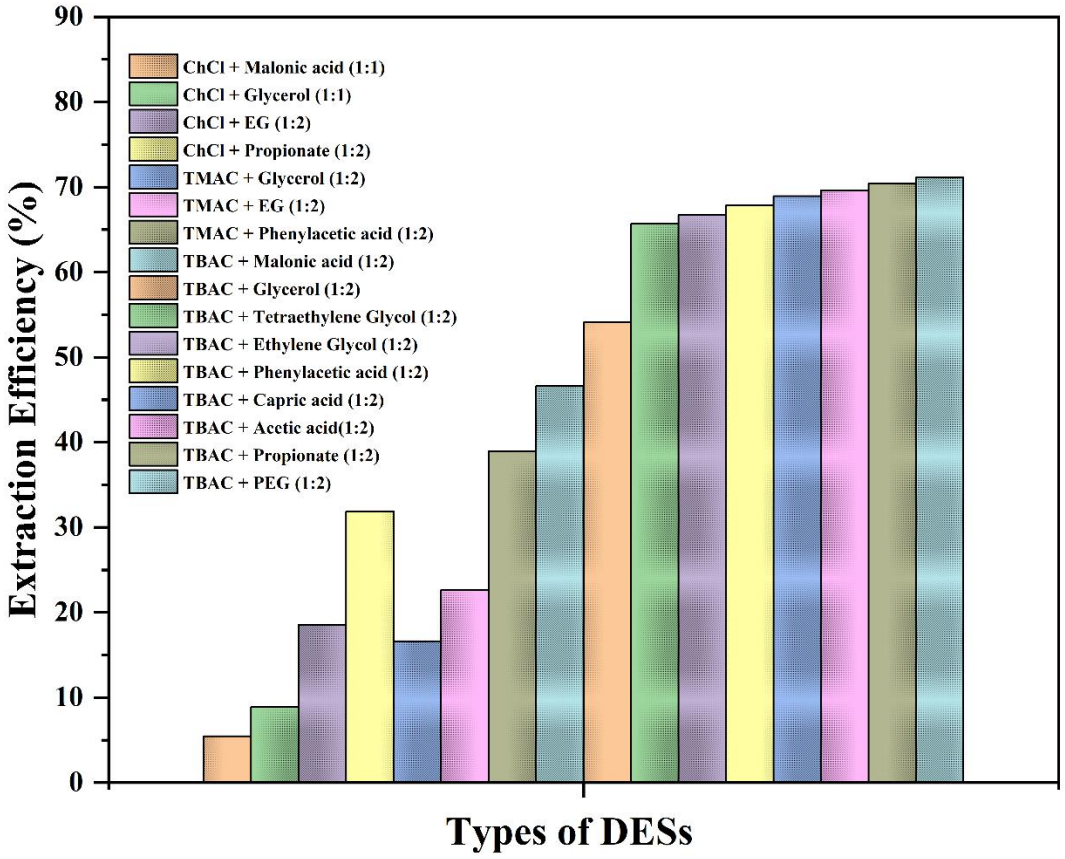

Figure 1.10. The desulfurization extraction efficiency using the different DESs.

1.10 Application of DESs in the Dispersion of Complex Heavy Fraction

With the depletion of more readily available conventional resources, heavy petroleum fraction has become a significant replacement feedstock for the petrochemical and liquid fuels industries. To be used as a feedstock, the material must be extracted from its geological matrix, fractionated, and greatly improved, typically by methods that are both energy-intensive and detrimental to the natural environment at the refinery. Solubility partitioning of heavy petroleum (SARA method) provides two main fractions. Maltenes are soluble in *n*-alkanes and can be further fractioned into what is incorrectly called saturates, volatiles, aromatics, and resins. Asphaltene makes up the bulk of the heavy crude oil and is the most difficult to work with because of its polarity and solubility in selective aromatic solvents. More importantly, the

asphaltene fraction directly promotes numerous undesirable physical and chemical outcomes during upgrading. These include precipitation during transport, storage, and thermal coke production, which leads to material loss and catalyst deactivation [101-103]. Even as renewable energy sources move closer to economic viability, fundamental research into asphaltene solvation is essential for optimizing the use of heavy petroleum resources and ensuring sustainability.

Asphaltene is a complex material, making it extremely difficult to determine its precise molecular arrangement at the atomic level. Recent separation and analytical technology developments have uncovered many of the asphaltene bulk material's structural components but not the molecules themselves. Asphaltene molecules contain medium to large PAHs, terminal and tethering saturated alkyl chains, heteroatoms (sulphur, nitrogen, and oxygen, in decreasing concentration), polar functional groups (e.g., alkyl carboxylic acids), biomarker residues (elaborated porphyrins, hopanes, etc.), and coordinated transition metals (principally vanadium and nickel)[104].

Asphaltene structures have been explained by two competing hypotheses, the merits of which are still contested in the academic literature. The first model to be presented was the "continental" model developed by Yen-Mullins[105]. According to this model, the "typical" asphaltene molecule possesses a big polycyclic aromatic/heteroaromatic core that is then surrounded by long alkyl chains and peripheral functionality. The significant aggregation pattern for such a system is face-to-face π–π stacking interactions between the aromatic centers (figure 1.11c). However, the "continental" concept cannot account for some critical properties. Under mild conditions, carbon-carbon bonds can be broken during pyrolysis, which is consistent with the breakdown of weak single bonds rather than the destruction of massive, condensed aromatic islands[106, 107]. It is implausible that massive island structures would

form at the observed temperatures, given thermal cracking of asphaltene under these conditions results in compounds with monocyclic to pentacyclic aromatic ring systems containing short-chain alkyl substituents.

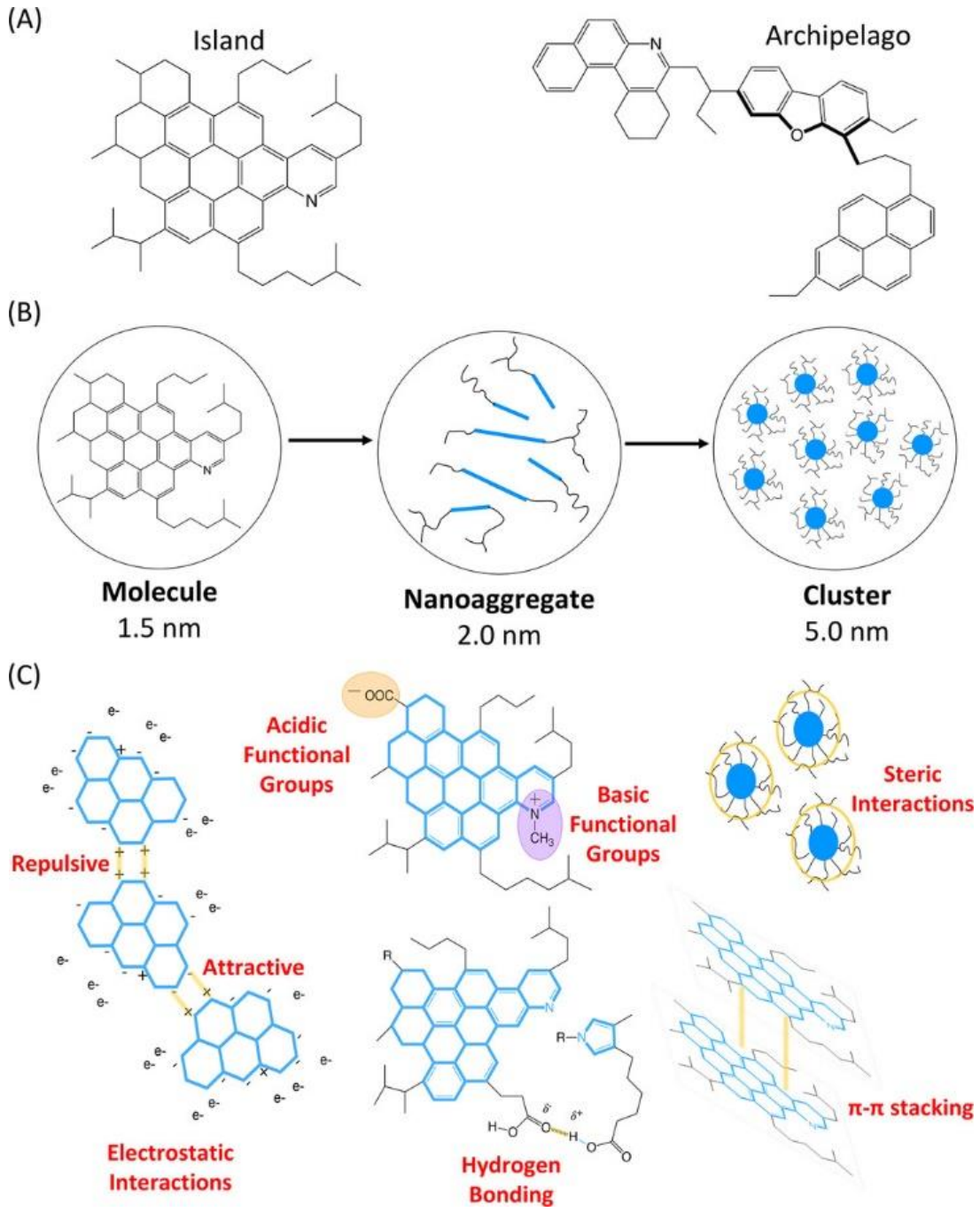

Figure 1.11. Schematic representation of Yen Mullin model [105] (b) asphaltene aggregation behaviour explained (c) the typical primary interaction between the different moieties responsible for the aggregation of asphaltene molecules.

In recent times, another model has emerged; it has been termed the "archipelago" model. Based on this theory, a typical asphaltene constituent is made up of two or more smaller, interconnected, polycyclic aromatic or heteroaromatic "islands" that are tethered by saturated alkyl bridges and further adorned with heteroatom functionality and short alkyl side chains[108]. This structural model is evidenced in aggregation driven by hierarchical cooperative association (figure 1.11c), which includes acid-base interactions, hydrogen bonding, hydrophobic interactions, π–π aromatic stacking, small molecule inclusion complexes (clathrates), and coordination to transition metals and metal complexes. Although, the archipelago model does a better job of explaining asphaltene experimental behaviour. The combination of the two models almost definitely represents something closer to the truth.

Because of the discovery of continental and archipelago molecules in native asphaltene, scientists have worked hard to create and synthesize more realistic model compounds that reflect this new topological definition and functioning. There is currently no available detailed study of synthetic asphaltene model structures. We focus on the logical design principles and state-of-the-art synthetic methodology required to develop representative analogues structure of asphaltene, to create a green solvent that can disperse the asphaltene in crude oil and further perform the study of chemistry responsible for the aggregation of heavy fractions in crude oil.

1.11 Objective of the Thesis

This work reports the computational and experimental framework for analysing a wide range of thermodynamic, structural, extraction, and transport parameters of DESs. It also includes valuable insights into the intermolecular interactions of DESs, aliphatic and aromatic compounds, including the heavy fraction of crude oil and the impact of these interactions on macroscopic properties. As a result, this thesis addresses both experimental and theoretical

aspects of aromatic compounds. In view of the existing literature and knowledge gap indicated in the previous sections, the following objectives have been established for the thesis study.

1. *To understand the liquid structure of aromatic and aliphatic compounds in deep eutectic solvents at the molecular level using molecular dynamics and quantum chemical calculations.* ***(Chapter-2)***
2. *COSMO-SAC model-based screening, adoption of appropriate DES, quantum chemical insights, and liquid-liquid extraction experiment for the reduction of aromatics and sulphur compounds from n-hexane and diesel fuel.* ***(Chapter-3 and 4)***
3. *The classical molecular dynamic (MD) simulation technique to investigate the equilibrium interphase behaviour of the ternary system with respect to DES-rich and hydrocarbon-rich phases.* ***(Chapter-5)***
4. *Extraction and characterisation of asphaltene structure and screening of NAtural Deep Eutectic solvents (NADES) utilizing the COSMO-RS model for dispersion.* ***(Chapter-6)***
5. *Quantum chemical calculation and experimental understanding of aggregation behaviour of asphaltene.* ***(Chapter-6)***

1.12 Thesis Overview

The current thesis is organized into the following chapters, and a schematic outline of the current thesis is given in figure S1.

In this thesis, we shall give novel and informative information on the intermolecular interactions of DESs and the influence of these interactions on the macroscopic properties, as well as a computational framework for analysing a wide range of thermodynamic, structural, and transport features of DESs. **Chapter 1** briefly reviews the inception of deep eutectic solvents and exploitation in the field of solubility and extraction of aromatic compounds. The

asphaltene solvation and precipitation inhibition were studied using the natural deep eutectic solvents.

The solute's impact on the liquid structure of choline-chloride based DESs is covered in detail in **chapter 2**. Compared to experimental studies, there are fewer theoretical and computational investigations on the solvation of aromatic and aliphatic compounds by DESs. The solubility characteristics of DESs based on choline chloride of varying aliphatic and aromatic compositions were estimated in this work using MD simulations. When determining a molecule's polarity (the strength of its intermolecular interactions) and, by extension, its miscibility with other molecules, one can use solubility as a thermodynamic parameter. It is helpful to have a wide range of HBA: HBD combinations that may be used to formulate the DESs and allow us to tune the physical properties by varying their molar ratio. It also necessitates an in-depth understanding of the structural characteristics of these solvents and their interactions with aliphatic and aromatic ring compounds. Therefore, it is necessary to have knowledge of the microscopic forces and structural changes of solute-solvent (DESs) interactions to effectively carry out solvation analysis in designated solvents. It has been shown that theoretical studies are vital in evaluating the solubility of various substances and helpful in designing the most favourable solvents. In the following sections, we have conducted an in-depth analysis of the molecular interactions between benzene, thiophene, aliphatic hydrocarbon, and DESs with varied molar ratios of monoethanolamine as an HBD and Choline chloride as HBA. The solubility data of the benzene, thiophene, and hexane were compared with the literature data of monoethanolamine-based DES at 298.15K and atmospheric pressure. After that, the solute-solvent interactions was studied using ^{1}H NMR and 2D ^{1}H–^{1}H NOESY (Nuclear Overhauser Effect Spectroscopy).

After understanding the liquid structure of DESs, the effect of adding aliphatic and aromatic compounds in terms of solute-solvent interaction was studied and reported. In

chapters 3-4, we determined the DESs solubility parameters by measuring the enthalpies of vaporisation, namely the Hildebrand[152] and Hansen[153] solubility parameters. When calculating solubility, Hansen uses a value that takes into consideration all intermolecular interactions (including dispersion, polar, and hydrogen bonding), while Hildebrand utilizes an average. This current work aims to estimate the suitability of deep eutectic solvents as extracting agents for the extraction of benzene and benzothiophene from representative *n*-hexane as well as diesel components such as *n*-decane, *n*-dodecane, and *n*-hexadecane. Initially, DES was synthesized by adding a Hydrogen Bond Acceptor (HBA), namely methyltriphenylphosphonium bromide (MTBP), along with ethylene glycol as a hydrogen bond donor (HBD) in a specific molar ratio of 1:4. The liquid−liquid equilibrium (LLE) data of four ternary systems {*n*-hexane + benzene + DES}, {*n*-decane + benzene + DES}, {*n*-dodecane + benzene + DES}, {*n*-hexadecane + benzene + DES}, and {*n*-decane + benzothiophene + DES} were then determined at T = 25°C and atmospheric pressure (p=0.1 MPa). To measure the separation suitability of the considered DES, the solute distribution coefficient, selectivity, and extraction efficiency was obtained from the experimental LLE data. The quantum computation-based COSMO-SAC model was then used to correlate the LLE experimental data. Thereafter, the COSMO-SAC based predicted sigma profile was used to provide insight into the interaction mechanism of representative diesel components and benzene. Finally, the extraction mechanism of benzene using DES was determined with the help of FT-IR and quantitative ^{1}H NMR.

Therefore, we have initiated a computation study to evaluate the interactions between DES and individual aliphatic and aromatic sulphur compounds using the COSMO-SAC model and Hansen solubility parameters. Finally, the extraction mechanism is discussed based on the molecular scale for which the quantum mechanical (QM) calculations were performed to understand how specific functional groups or metal components within conventional DES

interact with organosulphur compounds to control the extraction of these target molecules from sulphur contaminated liquid fuels. We systematically studied the different clusters of DES with the aliphatic and aromatic sulphur compounds, transfer of electron density in terms of charge transfer, interaction energies for different complex clusters, and bond lengths with the interaction between the different species of clusters. Our findings provide crucial atomistic insight into the interactions between DES and BT, which are vital for efficient aromatic sulphur compound extraction from sulphur-contaminated liquid fuels utilizing DES as the extractive medium in an extractive desulphurization process. Finally, quantitative ^{1}H NMR (Figure A1) and ^{13}C NMR (Figure A1) were used to check the purity of synthesized DES.

After understanding the extraction mechanism experimentally, atomistic MD simulations were carried out to study the transport of the solute(aromatic) to the DES phase. The present study in **chapter 5** aims to extract benzene from hexane using DES by classical MD simulations at 318.15 K and 1 atm conditions to understand the detailed molecular mechanism associated with the process. The prepared DES consists of the hydrogen bond acceptor (HBA; methyltriphenylphosphonium bromide, MTPB) and hydrogen bond donor (HBD; ethylene glycol) at a molar ratio of 1:4. The MD simulations were used to investigate the equilibrium phase behaviour of the DES + benzene + hexane ternary system with respect to solvent rich and hydrocarbon-rich phases.

Three different concentrations were considered from the reported experimental runs to observe the effect of feed concentration, which gave high selectivity and distribution coefficient values. The non-bonded interaction energies of different species and the structural properties such as radial distribution functions, spatial distribution functions (SDFs), and the average number of hydrogen bonds are then computed. To make a system comparable, atomic-scale simulation is performed at orders of nanoseconds. The trajectory velocities are computed after every ~1 fs, and real-time data is recorded for complete simulation. Phenomena occurring

at the atomic scale level occur within a fraction that is difficult to capture with a digital instrument. Therefore, theoretical calculations and simulations aim to validate this phenomenon through ensemble theory or statistical mechanical framework. The LLE simulation results defined in this research aim to study one such result or trajectory out of the numerous possible events in such a simulation environment. This essentially connects properties generated by chemical engineers, namely, the activity coefficient, implicitly to the computation of mole fractions using first principles.

After studying light aromatic and sulphur compound extraction using DESs, **chapter 6** reports the asphaltene dispersion studies. Asphaltene is one of the most polar and heavy fractions of crude oil that is complex from a molecular perspective. It starts to aggregate in crude oil to contribute to their disruption and significantly change their viscosity throughout the operation, shipment and refinement. The natural deep eutectic solvents (NADESs) with the combination of Hydrogen Bond Donor (HBD) and Hydrogen Bond Acceptor (HBA) have recently gained increasing interest as green solvents to address the different issues pertaining to extraction and dissolution. The selection of the model molecular structure is the crucial step in the COSMO-RS based screening of potential solvents for asphaltene dissolution.

The present study proposes a two-model structure of asphaltene based on the archipelago model and an island-type structure used in the literature. Initially, we predicted archipelago model-based asphaltene structure and then validated the same using DFT calculation based on theoretical IR-spectra. This was then validated with FT-IR spectra of experimentally obtained asphaltene extracted from crude oil. The several combinations of HBA and HBD were screened through the COSMO-RS model through various thermodynamic physical properties for their ability to prevent aggregation through dissolution. Thereafter, the experimental solubility measurement was performed, and different analytical techniques were adopted to understand the molecular-level interactions between green solvents and the heavy

fraction of crude oil. The FT-IR and 2D-NMR tools were then used to analyse the solvent's interaction chemistry with asphaltene to acquire a mechanistic, more profound knowledge of how various active sites interact to enhance the solubility of asphaltene. Finally, **Chapter 7** summarises the significant findings of the thesis work and a discussion of potential avenues for future research. An overall schematic of the entire thesis is given below in figure S3.

References

1. Makitra, R., *Reichardt, C., Solvents and Solvent Effects in Organic Chemistry, Weinheim: Wiley-VCH, 2003, 630 p.* Russian journal of general chemistry, 2005. **75**(4): p. 664-664.
2. Hayes, R., G.G. Warr, and R. Atkin, *Structure and nanostructure in ionic liquids.* Chemical reviews, 2015. **115**(13): p. 6357-6426.
3. Soper, A.K., *The radial distribution functions of water as derived from radiation total scattering experiments: Is there anything we can say for sure?* International Scholarly Research Notices, 2013. **2013**.
4. Tanaka, K., *Solvent-free organic synthesis*. 2009: John Wiley & Sons.
5. Peach, J. and J. Eastoe, *Supercritical carbon dioxide: a solvent like no other.* Beilstein journal of organic chemistry, 2014. **10**(1): p. 1878-1895.
6. Clarke, C.J., et al., *Green and sustainable solvents in chemical processes.* Chemical Reviews, 2018. **118**(2): p. 747-800.
7. Plechkova, N.V. and K.R. Seddon, *Ionic liquids: "designer" solvents for green chemistry.* Methods and Reagents for Green Chemistry, 2007: p. 105-130.
8. Sheldon, R.A., *The E factor 25 years on: the rise of green chemistry and sustainability.* Green Chemistry, 2017. **19**(1): p. 18-43.
9. Rogers, R.D. and K.R. Seddon, *Ionic liquids--solvents of the future?* Science, 2003. **302**(5646): p. 792-793.
10. Walden, P., *Molecular weights and electrical conductivity of several fused salts.* Bull. Acad. Imper. Sci.(St. Petersburg), 1914. **1800**.
11. Plechkova, N.V. and K.R. Seddon, *Applications of ionic liquids in the chemical industry.* Chemical Society Reviews, 2008. **37**(1): p. 123-150.
12. MacFarlane, D.R., et al., *New dimensions in salt–solvent mixtures: A 4th evolution of ionic liquids.* Faraday discussions, 2018. **206**: p. 9-28.
13. Mandai, T., et al., *Criteria for solvate ionic liquids.* Physical chemistry chemical physics, 2014. **16**(19): p. 8761-8772.
14. Ueno, K., et al., *Glyme–lithium salt equimolar molten mixtures: concentrated solutions or solvate ionic liquids?* The Journal of Physical Chemistry B, 2012. **116**(36): p. 11323-11331.
15. Shimizu, K., et al., *Structural and aggregate analyses of (Li salt+ glyme) mixtures: the complex nature of solvate ionic liquids.* Physical Chemistry Chemical Physics, 2015. **17**(34): p. 22321-22335.
16. Chen, Z., et al., *Structural effect of glyme–Li+ salt solvate ionic liquids on the conformation of poly (ethylene oxide).* Physical Chemistry Chemical Physics, 2016. **18**(22): p. 14894-14903.
17. Murphy, T., et al., *Bulk nanostructure of the prototypical 'good'and 'poor'solvate ionic liquids [Li (G4)][TFSI] and [Li (G4)][NO 3].* Physical Chemistry Chemical Physics, 2016. **18**(26): p. 17224-17236.
18. Abbott, A.P., et al., *Ionic liquid analogues formed from hydrated metal salts.* Chemistry–A European Journal, 2004. **10**(15): p. 3769-3774.
19. Estager, J., J. Holbrey, and M. Swadźba-Kwaśny, *Halometallate ionic liquids–revisited.* Chemical Society Reviews, 2014. **43**(3): p. 847-886.
20. Marsh, K.N., J.A. Boxall, and R. Lichtenthaler, *Room temperature ionic liquids and their mixtures—a review.* Fluid phase equilibria, 2004. **219**(1): p. 93-98.
21. Abbott, A.P., et al., *Novel solvent properties of choline chloride/urea mixtures.* Chemical communications, 2003(1): p. 70-71.

22. Zhang, Q., et al., *Deep eutectic solvents: syntheses, properties and applications.* Chemical Society Reviews, 2012. **41**(21): p. 7108-7146.
23. Martins, M.A., S.P. Pinho, and J.A. Coutinho, *Insights into the nature of eutectic and deep eutectic mixtures.* Journal of Solution Chemistry, 2019. **48**(7): p. 962-982.
24. Abbott, A.P., et al., *Preparation of novel, moisture-stable, Lewis-acidic ionic liquids containing quaternary ammonium salts with functional side chainsElectronic supplementary information (ESI) available: plot of conductivity vs. temperature for the ionic liquid formed from zinc chloride and choline chloride (2: 1). See http://www. rsc. org/suppdata/cc/b1/b106357j.* Chemical Communications, 2001(19): p. 2010-2011.
25. Abbott, A.P., et al., *Deep eutectic solvents formed between choline chloride and carboxylic acids: versatile alternatives to ionic liquids.* Journal of the American Chemical Society, 2004. **126**(29): p. 9142-9147.
26. Abbott, A.P., et al., *Ionic liquids based upon metal halide/substituted quaternary ammonium salt mixtures.* Inorganic chemistry, 2004. **43**(11): p. 3447-3452.
27. Abbott, A.P., et al., *Eutectic-based ionic liquids with metal-containing anions and cations.* Chemistry–A European Journal, 2007. **13**(22): p. 6495-6501.
28. Choi, Y.H., et al., *Are natural deep eutectic solvents the missing link in understanding cellular metabolism and physiology?* Plant physiology, 2011. **156**(4): p. 1701-1705.
29. Dai, Y., et al., *Natural deep eutectic solvents as new potential media for green technology.* Analytica chimica acta, 2013. **766**: p. 61-68.
30. Smith, E.L., A.P. Abbott, and K.S. Ryder, *Deep eutectic solvents (DESs) and their applications.* Chemical reviews, 2014. **114**(21): p. 11060-11082.
31. Florindo, C., L.C. Branco, and I.M. Marrucho, *Quest for green-solvent design: from hydrophilic to hydrophobic (deep) eutectic solvents.* ChemSusChem, 2019. **12**(8): p. 1549-1559.
32. van Osch, D.J., et al., *Hydrophobic deep eutectic solvents as water-immiscible extractants.* Green Chemistry, 2015. **17**(9): p. 4518-4521.
33. Duarte, A.R.C., et al., *A comparison between pure active pharmaceutical ingredients and therapeutic deep eutectic solvents: Solubility and permeability studies.* European Journal of Pharmaceutics and Biopharmaceutics, 2017. **114**: p. 296-304.
34. Paiva, A., et al., *Natural deep eutectic solvents–solvents for the 21st century.* ACS Sustainable Chemistry & Engineering, 2014. **2**(5): p. 1063-1071.
35. González, C.G., et al., *Application of natural deep eutectic solvents for the "green" extraction of vanillin from vanilla pods.* Flavour and Fragrance Journal, 2018. **33**(1): p. 91-96.
36. Abranches, D.O., et al., *Phenolic hydrogen bond donors in the formation of non-ionic deep eutectic solvents: The quest for type V DES.* Chemical Communications, 2019. **55**(69): p. 10253-10256.
37. El Achkar, T., et al., *Cyclodextrins: from solute to solvent.* Chemical Communications, 2020. **56**(23): p. 3385-3388.
38. El Achkar, T., et al., *New generation of supramolecular mixtures: Characterization and solubilization studies.* International Journal of Pharmaceutics, 2020. **584**: p. 119443.
39. Florindo, C., et al., *Insights into the synthesis and properties of deep eutectic solvents based on cholinium chloride and carboxylic acids.* ACS Sustainable Chemistry & Engineering, 2014. **2**(10): p. 2416-2425.
40. Gutiérrez, M.C., et al., *Freeze-drying of aqueous solutions of deep eutectic solvents: a suitable approach to deep eutectic suspensions of self-assembled structures.* Langmuir, 2009. **25**(10): p. 5509-5515.

41. Gomez, F.J., et al., *A greener approach to prepare natural deep eutectic solvents.* ChemistrySelect, 2018. **3**(22): p. 6122-6125.
42. Santana, A.P., et al., *Sustainable synthesis of natural deep eutectic solvents (NADES) by different methods.* Journal of Molecular Liquids, 2019. **293**: p. 111452.
43. García, G., et al., *Deep eutectic solvents: physicochemical properties and gas separation applications.* Energy & Fuels, 2015. **29**(4): p. 2616-2644.
44. Tang, B. and K.H. Row, *Recent developments in deep eutectic solvents in chemical sciences.* Monatshefte für Chemie-Chemical Monthly, 2013. **144**(10): p. 1427-1454.
45. Cui, Y., et al., *Design, synthesis and properties of acidic deep eutectic solvents based on choline chloride.* Journal of Molecular Liquids, 2017. **236**: p. 338-343.
46. Ibrahim, R.K., et al., *Physical properties of ethylene glycol-based deep eutectic solvents.* Journal of Molecular Liquids, 2019. **276**: p. 794-800.
47. García-Álvarez, J., *Deep eutectic mixtures: Promising sustainable solvents for metal-catalysed and metal-mediated organic reactions.* European Journal of Inorganic Chemistry, 2015. **2015**(31): p. 5147-5157.
48. Shahbaz, K., et al., *Prediction of deep eutectic solvents densities at different temperatures.* Thermochimica acta, 2011. **515**(1-2): p. 67-72.
49. Mitar, A., et al., *Physicochemical properties, cytotoxicity, and antioxidative activity of natural deep eutectic solvents containing organic acid.* Chemical and biochemical engineering quarterly, 2019. **33**(1): p. 1-18.
50. Yusof, R., et al., *Tetrabutylammonium bromide (TBABr)-based deep eutectic solvents (DESs) and their physical properties.* Molecules, 2014. **19**(6): p. 8011-8026.
51. Chen, Z., et al., *Effect of cation alkyl chain length on surface forces and physical properties in deep eutectic solvents.* Journal of colloid and interface science, 2017. **494**: p. 373-379.
52. Mjalli, F.S. and O. Ahmad, *Density of aqueous choline chloride-based ionic liquids analogues.* Thermochimica Acta, 2017. **647**: p. 8-14.
53. Nunes, R.J., B. Saramago, and I.M. Marrucho, *Surface tension of DL-menthol: octanoic acid eutectic mixtures.* Journal of Chemical & Engineering Data, 2019. **64**(11): p. 4915-4923.
54. Ribeiro, B.D., et al., *Menthol-based eutectic mixtures: hydrophobic low viscosity solvents.* ACS Sustainable Chemistry & Engineering, 2015. **3**(10): p. 2469-2477.
55. D'Agostino, C., et al., *Molecular motion and ion diffusion in choline chloride based deep eutectic solvents studied by 1 H pulsed field gradient NMR spectroscopy.* Physical Chemistry Chemical Physics, 2011. **13**(48): p. 21383-21391.
56. Abbott, A.P., et al., *Solubility of metal oxides in deep eutectic solvents based on choline chloride.* Journal of Chemical & Engineering Data, 2006. **51**(4): p. 1280-1282.
57. Lapeña, D., et al., *The NADES glyceline as a potential Green Solvent: A comprehensive study of its thermophysical properties and effect of water inclusion.* The Journal of Chemical Thermodynamics, 2019. **128**: p. 164-172.
58. Dai, Y., *van Spronsen., G. Witkamp, R. Verpoorte and YH Choi, Ionic liquids and deep eutectic solvents in natural products research: mixtures of solids as extraction solvents.* J. Nat. Prod, 2013. **76**: p. 2162-2173.
59. Hayyan, M., et al., *Are deep eutectic solvents benign or toxic?* Chemosphere, 2013. **90**(7): p. 2193-2195.
60. Reichardt, C., *Solvatochromic dyes as solvent polarity indicators.* Chemical reviews, 1994. **94**(8): p. 2319-2358.
61. Reichardt, C., *Pyridinium-N-phenolate betaine dyes as empirical indicators of solvent polarity: Some new findings.* Pure and Applied Chemistry, 2008. **80**(7): p. 1415-1432.

62. Kamlet, M.J., et al., *Linear solvation energy relationships. 23. A comprehensive collection of the solvatochromic parameters,. pi.*,. alpha., and. beta., and some methods for simplifying the generalized solvatochromic equation.* The Journal of Organic Chemistry, 1983. **48**(17): p. 2877-2887.
63. Kamlet, M.J., J.L. Abboud, and R. Taft, *The solvatochromic comparison method. 6. The. pi.* scale of solvent polarities.* Journal of the American Chemical Society, 1977. **99**(18): p. 6027-6038.
64. Valvi, A., J. Dutta, and S. Tiwari, *Temperature-dependent empirical parameters for polarity in choline chloride based deep eutectic solvents.* The Journal of Physical Chemistry B, 2017. **121**(50): p. 11356-11366.
65. Du, C., et al., *Effect of water presence on choline chloride-2urea ionic liquid and coating platings from the hydrated ionic liquid.* Scientific reports, 2016. **6**(1): p. 1-14.
66. El Achkar, T., S. Fourmentin, and H. Greige-Gerges, *Deep eutectic solvents: An overview on their interactions with water and biochemical compounds.* Journal of Molecular Liquids, 2019. **288**: p. 111028.
67. Hammond, O.S., D.T. Bowron, and K.J. Edler, *The effect of water upon deep eutectic solvent nanostructure: an unusual transition from ionic mixture to aqueous solution.* Angewandte Chemie International Edition, 2017. **56**(33): p. 9782-9785.
68. López-Salas, N., et al., *Looking at the "water-in-deep-eutectic-solvent" system: a dilution range for high performance eutectics.* ACS Sustainable Chemistry & Engineering, 2019. **7**(21): p. 17565-17573.
69. Zhekenov, T., et al., *Formation of type III Deep Eutectic Solvents and effect of water on their intermolecular interactions.* Fluid Phase Equilibria, 2017. **441**: p. 43-48.
70. Hammond, O.S., et al., *Resilience of malic acid natural deep eutectic solvent nanostructure to solidification and hydration.* The Journal of Physical Chemistry B, 2017. **121**(31): p. 7473-7483.
71. Weng, L. and M. Toner, *Janus-faced role of water in defining nanostructure of choline chloride/glycerol deep eutectic solvent.* Physical Chemistry Chemical Physics, 2018. **20**(35): p. 22455-22462.
72. Alcalde, R., et al., *An experimental and theoretical investigation of the physicochemical properties on choline chloride–Lactic acid based natural deep eutectic solvent (NADES).* Journal of Molecular Liquids, 2019. **290**: p. 110916.
73. Fetisov, E.O., et al., *First-principles molecular dynamics study of a deep eutectic solvent: Choline chloride/urea and its mixture with water.* The Journal of Physical Chemistry B, 2018. **122**(3): p. 1245-1254.
74. Kaur, S., A. Gupta, and H.K. Kashyap, *How hydration affects the microscopic structural morphology in a deep eutectic solvent.* The Journal of Physical Chemistry B, 2020. **124**(11): p. 2230-2237.
75. Kumari, P., et al., *Influence of hydration on the structure of reline deep eutectic solvent: A molecular dynamics study.* Acs Omega, 2018. **3**(11): p. 15246-15255.
76. Celebi, A.T., T.J. Vlugt, and O.A. Moultos, *Structural, thermodynamic, and transport properties of aqueous reline and ethaline solutions from molecular dynamics simulations.* The Journal of Physical Chemistry B, 2019. **123**(51): p. 11014-11025.
77. Zhang, Q., et al., *Electrodeposition in ionic liquids.* ChemPhysChem, 2016. **17**(3): p. 335-351.
78. Tang, B., H. Zhang, and K.H. Row, *Application of deep eutectic solvents in the extraction and separation of target compounds from various samples.* Journal of separation science, 2015. **38**(6): p. 1053-1064.

79. Wen, Q., et al., *Assessing the toxicity and biodegradability of deep eutectic solvents.* Chemosphere, 2015. **132**: p. 63-69.
80. Francisco, M., A. Van Den Bruinhorst, and M.C. Kroon, *New natural and renewable low transition temperature mixtures (LTTMs): screening as solvents for lignocellulosic biomass processing.* Green Chemistry, 2012. **14**(8): p. 2153-2157.
81. Abbott, A.P., et al., *Do group 1 metal salts form deep eutectic solvents?* Physical Chemistry Chemical Physics, 2016. **18**(36): p. 25528-25537.
82. Klamt, A., et al., *Refinement and parametrization of COSMO-RS.* The Journal of Physical Chemistry A, 1998. **102**(26): p. 5074-5085.
83. Meindersma, G.W. and A.B. de Haan, *Conceptual process design for aromatic/aliphatic separation with ionic liquids.* chemical engineering research and design, 2008. **86**(7): p. 745-752.
84. Rodriguez, N.R., P.F. Requejo, and M.C. Kroon, *Aliphatic–aromatic separation using deep eutectic solvents as extracting agents.* Industrial & Engineering Chemistry Research, 2015. **54**(45): p. 11404-11412.
85. Martins, P., et al., *Free fatty acid separation from vegetable oil deodorizer distillate using molecular distillation process.* Separation and Purification Technology, 2006. **48**(1): p. 78-84.
86. Qin, L., et al., *Selection of imidazolium-based ionic liquids for vitamin E extraction from deodorizer distillate.* ACS Sustainable Chemistry & Engineering, 2016. **4**(2): p. 583-590.
87. Ren, Y.-P., et al., *Reactive extraction of short-chain fatty acids from synthetic acidic fermentation broth of organic solid wastes and their stripping*. Journal of Chemical & Engineering Data, 2012. **57**(1): p. 46-51.
88. Kulkarni, P.S. and C.A. Afonso, *Deep desulfurization of diesel fuel using ionic liquids: current status and future challenges.* Green Chemistry, 2010. **12**(7): p. 1139-1149.
89. Weissermel, K. and H.-J. Arpe, *Industrial organic chemistry*. 2008: John Wiley & Sons.
90. Hadj-Kali, M.K., et al., *Separation of aromatic and aliphatic hydrocarbons using deep eutectic solvents: A critical review.* Fluid Phase Equilibria, 2017. **448**: p. 152-167.
91. Salleh, Z., et al., *Efficient removal of benzene from cyclohexane-benzene mixtures using deep eutectic solvents–COSMO-RS screening and experimental validation.* The Journal of Chemical Thermodynamics, 2017. **104**: p. 33-44.
92. Gouveia, A.S., et al., *Deep eutectic solvents as azeotrope breakers: liquid–liquid extraction and COSMO-RS prediction.* ACS Sustainable Chemistry & Engineering, 2016. **4**(10): p. 5640-5650.
93. Wang, Y., et al., *Roles of a hydrogen bond donor and a hydrogen bond acceptor in the extraction of toluene from n-heptane using deep eutectic solvents.* Green Chemistry, 2016. **18**(10): p. 3089-3097.
94. Wu, Z., et al., *Extractive separation of tetralin-dodecane mixture using tetrabutylphosphonium bromide-based deep eutectic solvent.* Chemical Engineering and Processing-Process Intensification, 2020. **149**: p. 107822.
95. Li, C., et al., *Extraction desulfurization process of fuels with ammonium-based deep eutectic solvents.* Green Chemistry, 2013. **15**(10): p. 2793-2799.
96. Li, C., et al., *Extraction desulfurization of fuels with 'metal ions' based deep eutectic solvents (MDESs).* Green Chemistry, 2016. **18**(13): p. 3789-3795.
97. Hadj-Kali, M.K., et al., *Removal of thiophene from mixtures with n-heptane by selective extraction using deep eutectic solvents.* Industrial & Engineering Chemistry Research, 2016. **55**(30): p. 8415-8423.

98. Li, J.-j., et al., *Green carboxylic acid-based deep eutectic solvents as solvents for extractive desulfurization.* Energy & Fuels, 2016. **30**(7): p. 5411-5418.
99. Wang, X., et al., *A simple and cost-effective extractive desulfurization process with novel deep eutectic solvents.* RSC advances, 2016. **6**(36): p. 30345-30352.
100. Warrag, S.E., et al., *Combined extractive dearomatization, desulfurization, and denitrogenation of oil fuels using deep eutectic solvents: A parametric study.* Industrial & Engineering Chemistry Research, 2020. **59**(25): p. 11723-11733.
101. Haji-Akbari, N., P. Teeraphapkul, and H.S. Fogler, *Effect of asphaltene concentration on the aggregation and precipitation tendency of asphaltenes.* Energy & fuels, 2014. **28**(2): p. 909-919.
102. Xu, C., H. Su, and M. Ghosh, *Hydro-treating of asphaltenes in supercritical toluene with MgO-supported Fe, Ni, NiMo, and CoMo catalysts.* Energy & fuels, 2009. **23**(7): p. 3645-3651.
103. Gray, M.R., et al., *Supramolecular assembly model for aggregation of petroleum asphaltenes.* Energy & Fuels, 2011. **25**(7): p. 3125-3134.
104. Dechaine, G.P. and M.R. Gray, *Chemistry and association of vanadium compounds in heavy oil and bitumen, and implications for their selective removal.* Energy & Fuels, 2010. **24**(5): p. 2795-2808.
105. Mullins, O.C., *The asphaltenes.* Annual review of analytical chemistry, 2011. **4**(1): p. 393.
106. Strausz, O.P., T.W. Mojelsky, and E.M. Lown, *The molecular structure of asphaltene: an unfolding story.* Fuel, 1992. **71**(12): p. 1355-1363.
107. Gray, M.R., *Consistency of asphaltene chemical structures with pyrolysis and coking behavior.* Energy & Fuels, 2003. **17**(6): p. 1566-1569.
108. Sheremata, J.M., et al., *Quantitative molecular representation and sequential optimization of Athabasca asphaltenes.* Energy & Fuels, 2004. **18**(5): p. 1377-1384.

CHAPTER 2

Insights of Liquid Structure of DES and Effect of Adding Solutes

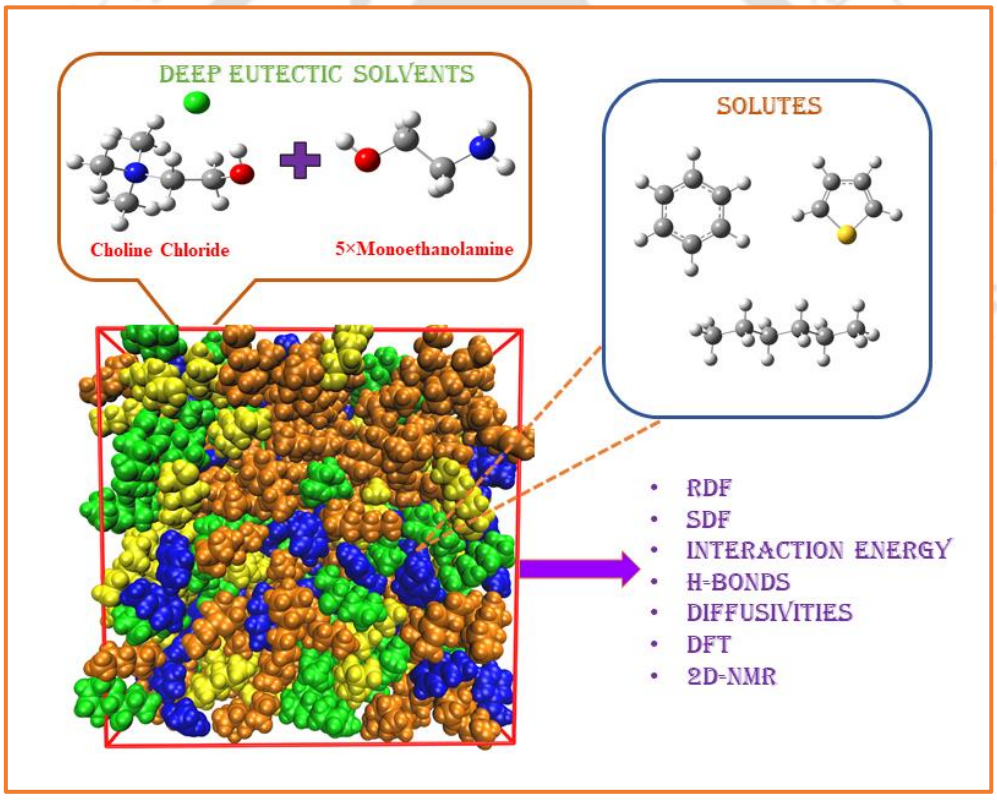

Deep eutectic solvents (DESs) are developing as an alternate medium for aromatic extraction, especially benzene and thiophene from aliphatic hydrocarbon mixtures. In this chapter, molecular dynamics (MD) simulations were first used to investigate the solvation structure of benzene, thiophene, and n-hexane in monoethanolamine-based DESs. It reveals the liquid structures in the adjacent neighbour shells, which is a function of electron-withdrawing sulphur attached to thiophene and the π-electron cloud of benzene. The intermolecular forces between aromatic, aliphatic, and DESs components are analysed in van der Waals and hydrogen bond interactions. The chloride ions serve as a charge carrier bridge between choline and monoethanolamine precursors. The solvation of benzene, thiophene, and n-hexane in the deep eutectic solvents depends on volume expansion and minor solvent structural changes. DFT results provided information on the mechanism of short-range interactions between organic solutes and studied DES. It aids in understanding the structural orientations of a DES with the addition of solutes is essential to understanding the formation of DES. The solvation shell structure and characteristics were investigated in tandem with the possibility of benzene and thiophene clustering. The ^{1}H NMR and 2D ^{1}H–^{1}H-NOESY were used to investigate the intermolecular interactions between benzene, thiophene, and n-hexane with monoethanolamine-based solvents. It concludes that high-ordered DES1 is more inclined to higher solubility than lower-ordered ones with a higher molar ratio of monoethanolamine. The solvation was reduced because the entropy gain was not maximised in the lower-ordered DES.

2.1 Introduction

This chapter discusses pure DES in general with respect to monoethanolamine-based DES solvents. The extraction of aromatic compounds from aliphatic mixtures is complex at low concentrations in the refinery and petrochemical sectors because of their close boiling points. However, an effective method for extracting aromatics at ambient temperature and pressure with less than 20% weight fraction has not yet been developed [1-3]. It is well accepted that

aromatic (such as benzene or thiophene) in refinery and petrochemical products be reduced due to their adverse health effects and risk of contamination of the ecological environment with aromatic hydrocarbons[4].

Carbon dioxide (CO_x), sulphur dioxide (SO_x), and nitrogen dioxide (NO_x) are produced by burning petroleum fuel, which is regarded as a significant environmental pollutant. It is primarily due to aromatics in fuel, which are both sulphur-rich and nitrogen-rich. Thus it is necessary to curtail the extent of aromatic, notably sulphur- and nitrogen-containing compounds, in petroleum fuels to produce high-purity food-grade hexane[5]. Catalytic hydrotreatment is widely utilized in the industrial sector to remove aromatics, sulphur, and nitrogen from petroleum fuels. However, these are carried out at a very high temperatures and pressure, making them difficult to handle. The aromatic and sulphur-containing compounds are still not recoverable, even after hydroprocessing reactions and hydrotreatment operations.

The environmental monitoring agency, namely EPA, reduced the allowable benzene percentage in gasoline from 1% (v/w) under EN-228 and ASTM D1319 recommendations to 0.62 percent (v/w) in 2011. The ASTM 5623, defines aromatic sulphur compounds as those that can inhibit or degrade catalysts and adversely affect product quality and corrosion of equipment[6]. The aromatic sulphur compounds in the fuels lead to SO_x emissions and are the primary cause of acid rain. The sulfolane or N-formylmorpholine (NFM) solvents are currently used in the petrochemical industry to separate aromatic from aliphatic mixtures. The use of these conventional solvents for extraction has some problems as these solvents are known as toxic substances and pollutants to the environment[7]. Further, the efficiency of the extraction process is low, and at least 5% by weight of the aromatic remains at the end of the extraction.

An effective solvent must have a low melting point, low viscosity, economic cost and be non-toxic and non-corrosive. Solvents such as eutectic mixtures have high thermal and chemical stability and possess a non-flammable and minimal vapour pressure character.

However, a more significant percentage of recently prepared DESs are liquid at room temperature[7-8]. The DESs are a liquid solvent that is formed by combining a hydrogen bond acceptor (HBA), a Brønsted or Lewis acid, with a hydrogen bond donor (HBD), containing an additional lone pair of electrons[9]. The specific molar ratio of each of these components must be combined to melt and initiate the transition to a liquid state at room temperature. Compared to ILs, the preparation of DESs is reported to be cost-efficient as it requires a lesser number of unit operations[10-13]. Moreover, some of them are made from non-fossil fuel precursors.

Molecular dynamic simulations efficiently couple microscopic and macroscopic properties of systems[14]. According to the latest review of DESs applications published in 2020, the challenge and future direction are to use molecular simulation, response surface analysis, and process simulation to understand the nature of such solvents that can help to develop these neoteric solvents[15]. Prior research has used experimental methods to determine the extraction of aromatics and the solubility of DESs[16]. At the same time, only a few studies have focused on the microscopic behaviour of DESs mixtures [17] and the solubility of aromatic and aliphatic compounds in solvents. However, microscopic level deep insights are critical for interpreting the internal mechanism of DESs extraction and directing the selection of DESs components[18]. The underlying process structure of solvents and the molecular interactions between their components are critical for producing both acceptable and efficient solvents. The relationship between solute and solvent interaction through computational tools is being explored, which can significantly help us design neoteric solvents that can improve the recovery of solvent and the purity of the product[19].

Compared to experimental studies, there are fewer theoretical and computational investigations on the solvation of aromatic and aliphatic compounds by DESs. Gutiérrez and co-workers[20] employed both density functional theory (DFT) and molecular dynamic simulation to analyse the solvation of lidocaine in solvents, namely synthesised from Choline

Chloride: Lactic acid and β-alanine: lactic acid in a molar ratio of 1:1. It reports that the effective solvation of lidocaine in DES is because of strong solute-solvent intermolecular interactions accompanied by a slight volume expansion and minor solvent structural change. In another study, the same group studied the nanoscopic properties of highly diluted water solutions in choline chloride + lactic acid DES[20-21]. They further revealed the confinement of water in DESs as a function of temperature and concentration. Malik et al. performed ab initio molecular dynamics (AIMD) simulations to elucidate the local solvation structure around CO_2 and SO_2 in choline chloride-based DESs, namely, reline and ethaline[22]. They observed that the non-bonded interactions are mainly responsible for its stabilization in the two DESs. It also demonstrated a charge transfer between the solute and the chloride anion, which in turn, decided the shape of the solvation shell around the solute. Maginn and co-workers[23] combined AIMD and classical MD simulations to study ethaline, correlating the obtained results with experimental density and neutron scattering measurements. Using force field (FF) as developed by Perkins *et al.* [24-25], they concluded that the experimental liquid structure is reproduced in simulations, although the existence of discrepancies between the experimental and calculated scattering curves was observed. Nonetheless, stronger hydrogen bonds between the anion and the HBD were reported.

It is helpful to have a wide range of HBA: HBD combinations that may be used to formulate the DESs and allow us to tune the physical properties by varying their molar ratio. It also necessitates an in-depth understanding of the structural characteristics of these solvents and their interactions with aliphatic and aromatic ring compounds. Therefore, it is necessary to have knowledge of the microscopic forces and structural changes of solute-solvent (DESs) interactions to carry out solvation analysis in designated solvents effectively. It has been shown that theoretical studies are vital in evaluating the solubility of various substances and helpful in designing the most favourable solvents. In the following sections, we have conducted an in-

depth analysis of the molecular interactions between benzene, thiophene, aliphatic hydrocarbon, and DESs with varied molar ratios of monoethanolamine as an HBD and Choline chloride as HBA. The solubility data of the benzene, thiophene, and hexane were compared with the literature data of monoethanolamine-based DES as given in table 2.1 at 298.15K and atmospheric pressure[16]. After that, the solute-solvent interactions are studied using ^{1}H NMR and 2D ^{1}H–^{1}H NOESY (Nuclear Overhauser Effect Spectroscopy).

Table 2.1. Benzene, thiophene, and *n*-hexane solubility in pure solvents and DESs. The experiments were done at 298.15 K and atmospheric pressure.

DES	Melting Point(K)	x_{HEX}	x_{BEN}	x_{TPH}
Choline chloride: Monoethanolamine (1:5); DES1	276.9	0.016	0.114	0.145
Choline chloride: Monoethanolamine (1:7); DES2	276.6	0.017	0.092	0.112
Monoethanolamine	283.4	0.012	0.098	0.117

2.2 Simulation Method Details

The chemical structures of individual choline cations, chloride anion, monoethanolamine, benzene, thiophene, and *n*-hexane were drawn by gauss view 05[26] software (Figure 2.2). The molecular geometries of different compounds were optimized by the *Gaussian09* program[27] using the B3LYP/6-311+G* level of theory[28] (Figure 2.2). For molecular dynamics (MD), the generalized AMBER force field (GAFF) parameters were employed[29]. Partial charges were obtained by the restrained electrostatic potential (RESP) charge method[30-31]. Nonpolarizable force fields consisting of bonded (i.e., bond stretching, angle bending, and torsions) and non-bonded (i.e., Lennard-Jones and Coulombic) terms were used to simulate all species in this work. For all systems studied here, the simulated densities align with experimental values when using ± 0.9e for the choline chloride and monoethanolamine,

as shown in table 2.2. The scaling of charge technique yields accurate predictions for various temperature-dependent properties of choline chloride-based DESs as shown by Perkins et al., [24-25] Salehi et al., [32] and Celebi et al. [33].

Table 2.2. Partial charges of different molecules used for solubility study.

Choline chloride		**Monoethanolamine**		**Benzene**		**Thiophene**		**Hexane**	
Atom Type	Partial Charge	Atom Type	Partial Charge	Atom Type	Partial Charge	Atom Type	Partial Charge	Atom Type	Partial Charge
C7	-0.3683	C12	0.2212	C18	-0.1329	C14	-0.2917	C1	-0.3047
H15	0.1836	H29	0.0036	H40	0.1329	H36	0.2337	H1	0.0663
H16	0.1836	H30	0.0036	C19	-0.1329	C15	-0.1014	H2	0.0663
H17	0.1836	C13	0.3623	H41	0.1329	H37	0.1409	H3	0.0663
C8	-0.1025	H31	-0.0102	C20	-0.1329	C16	-0.1014	C2	0.2371
H18	0.1383	H32	-0.0102	H42	0.1329	H38	0.1409	H4	-0.0432
H19	0.1383	N2	-0.9843	C21	-0.1329	C17	-0.2917	H5	-0.0432
C9	-0.3683	H33	0.3470	H43	0.1329	H39	0.2337	C3	-0.0484
H20	0.1836	H34	0.3470	C22	-0.1329	S1	0.0371	H6	0.0017
H21	0.1836	O2	-0.6805	H44	0.1329	--	--	H7	0.0017
H22	0.1836	H35	0.4003	C23	-0.1329	--	--	C4	-0.0484
C10	-0.3683	--	--	H45	0.1329	--	--	H8	0.0017
H23	0.1836	--	--	--	--	--	--	H9	0.0017
H24	0.1836	--	--	--	--	--	--	C5	0.2371
H25	0.1836	--	--	--	--	--	--	H10	-0.0432
C11	0.2656	--	--	--	--	--	--	H11	-0.0432
H26	0.0128	--	--	--	--	--	--	C6	-0.3047
H27	0.0128	--	--	--	--	--	--	H12	0.0663
O1	-0.6175	--	--	--	--	--	--	H13	0.0663
H28	0.4217	--	--	--	--	--	--	H14	0.0663
N1	0.0827	--	--	--	--	--	--	--	--
Cl1	-0.9000	--	--	--	--	--	--	--	--

The diffusion coefficient was within the range of (± 2%) with scaled charges, which indicates the values are similar to those reported by Doherty et al. [34]. Standard deviations in measurement of thermophysical properties ranged up to 3 % between the average values of the simulation boxes. The values were averaged over three simulation boxes after equilibration for thermodynamic and transport property analyses, each with different starting configurations. The partial charges for different atomic sites of these molecules are shown in table 2.2, and the corresponding atomic notation is represented in figure 2.1. The Lennard-Jones (L-J) parameters are reported in table 2.3 of the supporting information. The generalized AMBER force field parameters were developed using *Antechamber* [35] *tools of AMBER 12*[36].

The molecular dynamics simulation in NAMD 2.9 package recorded all the trajectories of different systems[37]. It consists of four subsets: energy minimization to achieve the global minima of energy, heating to the desired temperature, equilibration of the system, and production run. The energy minimization removes any unbalanced potential energy distribution of the molecules arising from random insertion during the packing into the simulation box[38]. The ramp heating and the annealing process are executed to attain the desired temperature for simulation. After that, the system is equilibrated with the isobaric-isothermal ensemble (NPT) for 10 ns, and subsequently, the time-resolved trajectories are recorded for 100 ns in the production run. The smooth truncation of Lennard jones parameters is corrected using a switching function at 10 Å distance. The cut-off distance was maintained at 12 Å. The long-range interaction was calculated using a particle mesh Ewald method. The periodic boundary condition (PBC) was used for momentum conservation.

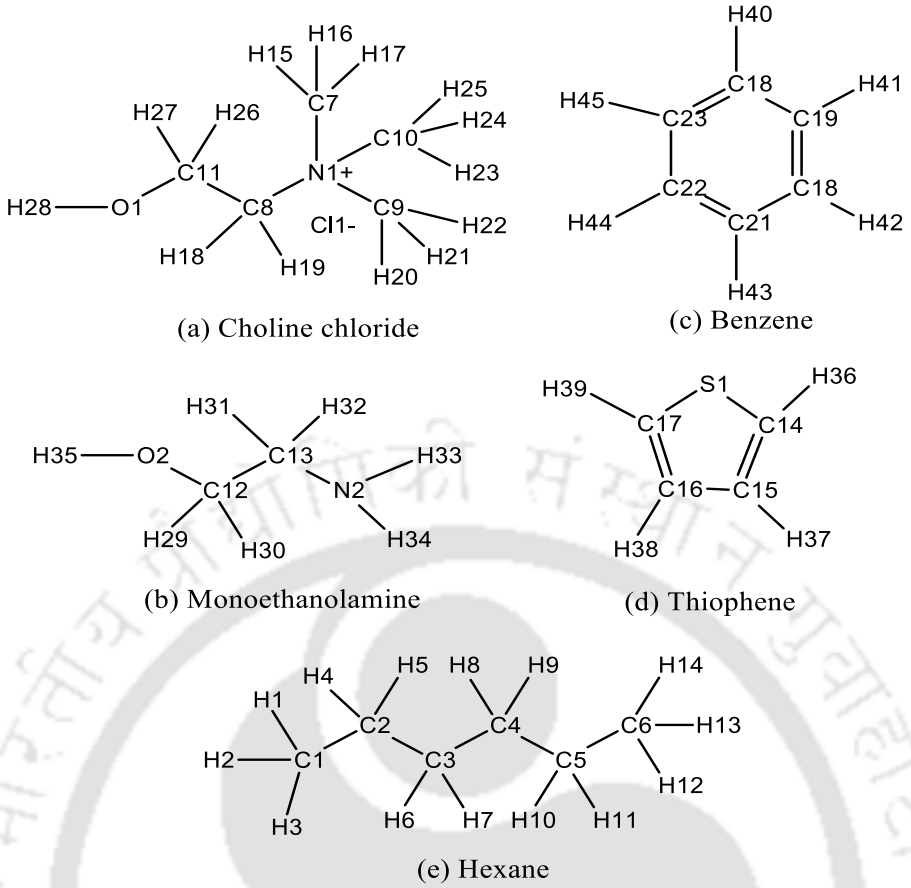

Figure 2.1. Chemical structures of different compounds with specific atom notations are used in different solvation characterization (Table 2.2).

To minimize the computational complexity, NAMD uses various time-stepping techniques to simulate electrostatic interactions. The splitting function in this model separates the electrostatic interactions and van der Waals interactions, which breaks the total force exerted on each atom into long and short-range interactions, respectively. The Langevin temperature dynamics and Nose-Hoover Langevin dynamics have been utilized as thermostats and barostats, respectively[39-40]. The damping time is set at 1 fs in Langevin temperature dynamics and pressure control for the damping period, while the decay is set at 0.2 ps and 0.1 ps accordingly. The NAMD trajectories data was visualized using VMD 1.9.3 packages[41].

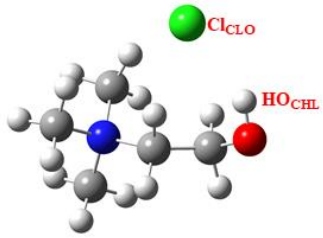

(a) Choline Chloride

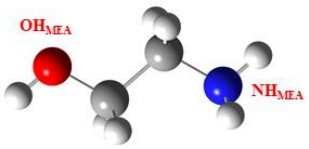

(b) Monoethanolamine

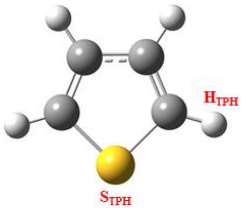

(c) Thiophene

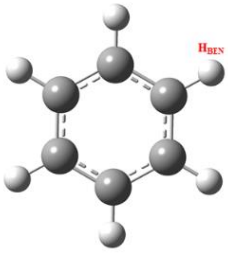

(d) Benzene

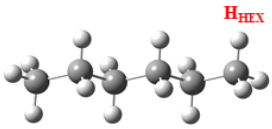

(e) Hexane

Figure 2.2. The optimised Chemical structures of different compounds with specific atom notations are used in different solvation characterization. Here, carbon, hydrogen, oxygen, nitrogen, chloride, and sulphur are rendered in dark grey, white, red, blue, green, and yellow, respectively.

Table 2.3. Lennard-Jones parameters used different atom types of molecule species.

Atom Type	ε (kcal/mol)	R^* (Å)	Atom Type	ε (kcal/mol)	R^* (Å)
Choline chloride			**Monoethanolamine**		
c3	0.1094	1.9080	c3	0.1094	1.9080
hx	0.0157	1.1000	h1	0.0157	1.3870
h1	0.0157	1.3870	n3	0.1700	1.8240
oh	0.2104	1.7210	hn	0.0157	0.6000
ho	0.0000	0.0000	oh	0.2104	1.7210
n4	0.1700	1.8240	ca	0.0860	1.9080
cl	0.2650	1.9480	ho	0.0000	0.0000
Hexane			**Thiophene**		
c3	0.1094	1.9080	cc	0.0860	1.9080
hc	0.0157	1.4870	cd	0.0860	1.9080
Benzene			ss	0.2500	2.0000
ca	0.0860	1.9080	h4	0.0150	1.4090

ha	0.0150	1.4590	ha	0.0150	1.4590

2.3 Results and Discussion

Earlier literature has emphasized the critical role of these solvents as extractive media in supporting the considerable solubility of solutes that compares well with ionic liquid analogues. Therefore, hydrogen bonding and the atomic-level interactions between the selected DESs and the specified compounds become necessary to understand the solubility mechanism. The molecular dynamics (MD) simulation studies of three different systems, namely BEN+DES1, TPH+DES1, and HEX+DES1, allowed an exact estimation of intermolecular forces using a basic model of those seen in bulk liquid phases.

Table 2.4. Details of the simulated different DESs systems and the comparison of simulated (ρ_{Sim}) and experimental (ρ_{Exp}) densities at 298.15 K and 1 bar. N_{Total} is the total number of molecules.

System	N_{Total}	ρ_{Sim} (g cm^{-3})	ρ_{Exp} (g cm^{-3})	% Error	Box-length (nm)
CHL: MEA (1:5); DES1	1000	1.031	1.053	2.10	50×25×25
CHL: MEA (1:7); DES2	1000	1.076	1.044	1.98	50×25×25
BEN: DES1 (1:5)	2000	1.015	1.018	1.21	60×30×30
BEN: DES2(1:7)	2000	0.979	1.010	3.10	60×30×30
TPH: DES1 (1:5)	2000	1.043	1.052	1.83	60×30×30
TPH: DES2 (1:7)	2000	1.057	1.045	1.21	60×30×30
HEX: DES1 (1:5)	2000	0.956	0.973	1.69	60×30×30
HEX: DES2 (1:7)	2000	0.947	0.966	2.36	60×30×30

[a]Error(%) = *abs* $((\rho_{exp} - \rho_{MD})/\rho_{exp}) \times 100$. [b]Standard uncertainty u are u (T) = 0.02 K, u (p) = 1 kPa; The expanded uncertainty is $u(\rho) = 0.0005$ (0.95 level of confidence).

The simulated and experimentally calculated density at 298.15 K and 1 bar pressure of DESs are initially compared to prove the authenticity of force field parameters for MD simulation. Further, we verified our force field by measuring the volume expansivity values as obtained from the slopes of the density versus temperature curve, as shown in figure 2.3 and table 2.5,

after dividing by the initial density. Table 2.4 shows the difference between experimental and MD-predicted densities that are less than 3%. It also includes the number of molecules in the simulated system.

Table 2.5: The comparison of simulated and experimental calculated volume expansivity for the force field validation for DESs.

Density data	Volume Expansivity (K^{-1})	
	DES1	DES2
Experimental	6.50×10^{-4}	6.57×10^{-4}
Simulated	6.07×10^{-4}	6.59×10^{-4}

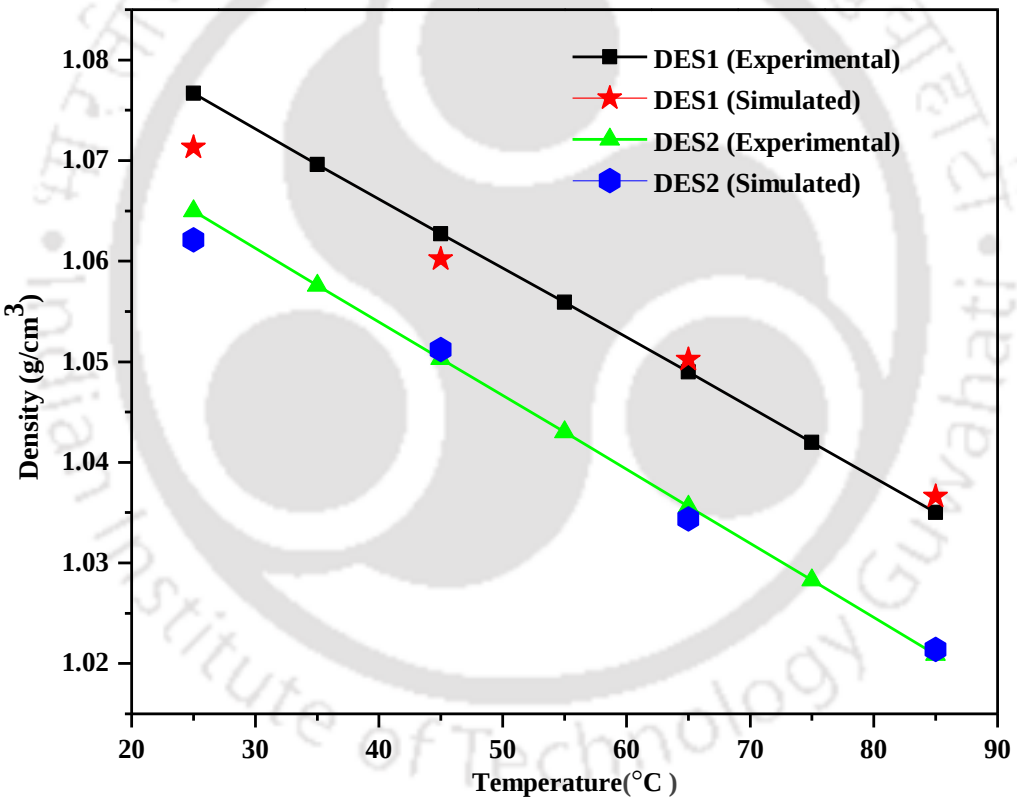

Figure 2.3. The comparison of experimental and simulated density variation with temperature.

2.3.1 DFT Calculation

DFT calculations were carried out with the Gaussian program[42], using the B3LYP[43-45] functional, with Grimme's method (DFT-D3) for treating dispersive interactions[46], and the 6-311++G(d, p) basis set. Several molecular clusters were studied, and interaction energy,

Δ*E*, was calculated as the difference between the energy of the molecular clusters and those of the corresponding monomers with counterpoise correction for the basis set superposition error (BSSE) [47]. The detailed procedure for the calculation of interaction energy for clusters is given in our earlier published work[48]. Structural orientations of a DES1 with the addition of solutes are essential to understanding the formation of DES. The specific interaction determines the drops in melting point and the physical properties of the DES. The dotted line provides a list of active sites for the possible formation of hydrogen bonds with the prescribed cut-off distance for hydrogen bonds (<3 Å). The DES1 system exhibits a highly interconnected hydrogen-bonding network, wherein the solutes molecule interacts strongly with both HBA and HBD. The chloride ion, as shown in RDF, remains intact with DESs, showing a lesser interaction with organic solutes. The distances (Å) for different active sites present in neat DES1 and after the addition of organic solutes are shown in Figure 2.4. Moreover, in figure 2.4, Cl^- is clearly acting as charge transfer bridge between the choline cation and monoethanolamine, which further confirms the rigid nature of DES1 after the solvation of organic solutes.

(a) DES1 **(b) DES1+BEN**

ΔE= – 389.520 kJ mol^{-1} **ΔE= – 37.157 kJ mol^{-1}**

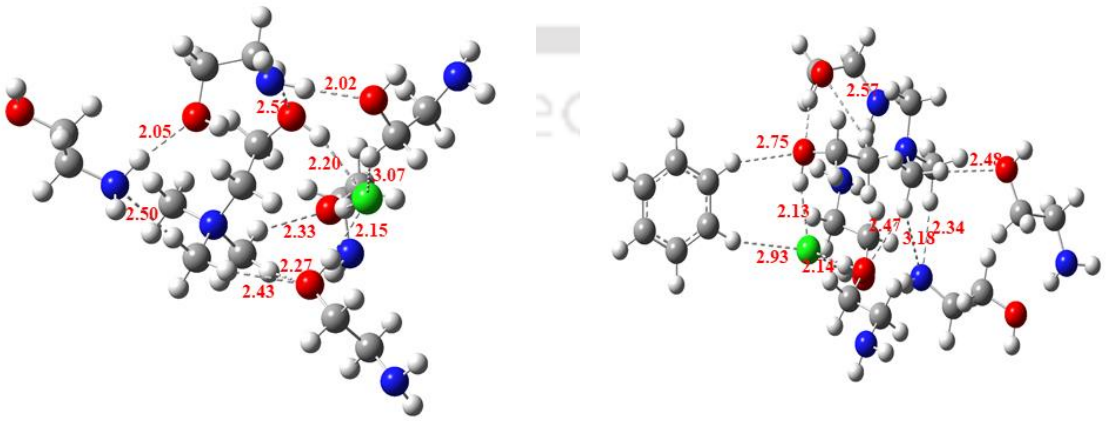

(c) DES1+TPH

ΔE= ─ 55.272 kJ mol^{-1}

(d) DES1+HEX

ΔE= 16.188 kJ mol^{-1}

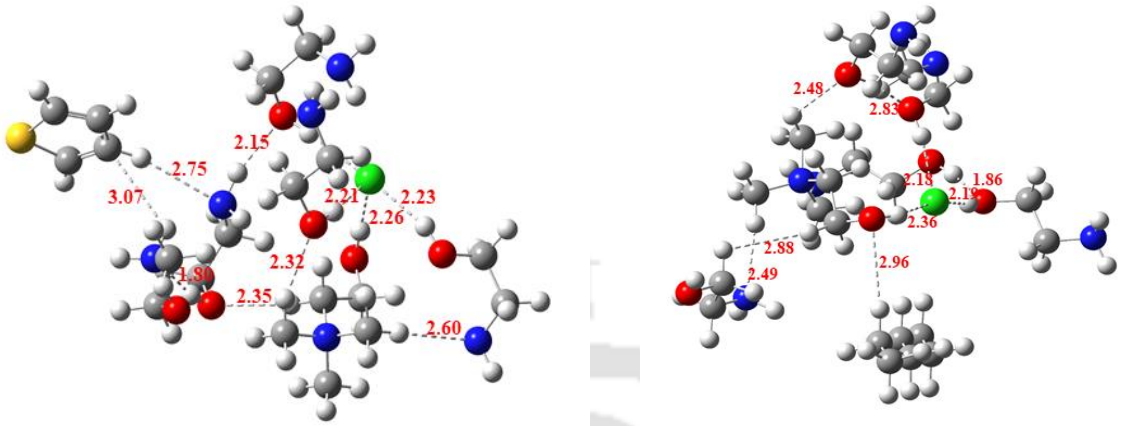

Figure 2.4. Structures and properties of the studied molecular clusters were calculated at the B3LYP/6-311++g (d, p) theoretical level. Hydrogen atoms are in white, carbon atoms are in ash, nitrogen atoms are in blue, Sulphur atom is in yellow, chlorine atoms are in green, and oxygen atoms are in red.

2.3.2 Atomic Distribution with Hydrogen Bond Donor (HBD)

The solvation capacity of aromatic compounds in different DESs decreases with an increase in the molar ratio of ChCl: MEA from 1:5 to 1:8 at constant temperature and pressure. Table 2.1 represents the solubility of benzene, thiophene, and *n*-hexane in studied DESs at 298.15K and atmospheric pressure[16]. As the molar ratio of HBD (MEA) increases in DESs, it influences the molar and accessible free volume, resulting in lower aromatic compounds solubility. While it may deduce that the observed trend is due to the free volume mechanism. The DESs with a higher molar ratio of HBD have a higher disorder and a lower free volume. This observation was supported by the Solvation of carbohydrates in choline chloride-based deep eutectic solvents, as reported by Häkkinen et al. [49]. The higher solubility of aromatic compounds in DESs may also be explained by concluding that the entropy change of solubility was the main deriving reason for benzene and thiophene solubility in higher-ordered DES, which rises with the increase in HBD concentration. The highly disordered DESs sustain the sufficiently lower

entropy gain of the solvent resulting in lower solubilisation, hence lowering the non-covalent active interaction sites responsible for the decreased solvation of aromatic compounds. The HBD of DESs, monoethanolamine, has hydroxyl and amine groups, thus creating a strong hydrogen bond network. The density, viscosity, and Surface tension values are reported in tables 2.6-2.7.

Table 2.6. Experimental density ($g.cm^{-3}$) of DES (ChCl: MEA): mole fraction and temperature under a pressure of 101.3 kPa.

Mole fraction of DES (ChCl: MEA)	Temperature (°C)						
	25	35	45	55	65	75	85
1:5	1.0757	1.0672	1.0603	1.0446	1.0390	1.0220	1.0150
1:6	1.0600	1.0527	1.0444	1.0322	1.0209	1.0115	1.0063
1:7	1.0650	1.0576	1.0503	1.0430	1.0356	1.0283	1.0209
1:8	1.0628	1.0552	1.0478	1.0404	1.0330	1.0256	1.0181

*Standard uncertainty, u, in temperature, pressure, DES composition, final DES mole fraction, and density measurements are: u(T) = 0.2 K, u(p) = 1 kPa, $u(x_{DES})$=0.01 and $u(\rho)$=0.0001 $g.cm^{-3}$ respectively.

Table 2.7. Experimental viscosity *(mPa.s)* of DES (ChCl: MEA): mole fraction and temperature under a pressure of 101.3 kPa.*

Mole fraction of DES (ChCl: MEA)	Temperature (°C)						
	25	35	45	55	65	75	85
1:5	48.5	28.8	20.1	13.5	9.8	7.5	5.9
1:6	36.7	25.0	16.8	11.2	8.8	6.6	5.3
1:7	37.7	25.5	13.8	10.1	7.9	6.0	5.2
1:8	32.7	22.6	15.0	10.5	7.1	5.9	4.7

*Standard uncertainty, u, in temperature, pressure, DES composition, final DES mole fraction and density measurements are: u(T) = 0.2 K, u(p) = 1 kPa, $u(x_{DES})$=0.01 and u(η)=5 % respectively.

Table 2.8. Experimental Surface tension ($mN.m^{-1}$) of DES (ChCl:MEA): mole fraction and temperature under a pressure of 101.3 kPa.*

Mole fraction of DES (ChCl: MEA)	Temperature (°C)						
	25	35	45	55	65	75	85
1:5	48.2	47.6	46.9	46.2	45.6	45.0	44.4
1:6	48.7	48.0	47.4	46.7	46.0	45.3	44.7
1:7	49.2	48.5	47.8	47.1	46.4	45.8	44.9
1:8	49.6	48.8	47.9	47.2	46.4	45.8	45.0

*Standard uncertainty, u, in temperature, pressure, DES composition, final DES mole fraction and density measurements are: u(T) = 0.2 K, u(p) =1 kPa, $u(x_{DES})$=0.01 and u(σ)= 0.1m $N.m^{-1}$ respectively.

The solubility of aromatic chemicals was greatly enhanced by comparing the different DESs formulations with varying monoethanolamine molar ratios, as indicated in table 2.1. The increased solubility of aromatics over aliphatic compounds is owing to the fact that benzene and thiophene molecules include a π–electron cloud and a sulphur atom, which enhances the interaction of the aromatic sulphur compounds with the functional group attached to HBA and HBD. Aliphatic hydrocarbon has lower solubility than aromatic compounds, mainly due to fewer interactions with HBA and HBD. The sulphur species compound was more soluble in the examined DES1 than benzene, owing to the sulphur atom's electron-withdrawing effect, which strengthens the interaction with the hydroxyl and amine group of DESs. Additionally, it was shown that the 1:5 molar ratio of DES1 (choline chloride and mono-ethanolamine) had the highest solubility for benzene and thiophene compared to the higher molar ratios of HBD. Consequently, our molecular dynamics studies focused only on DES1 in the presence of benzene, thiophene, and *n*-hexane. The HBD molar ratio reduced the number of free active sites as entropy increased, with a higher molar ratio as viscosity decreased, as shown in table 2.7. It was observed that DESs based on ethanolamines exhibit the following solubility sequence for aromatic and aliphatic compounds: thiophene > benzene > hexane.

2.3.3 Radial Distribution Function

The Coordination Number (CN) is computed from the RDF plot and indicates how many particles surround the reference atom or molecule. By integrating g(r) to its first minimal value (equation 1), the number of coordination numbers present in the first coordination shell of an individual pair of atoms or molecules can be obtained.

$$CN = 4\pi\rho \int_{0}^{r^{I}} g(r)\, r^{2}\, dr \qquad (2.1)$$

Where r^{I} is the radial distance at first minima, ρ is the number density, and g(r) is the radial distribution function that reveals the structural organization of the different solutes such as

benzene, thiophene, and *n*-hexane when calculated around DES1. The following section elaborates structural correlations of each system using the RDFs shown in figures 2.5-2.7. Table 2.9 provides the first minimum (r_{min}) corresponding to the first nearest neighbour shell and the corresponding coordination number (n_{coor}).

2.3.3.1 Atomic Distribution around Benzene in DES1

In the first step, the influence of solvation on the DES1 liquid structure was examined individually using BEN, TPH, and HEX molecules. After adding the required molecules, RDF was initially computed for the centre of mass comprising the examined DES1 in pure form. The site-site RDF of the system comprises *x* BEN+ (1─ *x*) DES1 mixtures for *x* = 0.20, were represented in figure 2.5. At the atomistic level, benzene and DES1 show a sharp and strong initial first peak, followed by a second peak extending beyond 1nm, showing that DES1 displays a higher order of degree in different coordination shells. While, the BEN molecules are solvated by DES1, even though HBA and HBD remain intact in the original form of DES1.

Table 2.9. Positions of the first minimum and respective coordination number for different RDF pairs in DES1 containing benzene, thiophene, and n-hexane as solutes at 298.15 K.

Benzene-DES			**Thiophene-DES**			**Hexane-DES**		
RDF Pair	**$R_{min(nm)}$**	**n_{coor}**	**RDF Pair**	**$R_{min(nm)}$**	**n_{coor}**	**RDF Pair**	**$R_{min(nm)}$**	**n_{coor}**
H_{BEN}-OH_{MEA}	0.26	1.06	H_{TPH}-OH_{MEA}	0.685	1.15	H_{HEX}-OH_{MEA}	1.04	0.374
H_{BEN}-N_{CHL}	0.38	2.53	H_{TPH}-N_{CHL}	0.465	2.58	H_{HEX}-N_{CHL}	1.09	0.392
H_{BEN}-N_{MEA}	0.31	1.25	H_{TPH}-N_{MEA}	0.262	1.30	H_{HEX}-N_{MEA}	1.03	0.369
H_{BEN}-Cl_{CLO}	0.75	1.37	H_{TPH}-Cl_{CLO}	0.275	1.55	H_{HEX}-Cl_{CLO}	1.37	0.760
H_{BEN}-HO_{CHL}	0.25	2.15	H_{TPH}-HO_{CHL}	0.285	2.06	H_{HEX}-HO_{CHL}	1.11	0.410
			S_{TPH}-CH_{CHL}	0.385	1.58			

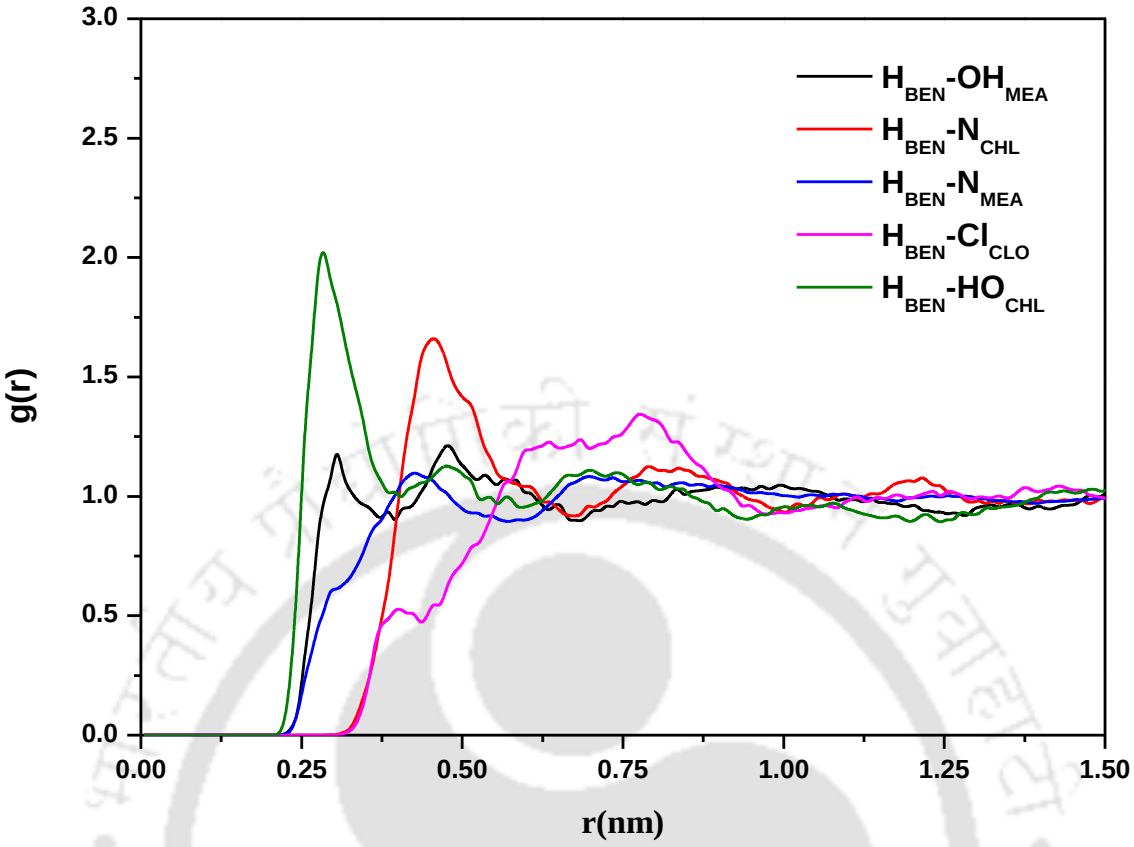

Figure 2.5. The site–site radial distribution function, g(r), for the benzene in (*x*)BEN+(1 − *x*) DES1 (DES1, *x* =0.20), obtained from MD simulations at 298.15 K and 1 bar.

The site–site radial distribution function corresponding to the interaction of different active atomic sites of solvents such as HBA and HBD with the hydrogen atom (H_{BEN}) of benzene is depicted in figure 2.5. It reveals a strong interaction peak between the hydroxyl group of choline HO_{CHL} and the hydrogen atom of benzene ring H_{BEN} (peak at 0.24 nm) compared to the interaction between the H_{BEN} and OH_{MEA} (peak at 0.27 nm). It confirms a strong non-covalent interaction with the hydroxyl group of choline cation, which signifies the higher local density of benzene around the CHL than the hydroxyl group of MEA (observed by the relative n_{coor} given in table 2.9). Thus, a closer association of HO_{CHL} and OH_{MEA} than Cl^- with benzene implies that chloride ion has a stronger association with choline cation than aromatic compounds. It confirms the intact nature of hydrogen bonding that is responsible for DES formation.

Further analysis reveals that the nitrogen atom of choline cation N_{CHL} is closer to $H_{BEN,}$ with the peak positioned at 0.32 nm followed by an MEA (N_{MEA}) peak at 0.34 nm. It means MEA approaches the benzene molecule π-electron cloud through the amine group. The arrangement of CHL and MEA species around the BEN molecule suggests that both components of DESs showed a significant interaction responsible for the solvation of benzene in DES1.

As shown in figure 2.5, we estimated the RDFs for the significant interactions between N_{CHL} and the hydroxyl group of the choline cation HO_{CHL} with the hydrogen atom of H_{BEN}. We observe a strong first peak correlation between N_{CHL} and H_{BEN}. In addition, HO_{CHL} is closer to H_{BEN} with peak positions at 0.27 and 0.46 nm, respectively, followed by N_{CHL}. It can be concluded that choline cation has a more local density with benzene as compared to MEA. This is confirmed by the higher coordination number of the hydroxyl group with hydrogen atom of benzene, as shown in table 2.9. Further, it infers that the choline cations approach benzene from their hydroxyl group side and have more local density of HBA compared to monoethanolamine.

2.3.3.2 Atomic Distribution around Thiophene in DES1

The site–site radial distribution function reveals the interaction of chloride anion, choline cation, and MEA with thiophene in DES1, as shown in figure 2.6. It is visible from the first solvation shell around TPH that the hydroxyl group of choline, i.e., HO_{CHL}, is closer to the hydrogen atom attached adjacent to sulphur, i.e., $H_{TPH.}$ Additionally, the positive charge carrying nitrogen atom of choline, i.e., N_{CHL}, has peaks at 0.47 nm and 0.34 nm with thiophene and S_{TPH}, respectively, although the coordination number is more significant in the case of the H_{TPH}-N_{CHL} pair, as shown in table 2.9. However, the Cl^{-} does not provide a significant peak because it has a higher interaction with choline and HBD, confirming the existence of DES as a single entity after aromatic sulphur compound solubility.

Additionally, as shown in table 2.9, the coordination numbers for the H_{TPH}-N_{CHL} and H_{TPH}-HO_{CHL} atomic pairs are more significant than those for the H_{TPH}-Cl_{CLO} and H_{TPH}-OH_{MEA} atomic pairs, indicating a higher interaction between the choline cation and MEA than with the chloride anion as shown similar trend with benzene in figure 2.6. The choline cation also affects the solvation structure of thiophene around DES1. Figure 2.6 illustrates the strong local density interactions between CHL and TPH. We detect a significant interaction between N_{CHL} and the TPH molecule. We discover a more substantial relationship of OH_{CHL} with H_{TPH} and CH_{CHL} in the first solvation shell surrounding TPH, peaks at 0.29 nm and 0.31 nm, respectively, followed by peaks for N_{CHL} at 0.51nm and 0.45 nm, respectively. It indicates that the CHL cation interacts with the active sites of TPH through the hydrogen atom of hydroxyl group. They convey information about the choline cations and HBD orientation in TPH's initial solvation shell.

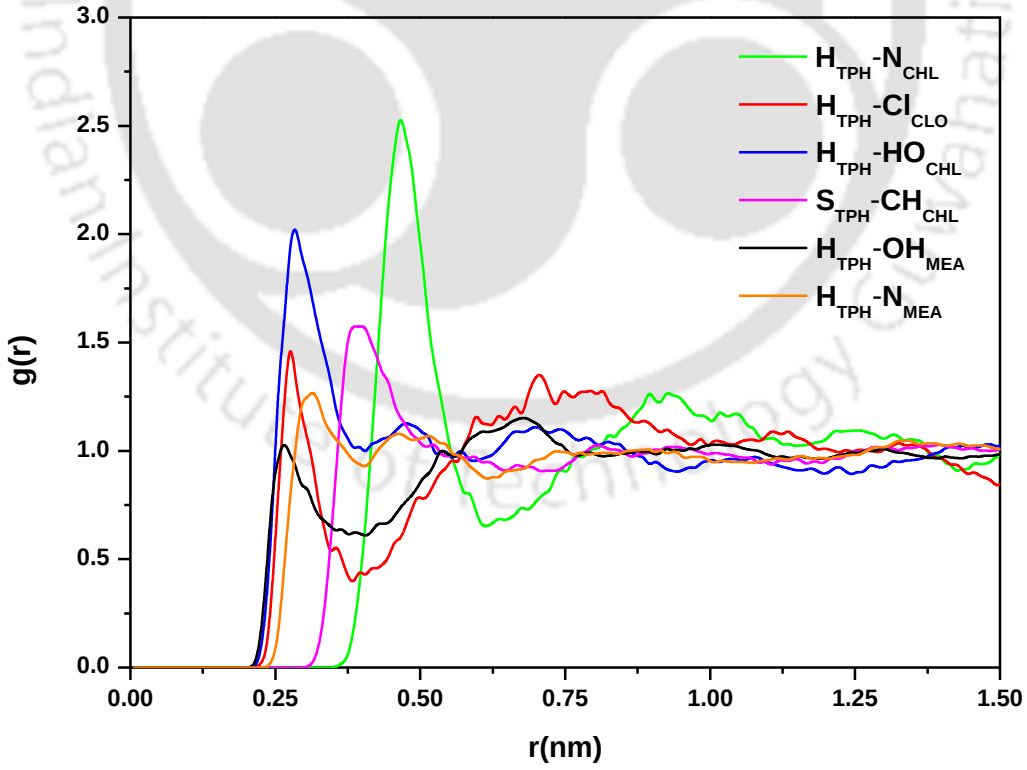

Figure 2.6. The site–site radial distribution function, g(r), for the thiophene in (*x*) TPH + (1−*x*) DES1 (DES1, *x* =0.20), obtained from MD simulations at 298.15 K and 1 bar.

The existence of numerous strong hydrogen bonds between the choline cation, chloride anion, and HBD precludes an interaction between the thiophene hydrogen atom and the chloride anion (H_{TPH}–Cl_{CLO}). A potential self-association between solute and solvent should be ruled out due to the uniform distribution of the solute and solvent, as depicted in figures 2.5-2.7. Around benzene and thiophene molecules, the DES1 contains more solvation shells than around *n*-hexane molecules. Nonetheless, the chloride anion has a lower preference for molecules because of the strong hydrogen bonds formed between HBA and HBD during the DES1 synthesis process.

2.3.3.3 Atomic Distribution around Hexane in DES1

To comprehend the local structure around the solute in DES1, the atomic site-site RDFs correlated to Cl^-, CHL, and MEA with *n*-Hexane were calculated. The atomic radial distribution function of the DES1-HEX system is shown in figure 2.7. Due to *n*-hexane's nonpolar nature, it exhibits a weak interaction with components of DES1. Additionally, atomic distribution confirms that RDF has fewer interactions than aromatic and sulphur species, reducing *n*-hexane solubility. The chloride anion exhibits similar behaviour to the DES1-BEN and DES1-TPH systems. It indicates that the chloride ion interacts more with the choline cation and HBD than with the organic solutes; hence, DES1 retains its original conformation as shown in figure 2.5-2.7. Table 2.9 shows the coordination numbers (n_{coor}) derived from the RDFs for the given pairs. These findings reveal that HBA and HBD have a lower average number of molecules in their initial solvation shells than aromatic compounds.

2.3.4 Spatial Density Function

Although the molecular arrangements inferred from the atomic level RDF results show that hydrogen bonding is the primary intermolecular interaction for solvation of BEN-DES1 and TPH–DES1 systems in contrast to the HEX-DES1 system.

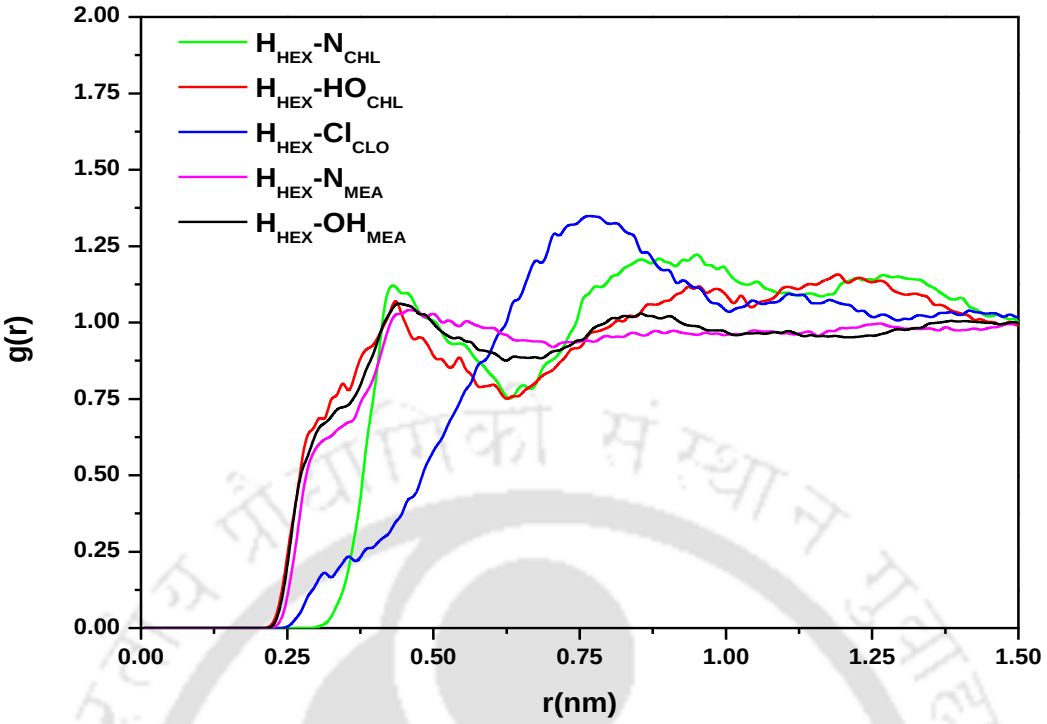

Figure 2.7. The site–site radial distribution function, g(r), for the hexane in (*x*) HEX + (1 − *x*) DES1 (DES1, *x* =0.20), obtained from MD simulations at 298.15 K and 1 bar.

Thereafter, to better understand the noncovalent interaction, spatial distribution functions (SDFs) for the chemical neighbourhood of benzene, thiophene, *n*-hexane compounds, and DES1 components such as HBA and HBD are obtained by the TRAVIS package [50]. The isovalues employed for the SDFs corresponding to the BEN-DES1, TPH-DES1, and HEX-DES1 systems are constant to maintain homogeneity in a different system. Aromatic compounds have a high affinity for HBA and HBD due to functional groups such as OH and NH_2 as well as the presence of a π-electron cloud in benzene and thiophene. The atomic site–site radial distribution was also confirmed by considering the possible hydrogen bonds involving all three systems, i.e., BEN–DES1, TPH–DES1, and HEX–DES1 with SDF. Self-hydrogen bonding between the same molecules was also computed to infer the clustering of the same molecules, but no such evidence was found similar to RDFs.

Three-dimensional isodensity surfaces of BEN, TPH, and HEX with different components of DES1 are given in figure 2.8. Figures 2.8(a)-2.8(c) depict the spatial distribution functions (SDFs) around the central benzene (BEN) molecule in DES1. The HBD forms a circular shell perpendicular to the BEN molecule, which confirms that the π-electron cloud of benzene forms the C–H···π, O–H···π, and N–H···π type non-covalent interaction with solute (figure 2.8a).

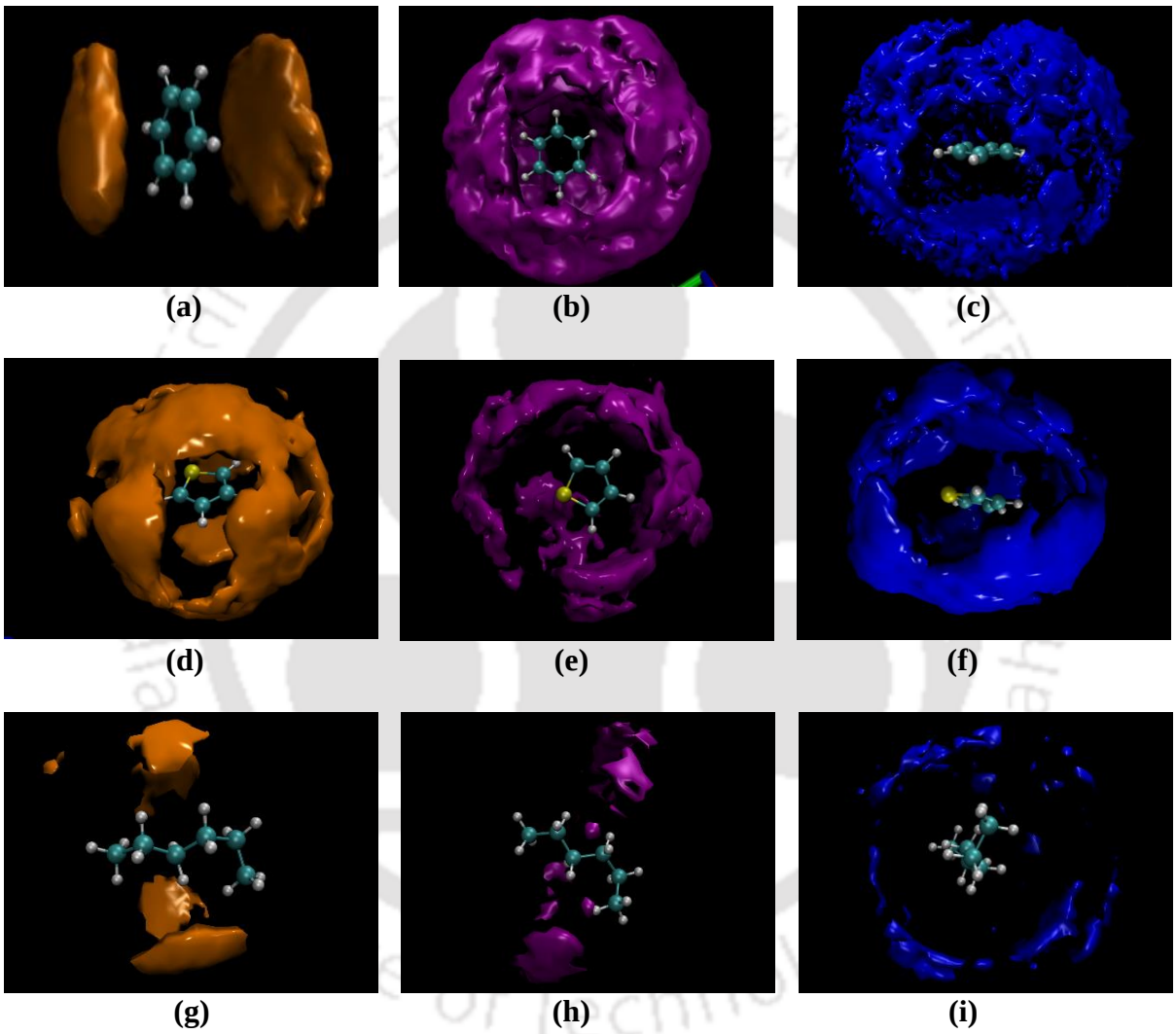

Figure 2.8. Spatial distribution functions of DES1 components around benzene, thiophene, and hexane in *x* (BEN, TPH, or HEX) + (1 – *x*) DES1 mixtures (*x* = 0.20) at 298.15 K and 0.1 MPa. Blue colour represents choline, violet represents chloride ion, and yellow represents MEA.

Similarly, the isosurface of the choline cation is also present in a circular fashion around the BEN molecules, as shown in figure 2.8b. The isosurface of the choline cation is present on all sides of the benzene, which shows that the choline cation interacts with the hydrogen atom

of BEN in the first solvation shell in RDF analysis, as shown in figure 2.5. Chloride ions have also appeared around the benzene molecule, but it is too far compared to choline cation and monoethanolamine, as depicted in figure 2.8c. Figures 2.8(d)-2.8(f) represent the SDFs around the central TPH molecule in DES1. It can be observed that the MEA isosurface is highly localized near the sulphur and adjacent hydrogen atom of the TPH molecule. In contrast to DES1-BEN system, it forms a uniform circular solvation shell around the TPH molecule. This observation can be explained based on the electron-withdrawing ability of the sulphur atom attached to thiophene that attracts the electron donor hydroxyl and amine group of MEA. Choline cation also forms the C–H$\cdots\pi$ and O–H$\cdots\pi$ type non-covalent interaction that is also evident from the RDF in figure 2.5. The chloride anion does not show any preferential bulk density around aromatic compounds, confirming the intact nature of DES1 as a single entity even after solvation. The SDFs around *n*-hexane molecule of DES1 components are shown in figures 2.8(g)-2.8(i). This aliphatic compound SDF confirms a weaker interaction, as shown in figure 2.7 of RDF, due to its non-polar nature.

2.3.5 Hydrogen Bonding

The criterion for determination of the hydrogen bond was decided by fixing the cut-off angle for the donor─H···acceptor bond at 120° and the distance between the acceptor and donor at 3.5 Å. It remains constant for all the systems to maintain uniformity. The HBD of DES1 shows a higher number of hydrogen bonds with benzene because of more active sites such as hydroxyl and amine functional groups than choline cation. It is envisaged that the MEA, via both functional groups, would create a more significant number of hydrogen bonds with aromatic and sulphur species than with aliphatic hydrocarbons. The average hydrogen bond per benzene molecule with MEA and choline cation are shown in figure 2.9 as a function of simulation time steps. Further, the presence of more active sites in MEA than choline cation forms more H-bonds with the solute.

Similarly, figure 2.10 reports the average number of hydrogen bonds per TPH with choline cation and MEA as a function of simulation time steps. The hydrogen bonding for TPH–CHL indicates that the only plausible mechanism is for the thiophene molecules to function as the hydrogen bond acceptor through the sulphur linked to the aromatic ring. It indicates that MEA creates more hydrogen bonds with aromatic sulphur species than it does with aliphatic *n*-hexane. The newly formed hydrogen bonds of chloride ions with benzene and thiophene are less due to strong intact hydrogen bonding between choline cation, chloride anion, and HBD. The non-covalent interactions, mainly hydrogen bonding and non-specific van der Waals contributions, are responsible for the significant solubility of aromatic compared to aliphatic compounds.

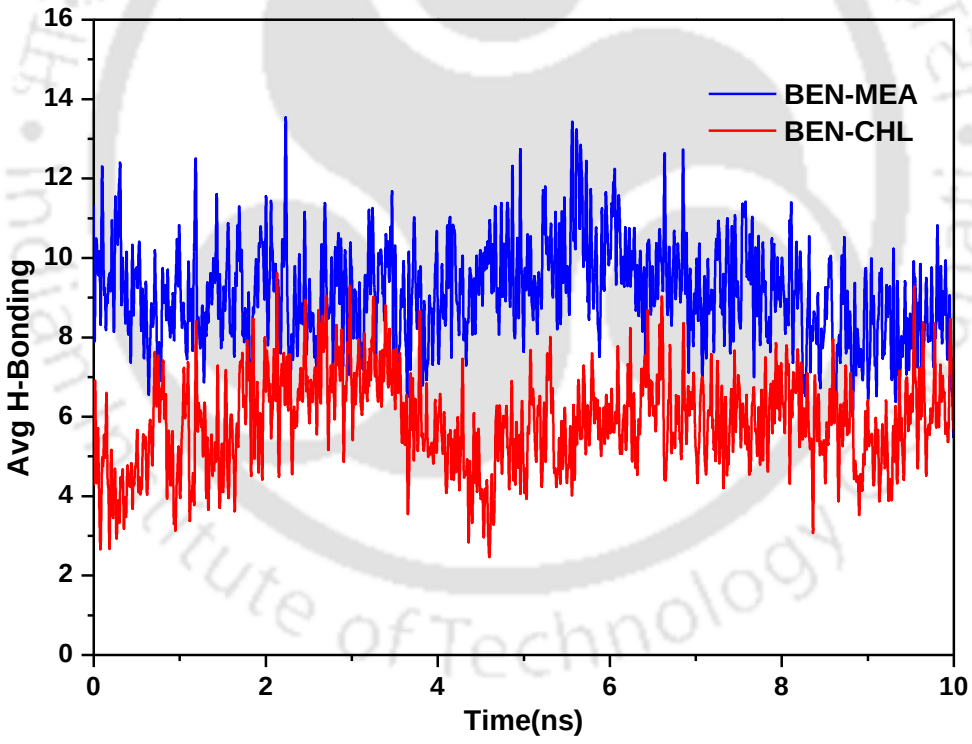

Figure 2.9. Percentage of BEN molecules which are hydrogen-bonded for (*x*)BEN + (1 − *x*) DES1 (DES1, *x* = 0.20) from MD simulations at 298.15 K and 1 bar.

Further, the polarity of the solvent, hydrogen bonding, and non-covalent interaction between the benzene, thiophene, and *n*-hexane depends on the presence of the functional group.

The hydrogen bonding of HBA and HBD with *n*-hexane are shown in figure 2.11, which indicates weak interaction due to its non-polar nature. It demonstrates that fewer hydrogen bonds are formed between the DESs active sites and *n*-hexane due to the lack of any functional group or free electron, resulting in less solubility than aromatic compounds.

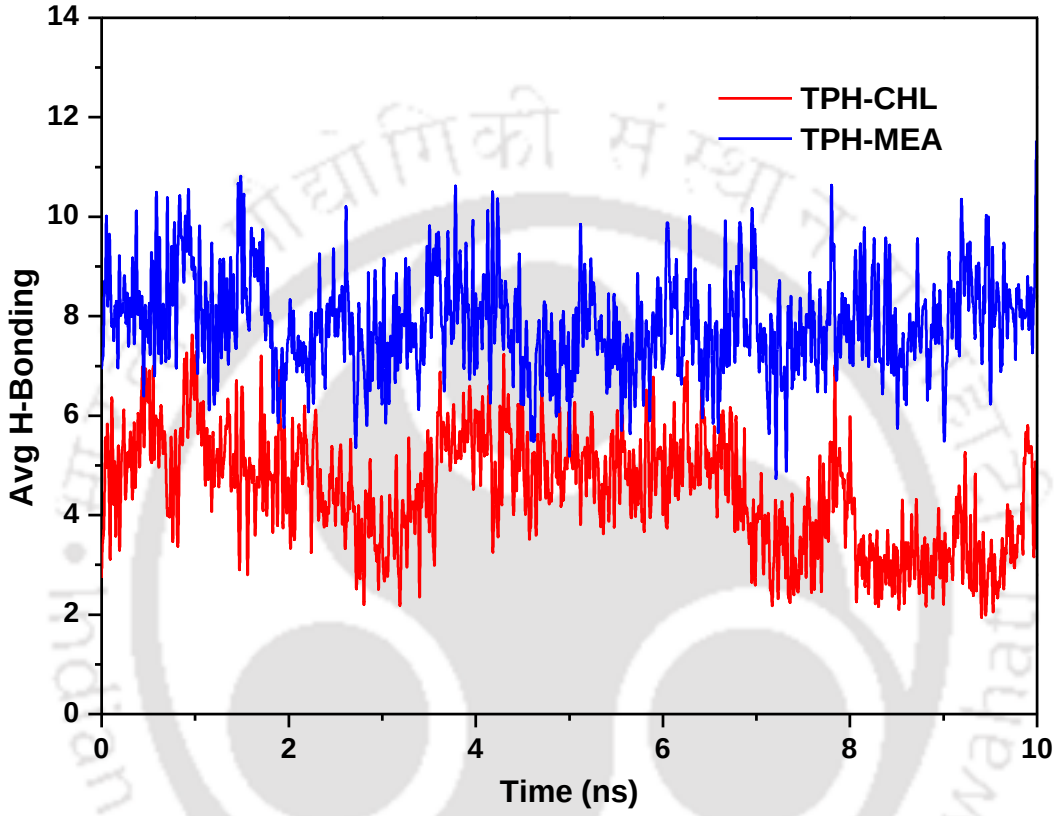

Figure 2.10. Percentage of TPH molecules hydrogen-bonded in *(x)TPH* + (1 − *x*)DES1 (DES1, *x* = 0.20) from MD simulations at 298.15 K and 1 bar.

2.3.6 Non-bonded Interaction Energy

The non-bonded interaction energies between DES1, aromatic, sulphur species, and aliphatic hydrocarbons are calculated using VMD software, a standard computational tool for studying the interactions between molecules in solute-solvent systems. The results were used to understand better the effects of chloride anions, choline cation, and HBD on dissolution. The solubilisation of benzene and thiophene in DES1 is thought to be controlled by non-covalent interaction. Accordingly, we hypothesize that both electrostatic and van der Waals interactions

play an essential role in the solvation of benzene and thiophene in monoethanolamine-based DESs.

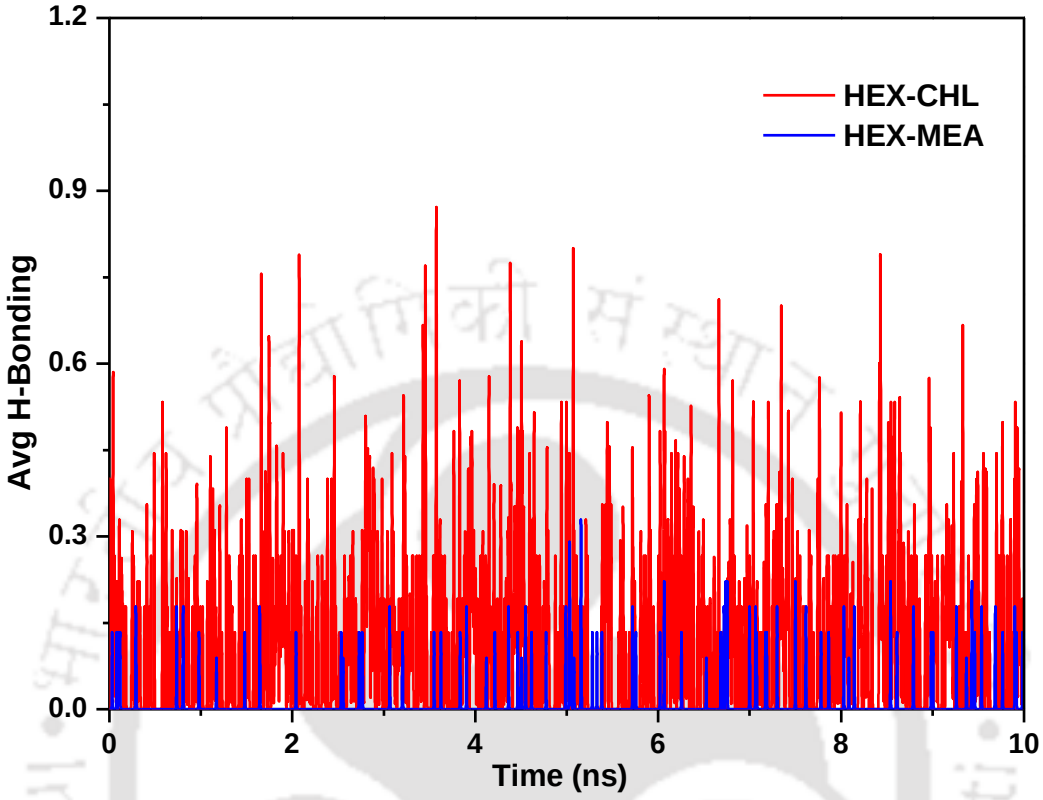

Figure 2.11. Percentage of HEX molecules hydrogen-bonded for (x)*HEX* + (1 − x)DES1 (DES1, x = 0.20) from MD simulations at 298.15 K and 1 bar.

Non-bonded interaction energies between benzene, sulphur species, aliphatic compound, and DES1 were calculated as the summation of van der Waals (E_{vdW}) and electrostatic (E_{elec}) interactions are depicted in table 2.7. The vdW interactions between the aromatic compound and the DES1 are more substantial (more negative) than the electrostatic interactions signifying that van der Waals interactions are the governing interaction for aromatic compounds with DES1. It is essential to mention that we decompose the total interaction energy into ion (cation, anion, and HBD)–BEN/TPH/HEX pairs to get deeper insights into each ion on the aromatic aliphatic solvation.

Table 2.10. Interaction energies (kJ/mol) between the different components of DES1 and solutes at 298.15 K and 1 bar pressure.

Interacting Components	Electrostatic Interactions (E_{elec})	vdW Interactions (E_{vdW})	Total Nonbonded Interactions (E_{total})
	BEN-DES1		
BEN-CHL	10.51434	-65.403	-54.8886
BEN-CLO	-62.9232	-7.87521	-70.7985
BEN-MEA	-28.8524	-166.083	-194.936
	TPH-DES1		
TPH-CHL	6.845522	-56.0271	-49.1815
TPH-CLO	-72.1636	-7.34931	-79.5129
TPH-MEA	-29.9146	-155.807	-185.721
	HEX-DES1		
HEX-CHL	6.8455	-6.1273	0.7182
HEX-CLO	-8.1626	-4.3493	-12.5119
HEX-MEA	-9.7143	-15.4807	-25.1950

The vdW interactions between benzene (−166.083 kJ mol^{-1}) and thiophene (−155.807 kJ mol^{-1}) are higher for (HBD) monoethanolamine than they are for more extended straight-chain length aliphatic compounds. For solvation, the electrostatic interactions between benzene (65.403 kJ/mol) and thiophene (56.0271 kJ/mol) are equivalent to those of the choline cation, which arises solely as a result of charge delocalization. The Cl^- ion carries the net negative charge leading to stronger electrostatic interactions but weaker than the original interaction between the choline cation, chloride anion, and HBD. The choline cation shows a repulsive interaction with the aromatic compounds due to the availability of a positive electron cloud charge with aromatic compounds. Contrary to electrostatic interactions, a longer alkyl chain of hexane results in repulsive interaction due to its non-polar nature. In addition, the stronger electrostatic interactions can also be explained based on the fact that the interaction between cation and anion weakens with the insertion of benzene and thiophene. Hence, the choline cation is seen to possess stronger interactions with benzene and thiophene compared to *n*-

hexane. In contrast, the vdW interactions between HBD and solute are higher for π-electron aromatic compounds than for longer chain-length aliphatic hydrocarbons.

2.3.7 Mean Square Displacement and Self-diffusion Coefficient

An analysis of the self-diffusion coefficient of deep eutectic solvents based on Einstein's relation was performed to describe their microscopic dynamics.

$$D = \frac{1}{6}\lim_{t\to\infty}\frac{d}{dt}\left\langle \sum_{i=1}^{N}\left|\mathrm{r}_i(t)-\mathrm{r}_i(0)\right|^2 \right\rangle \qquad (2.\ 2)$$

Here, D is the diffusion coefficient, $r_i(t)$ and $r_i(0)$ represent particle i at time t, and t=0, respectively, as given in equation 2. The average over a time interval is illustrated in angle brackets < >. The $\langle|r_i(t)-r_i(0)|^2\rangle$ represents the mean square displacement (MSD) of the particle i. The linearity of the MSD plots indicates that the Stokes-Einstein relation is correct.

The self-diffusion coefficients of relevant molecules are calculated from the gradient of the MSD curve, as given in Figures 2.12-2.14. Here, it is worthwhile to specify that the D values for different molecules are accounted for by averaging over various time inceptions. These are reported in table 2.8 against various time intervals with a time frame of 10 ns. With increasing time steps in the production run, the molecules diffuse according to their interaction with different components of DESs. At the initial stage of the production run (0–10 ns), the D values of all organic solutes have a higher deviation than DES1. With the increase in the simulation runtime (90–100 ns), aromatic molecules associated it with the DES phase, while hexane diffuses away from the DESs components. This is due to the fact that it has the most negligible affinity as compared to aromatic compounds such as benzene and thiophene.

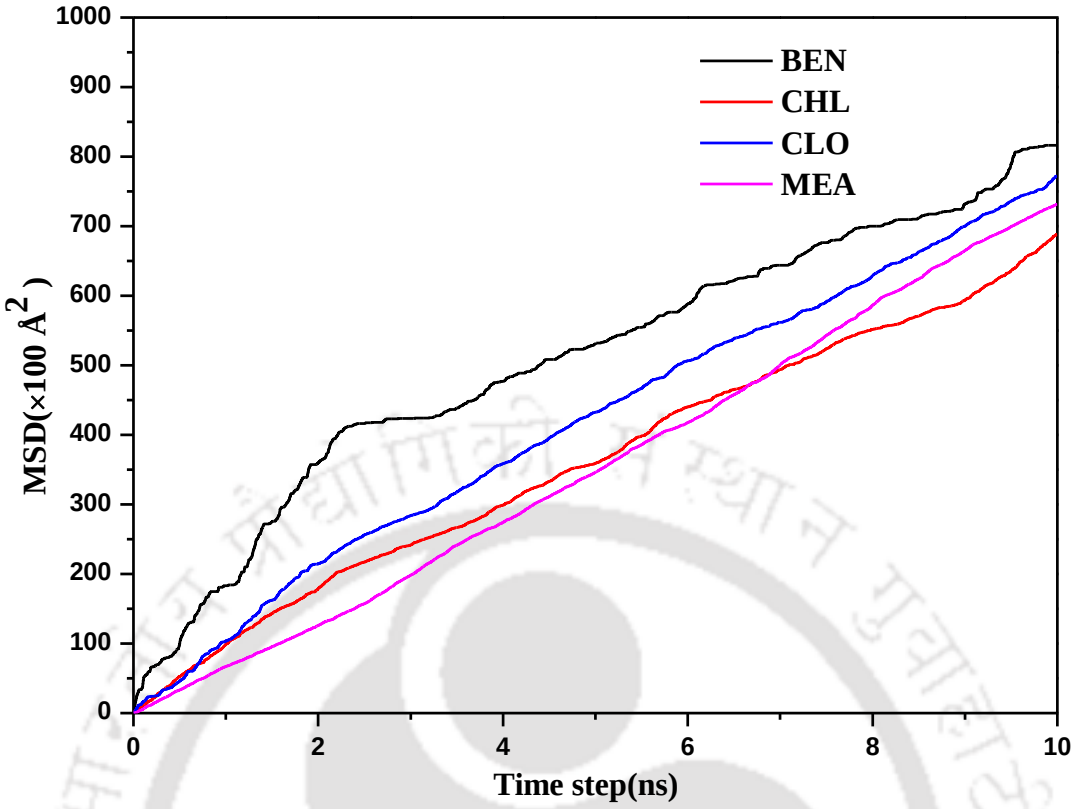

Figure 2.12. MSD plot of DES1 components around aromatic and aliphatic compounds in *(x)* BEN + (1 – *x*) DES1 mixtures (*x* = 0.20) at 298.15 K and 0.1 MPa for the final of the production run (90–100 ns).

As the simulation time increases in the production run (90-100ns), benzene and thiophene molecules reach the DESs components diffusion phase. Their self-diffusion values are now closer to each other at the end of the production run (90-100ns) as the migration of solutes across the solvents reaches the lowest energy state. The self-diffusion coefficient values for the aromatic compounds decrease with an increase in simulation time during the production run. On the contrary, hexane values increase as given in figures 2.14. Furthermore, the D values for components of DES1 with aromatic, sulphur compound, and *n*-hexane were also calculated for the initial phase (0-10ns) and final phase (90-100ns) of production run, as given in table 2.11.

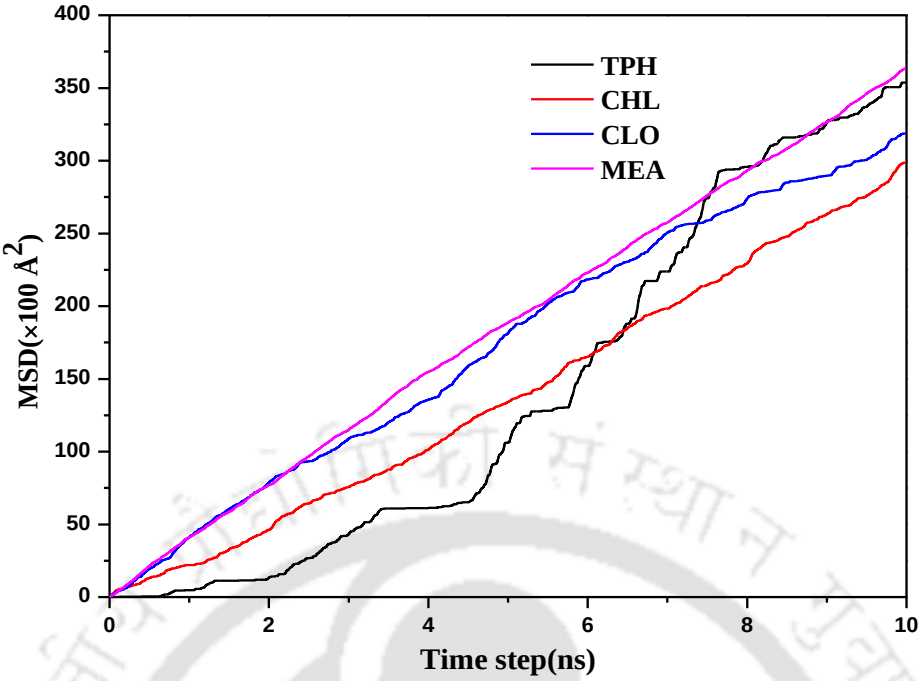

Figure 2.13. MSD plot of DES1 components around aromatic and aliphatic compounds in (*x)* TPH + (1 – *x*) DES1 mixtures (*x* = 0.20) at 298.15 K and 0.1 MPa for the final of the production run (90–100 ns).

Table 2.11. Self-Diffusivity coefficient (*D*) of different molecular species for solubility of benzene, thiophene, and *n*-hexane in DES1 at 298.15 K and 101.3 k Pa.

D×10^{-10} (m^2/s)		
Molecular Species	**0–10 ns**	**90–100 ns**
DES1+BEN		
CHL	1.137	1.062
CLO	1.149	1.121
MEA	1.132	1.147
BEN	1.393	1.122
DES1+TPH		
CHL	1.118	1.004
CLO	1.245	1.077
MEA	1.204	1.196
TPH	1.487	1.202
DES1+HEX		
CHL	0.827	1.000
CLO	1.122	1.162
MEA	1.287	1.279
HEX	0.832	1.856

The self-diffusion coefficient of HEX in DES1 is greater than TPH/BEN, as evident from the MSD plot in figure 2.14. It can also estimate that the self-diffusivity of HEX was found to be 2 times and 1.5 times higher than the value of TPH and BEN, respectively, as given in table 2.8. BEN and TPH diffusion coefficients decrease with simulation time as noncovalent interaction strengthens with HBA and HBD as the system reaches a more stable form, in contrast, with hexane, due to weaker interaction, it separates from DES1 phase as a result, the diffusion coefficient increases. As DES1 has exhibited excellent solubility ability for benzene and thiophene than *n*-hexane. It might also be noteworthy to highlight that the D value of hexane follows the opposite trend to that of an aromatic compound, leading to decreased solubility in DES1.

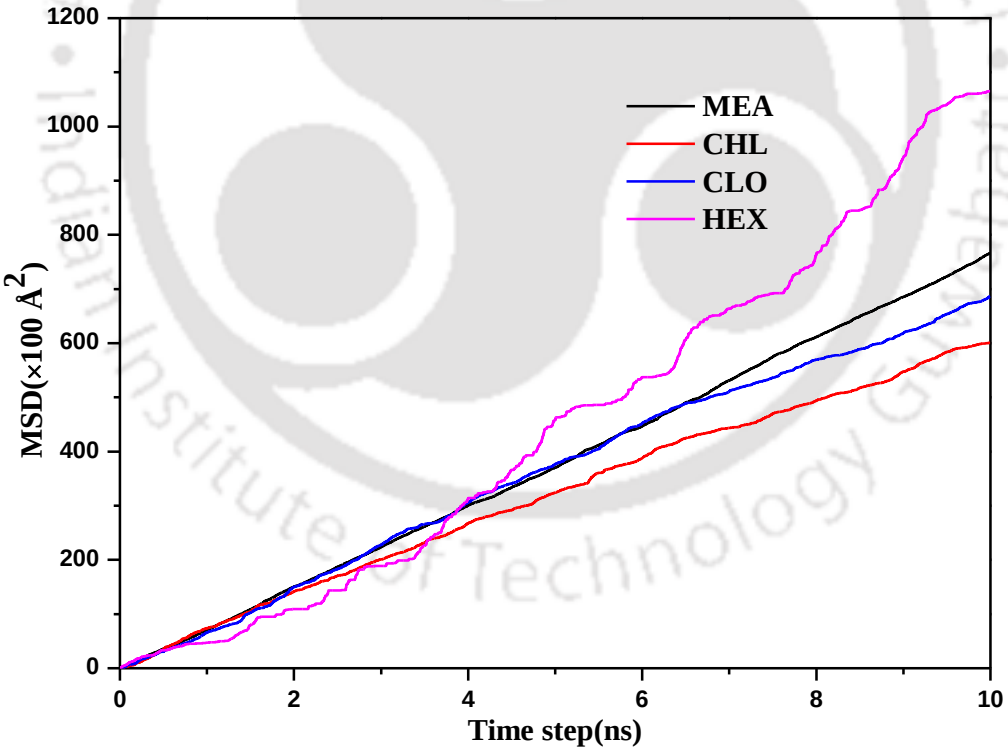

Figure 2.14. MSD plot of DES1 components around aromatic and aliphatic compounds in (*x)* HEX+ (1 – *x*) DES1 mixtures (*x* = 0.20) at 298.15 K and 0.1 MPa for the final of the production run (90–100 ns).

2.3.8. Solute-Solvents Interaction

The non-covalent interaction using ^{1}H NMR and 2D $^{1}H–^{1}H$-NOESY (nuclear overhauser effect spectroscopy) investigated the unique interactions between the components of DES1 and after solvation of 20 wt. % of benzene, thiophene, and *n*-hexane. The $^{1}H–^{1}H$ NOESY is a valuable technique that identifies the closely interacted protons in space, but that is not necessarily covalently bonded. The Phase-sensitive cross-peak signals may be generated by protons that are close to each other and that are exchanging (chemical or kinetic) protons, as well as J-coupled protons[51].

Abbott et al. recently studied intermolecular interactions between glucose and Ethaline molecules using the ^{1}H NMR [49], 2D $^{1}H–^{1}H$-NOESY, and $^{1}H–^{19}F$-HOESY[52], and they recently used the HOESY NMR spectroscopy to reveal that the anion and NH_2 protons on the urea molecule had a strong cross-connection. The dissolution of glucose in a DES primarily originated from the anion and HBD interactions studied by Mohan et al[53].

The molar ratio of choline chloride and monoethanolamine in the specific molar ratio of 1:5 in DES1 and after solubility of 20 wt.% of benzene, thiophene, and *n*-hexane in different systems were confirmed based on the integrated ^{1}H NMR. The ^{1}H and $^{1}H–^{1}H$ NOESY 2D NMR of neat DES1 as shown in figure 2.16. The pure choline chloride showed positive proton NOEs between the CH_2 groups of the monoethanolamine, which means they are near to each other, as shown in figure 2.16. The Cross-peaks in the NOEs spectrum show that ChCl interacts with itself as depicted from diagonal cross-peaks, although it is impossible to tell the difference between the CH_2 groups of ChCl and CH_2 of monoethanolamine as cross-peaks overlap with each other. The CH_3 (~2.50 ppm) group in ChCl shows high-intensity cross-peaks with the OH (~3.43 ppm) group and CH_2 (~3.32-3.14 ppm) group of MEA.

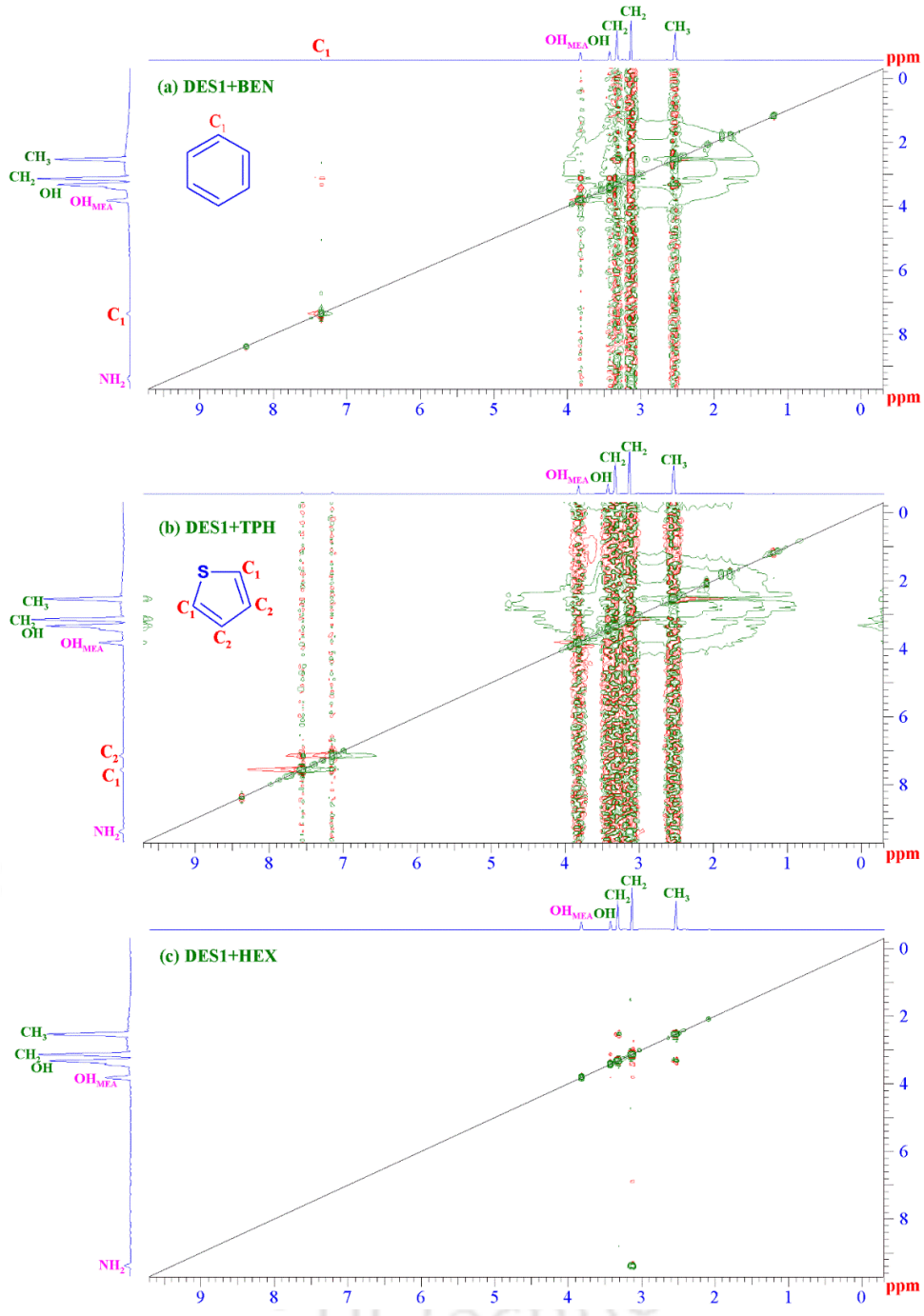

Figure 2.15. (a){^{1}H,^{1}H}-NOESY of 20 wt% benzene in monoethanolamine and ChCl; (b) {^{1}H,^{1}H}-NOESY of 20 wt% thiophenes in monoethanolamine and ChCl; (c) {^{1}H,^{1}H}-NOESY of 20 wt% hexane in monoethanolamine and ChCl.

It also shows weaker NOE cross-peaks with the monoethanolamine NH_2(~2.50 ppm) group. The hydroxyl protons of ChCl and monoethanolamine show a weak negative cross peak with the methyl protons of ChCl, which is attributed to the exchange of cross-peaks with aromatic protons. These observations indicate that hydrogen bonds were formed between the

DESs components, as indicated in figure 2.14. Furthermore, it shows that the individual components maintained their structure in the DES, which agrees with previous studies in other DESs [52-54].

After adding 20 wt. % benzene, thiophene, and *n*-hexane in DES1, all cross-peaks show the negative peaks. It indicates that the interaction is still achievable even if it is difficult to distinguish between negative NOEs and interaction exchange. However, the chemical shifts of protons of benzene (~7.32ppm) and thiophene (~7.21-7.53ppm) with protons of DES1 components show cross-peaks in figures 2.16(a) and 2.16(b), confirming the strong interaction revealed by hydrogen bonding as shown in figure 2.9-2.11. It is easy to observe that a strong cross interaction exists between the hydroxyl and NH_2 proton of monoethanolamine with benzene and thiophene. It shows a cross-correlation of OH-group and NH_2-group within the MEA moiety with benzene (~7.32ppm) and thiophene (~7.21-7.53 ppm). The CH_2 (~3.14-3.14 ppm) protons of monoethanolamine and methyl protons (~2.50 ppm) of ChCl remained in close space interaction, indicating a strong interaction.The hydroxyl group proton attached to ChCl, the evolution of NOEs to the benzene and thiophene protons is now favoured over the intramolecular NOEs in ChCl and monoethanolamine.

As NOEs are distance dependant, these observations suggest a more vital interaction between benzene, thiophene, and each of the DES1 components than intramolecular interaction between the own DES1 components. The formation of the new hydrogen bonds was also evident as both signals of monoethanolamine and the CH_2 protons of ChCl experienced a downfield shift by 0.05 ppm due to increased deshielding. In contrast, an up-field shift of 0.08 ppm was seen for the OH proton in ChCl, indicating a slight, moderate hydrogen bonding in ChCl. In the next chapter, we shall discuss the ternary systems in general. DESs comprise a hydrogen bond acceptor (HBA) in the form of methyltriphenylphosphonium bromide (MTPB) and a hydrogen bond donor (HBD) in the form of ethylene glycol, with a 1:4 molar ratio.

However, the aliphatic fraction is less promising in DES, as revealed by the present study, as their solubility for the aliphatic compounds increases with the chain length of alkyl groups, makes economically difficult for the solvents recovery. As a result, we choose the methyltriphenylphosphonium bromide (MTPB) based solvents for the extraction of aromatic fraction as they are considered the most promising solvents due to minimal solubility for the hydrocarbon stream. The DES shall then extract benzene from representative diesel fuel components, a mixture of *n*-decane, *n*-dodecane, and *n*-hexadecane.

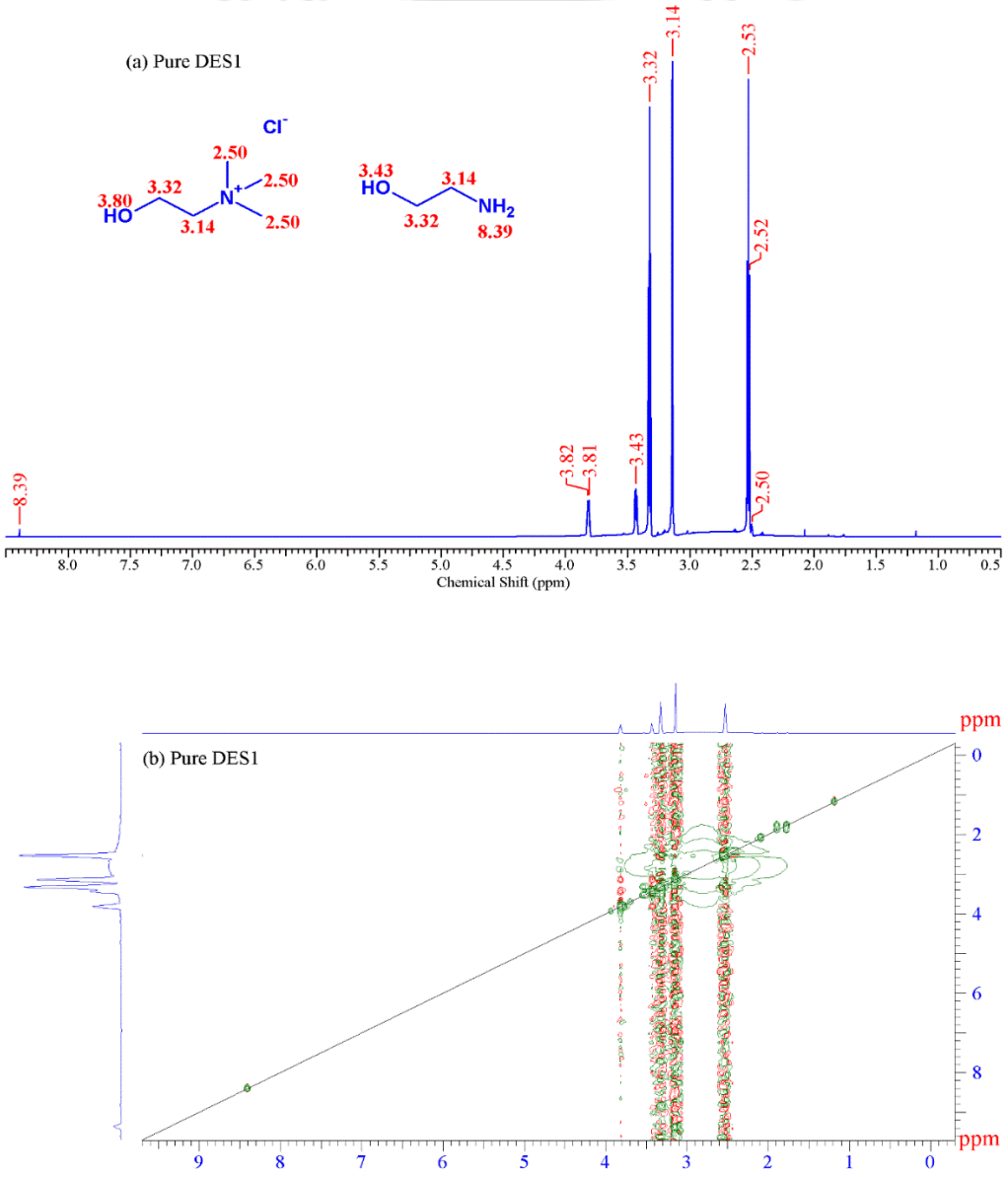

Figure 2.16. (a) ^{1}H NMR of monoethanolamine and ChCl in pure DES1 (b) NOE-interactions between monoethanolamine and ChCl in pure DES1.

2.4 Summary

The Monoethanolamine based DESs show better solvation for thiophene and benzene than *n*-hexane, which is interpreted by exploring the liquid structure through molecular dynamics and strong interactions confirmed by 2D NMR. The aromatic compounds show a higher non-bonded interaction between solute (benzene and thiophene) and components of DES1 than aliphatic hydrocarbons. The solvation of thiophene in the studied DES1 was more than benzene due to the electron delocalization effect of sulfur attached to the aromatic ring of thiophene. The benzene and thiophene are hydrogen-bonded to both the donor and acceptor of DES1 components, although MEA exhibits a stronger hydrogen bond than choline cation. The absence of chloride anion interactions results from the retention of strong hydrogen bonds between the Cl^-, the choline cation, and HBD. Benzene is seen to interact with the choline cation and HBD (MEA) components of the deep eutectic solvent through multiple weak non-covalent interactions (e.g., C–H$\cdots\pi$, O–H$\cdots\pi$, and N–H$\cdots\pi$). Similarly, thiophene's electron-withdrawing property improves its solubility in DES1 through non-covalent interactions (e.g., C–H$\cdots\pi$, O–H$\cdots\pi$, and N–H$\cdots\pi$). The sulphur atom's nonbonding electron pair is weakly nucleophilic, and thiophene forms hydrogen bonds with the hydroxyl and amine groups of monoethanolamine through the sulphur attached hydrogen and π-electron cloud. The choline cation also forms the non-covalent interaction through the $N_{CHL,}$ and OH_{CHL} through $N_{CHL}\cdots O$ and O-$H_{CHL}\cdots S$ hydrogen bonding. The ^1H and 2D NOESY spectroscopy revealed that the choline chloride and HBD were the primary interaction sites between aromatic compounds with DES1.

References

1. Meindersma, G. W.; Podt, A. J.; de Haan, A. B. Selection of ionic liquids for the extraction of aromatic hydrocarbons from aromatic/aliphatic mixtures. *Fuel Process. Technol.* **2005,** *87* (1), 59-70.
2. Kurnia, K. A.; Athirah, N. A.; Candieiro, F. J. M.; Lal, B. Phase behavior of ternary mixtures {aliphatic hydrocarbon+ aromatic hydrocarbon+ deep eutectic solvent}: A step forward toward "greener" extraction process. *Procedia Eng.* **2016,** *148*, 1340-1345.
3. Rodriguez, N. R.; Requejo, P. F.; Kroon, M. C. Aliphatic–aromatic separation using deep eutectic solvents as extracting agents. *Ind. Eng. Chem. Res.* **2015,** *54* (45), 11404-11412.
4. Rodriguez, N. R.; Gerlach, T.; Scheepers, D.; Kroon, M. C.; Smirnova, I. Experimental determination of the LLE data of systems consisting of {hexane+ benzene+ deep eutectic solvent} and prediction using the Conductor-like Screening Model for Real Solvents. *J. Chem. Thermodyn.* **2017,** *104*, 128-137.
5. Stanislaus, A.; Cooper, B. H. Aromatic hydrogenation catalysis: a review. *Catal. Rev. - Sci. Eng.* **1994,** *36* (1), 75-123.
6. ASTM, D. 5623, Sulfur Compounds in Light Petroleum Liquids by Gas Chromatography and Sulfur Selective Detection, Annual Book of Standards, 5, **1995**.
7. Hadj-Kali, M. K.; Salleh, Z.; Ali, E.; Khan, R.; Hashim, M. A. Separation of aromatic and aliphatic hydrocarbons using deep eutectic solvents: A critical review. *Fluid Phase Equilib.* **2017,** *448*, 152-167.
8. Sas, O. G. l.; Fidalgo, R. n.; Domínguez, I.; Macedo, E. A.; González, B. a. Physical properties of the pure deep eutectic solvent,[ChCl]:[Lev](1: 2) DES, and its binary mixtures with alcohols. *J. Chem. Eng. Data* **2016,** *61* (12), 4191-4202.
9. Zhang, Q.; Vigier, K. D. O.; Royer, S.; Jerome, F. Deep eutectic solvents: syntheses, properties and applications. *Chem. Soc. Rev.* **2012,** *41* (21), 7108-7146.
10. Smith, E. L.; Abbott, A. P.; Ryder, K. S. Deep eutectic solvents (DESs) and their applications. *Chem. Rev.* **2014,** *114* (21), 11060-11082.
11. Naik, P. K.; Dehury, P.; Paul, S.; Banerjee, T. Evaluation of Deep Eutectic Solvent for the selective extraction of toluene and quinoline at T= 308.15 K and p= 1 bar. *Fluid Phase Equilib.* **2016,** *423*, 146-155.
12. Verma, R.; Naik, P. K.; Diaz, I.; Banerjee, T. Separation of low molecular weight alcohols from water with deep eutectic solvents: Liquid-liquid equilibria and process simulations. *Fluid Phase Equilib.* **2021,** *533*, 112949.
13. Naik, P. K.; Kundu, D.; Bairagya, P.; Banerjee, T. Phase behavior of water-menthol based deep eutectic solvent-dodecane system. *Chem. Thermodyn. Therm. Anal.* **2021,** *3*, 100011.
14. (14) Zhang, W.; Chen, Z.; Shen, Y.; Li, G.; Dai, Y.; Qi, J.; Ma, Y.; Yang, S.; Wang, Y. Molecular mechanism and extraction performance evaluation for separation of methanol and n-hexane via ionic liquids as extractant. *ACS Sustain. Chem. Eng.* **2020,** *8* (23), 8700-8712.
15. Majid, M. F.; Zaid, H. F. M.; Kait, C. F.; Jumbri, K.; Yuan, L. C.; Rajasuriyan, S. Futuristic advance and perspective of deep eutectic solvent for extractive desulfurization of fuel oil: A review. *J. Mol. Liq.* **2020,** *306*, 112870.
16. Shekaari, H.; Zafarani-Moattar, M. T.; Mohammadi, B. Effective extraction of benzene and thiophene by novel deep eutectic solvents from hexane/aromatic mixture at different temperatures. *Fluid Phase Equilib.* **2019,** *484*, 38-52.

17. Kumar, N.; Naik, P. K.; Banerjee, T. Molecular modeling insights in the extraction of benzene from hydrocarbon stream using deep eutectic solvent. *J. Mol. Liq.* **2020,** *317*, 113909.
18. Naik, P. K.; Mohan, M.; Banerjee, T.; Paul, S.; Goud, V. V. Molecular dynamic simulations for the extraction of quinoline from heptane in the presence of a low-cost phosphonium-based deep eutectic solvent. *J. Phys. Chem. B* **2018,** *122* (14), 4006-4015.
19. Naik, P. K.; Paul, S.; Banerjee, T. Physiochemical properties and molecular dynamics simulations of phosphonium and ammonium based deep eutectic solvents. *J. Solut. Chem.* **2019,** *48* (7), 1046-1065.
20. Gutiérrez, A.; Atilhan, M.; Aparicio, S. A theoretical study on lidocaine solubility in deep eutectic solvents. *Phys. Chem. Chem. Phys.* **2018,** *20* (43), 27464-27473.
21. Gutiérrez, A.; Atilhan, M.; Aparicio, S. Molecular dynamics study on water confinement in deep eutectic solvents. *J. Mol. Liq.* **2021,** *339*, 116758.
22. Malik, A.; Dhattarwal, H. S.; Kashyap, H. K. Distinct solvation structures of CO2 and SO2 in reline and ethaline deep eutectic solvents revealed by AIMD simulations. *J. Phys. Chem. B* **2021,** *125* (7), 1852-1860.
23. Zhang, Y.; Poe, D.; Heroux, L.; Squire, H.; Doherty, B. W.; Long, Z.; Dadmun, M.; Gurkan, B.; Tuckerman, M. E.; Maginn, E. J. Liquid structure and transport properties of the deep eutectic solvent ethaline. *J. Phys. Chem. B* **2020,** *124* (25), 5251-5264.
24. Perkins, S. L.; Painter, P.; Colina, C. M. Molecular dynamic simulations and vibrational analysis of an ionic liquid analogue. *J. Phys. Chem. B* **2013,** *117* (35), 10250-10260.
25. Perkins, S. L.; Painter, P.; Colina, C. M. Experimental and computational studies of choline chloride-based deep eutectic solvents. *J. Chem. Eng. Data.* **2014,** *59* (11), 3652-3662.
26. Dennington, R.; Keith, T.; Millam, J. GaussView, version 5. **2009**.
27. Frisch, M.; Trucks, G.; Schlegel, H.; Scuseria, G.; Robb, M.; Cheeseman, J.; Scalmani, G.; Barone, V.; Petersson, G.; Nakatsuji, H. Gaussian 16 rev. *Gaussian Inc.: Wallingford, CT, USA* **2016**.
28. Frisch, M. Gaussian09. *http://www. gaussian. com/* **2009**.
29. Wang, J.; Wolf, R. M.; Caldwell, J. W.; Kollman, P. A.; Case, D. A. Development and testing of a general amber force field. *J. Comput. Chem.* **2004,** *25* (9), 1157-1174.
30. Jakalian, A.; Bush, B. L.; Jack, D. B.; Bayly, C. I. Fast, efficient generation of high-quality atomic charges. AM1-BCC model: I. Method. *J. Comput. Chem.* **2000,** *21* (2), 132-146.
31. Bayly, C. I.; Cieplak, P.; Cornell, W.; Kollman, P. A. A well-behaved electrostatic potential based method using charge restraints for deriving atomic charges: the RESP model. *J. Phys. Chem.* **1993,** *97* (40), 10269-10280.
32. Salehi, H. S.; Polat, H. M.; de Meyer, F.; Houriez, C.; Coquelet, C.; Vlugt, T. J.; Moultos, O. A. Vapor pressures and vapor phase compositions of choline chloride urea and choline chloride ethylene glycol deep eutectic solvents from molecular simulation. *J. Chem. Phys.* **2021,** *155* (11), 114504.
33. Celebi, A. T.; Vlugt, T. J.; Moultos, O. A. Structural, thermodynamic, and transport properties of aqueous reline and ethaline solutions from molecular dynamics simulations. *J. Phys. Chem. B* **2019,** *123* (51), 11014-11025.
34. Doherty, B.; Acevedo, O. OPLS force field for choline chloride-based deep eutectic solvents. *J. Phys. Chem. B* **2018,** *122* (43), 9982-9993.
35. Wang, J.; Wang, W.; Kollman, P. A.; Case, D. A. Antechamber: an accessory software package for molecular mechanical calculations. *J. Am. Chem. Soc.* **2001,** *222*, U403.
36. Wang, J.; Duke, R.; Luo, R.; Walker, R.; Zhang, W.; Merz, K.; Roberts, B.; Hayik, S.; Roitberg, A.; Seabra, G. Amber 12 Reference Manual. *University of California* **2012**.

37. Phillips, J. C.; Braun, R.; Wang, W.; Gumbart, J.; Tajkhorshid, E.; Villa, E.; Chipot, C.; Skeel, R. D.; Kale, L.; Schulten, K. Scalable molecular dynamics with NAMD. *J. Comput. Chem.* **2005,** *26* (16), 1781-1802.
38. Martínez, L.; Andrade, R.; Birgin, E. G.; Martínez, J. M. PACKMOL: a package for building initial configurations for molecular dynamics simulations. *J. Comput. Chem.* **2009,** *30* (13), 2157-2164.
39. Martyna, G. J.; Tobias, D. J.; Klein, M. L. Constant pressure molecular dynamics algorithms. *J. Chem. Phys.* **1994,** *101* (5), 4177-4189.
40. Feller, S. E.; Zhang, Y.; Pastor, R. W.; Brooks, B. R. Constant pressure molecular dynamics simulation: the Langevin piston method. *The Journal of chemical physics* **1995,** *103* (11), 4613-4621.
41. Humphrey, W.; Dalke, A.; Schulten, K. VMD: Visual molecular dynamics. *J. Mol. Graph.* **1996,** *14* (1), 33-38.
42. Frisch, M.; Trucks, G.; Schlegel, H.; Scuseria, G.; Robb, M.; Cheeseman, J.; Scalmani, G.; Barone, V.; Petersson, G.; Nakatsuji, H., Gaussian 16. Gaussian, Inc. Wallingford, CT: 2016.
43. Lee, C.; Yang, W.; Parr, R. G. Development of the Colle-Salvetti correlation-energy formula into a functional of the electron density. *Phys. Rev. B* **1988,** *37* (2), 785.
44. Becke, A. D. Density-functional exchange-energy approximation with correct asymptotic behavior. *Phys. Rev. A* **1988,** *38* (6), 3098.
45. Becke, A., Density-Functional Thermochemistry. III. The Role of Exact Exchange. *J. Chem. Phys.* **1993**, 98, 5648-5652..
46. Grimme, S.; Antony, J.; Ehrlich, S.; Krieg, H. A consistent and accurate ab initio parametrization of density functional dispersion correction (DFT-D) for the 94 elements H-Pu. *J. Chem. Phys.* **2010,** *132* (15), 154104.
47. Simon, S.; Duran, M.; Dannenberg, J. How does basis set superposition error change the potential surfaces for hydrogen-bonded dimers? *J. Chem. Phys.* **1996,** *105* (24), 11024-11031.
48. Kumar, N.; Banerjee, T. Molecular Mechanism and Solubility Performance Evaluation for Separation of Benzothiophene and Model Diesel Compounds through Deep Eutectic Solvents as Extractants. *Ind. Eng. Chem. Res.* **2022**, 61(3), 1464–1474
49. Häkkinen, R.; Abbott, A. Solvation of carbohydrates in five choline chloride-based deep eutectic solvents and the implication for cellulose solubility. *Green. Chem.* **2019,** *21* (17), 4673-4682.
50. Brehm, M.; Kirchner, B., TRAVIS-a free analyzer and visualizer for Monte Carlo and molecular dynamics trajectories. *J. Chem. Inf. Model.* **2011**, 51(8), 2007–2023
51. Claridge, T. D., *High-resolution NMR techniques in organic chemistry*. Elsevier: 2016; Vol. 27.
52. Abbott, A. P.; Capper, G.; Davies, D. L.; Rasheed, R. K.; Tambyrajah, V. Novel solvent properties of choline chloride/urea mixtures. *ChemComm.* **2003,** (1), 70-71.
53. Mohan, M.; Goud, V. V.; Banerjee, T. Solubility of glucose, xylose, fructose and galactose in ionic liquids: Experimental and theoretical studies using a continuum solvation model. *Fluid Phase Equilib.* **2015,** *395*, 33-43.
54. Wazeer, I.; Hizaddin, H. F.; El Blidi, L.; Ali, E.; Hashim, M. A.; Hadj-Kali, M. K. Liquid–Liquid Equilibria for Binary Azeotrope Mixtures of Benzene and Alcohols Using Choline Chloride-Based Deep Eutectic Solvents. *J. Chem. Eng. Data.* **2018,** *63* (3), 613-624.

CHAPTER 3

Liquid-liquid Extraction of Aromatic Compounds

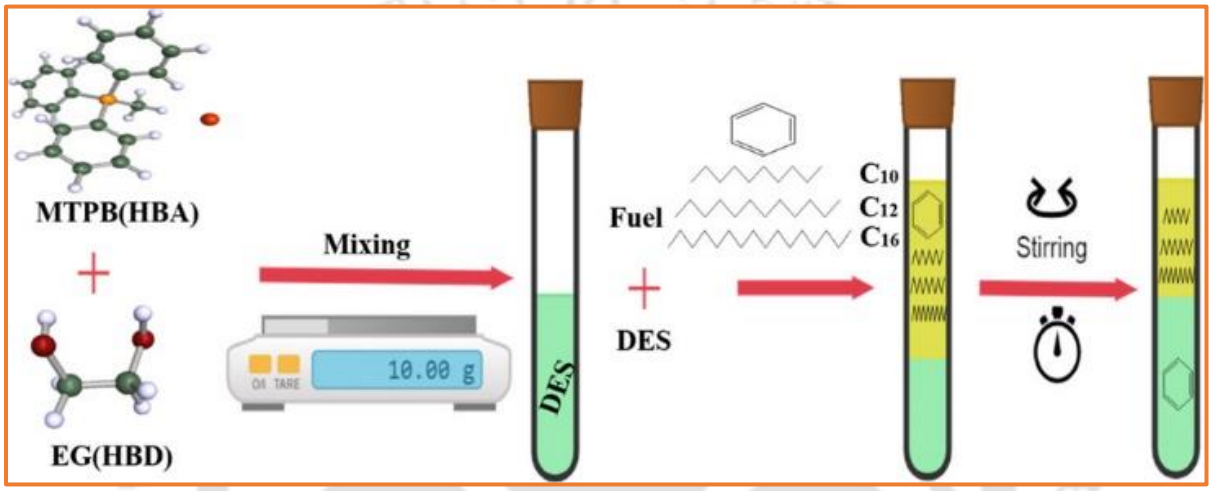

The current chapter discusses phosphonium-based DES for the dearomatisation of model diesel components at 25℃ and p=1 bar. The DES comprising of Hydrogen Bond Acceptor (HBA), namely methyltriphenylphosphonium bromide (MTPB), along with ethylene glycol as hydrogen bond donor (HBD), was formulated with a molar ratio of 1:4. The DES was then used to extract benzene from representative diesel fuel components, a mixture of n-decane, n-dodecane, and n-hexadecane. Ternary liquid-liquid equilibrium (LLE) experiments were then performed at ambient conditions with different benzene concentrations with feed varying from 2-20 wt %. An absence of solvent in the raffinate phase was found in all the tie lines, suggesting limited solvent recovery costs. Besides, it was also found that all three ternary systems show Type I phase activity with positive slopes, indicating that the desired removal of benzene requires a small amount of solvent. The quantum chemical-based COSMO-SAC model was then used to predict the tie lines giving an average RMSD value of 1.2%. The mechanism of the extraction process was also extensively studied with the help of quantitative ^{1}H NMR and FT-IR spectroscopy. Higher benzene extraction efficiencies were observed due to the strong non-covalent interaction between the DES and benzene.

3.1 Introduction

In the refining domain, the extraction of aromatic from aliphatic compounds in the order of ppm is challenging and cumbersome. Recently Environmental Protection Agency (EPA) limits the benzene percentage in motor fuels to an average of 0.62% by volume (maximum 1.3%). The extraction of aromatic compounds from the naphtha cracking stream is a vital step because of two significant factors: (1) new requirements on the petroleum products which demand a reduction of the aromatic compounds to minimize their environmental impact and ; (2) the economic importance of aromatic components when used as raw materials[1]. The partitioning of aromatics at the ultra-low level is complicated because of limitations in conventional methods[2-3]. In gasoline, aromatic compounds are desirable to increase the

octane number; however, for diesel fuel, they decrease the cetane number, and the benzene concentration needs to be limited below 50 ppm due to its high carcinogenicity. In comparison, because of the increased combustion in engines, low aromatic concentrations are ideal for kerosene and diesel oil. During combustion, aromatic components also create soot and decrease diesel fuel quality in terms of cetane number.

Industrially, the separation of aromatic ring compounds from straight-chain aliphatic compounds occurs using traditional methods with solvents such as sulfolane, ethylene glycol, tetraethylene glycol, N-methylpyrrolidone, and glycols. The industrial operation uses conventional solvents as an extracting agent with a liquid-liquid extraction process, accompanied by extractive distillation for solvent recovery[4]. However, they are not an effective separation method for mixtures with an aromatic content of less than 20 wt % due to the high-energy expenditure required for solvent recovery. Therefore, in fuels such as diesel and kerosene, where the desired aromatic content is lower, the separation of aromatics from aliphatic compounds is carried out using liquid-liquid extraction. However, if the issue of solvent recovery is solved, the extraction could be achieved at the starting of the naphtha cracking. Thus the energy requirements would be decreased during the entire cracking process due to the decrease in the flows to be heated in the columns[5-6].

In recent times, various solvents have been discovered as substitutes for the conventional sulfolane process. It has been stated that ionic liquids (ILs) [7] might be used in applications as extracting agents for aromatic decantation from aliphatic compounds[8-9]. Some ILs show similar values of solute distribution coefficient and selectivity as compared to sulfolane. Furthermore, the negligible vapour pressure of ILs eases the recovery cost as compared to the sulfolane process. For instance, ILs could be simply recuperated after flash distillation extraction. Due to their complicated synthesis, the high price of ILs is a major drawback for implementation in large-scale industrial applications.

A new generation of solvents, termed deep eutectic solvents (DESs) or simply eutectic mixtures, was first reported a decade ago[10]. DESs are binary or ternary mixtures with a eutectic point dependent on the specific composition of the constituents, namely the hydrogen bond donor (HBD) and hydrogen bond acceptor (HBA). Furthermore, the presence of a eutectic point in a mixture cannot be used to define or characterise a deep eutectic solvent because a eutectic point[11] would effectively represent the mixtures of all compounds that are essentially present as immiscible in the solid phase. Further, deep eutectic solvents are characterised as a mixture of two or more pure chemicals whose eutectic point temperature is lower than that of an ideal liquid mixture, resulting in considerable deviations from ideality ($\Delta T_2 > 0$) [12]. The temperature depression should also be such that the mixture is liquid at operating temperature for a specific composition range. The term 'eutectic solvent' could be used to describe mixtures that do not meet these criteria. The temperature depression should be defined as the difference (ΔT_2) between the ideal ($T_{E,\ ideal}$) and the real (T_E) eutectic point and not as the difference (ΔT_1) between the linear combination of the melting points of the pure components and the real eutectic point [13]. The scientific community has confirmed that available DES are eutectic mixtures of unique compositions [14-16]. DESs are formed when one or more hydrogen bond acceptors (HBAs) and one or more hydrogen bond donors (HBD's) are combined in the specific molar ratio. These mixtures of HBA and HBD display a substantial drop in the melting point compared to the individual melting points of initial compounds [17-19].

DESs share several properties with ionic liquids, e.g., low vapour pressure, wide liquid range, water compatibility, and non-flammability[20]. These properties are essential concerning the previously described issue of solvent recovery. They are essentially inexpensive compared to ILs, as some of them have precursors from renewable feedstock. Therefore, if any DES proves distribution coefficient and selectivity values similar to conventional solvents, it

is possible to resolve the solvent recovery of sulfolane and the high synthesis price of ILs. Apart from IL, recent studies on different DESs were published[21]. Tarek Lemaoui et al. studied the simultaneous dearomatization, desulfurization, and denitrogenation of diesel fuels *via* liquid-liquid extraction[22]. Similar studies were performed for NADESs in the extraction of thiophene, pyridine, and toluene from *n*-Decane[23]. The results showed an increase in distribution ratio, selectivity, and extraction efficiency in the order as follows: pyridine > thiophene > toluene. Marko Rogošić et al. performed the extraction using choline chloride-based DES. They found that the highest extraction efficiency is achieved with the most significant mass ratio of DES: model fuel of 1.00 kg/k [24].

This current work aims to estimate the suitability of deep eutectic solvents as extracting agents for the extraction of benzene from representative diesel components such as *n*-decane, *n*-dodecane, and *n*-hexadecane. Initially, DES was synthesized by adding a Hydrogen Bond Acceptor (HBA), namely methyltriphenylphosphonium bromide (MTBP), along with ethylene glycol as a hydrogen bond donor (HBD) in a specific molar ratio of 1:4. The liquid−liquid equilibrium (LLE) data of three ternary systems {*n*-decane + benzene + DES}, {*n*-dodecane + benzene + DES} and {*n*-hexadecane + benzene + DES} were then determined at $T = 25$ °C and atmospheric pressure (p=0.1 MPa). To measure the separation suitability of the considered DES, the solute distribution coefficient, selectivity, and extraction efficiency was obtained from the experimental LLE data. The quantum computation-based COSMO-SAC model was then used to correlate the LLE experimental data. Thereafter the COSMO-SAC based predicted sigma profile was used to provide insight into the interaction mechanism of representative diesel components and benzene. Finally, the extraction mechanism of benzene using DES was determined with the help of FT-IR and quantitative ^{1}H NMR.

3.2 Experimental Details

3.2.1 Chemicals

Table 3.1 gives the name of the chemicals, the purity of the chemicals, the CAS number, and the supplier's name. In order to remove moisture, the DES constituents (i.e., HBA and HBD) were dried overnight at 45°C in a vacuum oven. Benzene, *n*-decane, *n*-dodecane, and *n*-hexadecane were obtained from TCI India and were used as obtained. Solvent for NMR spectroscopy, namely deuterated chloroform (Sigma Aldrich, 99.8% atom) and deuterated dimethyl sulfoxide (Sigma Aldrich, 99.9%atom), was used to evaluate the extract and raffinate phase compositions.

Table 3.1. List of chemicals[a] used in this LLE experimental study.

Name of Compound	**CAS No.**	**Sample Purification Method[a]**	**Purity Grade**	**Supplier**
Methyltriphenylphophonium bromide	1779-49-3	HPLC[b]	≥98% (mass fraction)	Merck
Ethylene Glycol	107-21-1	GC[c]	≥98 % (mass fraction)	Merck
Benzene	71-43-2	GC	≥99 % (mass fraction)	Merck
n-dodecane	112-40-3	GC	≥99 % (mass fraction)	Merck
n-decane	124-18-5	GC	≥99% (mass fraction)	Merck
n-hexadecane	544-76-3	GC	≥99 % (mass fraction)	Merck
Chloroform-d_6	56391-91-3	NMR-grade	≥99.8% (mass fraction)	Sigma Aldrich
Dimethyl sulfoxide-d_6 (DMSO-d6)	2206-27-1	NMR-grade	≥99.8% (mass fraction)	Sigma Aldrich

[a] Chemicals used as supplied and purity as mentioned by the supplier,
[b]High performance liquid chromatography (HPLC)
[c] Gas Chromatography (GC).

3.2.2 Preparation of DES

To synthesize the DES, the HBA and HBD were mixed in a closed container under constant stirring conditions at 45°C until a clear homogeneous liquid was formed[25]. Hydrogen bond acceptor (HBA), namely Methyltriphenylphosphonium bromide (MTBP), and hydrogen bond donor (HBD), namely Ethylene glycol, were added in a specific molar ratio of 1:4 to prepare the DES [14, 15]. The mixture was kept for 12 hr and then cooled down slowly until it reached room temperature. Thereafter the DES prior to measurement was kept under 65 kPa (Waki Instruments, India) at 45℃ for 12 hr to remove any volatile matter and water content.

The physical properties of DES and solubility of benzene in solvent are given in Table 3.2 with uncertainties. The boiling point of the DES was then measured at ambient conditions by a boiling point apparatus (ANALAB Scientific, India). The density of the formulated DES was measured at atmospheric pressure by a digital density meter (Anton Paar DMA 4500), having an uncertainty of ±0.001g cm^{-3}. The viscosity of DES was measured in a rheometer (make: Anton Paar (Austria), model: Physica MCR 301) employing a parallel plate geometry at 25°C with a shear rate of u=1 s^{-1}.

Table 3.2. Physical properties of DES at Temperature T= 25 ℃ and Pressure p = 0.1 MPa[a]

HBA	HBD	Molar Ratio	Molar Mass (g/mol)	Density (ρ) (g/cm^3)	Boiling Point at 101.3 kPa (°C)	Viscosity (η) (mPa.s)	Solubility of Benzene in DES ($x_{benzene}$)
MTPB	EG	1:4	121.102	1.224	257	121 ± 1	0.135

[a] The standard uncertainties u are u (x) = 0.001, u (T) = 0.01 °C, u (B.P) = 2 °C and u (P) =2 kPa, u (ρ) = 0.004 g·cm^{-3}, mole basis u(xHBA) = u(xHBD) = 1.708 × 10^{-6} mol, u(M)=0.0001 g mol−1 and u (η) = 1 with 0.95 level of confidence (k ≈ 2).

Table 3.3 lists the measured, and literature-reported densities (ρ) and viscosities (η) of the studied DES. Values of density and viscosity agree reasonably well with the literature. However, specific points, especially prediction through artificial or empirical methods[26-27]

vary due to assumptions considered during the prediction. The viscosity reported in this article does not match with our earlier reported article[28], because the values were obtained at different shear rates. DES is a shear-thinning fluid, as a result, with the increase in shear rate, viscosity of solvent decreases. Therefore, the value of viscosity in the present study is reported at a much lower shear rate ($u=1s^{-1}$) than the earlier reported viscosity. Further, the variation in density can also be attributed to water content and/or impurities.

Table 3.3. The Experimental Values of Density ρ as a Function of Temperature T= 25-85°C and Pressure p= 0.1 MPa[a].

Temperature (°C)	Density (g/cm^3)
25	1.224
30	1.220
35	1.217
40	1.213
45	1.209
50	1.206
55	1.202
60	1.199
65	1.195
70	1.192
75	1.188
80	1.184
85	1.181

[a] Standard uncertainties, *u*, of T, ρ, and p are *u*(T) = 0.05 K, *u*(ρ) = 0.0040 g·cm^{-3}, and *u*(p)= 2.0 kPa, respectively. Density variation with temperature follows the equation: $\rho\left(\frac{\mathrm{gm}}{cm^3}\right) = -0.0007\mathrm{T} + 1.2417$

Karl Fisher Titrator (Model No.: 787 KF; Make: M/s Metrohm, Switzerland) was used for the measurement of water content in DES. The water content measured in DES was 0.001 wt %. The uncertainty of the apparatus was within ±100 ppm, and the measurement was confirmed with a triplicate run at each point. Later the vacuum-dried DES was characterised for purity with ^{1}H (Figure 3.6) and ^{13}C (Figure 3.6) NMR spectra through a composition

analysis by recording the NMR spectra (600 MHz NMR, Bruker, Germany). For the binary Benzene-DES mixture, the cloud point method was adopted to quantify the solubility of benzene in DES. In the cloud point method, a known amount of the solvent in a glass vial was inserted. Thereafter benzene was added dropwise until slight turbidity appeared in the top layer of the solvent.

3.2.3 Liquid-liquid Extraction Experiment

Benzene was used as an aromatic compound, while *n*-decane, *n*-dodecane, and *n*-hexadecane were used as characteristic representative diesel components. Benzene was mixed as an aromatic compound in the range of 2-20 wt % so that the mixtures lie within the homogeneous region. The LLE mixture formed was stirred at 25°C for 8 hr and then allowed for 12 hr for equilibration. Throughout the experiments, the feed (benzene+ model diesel) and the solvent (DES) ratio was maintained at 1:1 unless otherwise specified. All the experiments were conducted thrice in an identical environmental conditions to assess reproducibility. The overall experimental errors were less than ±3 percent within the binary mixtures as per the recorded ^{1}H NMR spectra.

3.2.4 LLE Experiments and Composition Analysis of Phases

A single-stage LLE phase equilibrium experiment for each tie line was conducted. This was performed by preparing an adequate mixture of the solvent and feed components in a 15 mL stoppered vial. Six compositions were chosen in such a way that they cover the concentration of aromatic content lower than 20 wt %. The equivalent feed volume was calculated according to the analogous molecular weight, density, and proportion of the individual compound. Using a thermomixer (Eppendorf, Germany), the mixtures were stirred for 5-10 minutes at 800 rpm and 298.15 K. Afterward, the mixture was then kept inside a horizontal shaker with an incubator (Daihan LabTech, China) with a PID-control of temperature having the uncertainty of ±0.1 K. This was subjected to rapid mixing at 25°C and 200 rpm for a total duration of 12

hr. The equilibration of the LLE mixture was then allowed for 8 hr to separate it into two distinct phases referred to as the bottom (solvent rich) and top (alkane rich) phases, respectively. The blends were allowed to settle for 12 hr at 25℃ to obtain a clear and stable phase separation. The samples of different phases were collected through a hypodermic syringe without disturbing the extract and raffinate phases coexistence interphase. Then corresponding compositions were then analysed using ^{1}H NMR (Bruker, ADVANCE III HD, and software ACD NMR). Throughout the LLE experiment, the DES was treated as a single pseudo compound as they are referred to as a binary eutectic mixture with a unique eutectic point. The term "*pseudo*" has been introduced to indicate that the DES was treated as a *pseudo*-pure species instead of a mixture of HBA and HBD. The composition of pure DES was justified experimentally using ^{1}H NMR.

^{1}H NMR has been studied extensively in multicomponent mixtures to analyse phase compositions [29]. We prepared a known sample in the homogeneous area similar to the binodal curve for checking the precision of NMR spectra and then conducted their ^{1}H NMR. The measured values were within an uncertainty of ±0.001 in the mole fraction. The number of hydrogen atoms corresponding to a moiety was calculated with the measured area under each of the proton resonances. Thereafter the mole fraction of each component was calculated with the corresponding area of a hydrogen atom when compared to the total calculated area in the spectra. Mathematically, it is given as,

$$x_i = \frac{H_i}{\sum_{i=1}^{3} H_i} \qquad (3.1)$$

H_i signifies the corresponding resonance area of the proton, and x_i is the mole fraction for single hydrogen of i^{th} component of the mixture.

The ^{1}H NMR spectra of DES are shown in Figure 3.6. In the spectrum, the total area of all hydrogen is normalized. Only one prominent resonance peak is chosen for the respective component to quantify the corresponding mole fraction in the respective phase. As discussed above, the number of hydrogens of the corresponding moiety is determined by calculating the area under the resonance and dividing the area (Eq.3.1) with the total hydrogen atom of that moiety to calculate a single hydrogen atom area. The detailed calculation steps can be found in our previous literature [29]. Here the chemical shift at δ = 0.83-0.84 ppm is assigned to the CH_3 moieties of aliphatic compounds such as *n*-decane, *n*-dodecane, *n*-hexadecane, respectively, whereas the chemical shift at δ = 3.3-3.7 ppm is given to the terminal –CH_3 moiety of MTPB. Benzene was calculated within the chemical shift of 7.10-7.30 ppm.

The degree of affinity of the solute with extract and raffinate phases is calculated by the distribution ratio (D_i). A considerable value of the distribution ratio implies a lower amount of solvent is required with respect to the feed. Selectivity (S_{ij}) is the ratio of the distribution ratio of solute-rich phase to the model diesel components-rich phases. The mathematical forms are given by,

$$D_i = \frac{x_i^{Extract}}{x_i^{Raffinate}} \tag{3.2}$$

$$S_{ij} = \frac{x_i^{Extract}}{x_i^{Raffinate}} \Bigg/ \frac{x_j^{Extract}}{x_j^{Raffinate}} \tag{3.3}$$

$$\%EE = \left[\frac{x_{2,\text{initial}} - x_{2,R}}{x_{2,\text{initial}}}\right] \times 100 \tag{3.4}$$

Here, $x_i^{Extract}$ and $x_i^{Raffinate}$ represent the mole fractions of i^{th} component, i.e., benzene, and $x_j^{Extract}$ $x_j^{Raffinate}$ represent the mole fractions of the j^{th} component, i.e., diesel representative

compound in the extract and raffinate phase, respectively. In Extraction Efficiency (EE) $x_{2,\text{initial}}$ refers to the initial mole fraction of benzene in the feed, and $x_{2,R}$ is the final mole fraction of benzene in the aliphatic rich phase after extraction.

3.3 Results and Discussion

We shall now discuss the ternary liquid-liquid equilibrium (LLE) experiments with different benzene concentrations in feed varying from 2-20 wt % to explain the extraction insights. We first delve into the COSMO-based sigma profile to account for the polar and non-polar screening segments and develop an understanding of the interaction of different compounds with DES. This provides us with qualitative information of the hydrogen bond donors and acceptors, which quantify any non-covalent interaction effect within the moieties.

3.3.1 COSMO-SAC Model

The prediction of the LLE tie lines from the experimental data was performed using the COSMO-SAC model. With the Gauss view[30], the chemical structures of HBA, HBD, benzene, and aliphatic compounds were drawn. The molecular structure optimization of the compounds was then performed using the B3LYP level of theory and 6-31* basis set within Gaussian 09[31]. After the optimization of geometry, the COSMO file was generated at the P BVP86 level of density functional theory [32] using the triple zeta valence potential (TZVP) basis set with the DGA1[33] density fitting. COSMO calculation generates the sigma profiles, which comprise the surface screening charges of molecules. The Sigma profile of DES was then calculated by inserting the specific molar ratio of HBA and HBD. The screening charge distribution of DES was calculated by adding the normalized sigma profiles calculated separately.

$$p_{DES}(\sigma) = p_{HBA}(\sigma) + p_{HBD}(\sigma) = f_{HBA}p_{HBA}(\sigma) + f_{HBD}p_{HBD}(\sigma) \qquad (3.5)$$

Here, $p_{HBA}(\sigma)$ *and* $p_{HBD}(\sigma)$ denotes the σ-profile of HBA and HBD of given DES, f_{HBA}, and f_{HBD} are the mole fraction that has been used in the LLE experimental work (*i.e.*, 1:4). The

σ-profile of HBA and HBD are then normalised to obtain the sigma profile of a solvent. COSMO-SAC predicted pseudo ternary tie lines of LLE are then estimated and matched with experimental calculated tie lines[34] with a modified Rachford Rice algorithm[35]. The equations and methodology can be obtained from our earlier work[36-38] and the earlier COSMO-SAC implementation[39]. COSMO-SAC data and experimental data of pseudo ternary tie lines of LLE were then compared[40] using root mean square deviation (RMSD) given in equation 3.6.

$$rmsd = 100 \times \left[\sum_{i=1}^{c} \sum_{j=1}^{p} \sum_{t=1}^{m} \frac{\left(x_{calc,i,t}^{j} - x_{\exp t,i,t}^{j} \right)^2}{mcp} \right]^{1/2} \qquad (3.6)$$

Here x_{ik}^{j} and $\hat{x}_{ik}^{j}$ are the experimental and predicted mole ratios, and the given subscripts *i*, *j*, and *k* represent the component, phase, and tie lines, respectively.

3.3.2 *σ*-Profiles of DES and Model Diesel Components

The extraction efficiency of DES can be described by comparing the σ-profiles interaction between benzene and aliphatic compounds with respect to the σ-profiles given by the COSMO-RS model as described in detail by Klamt [41]. Using updated COSMO-SAC based σ-profiles[42], the extraction mechanism for benzene using DES from model diesel components can be explained and then corroborated to its high extraction efficiency. σ-Profiles are the probability distribution of the screening charges in a specified compound. Figure 3.1 shows the *σ*-profiles of benzene and representative diesel components with DES used in this work. Model diesel components *n*-decane, *n*-dodecane, and *n*-hexadecane σ-profiles are non-polar but vary in magnitude because of the extra carbon atoms or methyl groups. The *σ*-profiles of DES and benzene overlap each other in the non-polar region. The donor and acceptor regions are explained from the value of ± σ_{hb}=*0.0084 e/Å*^{2}. The peaks in the range of +0.010 to +0.025 correspond to the O or N electron-withdrawing parts of the O–H and Br^- parts, respectively, of the DES. The solubility of benzene is relatively much higher than *n*-alkane, which results in

higher extraction efficiency of DES. This could be attributed to the presence of π-electrons around the benzene component, which is absent in the *n*-alkane compound. As a consequence, the DES has more ability as a hydrogen bond acceptor than a hydrogen bond donor.

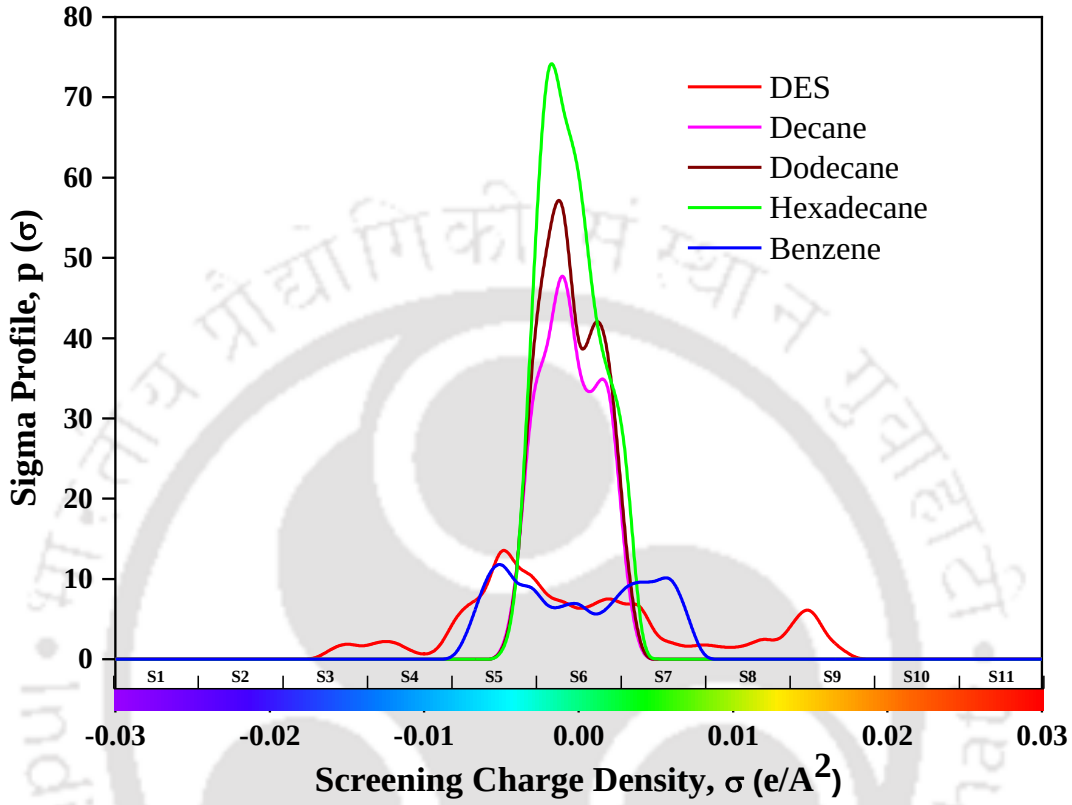

Figure 3.1. *σ*-Profiles of DES and model diesel compounds using the COSMO-SAC model.

Overall it is seen that the phase separation between the hydrophilic and hydrophobic have an explicit dependency with the octanol−water partition coefficient log (K_{OW}) [43]. The partition toward the more hydrophilic phase, rich phase, decreases with increasing log (K_{OW}). The log (K_{OW}) for benzene, *n*-decane, *n*-dodecane, *n*-hexadecane are 2.13, 5.01, 6.10, and 8.20, respectively. Higher values of K_{OW} indicate that partition towards hydrophilic (solvent-rich phase) decreases as alkane chain length increases. This is also attributed to the sigma profile that non-polarity increases with higher *n*-alkane chain length. On the contrary, the log K_{OW} value of ethylene glycol is -1.36, indicating its higher polarity that helps in initiating the non-covalent interaction with benzene, and MTPB shows the log K_{OW} value of 0.6143. This is the

reason for the high solubility of benzene compared to the model diesel fuel components, which are more or less non-polar and have few regions in the acceptor or donor region. We shall confirm this in our LLE experiments, which are discussed in the next section.

3.3.3 LLE Phase Behaviour

LLE data of three experimental systems consisting of {*n*-decane + benzene + DES}, {*n*-dodecane + benzene + DES}, and {*n*-hexadecane + benzene + DES} were measured at T = 25°C and Pressure p = 0.1 MPa. The distribution ratio (D), selectivity (S), and extraction efficiency (EE) were considered for the purpose of estimating the performance of each model diesel fuel component explicitly with a particular DES. The experimental LLE data are plotted through a triangular phase diagram for each system in figure 3.2. The numerical values of experimentally obtained tie lines data of the equilibrium composition are given in Tables 3.4-3.6, and the respective ^{1}H NMR of extract and raffinate phases of all three systems are given in Figure 3.3-3.5. These Tables also contain the calculated values of D (Eq. 2) and S (Eq. 3) for the solvent to feed ratios of 1:1. Based on the calculated LLE composition data, it is found that the concentrations of *n*-decane, *n*-dodecane, and *n*-hexadecane in the extract phase for all three ternary systems are less. Furthermore, based on the obtained NMR results, there is no noticeable amount of DES in the raffinate phases of all three ternary systems. It gave an insignificant amount of *model diesel compounds* in the extract phases and the nonappearance of DES compound in the raffinate phases, which specify negligible cross-contamination between the extract and raffinate phases[44]. This is highly favourable for the solvent recovery of the LLE process. It should be mentioned that the results obtained from ^{1}H NMR showed a distinctive peak for each impurity in both the DES-rich phase and *n*-alkane rich phase, and no new peaks were detected.

Table 3.4. Experimental Liquid-liquid Equilibrium (LLE) tie-line data for the ternary system: DES + benzene+ *n*-decane at Temperature T= 25°C and Pressure p=0.1 MPa[a]. The mole fractions of DES, benzene and *n*-decane are represented by x_1, x_2, and x_3, respectively.

Extract phase			Raffinate phase			*D*	Selectivity (S)
x_{DES}	x_{ben}	x_{dec}	x_{DES}	x_{ben}	x_{dec}		
0.944	0.053	0.008	0.000	0.048	0.953	1.12	129.9
0.891	0.099	0.010	0.000	0.099	0.901	1.00	94.0
0.845	0.139	0.016	0.000	0.180	0.821	0.77	39.7
0.806	0.179	0.015	0.000	0.288	0.713	0.62	29.8
0.757	0.227	0.016	0.000	0.365	0.635	0.62	25.0
0.718	0.263	0.019	0.000	0.418	0.582	0.63	18.8

[a] Standard uncertainties are $u(T) = 0.01$ °C, $u(x) = 0.001$, and $u(p) = 2$ kPa.

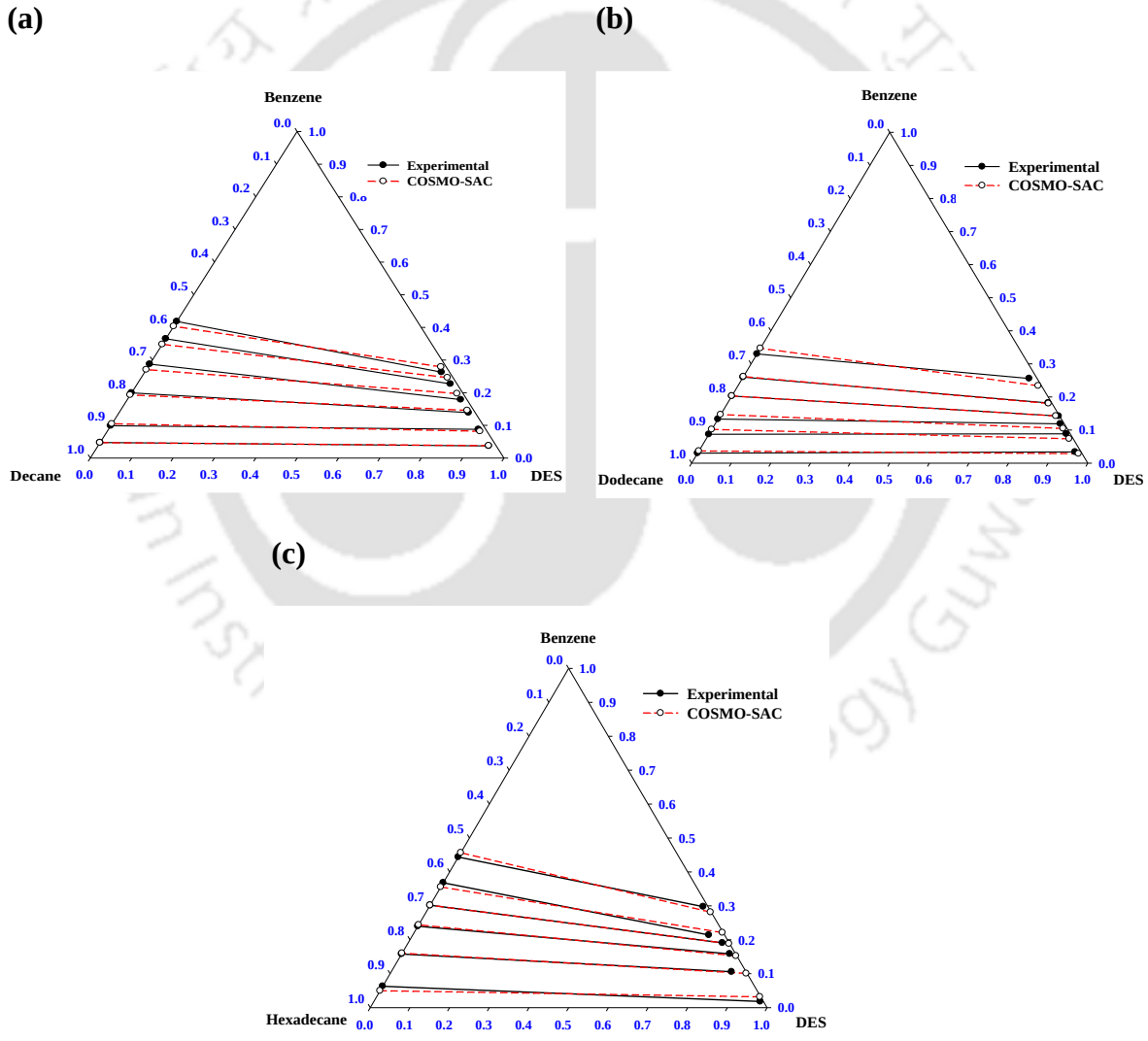

Figure 3.2. Experimental tie lines (●, Solid line) in mole fractions for the ternary systems (a) {*n*-decane + benzene + DES} (b) {*n*-dodecane + benzene + DES} (c) {*n*-hexadecane + benzene+ DES} at *T*= 25°C and atmospheric pressure; Predicted equilibrium tie lines (○, dotted line) using COSMO-SAC model.

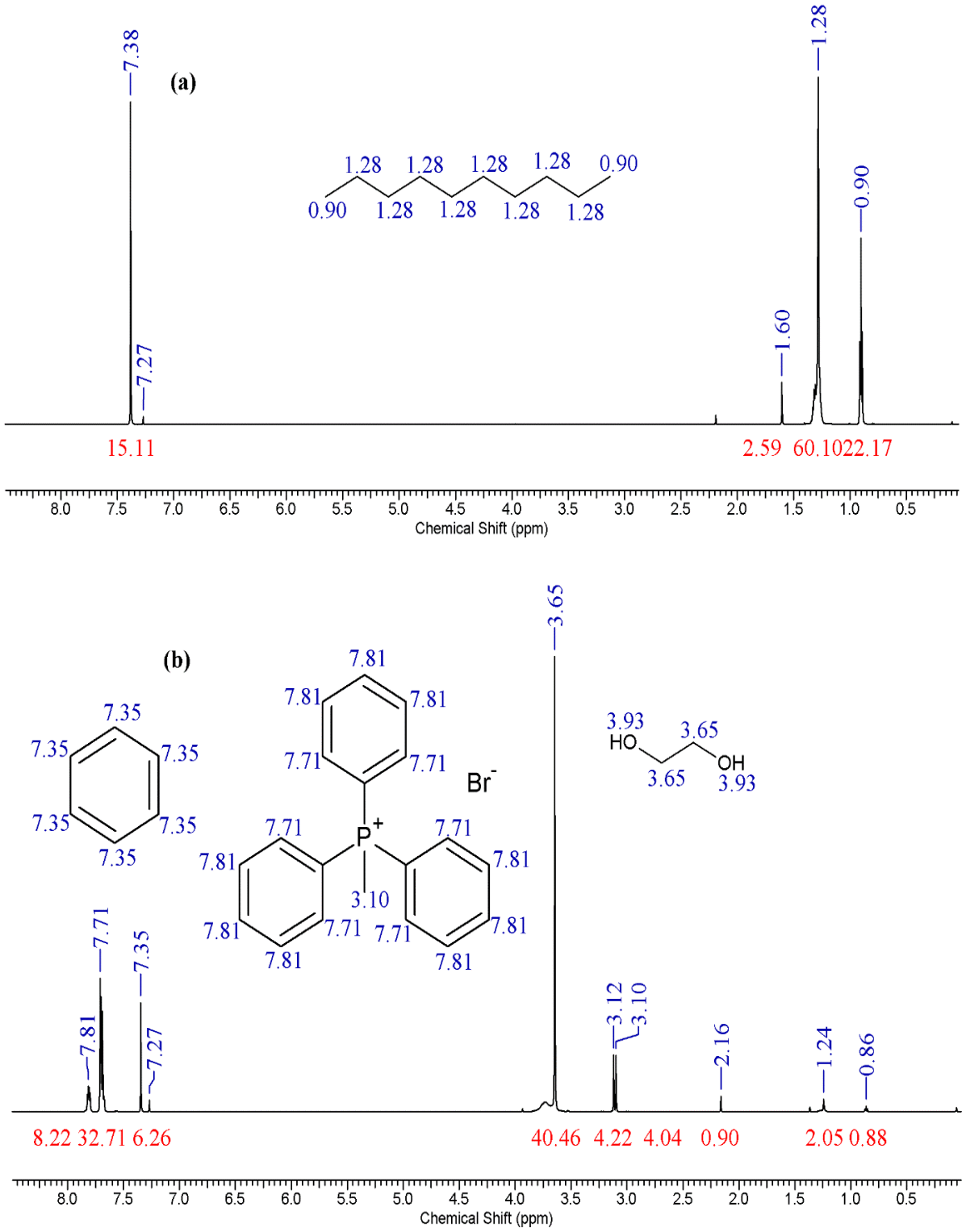

Figure 3.3. ^{1}H NMR spectra for LLE system of DES-benzene-*n*-decane ternary system at 25°C and 1 bar pressure for (a) Raffinate phase (b) Extract phase.

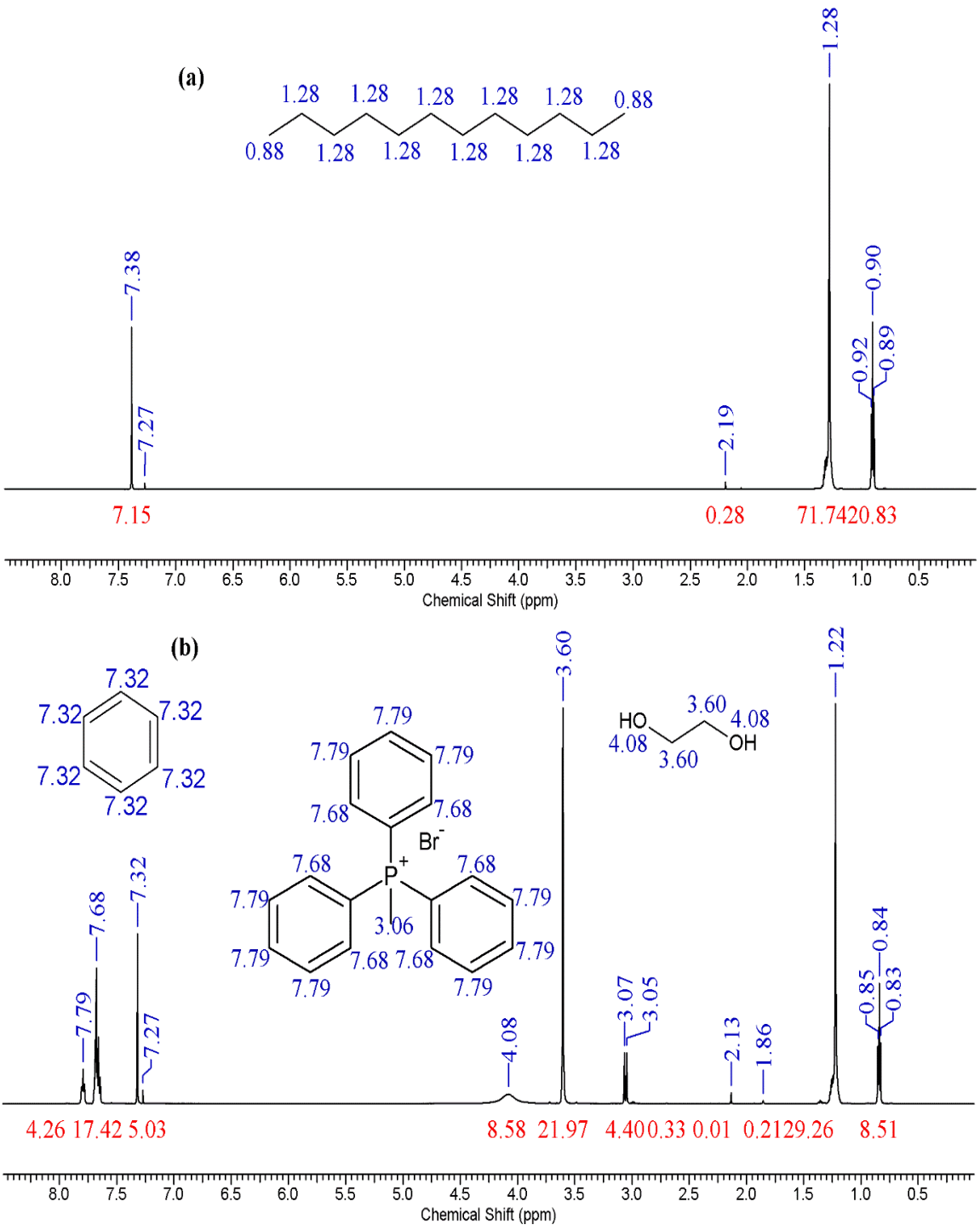

Figure 3.4. ^{1}H NMR spectra for LLE system of DES-benzene-*n*-dodecane ternary system at 25°C and 1 bar pressure for (a) Raffinate phase, (b) Extract phase

It can be established that the usage of DES for benzene extraction is reasonable for model diesel fuel, as it requires a smaller amount of solvent to feed ratio, which in turn gives higher values of selectivity and distribution coefficients. The main reason for a significant

extraction was the higher solubility of benzene in DES as compared to aliphatic hydrocarbons, as shown in Table 3.2. Higher solubility behaviour can be explained by considering the π-electrons cloud around the benzene (due to the molecule's aromatic nature), due to which a strong electrostatic field is generated around the molecule. The presence of a strong π-electron cloud of benzene molecules induces the interactions within the phenyl and hydroxyl group of DES and, as a result, provides higher extraction efficiency.

Table 3.5. Experimental Liquid-liquid Equilibrium (LLE) tie-line data for the ternary system: DES + benzene+ *n*-dodecane at Temperature T= 25°C and Pressure p = 0.1 MPa[a]. The mole fractions of DES, benzene, and dodecane, are represented by x_1, x_2, and x_3, respectively [a].

Extract phase			Raffinate phase			*D*	Selectivity (S)
x_{DES}	x_{ben}	x_{dodec}	x_{DES}	x_{ben}	x_{dodec}		
0.961	0.034	0.005	0.000	0.030	0.970	1.23	218.47
0.901	0.089	0.010	0.000	0.087	0.913	1.02	91.00
0.861	0.119	0.020	0.000	0.133	0.867	0.89	38.92
0.835	0.142	0.022	0.000	0.203	0.797	0.70	25.08
0.789	0.182	0.029	0.000	0.260	0.740	0.70	18.01
0.724	0.256	0.020	0.000	0.330	0.670	0.78	26.11

[a]Standard uncertainties are *u*(T) = 0.01°C, *u*(*x*) = 0.001, and *u*(p) = 2 kPa.

Table 3.6. Experimental Liquid-liquid Equilibrium (LLE) tie-line data for the ternary system: DES + benzene+ *n*-hexadecane at Temperature T= 25°C and Pressure p = 0.1 MPa[a]. The mole fractions of DES1, benzene, and hexadecane, are represented by x_1, x_2, and x_3, respectively [a].

Extract phase			Raffinate phase			*β*	Selectivity (S)
x_{DES}	x_{ben}	$x_{hexadec}$	x_{DES}	x_{ben}	$x_{hexadec}$		
0.921	0.071	0.008	0.000	0.033	0.967	2.16	261.16
0.848	0.141	0.011	0.000	0.108	0.892	1.30	105.72
0.811	0.169	0.020	0.000	0.240	0.760	0.70	26.70
0.778	0.191	0.031	0.000	0.302	0.698	0.63	14.23
0.735	0.231	0.034	0.000	0.368	0.632	0.63	11.76
0.690	0.272	0.038	0.000	0.424	0.576	0.64	9.73

[a]Standard uncertainties are *u*(T) = 0.01°C, *u*(*x*) = 0.001, and *u*(p) = 2 kPa.

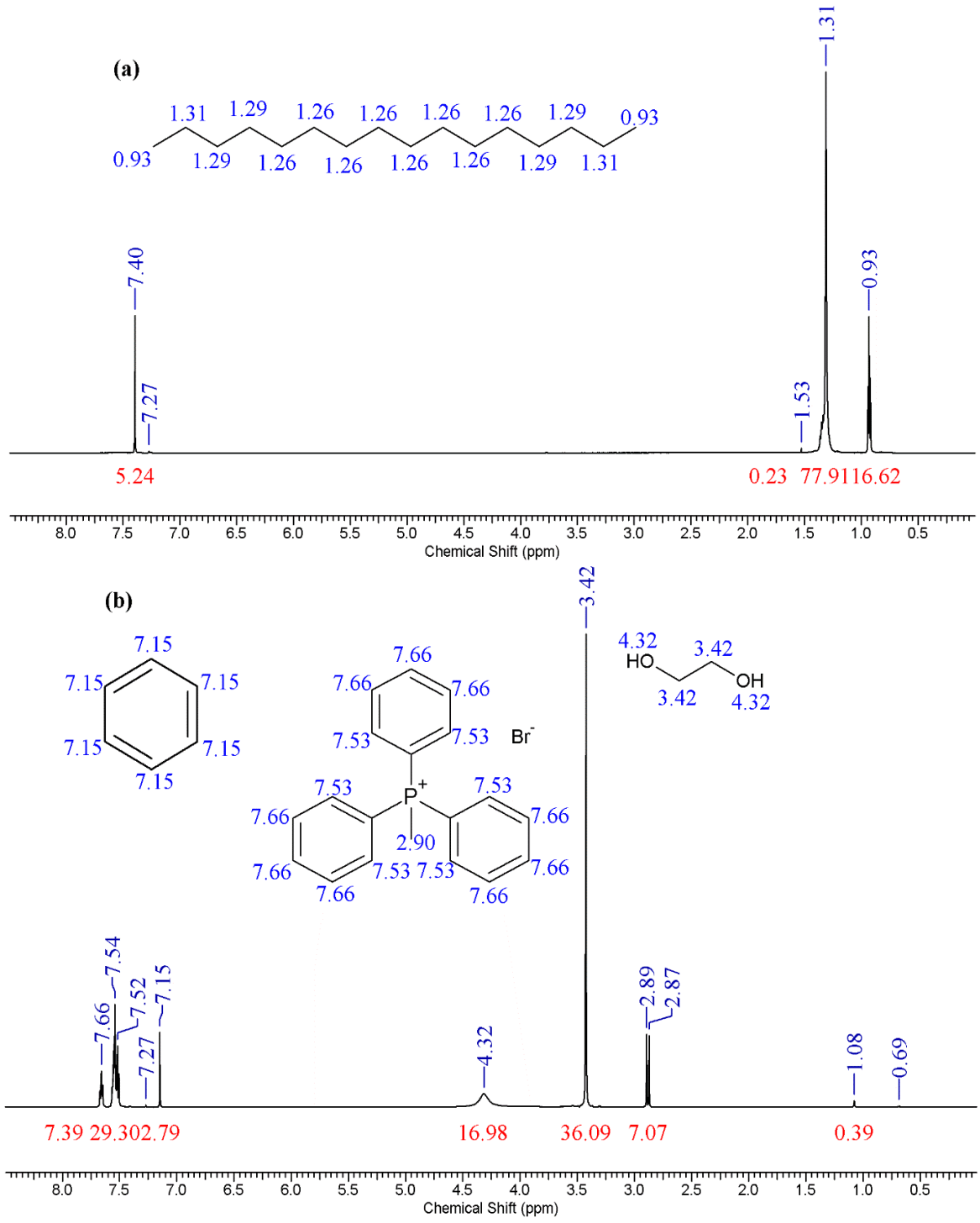

Figure 3.5. ^{1}H NMR spectra for LLE system of DES-benzene-*n*-hexadecane ternary system at 25°C and 1 bar pressure for (a) Raffinate phase (b) Extract phase.

On the other hand, no such π-electron cloud is available around the aliphatic hydrocarbons molecule; consequently, the aliphatic hydrocarbons-DES interactions are weaker than the benzene-DES interactions. As discussed earlier, this is also corroborated by sigma

profiles (Figure 3.1). It can be observed that increasing the initial concentration gradually decreases the extraction efficiency of benzene. For a single-stage extraction, the highest efficiencies were found for *n*-hexadecane followed by *n*-dodecane and *n*-decane. For all three systems, extraction efficiencies for the single-stage were found to be in the range of 60-72%. It also shows DES as an effective extractant that follows the order of *n*-hexadecane>*n*-dodecane>*n*-decane for benzene extraction from model diesel components.

The distribution coefficients and selectivities calculated at T=25℃ and atmospheric pressure for the systems {*n*-decane + benzene + DES}, {*n*-dodecane + benzene + DES} and {*n*-hexadecane + benzene + DES} were compared to those systems using different DESs as extractants. From Table 3.7, it can be observed that the selectivities of the reported systems follow the order of *n*-hexadecane > *n*-dodecane > *n*-decane, and distribution coefficients was also found highest for {*n*-hexadecane + benzene + DES} system. Overall, both the distribution coefficients and selectivity values are higher when compared to ammonium-based DES. It is worthwhile to note that this is higher with the ammonium-based DES when combined with the conventional solvent, namely sulfolane, or with a similar HBD, namely ethylene glycol. Overall, the higher values of distribution coefficients and selectivity values of the current DES can be explained through the strong non-covalent interaction, as explained earlier through COSMO-SAC Model (figure 3.1) between the DES and benzene within the sigma profile analysis.

3.3.4 Extraction Mechanism of Benzene

For the mechanistic studies, we have quantified the ^{1}H NMR and FT-IR, as given in Figure 3.6-3.8. MTPB: EG (1:4) was used as a solvent in this mechanistic study to understand the extraction mechanism of benzene from representative model diesel fuel. Figure 3.7 demonstrates the influence of varying concentrations between MTPB: EG and benzene in the ^{1}H NMR spectra[45].

Table 3.7. Comparison of distribution coefficients and selectivity for benzene extraction from *n*-alkanes using different DESs at *T*=25°C and Pressure p = 0.1 MPa.

System	Distribution Coefficient	Selectivity	References
{*n*-decane + benzene + DES}	1.12-0.63	129.9-18.8	Present study
{*n*-dodecane + benzene + DES}	1.23-0.70	218.47-18.01	Present study
{*n*-hexadecane + benzene + DES}	2.16-0.63	261.16-9.73	Present study
{*n*-hexane+benzene+DES1 [tetrahexylammonium bromide: ethylene glycol(1:2)]}	1.07-0.83	4.94-1.17	Rodriguez et al. [1]
{*n*-hexane+benzene+DES2 [tetrahexylammonium bromide: glycerol (1:2)]}	1.41-0.74	8.58-1.26	Rodriguez et al. [1]
{*n*-octane +benzene+DES3 [tetrabutylammoniumbromide: sulfolane (1:4)]}	0.31–0.74	9.20–46.40	Mulyono et al. [47]

As the amount of benzene ratio increases, the higher and narrower peaks (7.79 and 7.67ppm) change to shorter and broader (7.89 and 7.77 ppm) peaks due to the deshielding effect owing to the higher concentration of electron density on the respective nucleus of the benzene and the phenyl ring (figure 3.8).

Overall, it can be said that with the rise in the concentration of benzene in the DES/benzene mixture, the hydrogen atoms: chemical shift (7.67 ppm) and (7.79 ppm) move towards lower field intensities, namely (7.89 ppm, 7.77 ppm), respectively. Here the opposing magnetic field becomes smaller; hence, both the peak areas are smaller in magnitude. This downfield shift of MTPB can be attributed to the decrease in electron density through the electron-withdrawing effect of benzene. With the addition of benzene in different mole fractions, the non-covalent interaction of benzene is formed between the hydroxyl group of

HBD and the active sites of HBA. This could be attributed to the presence of π-electrons around the benzene component, which is absent in the *n*-alkane compound.

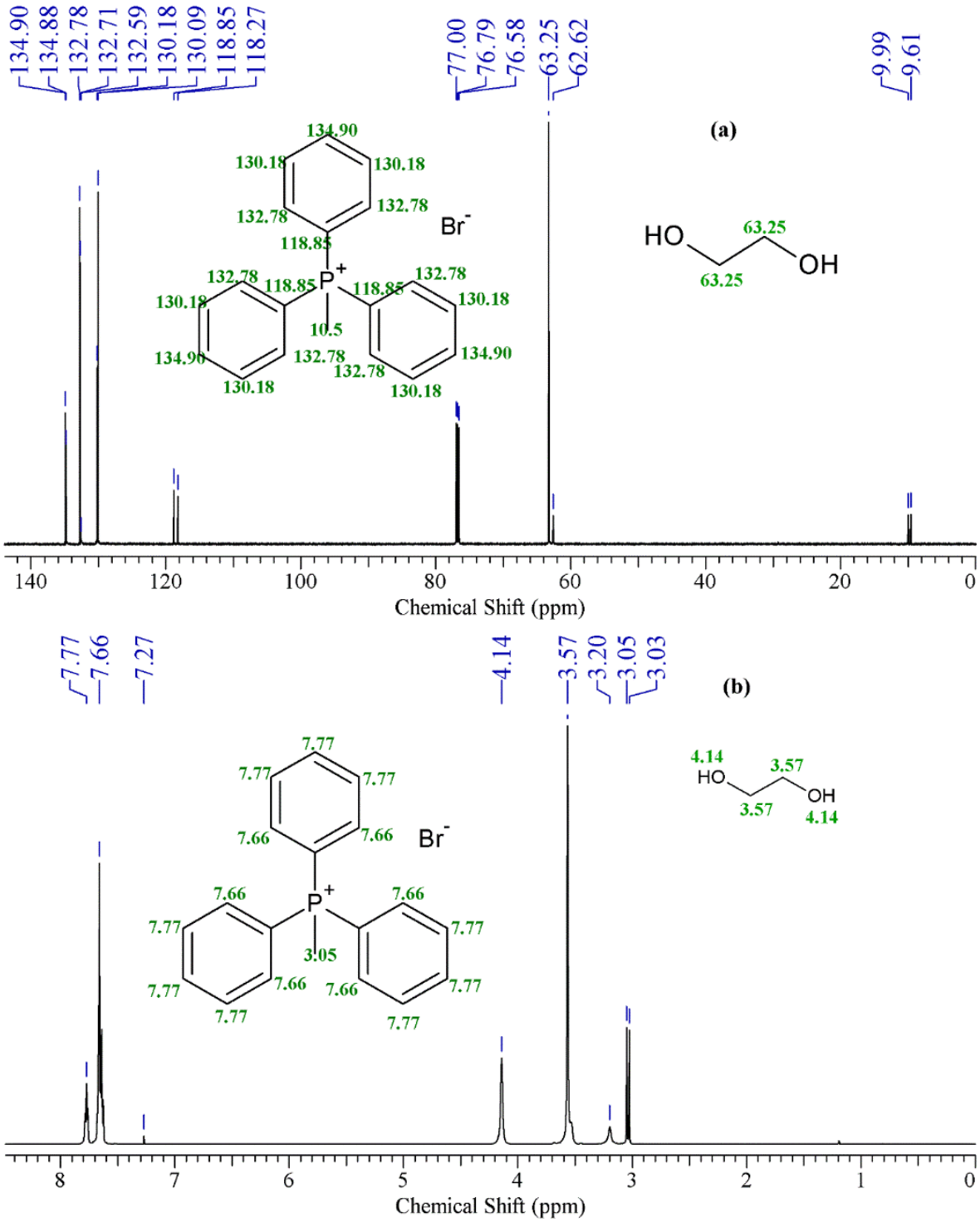

Figure 3.6. NMR spectra of pure DES (a) ^{13}C and (b) ^{1}H.

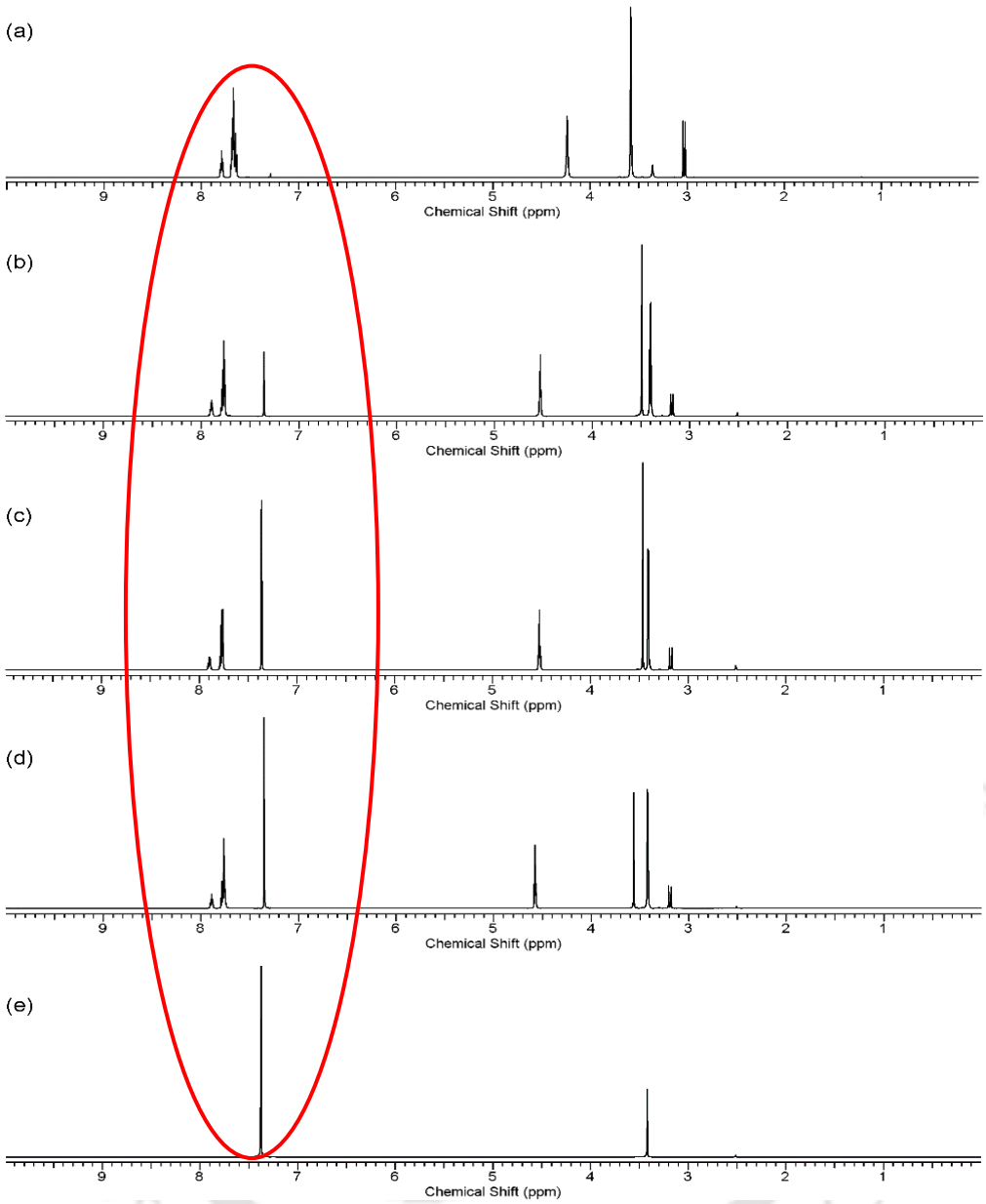

Figure 3.7. Molar ratios ^{1}H NMR of Solvent and Solute (MTPB+EG : benzene) at molar ratio of (a)1: 0, (b)1: 0.1, (c)1: 0.5, (d)1:1, (e) 0:1.

The π-electrons generate an electrostatic cloud around the aromatic molecule which facilitates the interaction with the DES through such type of bond (C–H···π, O–H···π, and N–H···π) which leads to higher solubility. This confirms our earlier work[46], where MD simulations using Spatial Density Function (SDF) reveal that the benzene molecules are evenly distributed around the active sites of the MTP molecule. In contrast, hexane molecules are found to be distributed around the non-active sites of the DES.

The sigma profiles also confirm this effect, where a non-covalent interaction between DES and benzene ring is established by the overlapping sigma profiles (Figure 3.1). This also results in the enhancement of the electron-withdrawing potential of benzene, leading to an improvement in the density of the benzene ring electron and its associated electron density of the hydrogen nucleus. Therefore, it can be concluded that the non-covalent interaction formed between MTPB/EG and the π-electron cloud of benzene mainly accounts for the greater efficiency of benzene extraction. The spectra of the ^{1}H NMR at various concentrations between MTPB/EG and benzene are shown in Figure 3.7.

Along with NMR, the hydrogen bond relationship between extracting agent and benzene was also corroborated using FT-IR (Figure 3.8). The same conclusion is inferred from FTIR, wherewith an increase in the mole ratio of benzene, the interaction of Br^- and the hydroxyl group of EG with benzene becomes stronger and stronger, and in turn, weakens the covalent interaction of DES (Br of HBA and HBD, i.e., EG). The exact inference is drawn from FTIR, where the interaction of Br^- with benzene gets stronger with an increase in the mole fraction of benzene, and in turn, decreases the influence of the hydrogen bond of DES (Br and EG). This confirms the fact that the peak of the hydroxyl group becomes narrower with composition. Thus, it can be safely inferred from the quantitative ^{1}H NMR and FT-IR spectra that non-covalent interactions are the primary driving force for dearomatisation.

3.3.5 Regeneration of Solvent

As reported in Tables 3.4-3.6, the composition of the experimental Liquid-liquid equilibrium tie-line data reveals that the extract phase was free of representative model diesel components. Therefore, for the regeneration experiment, a sample of the extract phase, "DES-rich phase," with a composition {10% benzene + 90% MTPB/EG} was taken and performed using a vacuum evaporator at a pressure of 65 kPa and a temperature of 35°C. The sample was placed

for 12 hr inside the vacuum evaporator. The regenerated DES was then analysed using ^{1}H NMR analysis. A single regeneration stage result showed that 96.8% of benzene from DES has been removed.

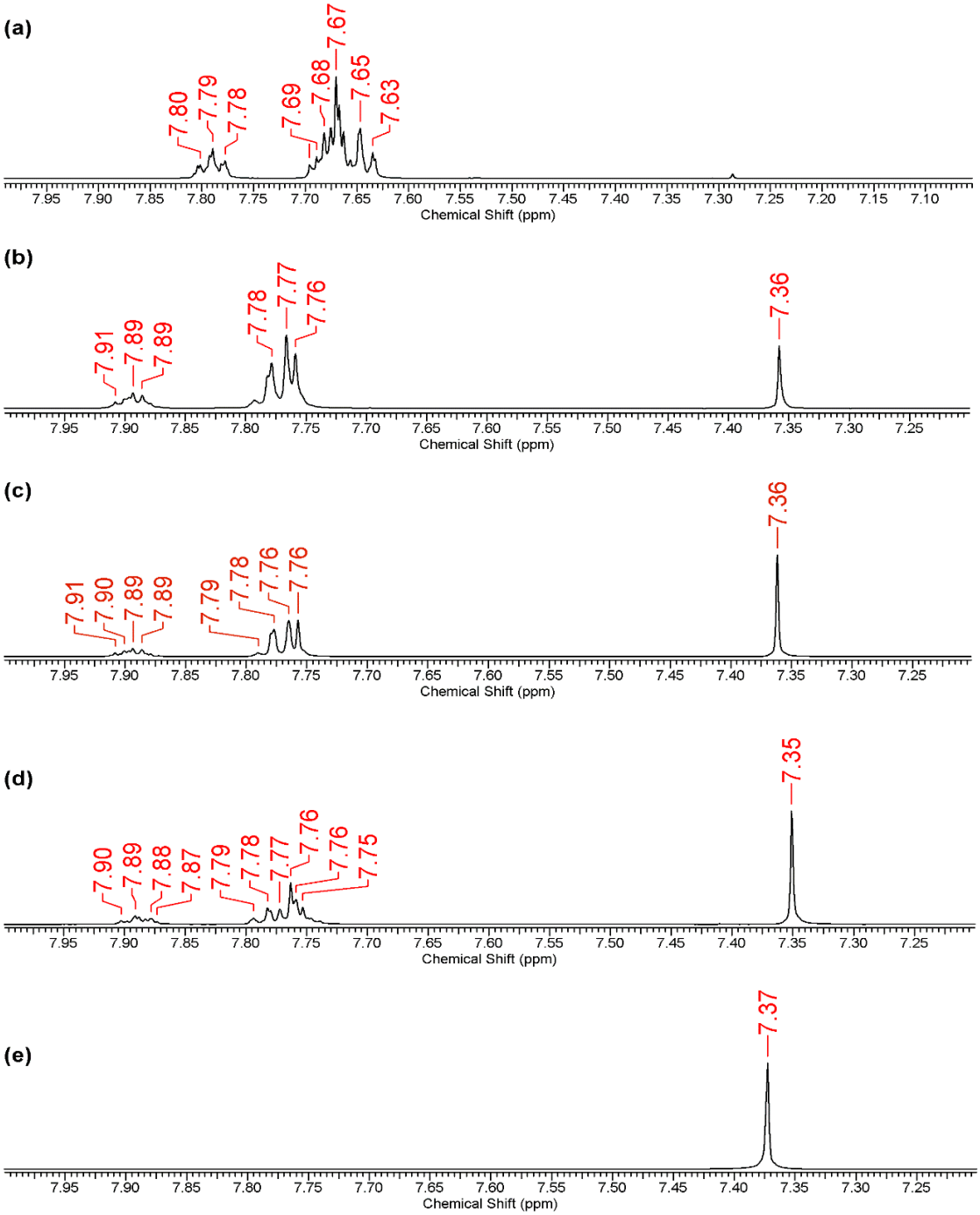

Figure 3.8. ^{1}H NMR of (MTPB+EG : benzene) mixtures having molar ratio of (a) 1: 0, (b) 1: 0.1, (c) 1: 0.5, (d) 1: 1, (e) 0:1.

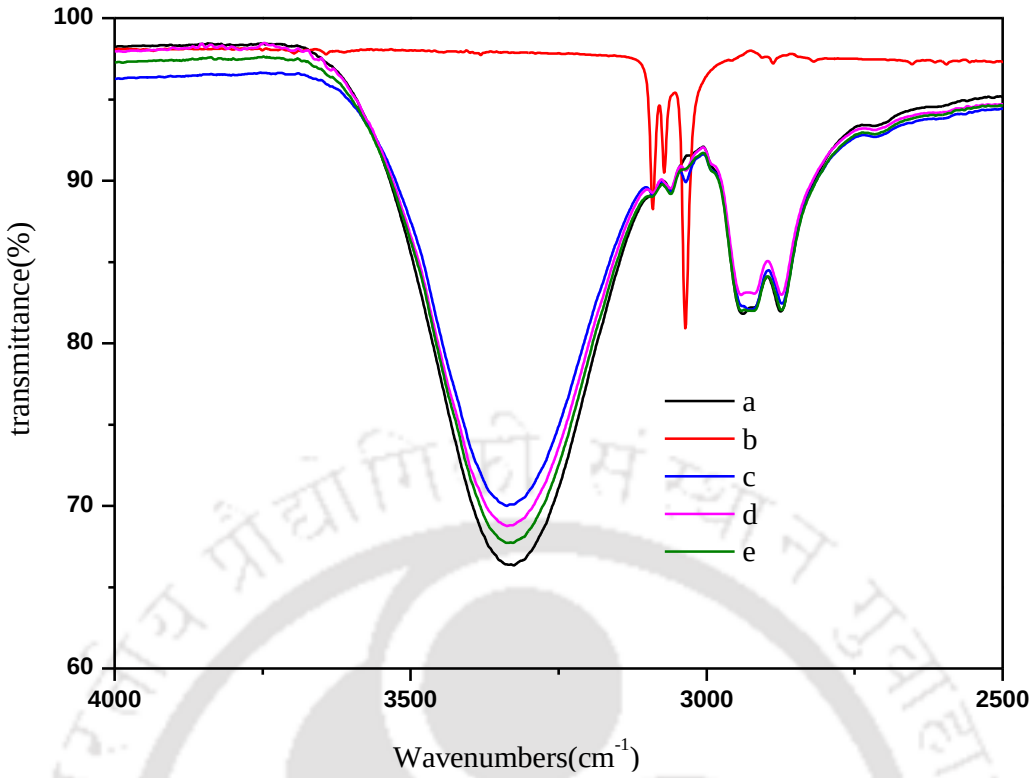

Figure 3.9. FT-IR of different molar ratios (MTPB +EG: benzene) for molar ratio of (a) 1:0, (b) 0:1, (c) 1: 1, (d) 1: 0.5, (e) 1: 0.1.

After that, solvent regeneration at higher T=45°C and maintained constant pressure gives overall removal of benzene 98.8%. This confirms that the vacuum evaporator is the ideal regeneration method for low-boiling impurities such as benzene (boiling point = 80.1°C). Therefore, this regenerated DES can be used repetitively for performing extraction using the same DES added to a fresh feed in every cycle. Having completed our investigations on aromatic solutes, we shall discuss the desulphurization efficiency of these phosphonium-based DES for sulphur-based aromatic such as benzothiophene in the next chapter.

3.4 Summary

In this chapter, DES of MTPB and Ethylene Glycol have been studied as extracting agents for separating benzene + diesel components. The studied DES is considered the most promising solvent due to its high benzene solubility compared to aliphatic compounds. The quantum chemical-based COSMO-SAC model was used to predict and compare the experimental tie lines by considering the DES as a pseudo-pure compound. The experimental results revealed an increase in distribution ratio, selectivity, and extraction efficiency for aromatic extraction from model diesel components in the following order: *n*-hexadecane > *n*-dodecane > *n*-decane. The three systems presented values of RMSD (%) of ~1%, which specifies definitive agreement amid the experimental and the COSMO-SAC model predictions. An absence of DES was found in the *n*-alkane rich phase, indicating this would decrease the operational cost of the extraction process, as it will reduce the extra cost on solvent recovery systems. COSMO-SAC based sigma profile studies also signify a high interaction between DES and benzene, especially in the hydrogen bond acceptor regions. FT-IR and NMR spectroscopy revealed the benzene extraction mechanism, where the non-covalent interaction between DES and benzene accounts for the higher dearomatisation efficiencies.

References

1. Rodriguez, N. R.; Requejo, P. F.; Kroon, M. C., Aliphatic–aromatic separation using deep eutectic solvents as extracting agents. *Ind. Eng. Chem. Res.* **2015,** 54, (45), 11404-11412.
2. Meindersma, G. W.; Podt, A.; Klaren, M. B.; De Haan, A. B., Separation of aromatic and aliphatic hydrocarbons with ionic liquids. *Chem. Eng. Commun.* **2006,** 193, (11), 1384-1396.
3. Meindersma, G. W.; Podt, A. J.; de Haan, A. B., Ternary liquid–liquid equilibria for mixtures of toluene+ n-heptane+ an ionic liquid. *Fluid Phase Equilib.* **2006,** 247, (1-2), 158-168.
4. Meindersma, G. W.; De Haan, A. B., Cyano-containing ionic liquids for the extraction of aromatic hydrocarbons from an aromatic/aliphatic mixture. *Sci. China. Chem.* **2012,** 55, (8), 1488-1499.
5. Meindersma, G. W.; de Haan, A. B., Conceptual process design for aromatic/aliphatic separation with ionic liquids. *Chem. Eng. Res. Des.* **2008,** 86, (7), 745-752.
6. Orr, W. L., Sulfur in heavy oils, oil sands and oil shales. *Oil sand and oil shale chemistry* **1978**, 223-243.
7. Ghandi, K., A review of ionic liquids, their limits and applications. *Green Sustain. Chem.* **2014,** 2014.
8. Hossain, M. A.; Lee, J.-S.; Kim, D.-H.; Nguyen, D. Q.; Cheong, M.-S.; Kim, H.-S., Ionic liquids as benign solvents for the extraction of aromatics. *Bull. Korean Chem. Soc.* **2012,** 33, (10), 3241-3247.
9. Domínguez, I.; Gonzalez, E. J.; Domínguez, Á., Liquid extraction of aromatic/cyclic aliphatic hydrocarbon mixtures using ionic liquids as solvent: Literature review and new experimental LLE data. *Fuel Process. Technol.* **2014,** 125, 207-216.
10. Abbott, A. P.; Capper, G.; Davies, D. L.; Rasheed, R. K.; Tambyrajah, V., Novel solvent properties of choline chloride/urea mixtures. *ChemComm* **2003**, (1), 70-71.
11. Coutinho, J. A.; Pinho, S. P., Special issue on deep eutectic solvents: a foreword. *Fluid Phase Equilib.* **2017,** 448, (1).
12. Martins, M. A.; Pinho, S. P.; Coutinho, J. A., Insights into the nature of eutectic and deep eutectic mixtures. *J. Solut. Chem.* **2019,** 48, (7), 962-982.
13. Smith, E. L.; Abbott, A. P.; Ryder, K. S., Deep eutectic solvents (DESs) and their applications. *Chem. Rev.* **2014,** 114, (21), 11060-11082.
14. Marcus, Y.; Marcus; Zakharchenko, *Deep Eutectic Solvents*. Springer: 2019.
15. Ramón, D. J.; Guillena, G., *Deep Eutectic Solvents: Synthesis, Properties, and Applications*. John Wiley & Sons: 2020.
16. Fourmentin, S., Deep Eutectic Solvents for Medicine, Gas Solubilization and Extraction of Natural Substances. In Springer: 2020.
17. Dai, Y.; van Spronsen, J.; Witkamp, G.-J.; Verpoorte, R.; Choi, Y. H., Natural deep eutectic solvents as new potential media for green technology. *Anal. Chim. Acta* **2013,** 766, 61-68.
18. Zhang, Q.; Vigier, K. D. O.; Royer, S.; Jerome, F., Deep eutectic solvents: syntheses, properties and applications. *Chem. Soc. Rev.* **2012,** 41, (21), 7108-7146.

19. Hayyan, A.; Mjalli, F. S.; AlNashef, I. M.; Al-Wahaibi, Y. M.; Al-Wahaibi, T.; Hashim, M. A., Glucose-based deep eutectic solvents: Physical properties. *J. Mol. Liq* **2013,** 178, 137-141.
20. Francisco, M.; van den Bruinhorst, A.; Kroon, M. C., Low-transition-temperature mixtures (LTTMs): A new generation of designer solvents. *Angew. Chem. Int. Ed.* **2013,** 52, (11), 3074-3085.
21. Naik, P. K.; Dehury, P.; Paul, S.; Banerjee, T., Evaluation of Deep Eutectic Solvent for the selective extraction of toluene and quinoline at T= 308.15 K and p= 1 bar. *Fluid Phase Equilib.* **2016,** 423, 146-155.
22. Lemaoui, T.; Benguerba, Y.; Darwish, A. S.; Hatab, F. A.; Warrag, S. E.; Kroon, M. C.; Alnashef, I. M., Simultaneous dearomatization, desulfurization, and denitrogenation of diesel fuels using acidic deep eutectic solvents as extractive agents: A parametric study. *Sep. Purif. Technol.* **2021,** 256, 117861.
23. Hatab, F. A.; Darwish, A. S.; Lemaoui, T.; Warrag, S. E.; Benguerba, Y.; Kroon, M. C.; AlNashef, I. M., Extraction of Thiophene, Pyridine, and Toluene from n-Decane as a Diesel Model Using Betaine-Based Natural Deep Eutectic Solvents. *J. Chem. Eng. Data* **2020,** 65, (11), 5443-5457.
24. Rogošić, M.; Kučan, K. Z., Deep eutectic solvents based on choline chloride and ethylene glycol as media for extractive denitrification/desulfurization/dearomatization of motor fuels. *J. Ind. Eng. Chem* **2019,** 72, 87-99.
25. Abbott, A.; Boothby, D.; Capper, G.; Davies, D.; Rasheed, R. In *Ionic liquids in biotransformations and organocatalysis: solvents and beyond*, Chem. Soc, 2004; 2004; pp 9142-9147.
26. Kareem, M. A.; Mjalli, F. S.; Hashim, M. A.; AlNashef, I. M., Phosphonium-based ionic liquids analogues and their physical properties. *J. Chem. Eng. Data* **2010,** 55, (11), 4632-4637.
27. Mjalli, F. S.; Vakili-Nezhaad, G.; Shahbaz, K.; AlNashef, I. M., Application of the Eötvos and Guggenheim empirical rules for predicting the density and surface tension of ionic liquids analogues. *Thermochim. Acta* **2014,** 575, 40-44.
28. Naik, P. K.; Paul, S.; Banerjee, T., Physiochemical properties and molecular dynamics simulations of phosphonium and ammonium based deep eutectic solvents. *J. Solut. Chem.* **2019,** 48, (7), 1046-1065.
29. Bharti, A.; Kundu, D.; Rabari, D.; Banerjee, T., *Phase equilibria in ionic liquid facilitated liquid-liquid extractions*. CRC Press: 2017.
30. Dennington, R.; Keith, T.; Millam, J., GaussView, version 5. **2009**.
31. Frisch, M.; Trucks, G.; Schlegel, H. B.; Scuseria, G. E.; Robb, M. A.; Cheeseman, J. R.; Scalmani, G.; Barone, V.; Mennucci, B.; Petersson, G., gaussian 09, Revision d. 01, Gaussian. *Inc., Wallingford CT* **2009,** 201.
32. Perdew, J. P., Density-functional approximation for the correlation energy of the inhomogeneous electron gas. *Phys. Rev. B.* **1986,** 33, (12), 8822.
33. Sosa, C.; Andzelm, J.; Elkin, B. C.; Wimmer, E.; Dobbs, K. D.; Dixon, D. A., A local density functional study of the structure and vibrational frequencies of molecular transition-metal compounds. *J. Phys. Chem.* **1992,** 96, (16), 6630-6636.

34. Kundu, D.; Banerjee, T., Multicomponent vapor–liquid–liquid equilibrium prediction using an a priori segment based model. *Ind. Eng. Chem. Res.* **2011,** 50, (24), 14090-14096.
35. Seader, J. D.; Henley, E. J.; Roper, D. K., *Separation process principles*. Wiley New York: 1998; Vol. 25.
36. Banerjee, T.; Singh, M. K.; Khanna, A., Prediction of binary VLE for imidazolium based ionic liquid systems using COSMO-RS. *Ind. Eng. Chem. Res.* **2006,** 45, (9), 3207-3219.
37. Banerjee, T.; Sahoo, R. K.; Rath, S. S.; Kumar, R.; Khanna, A., Multicomponent liquid− liquid equilibria prediction for aromatic extraction systems using COSMO-RS. *Ind. Eng. Chem. Res.* **2007,** 46, (4), 1292-1304.
38. Banerjee, T.; Khanna, A., Infinite dilution activity coefficients for trihexyltetradecyl phosphonium ionic liquids: measurements and COSMO-RS prediction. *J. Chem. Eng. Data* **2006,** 51, (6), 2170-2177.
39. Lin, S.-T.; Sandler, S. I., A priori phase equilibrium prediction from a segment contribution solvation model. *Ind. Eng. Chem. Res.* **2002,** 41, (5), 899-913.
40. Verma, R.; Banerjee, T., Liquid–liquid extraction of lower alcohols using menthol-based hydrophobic deep eutectic solvent: experiments and COSMO-SAC predictions. *Ind. Eng. Chem. Res.* **2018,** 57, (9), 3371-3381.
41. Klamt, A., *COSMO-RS: from quantum chemistry to fluid phase thermodynamics and drug design*. Elsevier: 2005.
42. Xiong, R.; Sandler, S. I.; Burnett, R. I., An improvement to COSMO-SAC for predicting thermodynamic properties. *Ind. Eng. Chem. Res.* **2014,** 53, (19), 8265-8278.
43. Pence, H. E.; Williams, A., ChemSpider: an online chemical information resource. In ACS Publications: 2010.
44. Alli, R. D.; Kroon, M. C., Extraction of benzothiazole and thiophene from their mixtures with n-heptane using tetrahexylammonium bromide-based deep eutectic solvents as extractive denitrogenation and desulfurization agents. *Fluid Phase Equilib.* **2018,** 477, 1-11.
45. Li, C.; Li, D.; Zou, S.; Li, Z.; Yin, J.; Wang, A.; Cui, Y.; Yao, Z.; Zhao, Q., Extraction desulfurization process of fuels with ammonium-based deep eutectic solvents. *Green Chem.* **2013,** 15, (10), 2793-2799.
46. Kumar, N.; Naik, P. K.; Banerjee, T., Molecular modeling insights in the extraction of benzene from hydrocarbon stream using deep eutectic solvent. *J. Mol. Liq* **2020,** 317, 113909.
47. Mulyono, S.; Hizaddin, H. F.; Alnashef, I. M.; Hashim, M. A.; Fakeeha, A. H.; Hadj-Kali, M. K., Separation of BTEX aromatics from n-octane using a (tetrabutylammonium bromide+ sulfolane) deep eutectic solvent–experiments and COSMO-RS prediction. *RSC Adv.* **2014,** 4, (34), 17597-17606.

Chapter 4

Desulphurisation of Model Diesel Compounds and Quantum Chemical Insights

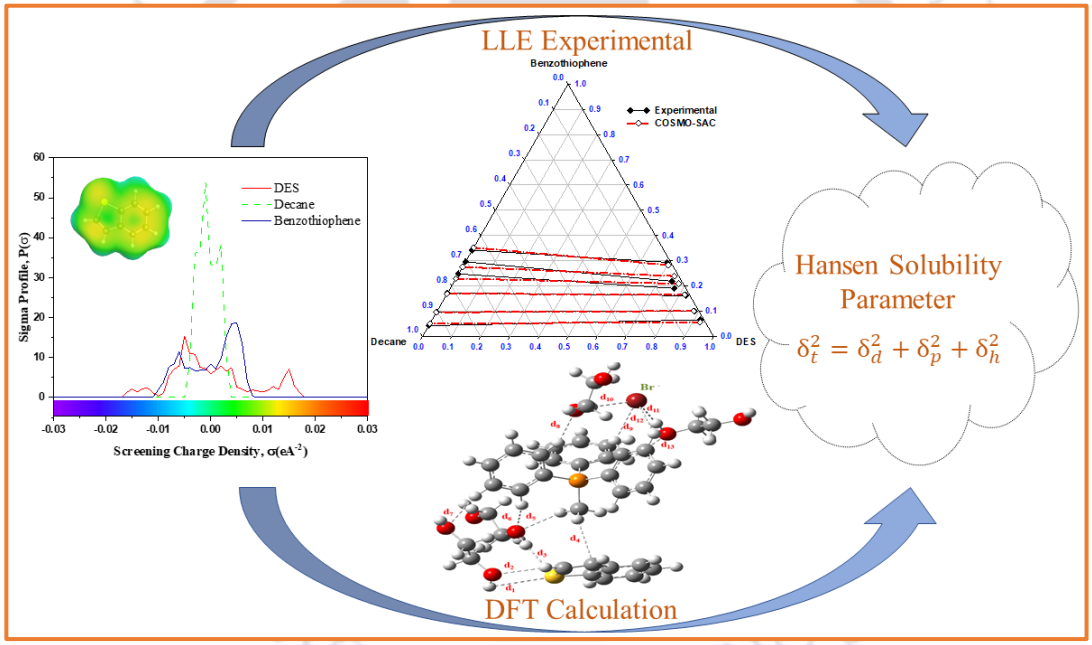

During combustion, sulphur compounds in fuels are oxidised to SO_x, poisoning automatic catalytic converters and posing severe environmental risks (e.g., acid rain). As an outcome, effective liquid fuel desulphurization is a vital step in reducing SO_x emissions and their inherent ecological impacts. The extraction of ultra-low benzothiophene from n-decane as representative model diesel fuel was analysed using phosphonium-based deep eutectic solvents (DESs) at 308.15 K and 1 bar pressure. The Liquid-liquid equilibria studies were conducted on the ternary system of DES-benzothiophene-n-decane for all six feed point concentrations. The ^1H NMR analysis was used to determine the molar composition of each raffinate and extract phase. The LLE experimental findings were examined using the COnductor-like Screening MOdel for Segment Activity Coefficient (COSMO-SAC) based on quantum calculation. The average RMSDs of the studied LLE ternary system is 1.07 percent, which is suitable considering the priori nature of the approach. The σ-Profiles calculation using the COSMO-SAC model and Hansen solubility parameters (HSPs) using different predicted models were used to provide insights into the molecular mechanism of benzothiophene extraction efficacy using DES. We observed a higher extraction of benzothiophene due to the higher proportion of hydrogen bonding and dispersion-type interactions. The Charge transfer analysis using the DFT calculation of the DES cluster suggests that the bromide (Br^-) ion can act as a charge transfer bridge between MTP cation and the hydrogen bond donor. The MTP cation and ethylene glycol also aid in the extraction of benzothiophene by dislocating the charge from the aromatic sulphur compound. The bromide (Br^-) ion is essentially non-interactive with the benzothiophene due to retention of the conventional hydrogen bond network existing within the initial components of DES, mainly hydrogen bond donor and hydrogen bond acceptor.

4.1 Introduction

The requirement for zero-emission diesel fuel is getting substantial attention in the petrochemical industry due to strict limitations adopted by the central agencies to control the sulphur content in diesel. Environmental Protection Agency (EPA) recently adopted the latest protocols, which permit the maximum permissible sulphur amount in ultra-low diesel (ULSD) fuels to be below 10 ppm [1]. The deep desulphurization of petroleum fuels is a significant problem worldwide, and many scientific laboratories are looking for an economical solution to this problem. Liquid fuels consist of petrol, diesel, aviation fuel, and petroleum fuels containing primarily sulphur compounds, namely mercaptans, sulphides, thiophene, alkyl thiophene derivatives, and benzothiophene [2].

The conventional method, such as hydrodesulphurisation (HDS), is used at an industrial scale to remove sulphur compounds from petroleum fuels. It involves hydrogen reaction with sulphur compounds at severe temperatures and pressure in the presence of an expensive catalyst[3]. Apart from the stringent requirements for the hydrodesulphurization process, an obvious drawback of this approach is that it lowers the cetane number of diesel fuel and emits poisonous hydrogen sulphide [4]. It is an arduous task to remove aromatic sulphur compounds such as thiophene, benzothiophene, dibenzothiophene[5], and their derivatives by conventional methods. The failure of HDS to isolate a wide variety of sulphur compounds has led researchers to look for alternative methods of deep desulphurization of fuels that would allow for adequate sulphur compound separation under reasonable conditions.

Extractive desulphurization has been evolved in many research studies [6] as an alternative to sulphur capture to reduce the cost involved in the HDS process. Liquid-liquid extraction is a straightforward procedure that is highly selective for specific compounds that can be removed at ambient conditions[7]. However, solvent selection remains challenging due

to the environmental restrictions associated with volatile organic compounds (VOCs). VOCs were incompatible with this separation due to the difficulties of solvent recovery.

Previous work from our group has been devoted to a systematic effort in isolating aromatic sulphur compounds in fuel desulphurization [8] employing green solvents such as ionic liquids [9]. DES or Deep Eutectic Solvents [10-11], or a combination of HBD and HBA are suitable as extractive media that possess similar physiochemical properties to ionic liquids. It allows us to assume that DESs are likely to be more successful than ionic liquids for deep fuel desulphurization. These DESs are extensively studied, including fuel desulphurization due to the extremely low vapour pressure and low cost compared to ionic liquids.

Deep eutectic solvents[12] are characterized as a combination of two or more pure compounds whose eutectic point temperature is lower than that of an ideal liquid mixture, resulting in substantial departures from ideality. An operating temperature[13] of a specific composition range necessitates an appropriate temperature drop. The mixtures that do not fulfill these requirements might be considered only a 'eutectic solvent'. The temperature depression should be defined as the difference (ΔT_2) between the ideal ($T_{E,\,ideal}$) and the real (T_E) eutectic point and not as the difference (ΔT_1) between the linear combination of the melting points of the pure components and the real eutectic point.

Recently, DESs have been investigated as potential solvents for extracting organosulfur compounds from liquid fuels through the liquid-liquid extraction process[14]. The extraction of aromatic sulphur compounds includes DESs based on a different combination of choline chloride[15], and those derived from other quaternary ammonium halide salts, amino acids, and metal halides fall under category (e.g., $ZnCl_2$, $FeCl_3$)[16-17]. The development of computational tools to better understand the structure, dynamics, and interactions inherent in DESs systems has occurred in tandem with the expansion of these solvents into new

domains[17-19]. Although little is known about how the shape and content of DES molecules influence the interaction with aromatic sulphur compounds, these interactions are essential as refractory targets in the desulfurization of fossil fuels.

Several attempts were made to simultaneously perform desulfurization, denitrification, and dearomatization from a model diesel fuel composition using different deep eutectic solvents. Lemaoui [20] et al. explored the extraction by mixing tetrapropylammonium bromide and acetic acid in a 1:4 molar ratio to form DES and performed the extraction. In a similar study, Darwish [21] et al. recently explored ethyl triphenylphosphonium bromide and acetic acid in a specific molar ratio to extract thiophene, pyrrole, and other aromatic compounds from *n*-decane in a method that replicates the commercial extraction process. Liquid-liquid extraction of *n*-decane using the NADES[22] (betaine as an HBA and levulinic acid as an HBD) method resulted in the separations of pyridine, toluene, and thiophene from the solvent. Rogošić [23] et al. discovered that the most significant mass ratio of DES: model fuel of 1.00 kg/kg yielded the maximum extraction efficiency. Our earlier work reported the desromatization[24] of benzene from model diesel fuel consisting of long-chain hydrocarbons in the range of C_{10}-C_{16} using the Phosphonium-based deep eutectic solvents. It reveals that the non-covalent interaction between the DES and benzene is mainly responsible for the higher selectivity and distribution coefficient at a minimal concentration.

In this analysis, the HBA, Methyltriphenylphosphonium bromide (MTPB), was combined with Ethylene glycol (EG) as a hydrogen bond donor (HBD) in a specific molar ratio of 1:4 to synthesize potential solvent. All six feed point concentrations were carried out using the ternary system of DES-benzothiophene-*n*-decane, liquid-liquid equilibria experiments. The molar composition of extract and raffinate phases for each tie line was calculated using ^{1}H NMR. The distribution coefficient, selectivity, and extraction efficiency were then calculated and reported in the present study. The cause for a higher yield for extraction of benzothiophene

during the liquid-liquid extraction using DES is not well understood. Therefore, we have initiated a computation study to evaluate the interactions between DES and individual aliphatic and aromatic sulphur compounds using the COSMO-SAC model and Hansen solubility parameters. Finally, the extraction mechanism is discussed based on the molecular scale for which the quantum mechanical (QM) calculations were performed to understand how specific functional groups or metal components within conventional DES interact with organosulphur compounds to control the extraction of these target molecules from sulphur contaminated liquid fuels. We systematically studied the different clusters of DES with the aliphatic and aromatic sulphur compounds, transfer of electron density in terms of charge transfer, interaction energies for different complex clusters, and bond lengths with the interaction between the different species of clusters. Our findings provide crucial atomistic insight into the interactions between DES and BT, which are vital for efficient aromatic sulphur compound extraction from sulphur-contaminated liquid fuels utilizing DES as the extractive medium in an extractive desulphurization process. Finally, quantitative ^{1}H NMR and ^{13}C NMR were used to check the purity of synthesized DES, as given in chapter 3.

4.2 Computational Details

4.2.1 COSMO-SAC Model

Klamt and Schüürmann [25] conceptualized the Conductor-like Screening Model (COSMO), which computes the solvation energy. COSMO-SAC divides the interaction energies between the various segments into two types: misfit energy, E_{misfit}, and hydrogen bond energy, E_{hb}. Details of previous work [26-27] include the terminology and methods for obtaining these pairwise parameters, namely the COSMO-SAC parameters. In the present study, we used the COSMO-SAC model to predict the composition of DES-benzothiophene(BT)-*n*-decane(DC) ternary systems tie-lines with extract and raffinate phase compositions calculated using the modified Rachford Rice algorithm[28]. The σ-Profiles of these compounds were then analysed

to understand the insights of the extraction mechanism of aromatic sulphur compounds from representative model diesel fuel.

The chemical structures of HBA, HBD, benzothiophene, and *n*-decane were drawn using Gauss view 05 [29]. The geometry optimization of these compounds was performed at the B3LYP level of theory using a 6–311 + G** basis set using Gaussian 16 [30]. After the geometry optimization, the COSMO files were generated at the PBVP86 level of density functional theory using the triple zeta valence potential(TZVP)basis set with the DGA1[28]density fitting. The σ-Profiles, which include the surface screening charges of compounds, are generated by the COSMO-SAC calculation. The σ-Profile of DES was calculated by adding the normalized sigma profiles of HBA and HBD in a specific molar ratio as given in equation 4.1.

$$p_{DES}(\sigma) = p_{HBA}(\sigma) + p_{HBD}(\sigma) = f_{HBA}p_{HBA}(\sigma) + f_{HBD}p_{HBD}(\sigma) \quad (4.1)$$

The COSMO-SAC predicted ternary tie lines are compared with the experimental obtained ternary system tie line compositions[28] as shown in figure 4.1. The root mean square deviation (RMSD) is used to compare the convergence between the predicted and experimental data as given in equation 4.2.

$$rmsd = 100 \times \left[\sum_{i=1}^{c} \sum_{j=1}^{p} \sum_{t=1}^{m} \frac{\left(x_{calc,i,t}^{j} - x_{\exp t,i,t}^{j} \right)^2}{mcp} \right]^{1/2} \quad (4.2)$$

Here x_{ik}^{l} and $\hat{x}_{ik}^{l}$ are the experimental and predicted mole fractions, and the subscripts *i*, *j*, and *k* are component, phase, and tie lines, respectively.

4.2.2 Computational Details for DFT Theory

The chemical structures of HBA, HBD, benzothiophene, and *n*-decane were drawn using Gauss view suite 05 [29]. Geometry optimizations of different clusters and individual components

were performed using the Gaussian 16 [30]. DFT theory of B3LYP-D3 was used considering dispersion corrections according to Grimme's three-parameter with Becke–John–son damping, along with the 6–311 + G** basis set[31]. Three initial configurations were used for cluster calculations involving two or more components to investigate the lowest energy state of different DES clusters. Therefore, it aids us in locating the most stable configuration with a minimal amount of energy. There were no imaginary frequencies in the vibrational spectrum of these optimized structures, thus, they achieved an actual minimum on the potential energy surface. Among the different optimized cluster configurations, the minimum energy state and most stable DES structures were selected and used for further studies to probe hydrogen bonding and charge transfer interaction responsible for the higher extraction efficiency of BT from the DES.

4.3 Experimental

4.3.1 Chemicals and Material

Table 4.1 shows the purity of chemicals, purity method, CAS registration number, and supplier name. The DES components (i.e., salt and HBD) were dried overnight at 308.15 K in a vacuum to remove moisture and other volatile compounds. In contrast, the aromatic and aliphatic compounds were used as collected from the supplier. The solvent for NMR spectroscopy was deuterated DMSO, which was used to calculate the raffinate and extract phase tie line compositions using ^{1}H NMR.

Table 4.1. The following Chemicals[a] are used in the present work.

Chemical Name	CAS Registration No.	Purity (%)	Purification Method[b]	Supplier Name
Methyltriphenyl phosphonium bromide	1779-49-3	≥99 % (mass fraction)	HPLC	Merck
Ethylene Glycol	107-21-1	≥98 % (mass fraction)	GC	Merck

Benzothiophene	95-15-8	≥95 % (mass fraction)	GC	Merck
n-decane	124-18-5	≥99 % (mass fraction)	GC	Merck
Dimethyl sulfoxide-d_6 (DMSO-d6)	2206-27-1	≥99.8% (mass fraction)	NMR-grade	Sigma Aldrich

[a] Chemicals used in this experiment were provided with the purity specified by the supplier.

[b] Purification method as reported by Supplier.

4.3.2 Synthesis of DES

The DES used in this analysis was synthesized using the specific molar ratio of a precisely weighted amount of HBD, and HBA mixed in a sealed flask at a given temperature while stirring until a transparent liquid was formed. The HBD and HBA were weighed using a digital machine (Anton Paar DMA 4500), with a measurement uncertainty of $\pm 0.1 \times 10^{-4}$ g. The HBA and HBD mixture was heated in a thermostatic bath with a temperature controller at T =313.2 K, with a measuring error of T/K = 0.1. Finally, the vacuum-dried pure DES was characterised for purity with ^{1}H (Figure S1) and ^{13}C (Figure S1) using the composition analysis through the NMR (600 MHz NMR, Bruker, Germany). DES was vacuum dried at 35 mbar and 318.2 K for 12 hours. The Karl Fisher Titrator (Model No. 787 KF; Make: M/s Metrohm, Switzerland) was used to determine the remaining water content. In terms of weight percent, the water content was 0.001 wt %. The boiling point of DES was measured using the Analab Scientific apparatus with an uncertainty of ±2°C, as given in table 4.2.

Table 4.2. The physical properties of DES at temperature T = 25°C and pressure p= 0.1MPa.

HBA	**HBD**	**Molar Ratio**	**Molar Mass(g/mol)**	**Density**	**Boiling Point(°C) at 101.3kPa**	**Viscosity (η) (mPa.s)**
MTPB	EG	1:4	121.10	1.228	257	121 ± 1

[a] The standard uncertainties *u* are *u* (*x*) = 0.001, *u* (*T*) = 0.01 °C, *u* (*P*) =2 kPa, u (B.P) = 2 °C, *u* (ρ) = 0.002 g·cm^{-3}, and *u* (η) = 1 with 0.95 level of confidence (*k* ≈ 2).

4.3.3 Experimental Details of Liquid-liquid Extraction

Benzothiophene (BT) was selected as the model diesel sulphur compound, while *n*-decane was designated as a representative model diesel fuel. Feed compositions were prepared in such a manner that the mixture resulted in a homogeneous domain. Here BT was dissolved in *n*-decane with its feed composition maintained at less than 20 % by weight. The desulphurization was conducted using indigenous instruments, consisting of a quartz beaker with an extraction reactor cover placed on a magnetic stirring unit with a temperature control system with 0.1K uncertainty. All the LLE experiments were performed by considering the phase ratio of DES to model diesel oil at 1:1 unless otherwise specified. In this work, the DES was treated as a *pseudo*-pure species instead of a mixture of HBA and HBD. This terminology was justified experimentally using ^{1}H NMR, where DES components were found to be intact as a single entity. All the experimental results reported in this analysis were performed in triplicate to evaluate reproducibility, and the experimental errors were found in the range of ±3 percent.

4.3.4 Compositional Analysis using NMR

Samples of both phases in equilibrium, namely the extract (solvent-rich) and raffinate (hydrocarbon-rich), were taken for compositional analysis using the syringes without disturbing the interface between the phases. Each phase sample, namely extracts and raffinate, was dissolved in 0.6 mL DMSO solvent and placed in NMR tubes that were adequately sealed. The ^{1}H NMR spectral analysis for calculating the peak areas of the hydrogen molecule of each component.

The model sulphur compound available in model diesel was found in the range of 7.2-7.6. The model diesel compounds (i.e., *n*-decane) were in the range of 1-1.3 for the –CH_2– linkage and below 0.9 for the –CH_3 group. The peaks of the CH_3 moiety of DES were found in the range of 3.14-3.17(figure 4.2). The individual hydrogen atoms peak areas belonging to the

respective component ranges were obtained by manually integrating the ^{1}H NMR of respective extract and raffinate phases. The equation used to calculate the mole fraction of individual components is given below,

$$x_i = \frac{H_i}{\sum_{i=1}^{3} H_i} \tag{4.3}$$

Where x_i represents the mole fraction of species, i and H_i is the peak area of a single hydrogen atom in component i. We prepared some known mixtures near the binodal curve in the homogeneous region and then obtained the ^{1}H NMR to verify the accuracy. The mole fractions obtained were found to be in good agreement with the actual compositions. Measurement of tie-lines was obtained corresponding to standard deviations of <0.007. The maximum absolute variation of the mole fraction was found to be 0.001 the mole fraction.

4.3.5 LLE Results and COSMO-SAC Prediction

Figure 4.1 represents the LLE experiments that were conducted for the ternary system of DES(1)-benzothiophene(2)-*n*-decane(3) at 308.15 K and 1 bar pressure. These experiments were carried out to assess the efficacy of the given DES as an extractive media for benzothiophene from a model diesel representative compound. For LLE, the experimental tie-line concentration of benzothiophene in model diesel varies in the range of less than 20% by weight. It implies that only the feed % in BT+*n*-decane was varied, but the overall moles of the feed was equal to the solvent for each tie line. The tie line compositions for the given system are reported in table 4.3. The selectivity, distribution coefficient, and Extraction Efficiency for the corresponding tie-line are calculated from equations (4.4), (4.5), and (4.6), respectively.

$$D_i = \frac{x_i^{Extract}}{x_i^{Raffinate}} \tag{4.4}$$

$$S_{ij} = \frac{x_i^{Extract}}{x_i^{Raffinate}} \Big/ \frac{x_j^{Extract}}{x_j^{Raffinate}} \quad (4.5)$$

$$\%EE = \left[\frac{x_{2,\text{initial}} - x_{2,R}}{x_{2,\text{initial}}}\right] \times 100 \quad (4.6)$$

Here the symbols have their usual meaning while '*i*' refers to BT and '*j*' refers to DC. 'Extract' and 'Raffinate' refer to the solvent-rich and aliphatic hydrocarbon-rich phases, respectively. In equation 6, $x_{2,\text{initial}}$ refers to the initial mole fraction of BT in the feed, and $x_{2,\text{R}}$ is the final mole fraction of BT in the *n*-decane-rich phase after extraction.

Where x_{BT} and x_{DC} denote the mole fraction of benzothiophene and *n*-decane in both extract phase and raffinate phase, respectively. Distribution coefficient and selectivity values decrease for the given system as benzothiophene concentration in the feed increases. Still, in lower concentrations of benzothiophene in the feed, the distribution coefficient and selectivity are significantly higher. These reported results suggest that DES is an excellent option for aromatic sulphur extraction on an industrial scale because of the amount of sulphur compounds required to be maintained at the ppm-level. Analysis of LLE results shows that the concentration of *n*-decane in the extract phase was as high as 3.9 % in the studied DES, as shown in figure 4.2. This concentration was found at a higher concentration of feed tie line and became negligible at a lower concentration of the aromatic sulphur compound.

Therefore, these results are favourable as the actual model diesel fuel contains minimal benzothiophene at ppm level. From the regeneration point of view of DES, it demonstrates that solvent regeneration at intermediate and lower benzothiophene levels can be accomplished with limited hydrocarbon loss. The corresponding DES concentration in the raffinate phase was found to be zero, reducing the recovery cost for the solvent. Therefore, it reveals that no transfer of DES in the hydrocarbon-rich phase as an impurity reduces solvent recovery costs.

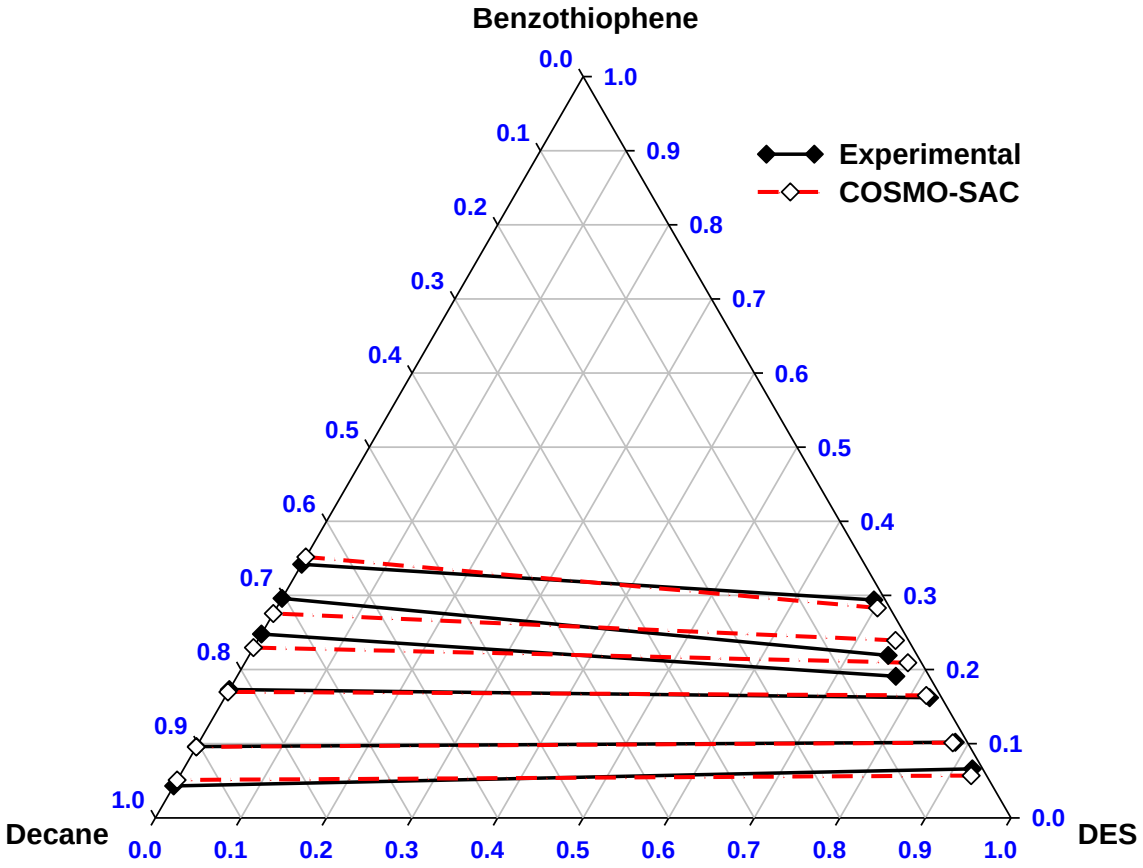

Figure 4.1. Experimental vs. COSMO-SAC predictions for the system DES (1)–benzothiophene (BZ) (2) –*n*-decane(DC) (3) at 308.15 K and atmospheric pressure.

Table 4.3. Liquid-liquid equilibrium tie-line data for the ternary system DES+ benzothiophene(BT)+*n*-decane(DC), at 308.15 K and 0.1 MPa pressure. The molar fractions of DES, benzothiophene and *n*-decane are represented by x_1, x_2, and x_3, respectively [a].

Extract phase			Raffinate phase			Distribution Coefficient (D_{BT})	Selectivity (S)	% EE
x_{DES}	x_{BT}	x_{DC}	x_{DES}	x_{BT}	x_{DC}			
0.922	0.066	0.012	0.000	0.043	0.957	1.53	122.41	78.36
0.884	0.102	0.014	0.000	0.096	0.904	1.06	68.61	69.26
0.824	0.162	0.014	0.000	0.173	0.827	0.94	55.32	63.52
0.770	0.191	0.039	0.000	0.248	0.752	0.77	19.31	53.41
0.747	0.219	0.034	0.000	0.296	0.704	0.74	15.32	47.62
0.693	0.294	0.013	0.000	0.342	0.658	0.86	12.57	43.72

[a] Standard uncertainties are u(T) = 0.01 K, $u(x)$ = 0.001, and u(p) = 2 kPa.

Table 4.3 gives the detail of extract and raffinate phase selectivity, distribution coefficients, and extraction efficiency with feed concentration. The reported DES of MTPB/EG (1:4) at 308.15 K and 1 bar was superior to previously reported solvents in the literature for benzothiophene extraction in terms of extraction efficiency, distribution ratio, and selectivity.

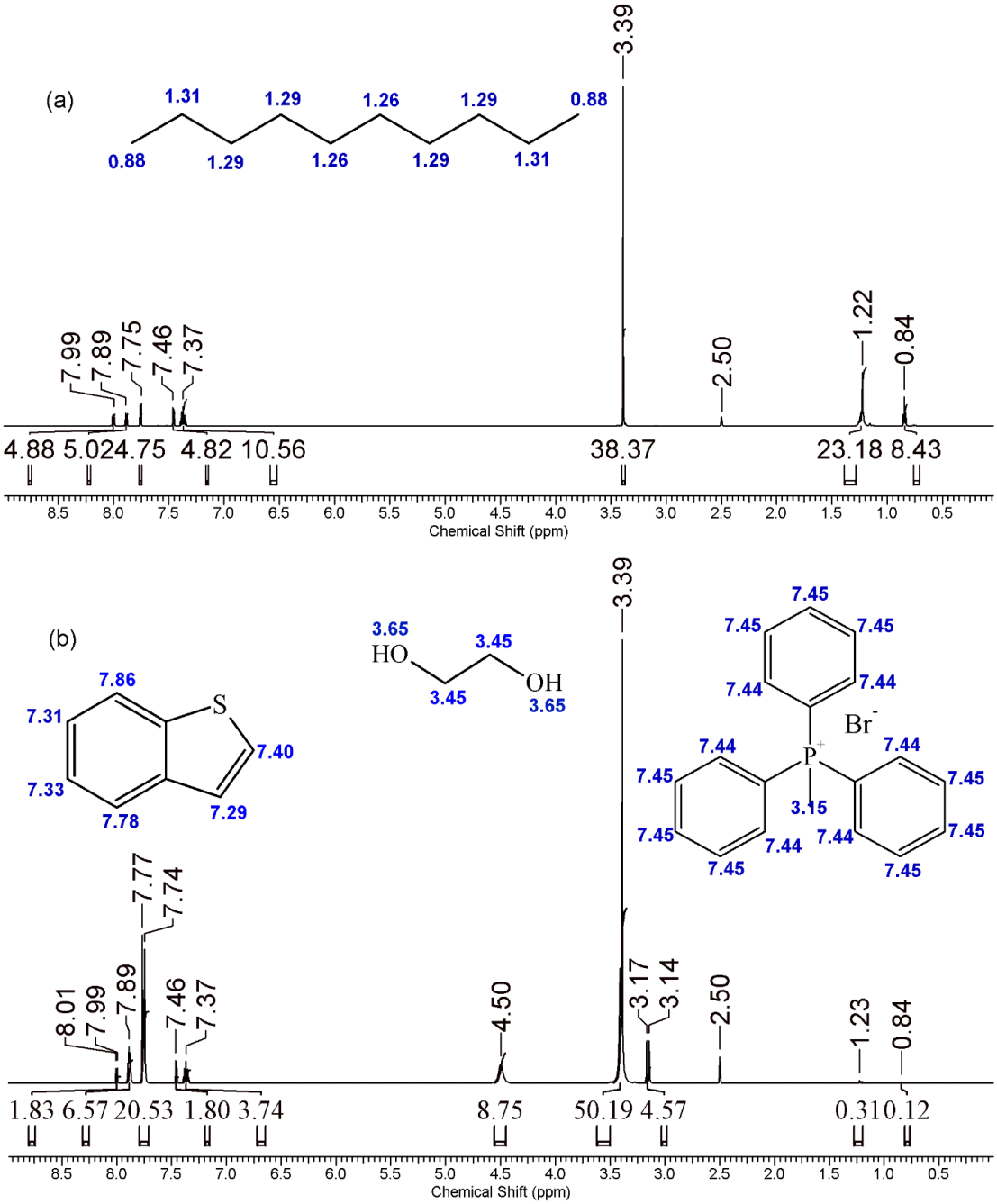

Figure 4.2. ^{1}H NMR Spectra of DES (1) +Benzothiophene (BT) (2) + *n*-decane (DC) (3) system of (a) Raffinate phase (b) Extract Phase.

4.3.6 σ-Profiles Prediction

The extraction efficiency of DES can be described by correlating the σ-profiles interaction between benzothiophene and *n*-decane as a model diesel representative concerning the sigma profiles given by the COSMO-RS model as described earlier in detail by Klamt [32]. The probability distribution of screening charges on the surface of a specific compound is given in the σ-profiles. Figure 4.3 represents the surface screening charges in terms of *σ*-profiles of benzothiophene and model diesel compound with DES studied in the present work. The σ-profile of model diesel compound lies in the non-polar region and has a higher magnitude due to the large alkane chain. The non-polar alkyl groups of the *n*-decane (–CH_3, –CH_2, and –CH) correspond to the peaks in the non-polar region around zero charge densities. The screening charge density regions of the acceptor and donor are described from the value of $\pm \sigma_{hb}=0.0084$ $e/Å^2$. The *σ*-profiles of DES and benzothiophene are in close range with each other, but the sulphur atom in benzothiophene has a higher tendency to act as an electron acceptor. Thus, benzothiophene contains the aromatic ring and sulphur compound, as a result, the complementarity of the curve peak in the H-bond acceptor region can be used to describe the interaction ability between DES and solute molecule.

In addition, the curve of σ-profiles in the H-bond acceptor region also shows that the interaction between the BT and the hydroxyl group of the EG plays a vital role in the solvation process. Therefore, the σ-profile obtained from the COSMO-SAC model also reveals that the strong formation of non-covalent interactions consists mainly of hydrogen bonding and dispersion interactions between the non-polar sulphur species and DES, which can be responsible for the higher extraction efficiency of benzothiophene from model diesel compounds.

4.3.7 Quantum Chemistry (QC) Insights

In an extraction process, the transfer of aromatic sulphur compound from the alkane-rich phase to the solvent-rich phase is essentially due to the atomistic level molecular interactions. Therefore, the molecular interactions were investigated by DFT calculations to explore the extraction mechanism, charge transfer, and interactive sites of DES responsible for the higher solvation of the model aromatic sulphur compound.

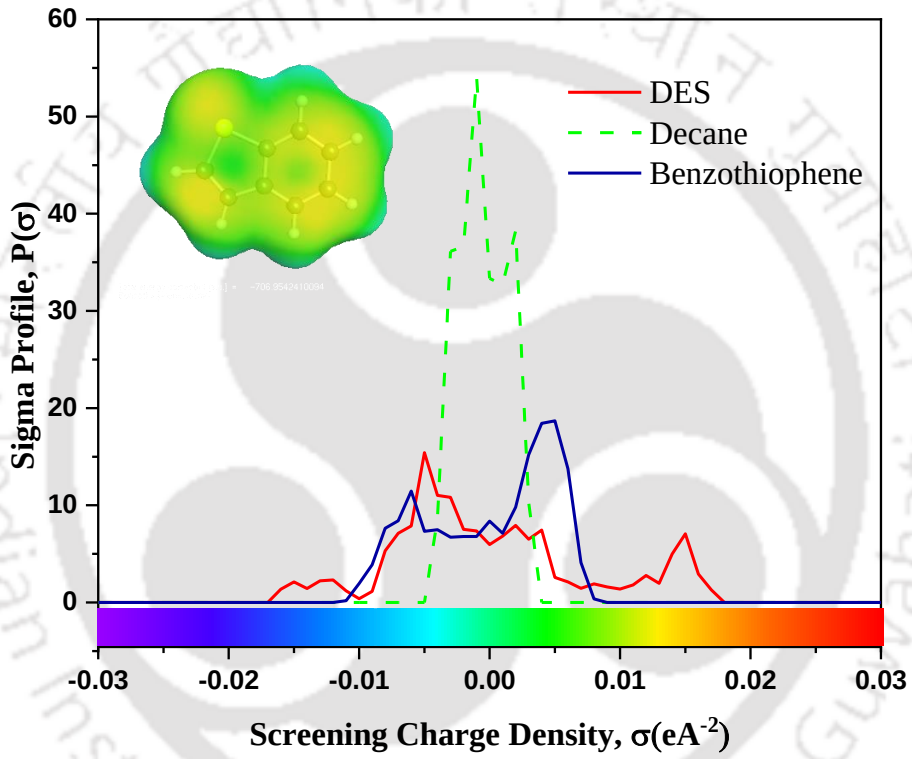

Figure 4.3. σ-Profiles of DES (red), *n*-decane (green), and benzothiophene (blue).

Interaction energies (ΔE) of each cluster for different processes associated with the formation of DES and with different DES complexes were computed using Equation 4.7-4.8, where X represents the denoted BT or DC in complexes. Finally, the effects of basis set superposition error (BSSE) on all the interaction energies of clusters have also been considered.

$$\Delta E_{DES} = E_{DES} - (4E_{HBD} + E_{MTPB}) \quad (4.7)$$

$$\Delta E_{DES-X} = E_{DES-X} - (E_{DES} + E_X) \quad (4.8)$$

Figure 4.4. B3LYP-D3/6–311 + G** optimized geometries of DES, *n*-decane, and aromatic sulphur compound clusters, along the significant structural distances associated with intermolecular interactions. The dark grey colour is applied for carbon atoms, red for oxygen atoms, yellow for sulphur atoms, orange for phosphorus atoms, and light grey for hydrogen atoms.

(a) MTPB+BT **(b) EG+BT**

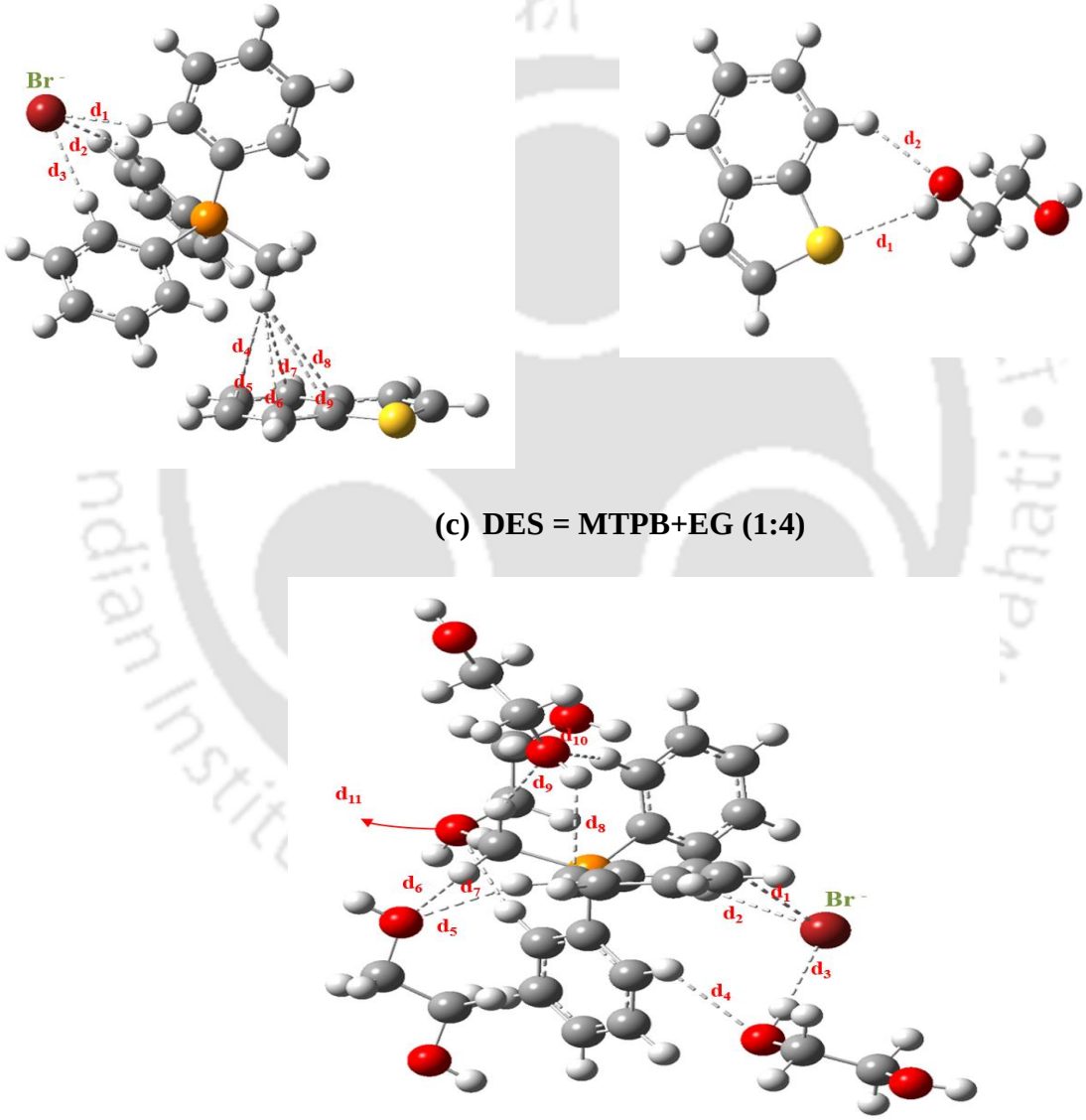

(d) DES+BT

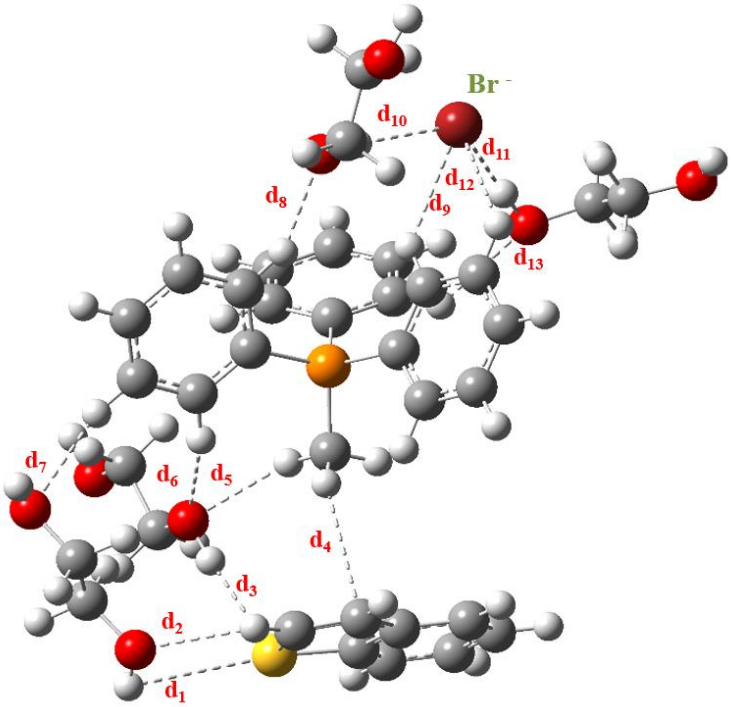

(e) DES+DC

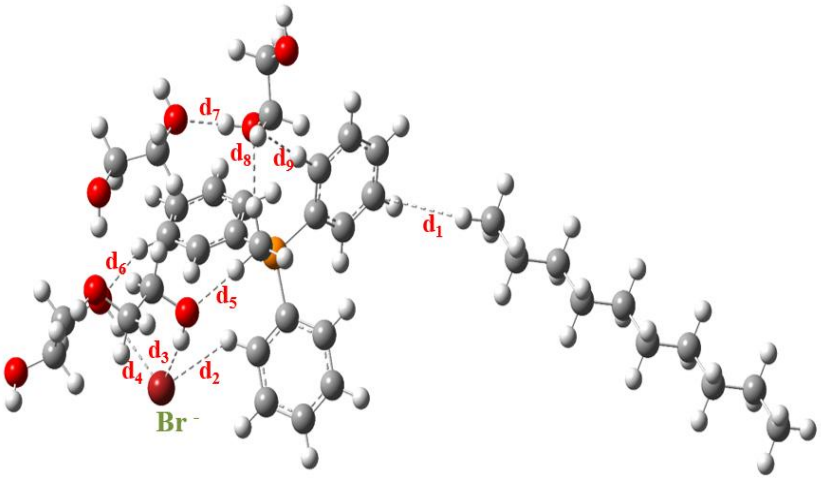

The intermolecular interactions between individual MTPB, HBD, and the aromatic sulphur compound were explored to infer their viability for effective BT solvation in figure 4.4a-4.4b. The higher solubility of BT was responsible for the higher extraction efficiency compared to the representative model diesel component. In figure 4.4a, the bromine (Br^-) ion forms strong hydrogen bonds interaction with the hydrogen attached to the phenyl ring of MTP cation.

The aromatic benzene ring of benzothiophene forms the C−H···π type bonds by aligning itself parallel to the methyl moiety of MTP cation. These interactions are mainly non-covalent types, and distances between the different bonds formed between HBA and benzothiophene lie in a distance of 2.92-3.36 Å. Thereafter, figure 4.4b represents the interaction of aromatic sulphur compound and ethylene glycol. Consequently, it reveals that the positively charged sulphur atom of BT forms a strong hydrogen bond with the hydroxyl group of ethylene glycol with distance d_1=2.83 Å by withdrawing the electron density, and the hydroxyl group of HBD also forms a strong hydrogen bond with the hydrogen attached to the benzene ring of BT with the distance of d_2=2.47 Å.

Table 4.4. Interaction energy between DES, BT, and DC for different complex clusters**.**

System	E (hartree[a])	△E (kJ·mol^{-1})
MTPB	-3647.59304	-
EG	-230.252217	-
BT	-706.66000	-
DC	-394.371071	-
MTPB+BT	-4354.611772	-
EG+BT	-937.921712	-
DES(MTPB+4EG)	-4571.890891	-220.12
DES+BT	-4569.69082	-176.36
DES+DC	-4563.418965	-68.19

[a]1 hartree = 27.211 eV = 627.509 kcal·mol $^{-1}$ = 2625.753 kJ· mol $^{-1}$

Figure 4.4c depicts the complex DES cluster, which shows the molecular arrangement of HBA and HBD in the molar ratio of 1:4 to form the potential DES. It can also be observed that it forms a strong hydrogen bond mainly of O−H···Br^- interaction with distances of 2.30 Å. Bromine (Br^-) ion with negative charge also forms C−H···Br^- type multiple bonds with the positively charged hydrogen atom attached to the phenyl ring of MTP cation with distance d_1 and d_2 of 2.67 and 2.95 Å, respectively. The ethylene glycol (HBD) part of DES also confirms

the multiple strong non-covalent bonds of C−H···O type with the methyl or phenyl groups of the HBA within the distance range of 2.42-2.69 Å (figure 4.4c). The strong hydrogen bonding interactions between the MTP cation and the bromide (Br^-) anion were found at a close distance of d_3=2.30 Å and d_1=2.51 Å. Experimentally, DES formation shows a drop in melting point due to the formation of such a strong hydrogen bond between HBA and HBD. In the DES cluster, the most significant distances of MTPB and EG were also highlighted for O−H···Br, C−H···Br, and C−H···O type non-covalent interactions in table 4.4. This strong interaction validates the integrity of the DES structure with reasonable interatomic distances between the MTPB and EG molecules in the specific molar ratio of 1:4.

Table 4.5. Intermolecular distances (A°) calculated at the B3LYP-D3/6–311 + G** theoretical level for the significant intermolecular interactions in various DES clusters (figures 4.4a-4.4e).

Distance(A°)	MTPB–BT	EG–BT	DES	DES–BT	DES–DC
d_1	2.47	2.83	2.67	3.19	3.27
d_2	2.47	2.47	2.94	2.50	2.77
d_3	2.46		2.30	2.49	2.16
d_4	3.03		2.55	3.06	2.27
d_5	2.92		2.42	2.34	2.06
d_6	3.07		2.32	2.43	2.17
d_7	3.22		2.54	2.43	1.83
d_8	3.36		2.69	2.19	2.25
d_9	3.27		2.35	2.70	2.33
d_{10}			2.44	2.31	
d_{11}			2.38	2.82	
d_{12}				2.32	
d_{13}				2.41	

The optimised geometry of the DES-BT cluster shown in figure 4.4d suggests that DES maintains their original geometry and orientations incorporating HBA and HBD in the presence

of (non-polar) sulphur species benzothiophene. In particular, the optimized cluster reveals the absence of interaction between bromide (Br^-) ion with the aromatic sulphur compound. In contrast, phenyl rings of MTP cation and the ethylene glycol interact with the aromatic rings of BT with multiple non-covalent (C−H···π, C−H···Br^-, C−H···O and O−H···π) interactions. The DES clusters essentially preserve their original intermolecular hydrogen-bonding network after the addition of model diesel sulphur compound, implying a preference for retaining strong hydrogen-bonding inside the DES cluster over forming new interactions with a non-polar aromatic species (BT). As illustrated in figures 4.4a-4.4e, the methyl group of the MTP cation preferentially forms a strong interaction with the parallel plane of the benzothiophene (BT) from the top and forms a non-covalent C−H···π type bond, while HBD interacts with the sulphur atom of BT through the hydroxyl group of ethylene glycol. The interatomic distances between the different active sites of DES and BT are given in table 4.5. Interestingly, it was observed that DES essentially preserves their initial geometries and orientations with ethylene glycol in the presence of the model diesel compound and shows minimal interaction, as summarized in the optimized geometries presented in Figure 4.4e. The interaction energies of different DES clusters, as shown in table 4.4, also reveal the nature of the interaction between DES and the aromatic sulphur compound. The higher interaction energies of DES and benzothiophene cluster than the model diesel compound were responsible for the higher extraction efficiency. The interaction energy of different clusters follows the following order: MTPB+EG (1:4) > BT-DES > DC-DES.

4.3.8 Charge Transfer Behaviour

Charge transfer (CT) transfers a fraction of an electronic charge within a molecule or between species of a cluster intermolecularly. The associated CT complex cluster is usually composed of two or more molecules or charge distribution between different parts of a cluster. In a complex cluster, one section acts as an electron donor and another as an electron acceptor. The

charge is carried out by molecular orbitals, which transfer from the highest occupied molecular orbital (HOMO) to the lowest unoccupied molecular orbital (LUMO). As a result, the direction of CT is determined by the physical placement of these orbitals within the cluster structures. The Charge transfer in different DES clusters was calculated using charges from electrostatic potentials using a grid-based method (CHELPG) developed by Breneman and Wiberg[33]. The obtained CHELPG charges were also compared with the charge obtained from Mulliken charge population analysis. The charges calculated from both of these methods follow the same trends, but they differ quantitatively. The charge transfer analyses like this one helped to identify the active sites of DES that interact with the target sulphur compound and quantify the intensity of these interactions. Table 4.6 shows that interaction with the BT causes a considerable alteration of the travel of charge within an initial (BT-free) cluster of DES.

Table 4.6. Charge transfer analysis of benzothiophene(BT) in different clusters of DES components.

Charge on benzothiophene(BT)		**Quantity of charge on the MTP cation in BT−DES cluster and pure DES**		**Quantity of charge on the bromide (Br^-) ion in BT−DES cluster and pure DES**		**Quantity of Charge on the ethylene glycol in BT−DES clusters and the pure DES**	
Pure DES	With DES	Pure DES	BT-DES cluster	Pure DES	BT-DES cluster	Pure DES	BT-DES cluster
CHELPG Charges							
0.0000	0.1155	0.9025	0.8532	−0.7568	−0.7538	−0.3701	−0.3640
Mulliken Charges							
0.0000	0.2701	1.0410	0.6740	−0.7820	−0.6950	−0.4130	−0.3512

The Charge transfer analysis reveals that the aromatic sulphur compound loses electron density in the DES-BT cluster upon interaction with the DES. The distance between the MTP cation and the BT can be correlated to the loss of electron density. The loss of electron density from the BT depends on the MTP cation proximity with the non-polar sulphur species (figures

4.4d). Overall, during the formation of DES-BT clusters, electron density transfers from the BT to the DES (Table 4.6). The transfer of charge from the aromatic sulphur compound to MTP cation is accompanied by a weakening of the interaction between the MTP cation and Br^- anion or HBD species, concomitant with an increased number of BT−HBD and BT−MTP interactions.

Fascinatingly, the Br^- ion loses electron density in the BT−DES cluster dictated by the HBD species (EG) ability to accept electron density. The CT analysis further revealed that several hydrogen bonds could be formed between HBA and the HBD, especially with the hydroxyl group of EG, MTP cation, and bromide (Br^-) ion of MTPB. The bromide (Br^-) ion can act as a charge transfer bridge between MTP cation and the EG in the DES cluster. The bonding features of MTP cation, bromide (Br^-) ion, and EG could be the most thermodynamically stable DES cluster because it forms the highest number of H-bonds amongst each other, which are non-covalent type interactions originating from the charge transfer process. Charges determined from a Mulliken population analysis were consistent with charges calculated from the CHELPG method[34]. Therefore, the CT process promotes DES formation at room temperature and even helps in DES stability up to higher temperatures. Overall, both CT analysis reveals that the presence of the BT significantly alters the CT interactions between the constituents of the DES. Charge transfer analysis of different clusters provides a broader perspective and a more profound understanding of DES synthesis.

4.3.9 Hansen Solubility Parameters (HSPs)

The Hansen solubility parameters (HSPs) were computed to predict the solubility of BT in studied DES to justify the higher extraction efficiency through the molecular mechanism. The HSPs for BT, DC, and DES have been calculated using the different predictive models as mentioned in table 4.7. One of the earliest but widely used Quantitative and structural property

relationship (QSPR) approaches the solubility parameter approach[35-38]. In this investigation, three chemical descriptors are known as partial or Hansen Solubility Parameters (HSPs) [39], were used. Charles Hansen's three-dimensional solubility parameter system is the most well-known and widely used of the various multi-component solubility parameter systems. As seen in equation 4.9, total cohesive energy density is also defined as the sum of square roots of the partial cohesive energy densities.

$$\delta_t^2 = \delta_d^2 + \delta_p^2 + \delta_h^2 \qquad (4.9)$$

Hansen's solubility parameters are represented by δ_d, δ_p, δ_h, and δ_t where d represents the dispersion contribution, p represents the polarity contribution, h represents the hydrogen bonding contribution, and t represents the total contribution of the particular compound. Hansen's solubility parameters were computed for each compound using Hoftyzer and Krevelen's group contribution technique[40].

$$\delta_d = \frac{\sum_i F_{di}}{V} \qquad (4.10)$$

$$\delta_P = \frac{\sqrt{\sum_i F_{pi}^2}}{V} \qquad (4.11)$$

$$\delta_h = \sqrt{\frac{\sum_i E_{hi}}{V}} \qquad (4.12)$$

Here F_{di} and F_{pi} are the group contributions to the dispersion and polar components per structural group to the molar attraction constant F as postulated by Small[40]. The hydrogen bonding energy per structural group is E_{hi}, and V is the molar volume of the compound.

To determine whether compound '*i*' dislikes or likes compound '*j*', the radius of interaction between the solute and solvent, R_{ij}, is defined as in equation 13 [41]. The narrower the radius, the better the miscibility of compound i with compound j, thus benzothiophene's R_{ij} value in the investigated DES was lesser than model diesel.

$$R_{ij}^2 = 4\left[\left(\delta_{di} - \delta_{dj}\right)^2 + \frac{1}{4}\left(\delta_{pi} - \delta_{pj}\right)^2 + \frac{1}{4}\left(\delta_{hi} - \delta_{hj}\right)^2\right] \qquad (4.13)$$

Table 4.7. Solubility parameters of benzothiophene, *n*-decane, and DES. The listed HSPs include various contributors' dispersion, polar, and hydrogen to the HSPs.

Compounds	$\delta_{d\ (MPa)}^{0.5}$	$\delta_{p\ (MPa)}^{0.5}$	$\delta_{h\ (MPa)}^{0.5}$	$\delta_{t\ (MPa)}^{0.5}$	**Predicted Model**
Benzothiophene	20.2	3.5	5.4	21.20	Charles M. Hansen[40]
n-decane	15.70	0	0	15.70	Hoftyzer and Krevelen[40]
EG	17	11	26	32.95	Hoftyzer and Krevelen[40]
MTPB	18.46	13.32	15.92	27.79	Using Different Conformers in the COSMO model
DES[a]	17.29	11.46	23.98	31.70	By normalising HBA and HBD in a specific molar ratio

[a] DES = 0.2× [MTPB] + 0.8 ×[EG].

The solubility parameter operates on the "like-dissolves-like" principle. If the solvent and solute solubility parameters are comparable, it signifies the higher solubility of the BT in the studied DES. As expected, the polarity (δ_p) and hydrogen-bonded (δ_h) solubility parameters of BT and DES contribute significantly compared to the aliphatic model diesel compound, which has zero contribution in terms of polarity and hydrogen bonding.

Table 4.8. The radius of interaction for benzothiophene, *n*-decane in the studied DES and model diesel fuel mixture.

Solvent	**Solute**	$\delta_{d\ (MPa)}^{0.5}$	$\delta_{p\ (MPa)}^{0.5}$	$\delta_{h\ (MPa)}^{0.5}$	$\delta_{t\ (MPa)}^{0.5}$	R_{ij}
DES	Benzothiophene	17.29	11.46	23.98	31.70	21.03
	n-decane					26.77
Benzothiophene	*n*-decane	20.2	3.5	5.4	21.2	11.06

As a result, the dominating interactions from hydrogen-bonding and electrostatic interactions are the reason for the higher solvation for BT in DES (Table 4.7). As shown in table 4.7-4.8, dispersion contributions (δ_d) were the most critical parameter in our studies, followed by hydrogen, and then polar interaction dominates. The solubility of benzothiophene was superior to that of aliphatic hydrocarbons; as a result, DES gives the higher extraction efficiencies. The lower value of the radius of interaction for benzothiophene and *n*-decane indicates the strong interaction in model diesel feed. The radius of interaction for DES with benzothiophene and *n*-decane indicated the higher extraction due to the smaller radius of interaction for benzothiophene in DES compared to the model diesel fuel. The radius of interaction (R_{ij}) value of benzothiophene and *n*-decane mixture (R_{ij} = 11.06) is smaller compared to the DES in benzothiophene (R_{ij} = 21.03). Based on the solubility parameters of benzothiophene and DFT calculation, it was also confirmed that both vdW and electrostatic interactions played a predominant role in the extraction of the sulphur compound, whereas in the case of *n*-decane, the weak non-covalent interactions govern the extraction process based on solubility in DES[42-43]

4.4 Summary

This chapter reported the Liquid-Liquid Equilibria studies of DES comprising Methyltriphenylphosphonium bromide (MTPB) and Ethylene glycol (EG) in the specific molar ratio of 1:4 was analysed in the extraction of benzothiophene from *n*-decane as representative model diesel. The LLE experiments resulted in minimal DES cross-contamination in the raffinate phase, making solvent recovery feasible. The LLE experimental data was then validated with the quantum chemical-based COSMO-SAC predictions with deviations within 1.07% in average RMSDs. We also studied the interaction mechanism of benzothiophene solvation in DES by employing quantum calculations, such as the σ-Profiles predictions through the COSMO-SAC model and Hansen solubility parameters. They reveal that the higher extraction of benzothiophene is due to the higher contribution of hydrogen bonding and dispersion-type interactions. Within the DFT theory, the BT interacts with the MTP cation and EG of the deep eutectic solvent through multiple non-covalent interactions (e.g., C−H···π, Br^{-}···O−H, Br^{-}···C−H and O−H···π) but do not interact directly with the bromide (Br^{-}) ion. The charge transfer analysis using the CHELPG and Mulliken population charge analysis reveals substantial charge transfer from the aromatic sulphur compound to the DES, indicating strong interaction compared to the aliphatic model diesel compound. The absence of benzothiophene and bromide (Br^{-}) ion interactions results from the retention of multiple, strong hydrogen bonds between the ethylene glycol as HBD, MTP cation, and bromide (Br^{-}) ion species upon formation of the DES clusters. Notably, all the intermolecular interactions within the DES cluster are preserved after a complex cluster formation, confirming DES stability during the liquid-liquid extraction studies.

Reference

1. Verma, N. R.; Gopal, G.; Anantharaj, R.; Banerjee, T., (Solid+ liquid) equilibria predictions of ionic liquid containing systems using COSMO-RS. J. Chem. Thermodyn. 2012, 48, 246-253.
2. Hansmeier, A. R.; Meindersma, G. W.; de Haan, A. B., Desulfurization and denitrogenation of gasoline and diesel fuels by means of ionic liquids. Green Chem. 2011, 13, (7), 1907-1913.
3. Shang, H.; Du, W.; Liu, Z.; Zhang, H., Development of microwave induced hydrodesulfurization of petroleum streams: A review. J. Ind. Eng. Chem. 2013, 19, (4), 1061-1068.
4. Zhao, H.; Baker, G. A., Oxidative desulfurization of fuels using ionic liquids: A review. Front. Chem. Sci. Eng. 2015, 9, (3), 262-279.
5. Babich, I.; Moulijn, J., Science and technology of novel processes for deep desulfurization of oil refinery streams: a review☆. *Fuel*. 2003, 82, (6), 607-631.
6. Plechkova, N. V.; Seddon, K. R., Applications of ionic liquids in the chemical industry. Chem. Soc. Rev. 2008, 37, (1), 123-150.
7. Zhang, S.; Zhang, Z. C., Novel properties of ionic liquids in selective sulfur removal from fuels at room temperature. Green Chem. 2002, 4, (4), 376-379.
8. Varma, N. R.; Ramalingam, A.; Banerjee, T., Experiments, correlations and COSMO-RS predictions for the extraction of benzothiophene from n-hexane using imidazolium-based ionic liquids. Chem. Eng. J. 2011, 166, (1), 30-39.
9. Kumar, A. A. P.; Banerjee, T., Thiophene separation with ionic liquids for desulphurization: A quantum chemical approach. *Fluid Phase Equilib*. 2009, 278, (1-2), 1-8.
10. Li, C.; Li, D.; Zou, S.; Li, Z.; Yin, J.; Wang, A.; Cui, Y.; Yao, Z.; Zhao, Q., Extraction desulfurization process of fuels with ammonium-based deep eutectic solvents. Green Chem. 2013, 15, (10), 2793-2799.
11. Kumar, N.; Naik, P. K.; Banerjee, T., Molecular modeling insights in the extraction of benzene from hydrocarbon stream using deep eutectic solvent. J. Mol. Liq. 2020, 317, 113909.
12. Smith, E. L.; Abbott, A. P.; Ryder, K. S., Deep eutectic solvents (DESs) and their applications. Chem. Rev. 2014, 114, (21), 11060-11082.
13. Martins, M. A.; Pinho, S. P.; Coutinho, J. A., Insights into the nature of eutectic and deep eutectic mixtures. *J. Solut. Chem.* 2019, 48, (7), 962-982.
14. Warrag, S. E.; Peters, C. J.; Kroon, M. C., Deep eutectic solvents for highly efficient separations in oil and gas industries. Curr. Opin. Green Sustain. Chem. 2017, 5, 55-60.
15. Liu, W.; Jiang, W.; Zhu, W.; Zhu, W.; Li, H.; Guo, T.; Zhu, W.; Li, H., Oxidative desulfurization of fuels promoted by choline chloride-based deep eutectic solvents. *J.* Mol. Catal. A: Chem. 2016, 424, 261-268.
16. Li, C.; Zhang, J.; Li, Z.; Yin, J.; Cui, Y.; Liu, Y.; Yang, G., Extraction desulfurization of fuels with 'metal ions' based deep eutectic solvents (MDESs). Green Chem. 2016, 18, (13), 3789-3795.

17. Warrag, S. E.; Rodriguez, N. R.; Nashef, I. M.; van Sint Annaland, M.; Siepmann, J. I.; Kroon, M. C.; Peters, C. J., Separation of thiophene from aliphatic hydrocarbons using tetrahexylammonium-based deep eutectic solvents as extracting agents. J. Chem. Eng. Data 2017, 62, (9), 2911-2919.
18. Wagle, D.; Adhikari, L.; Baker, G., Computational perspectives on structure, dynamics, gas sorption, and bio-interactions in deep eutectic solvents. Fluid Phase Equilib. 2017, 448, 50-58.
19. Zahn, S.; Kirchner, B.; Mollenhauer, D., Charge spreading in deep eutectic solvents. *ChemPhysChem* 2016, 17, (21), 3354-3358.
20. Lemaoui, T.; Benguerba, Y.; Darwish, A. S.; Hatab, F. A.; Warrag, S. E.; Kroon, M. C.; Alnashef, I. M., Simultaneous dearomatization, desulfurization, and denitrogenation of diesel fuels using acidic deep eutectic solvents as extractive agents: A parametric study. Sep. Purif. Technol. 2021, 256, 117861.
21. Darwish, A. S.; Hatab, F. A.; Lemaoui, T.; Ibrahim, O. A.; Almustafa, G.; Zhuman, B.; Warrag, S. E.; Hadj-Kali, M. K.; Benguerba, Y.; Alnashef, I. M., Multicomponent Extraction of Aromatics and Heteroaromatics from Diesel Using Acidic Eutectic Solvents: Experimental and COSMO-RS Predictions. J. Mol. Liq. 2021, 116575.
22. Hatab, F. A.; Darwish, A. S.; Lemaoui, T.; Warrag, S. E.; Benguerba, Y.; Kroon, M. C.; AlNashef, I. M., Extraction of Thiophene, Pyridine, and Toluene from n-Decane as a Diesel Model Using Betaine-Based Natural Deep Eutectic Solvents. J. Chem. Eng. Data 2020, 65, (11), 5443-5457.
23. Rogošić, M.; Kučan, K. Z., Deep eutectic solvents based on choline chloride and ethylene glycol as media for extractive denitrification/desulfurization/dearomatization of motor fuels. *J. Ind*. Eng. Chem. 2019, 72, 87-99.
24. Kumar, N.; Banerjee, T., Dearomatization Insights with Phosphonium-Based Deep Eutectic Solvent: Liquid–Liquid Equilibria Experiments and Predictions. J. Chem. Eng. Data 2021, 66, (9), 3432-3442.
25. Klamt, A.; Schüürmann, G., COSMO: a new approach to dielectric screening in solvents with explicit expressions for the screening energy and its gradient. *J Chem Soc, Perkin trans 2* 1993, (5), 799-805.
26. Frisch, M.; Trucks, G.; Schlegel, H.; Scuseria, G.; Robb, M.; Cheeseman, J.; Scalmani, G.; Barone, V.; Mennucci, B.; Petersson, G., Gaussian, Inc., Wallingford CT. *Gaussian 09* 2009.
27. Frisch, M.; Trucks, G.; Schlegel, H.; Scuseria, G.; Robb, M.; Cheeseman, J.; Scalmani, G.; Barone, V.; Mennucci, B.; Petersson, G., Gaussian 09, Revision D. 01, 2009, Gaussian. *Inc., Wallingford CT* 2009.
28. Sosa, C.; Andzelm, J.; Elkin, B. C.; Wimmer, E.; Dobbs, K. D.; Dixon, D. A., A local density functional study of the structure and vibrational frequencies of molecular transition-metal compounds. J. Phys. Chem. 1992, 96, (16), 6630-6636.
29. Dennington, R.; Keith, T.; Millam, J., GaussView, version 5. 2009.
30. Frisch, M.; Trucks, G.; Schlegel, H.; Scuseria, G.; Robb, M.; Cheeseman, J.; Scalmani, G.; Barone, V.; Petersson, G.; Nakatsuji, H., Gaussian 16 rev. *Gaussian Inc.: Wallingford, CT, USA* 2016.

31. Grimme, S.; Ehrlich, S.; Goerigk, L., Effect of the damping function in dispersion corrected density functional theory. J. Comput. Chem. 2011, 32, (7), 1456-1465.
32. Klamt, A., *COSMO-RS: from quantum chemistry to fluid phase thermodynamics and drug design*. Elsevier: 2005.
33. Breneman, C. M.; Wiberg, K. B., Determining atom-centered monopoles from molecular electrostatic potentials. The need for high sampling density in formamide conformational analysis. J. Comput. Chem. 1990, 11, (3), 361-373.
34. Wagle, D.; Kamath, G.; Baker, G. A., Elucidating interactions between ionic liquids and polycyclic aromatic hydrocarbons by quantum chemical calculations. J. Phys. Chem. C 2013, 117, (9), 4521-4532.
35. Barton, A. F., *CRC handbook of solubility parameters and other cohesion parameters*. Routledge: 2017.
36. Burke, J., Solubility parameters: theory and application. AIC: 1984.
37. Kodolikar Kulkarni, S. P.; Bhatkhande, D. S.; Pangarkar, V.; Kulkarni, P., Extraction of toluene and n-heptane mixture using ionic liquid Aliquat 336 and mathematical modeling for solvent selection. Sep. Sci. Technol. 2018, 53, (1), 61-70.
38. BURKE, J., Solubility parameters-Theory and application. *The AIC book and paper group annual* 1984, 3, 13-58.
39. Van Krevelen, D. W.; Te Nijenhuis, K., Properties of polymers: their correlation with chemical structure; their numerical estimation and prediction from additive group contributions. Elsevier: 2009.
40. Hansen, C. M., *Hansen solubility parameters: a user's handbook*. CRC press: 2007.
41. Panayiotou, C., Partial solvation parameters and mixture thermodynamics. J. Phys. Chem. B 2012, 116, (24), 7302-7321.
42. Mohan, M.; Huang, K.; Pidatala, V.; Simmons, B.; Singh, S.; Sale, K. L.; Gladden, J., Prediction of Solubility Parameters of Lignin and Ionic Liquids Using Multi-resolution Simulation Approaches. Green Chem. 2021.
43. Huang, K.; Mohan, M.; George, A.; Simmons, B. A.; Xu, Y.; Gladden, J. M., Integration of acetic acid catalysis with one-pot protic ionic liquid configuration to achieve high-efficient biorefinery of poplar biomass. Green Chem. 2021, 23, (16), 6036-6049.

Chapter 5

Molecular Dynamic Insights for the Ternary System

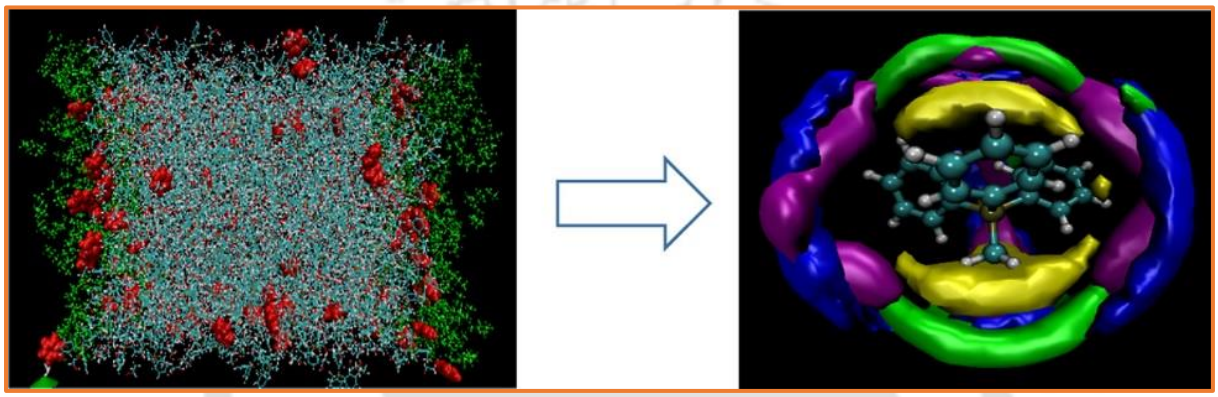

The present study aims to elucidate molecular insights into benzene extraction from a hydrocarbon mixture using a phosphonium-based deep eutectic solvent (DES). The prepared DES consists of the hydrogen bond acceptor (HBA; methyltriphenylphosphonium bromide, MTPB) and hydrogen bond donor (HBD; ethylene glycol) at a molar ratio of 1:4. The atomistic level of classical molecular dynamic (MD) simulation technique is then employed to investigate the equilibrium phase behaviour of the DES + benzene + n-hexane ternary system with respect to DES rich and hydrocarbon-rich phases. Three different concentrations were considered from the reported experimental tie lines to observe the effect of feed concentration, which gave high selectivity and distribution coefficient values. The non-bonded interaction energies of different species and the structural properties such as radial distribution functions, spatial distribution functions (SDFs), combined distribution functions (CDFs), and the average number of hydrogen bonds are then computed. It is found that the cation within the HBA, namely, MTP, initiates interactions with benzene compared to HBD or its anion (Br). MTP and ethylene glycol both are seen to contribute to the hydrogen bonding with benzene, which results in a higher experimental solubility value. The calculations of SDFs further reveal that the benzene molecules are evenly localised around the active sites of the MTP molecule. In contrast, hexane molecules are found to be distributed around the non-active sites of the HBA and HBD. The concentration in both phases was compared to the existing LLE experimental results to validate the simulation procedure. In the penultimate part, 2D ^{1}H-^{13}C Heteronuclear Multiple Bond Correlation (HMBC) NMR is performed to investigate and confirm the long-range interactions among components of DES and benzene.

5.1 Introduction

After examining both experimental and COSMO-SAC-predicted LLE data in the previous chapter 4 and 5, the following chapter will provide molecular insights into benzene extraction from a hydrocarbon mixture by means of a phosphonium-based deep eutectic solvent (DES).

The atomistic molecular dynamic (MD) simulation technique is used to examine the equilibrium phase behaviour of the DES + benzene + n-hexane ternary system with regard to the DES-rich and hydrocarbon-rich phases.

The extraction of benzene components from naphtha streams is of great significance for the petrochemical industry. Both aromatic and aliphatic components have high economic value as raw materials in several processes [1]. Moreover, current changes in the environmental regulation policy demand a meager amount of aromatic content, especially in food-grade and pharmaceutical-grade hexane. The removal of aromatic components from naphtha streams is a complicated process mainly due to the close boiling points, which results in an azeotropic mixture[2,3]. Different separation processes could be used for separation, but the concentration of aromatic compounds determines the economic feasibility of the process. Based on feed composition, i.e., azeotropic distillation is only suitable if the concentrations of aromatic compounds in the feed stream are more significant than 90 wt %. Extractive distillation is only appropriate for concentrations of 65-90 wt % of aromatic compounds. The Liquid-Liquid Extraction (LLE) process is widely used for aromatic compounds between 20 and 65wt % concentrations. However, there is no recommended process for separating aromatic compounds from mixtures with an aromatic concentration lower than 20 wt % of the total amount [4]. Among all other processes, LLE is the most efficient technique for removing a low concentration of aromatics present in naphtha. This extraction process is reliable, cost-effective, and compatible with other conventional processes [5]. It is to be noted here that this extraction process entirely depends on the efficiency of the suitable solvent used, its recyclability, cost, and environmental friendliness.

Deep Eutectic Solvents (DESs) and Ionic Liquids (ILs) share similar physiochemical properties such as low vapour pressure, wide liquid range, and non-flammability. Due to their tunable nature, the Deep Eutectic Solvents (DESs) are sometimes termed analogues of ILs. At

the same time, the behaviour of ILs is dominated by ionic interactions, and DESs exhibit a substantial contribution from hydrogen bonding. Further, due to the high hydrogen bonding interaction, the characteristics of ILs as solvents are shared by DESs. DESs are frequently used as an alternative solvent in place of conventional organic solvents for extraction processes [6-8]. DESs are systems formed from a eutectic mixture of Lewis or Bronsted acids and bases, which can contain a variety of hydrogen bond donor and acceptor species; in contrast, ILs are developed from systems composed primarily of discrete anions and cations.

Furthermore, DESs are mixtures of one or more molecules of hydrogen bond acceptor (HBA) and one or more hydrogen bond donor molecules (HBD). When mixed in proper molar ratio, they show a substantial drop in the melting point compared to the initial starting pure components. Likewise ILs, the DESs also show tunable properties by varying the HBA and HBD. They can be specifically designed for an application by modifying both, namely, (a) the selection of unique HBD and HBA and (b) their molar ratio [9,10]. These solvents are widely gaining attention as extractive solvents for LLE [11-15] and applications such as catalysis [16,17], electrochemistry [18-20], hydrogel [21], and biochemistry [22]. In our previous work, it is reported that DES consisting of methyltriphenylphosphonium bromide (MTPB) salt and ethylene glycol (ETG) can effectively remove polyaromatic (quinolone) from the aliphatic mixture (heptane) [7,23,24]. Mahmoudi et al. [25] used common organic solvents like sulfolane and N-formylmorpholine to extract benzene from hexane. We have also observed the excellent use of different DESs to extract benzene from hexane [26]. It has been found that the DES, as the green solvent, has a superior ability to extract benzene from hexane; hence, the current study focuses on the atomic level insights using the DES, which influences the extraction process.

In ILs, the toxicity part was always in doubt owing to the source of their starting materials, which made their synthesis non-environment friendly. Further, the purification and

synthesis costs added to their disadvantages. In this sense, specific DES or Natural Deep Eutectic Solvents (NADES) are now becoming competitive in terms of readily available starting materials and cost of production. However, the toxicity issues of most of these solvents are scarce, and the scientific community has yet to coin them as green solvents.

Overall the LLE experiments performed uses a favourable solvent [24,26-29], however, in order to observe its effectiveness, an understanding of the extraction mechanism using simulation-based methods such as molecular dynamics (MD) simulations are required. There are few studies available with DES [9,23,30-32]. Classical MD simulation gives the fundamental molecular-level understanding, which can provide the driving force for the development of neoteric solvents for the extraction process. Moreover, classical MD simulations are used to study processes under severe conditions that cannot be performed with conventional experimental methods. Further, these computational methods also allowed us to explore new solvent systems and the screening of many alternatives present in an economical way [33-36]. Although theoretical studies are essential to understand the mechanism, they are not expected to replace experiments but only to accompany them and enhance their use. For example, using classical MD simulations, Stephenson et al. [37] performed MD simulations for extracting ethanol from long-chain alcohols using classical MD simulations. Taha and Lee. [38] observed the phase separation of organic solvents from water using a biological buffer as an external solvent by MD simulations. Celebi et al. [36] also reported the thermodynamic and transport properties of aqueous to reline and ethaline-based DES from MD simulations. Dehury et al. [30] explored the phase behaviour of butanol in two different phases of IL and water by both LLE and MD simulation studies. Perkins et al. [32] also investigated the experimental and computational study to get insight into the most common DES, i.e., choline chloride-urea-based DES. In a recent study, our research group, Naik et al. [23], performed experimental and computational studies for the LLE of quinoline extraction from heptane.

Experimental studies at the laboratory scale usually conclude after a long time, which is in the order of hours or seconds. Still, atomic simulation can not be performed for such a long time due to computational restrictions. The atomic-scale simulation is performed at orders of nanoseconds to decode the interfacial transfer between the extract and raffinate phase. The trajectory velocities are computed after every ~1 fs, and real-time data is recorded for complete simulation. Phenomena occurring at the atomic scale level occur within a fraction and are challenging to capture with a digital instrument. Therefore, theoretical calculations and simulations aim to validate this phenomenon through ensemble theory or statistical mechanical framework. The LLE simulation results defined in this research aim to study one such result or trajectory out of the numerous possible events in such a simulation environment. This essentially connects properties generated by chemical engineers, namely, the activity coefficient, to the computation of mole fractions using first principles. The present study aims to extract benzene from hexane using DES by classical MD simulations at 318.15 K and 1 atm conditions to understand the detailed molecular mechanism associated with the extraction process. In the present study, we have followed the previous experimental results [26], which report benzene extraction from a hydrocarbon mixture.

5.2 MD Simulation Details

The structures of isolated ions of HBA (MTP cation), HBD (ETG), bromide anion (Br), benzene (BEN), and hexane (HEX) were drawn in Gauss View 05 along with their geometries which were optimized by Gaussian 09 [39] at the B3LYP/6-31G* level of theory [40]. The partial charges for these different atomic sites were calculated at the same level of theory. The chemical structures of these species are shown in Figure 5.1, and their atom types are represented in Figure 5.2. The partial charges for different species (as obtained from the quantum calculations) were then fitted with a restricted electrostatic potential [41] module of AMBER 12 [42]. The final partial charges for different atomic sites of these molecules are

shown in Table 5.1. All the force field parameters required for performing MD simulation were generated according to the generalized Amber force field [43] functional form using the ANTECHAMBER [44] module of AMBER 12 [42]. The Lennard-Jones (L-J) parameters used for DES, benzene, and hexane are reported in Table 5.2. The obtained force field parameters are additionally validated by comparing the simulated density of DES (1.235 gm/cm^3) at 318.15 K temperature and ambient pressure condition with the experimental density value (1.214 gm/cm^3) at the same temperature and pressure condition. Results from both experiments and simulations showed high levels of agreement.

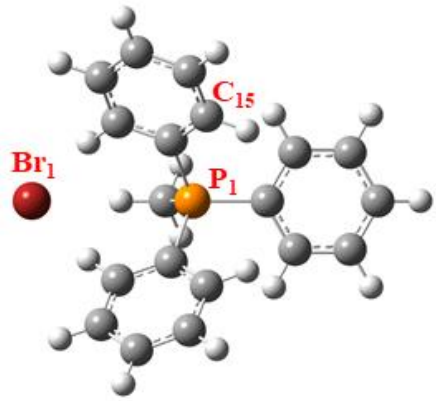

(a) Methyltriphenylphosphonium bromide (MTPB)

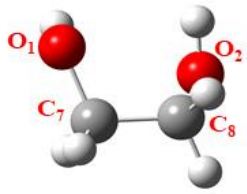

(b) Ethylene Glycol (ETG)

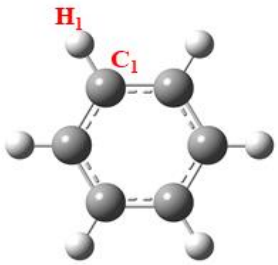

(c) Benzene(BEN)

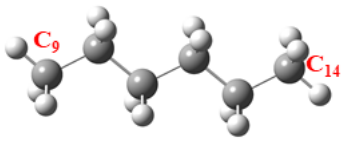

(d) Hexane (HEX)

Figure 5.1. Molecular structure of compounds used in this work. Here the DES (MTPB: ETG) has a molar ratio of 1:4. Atom labels for selected atoms are indicated in red.

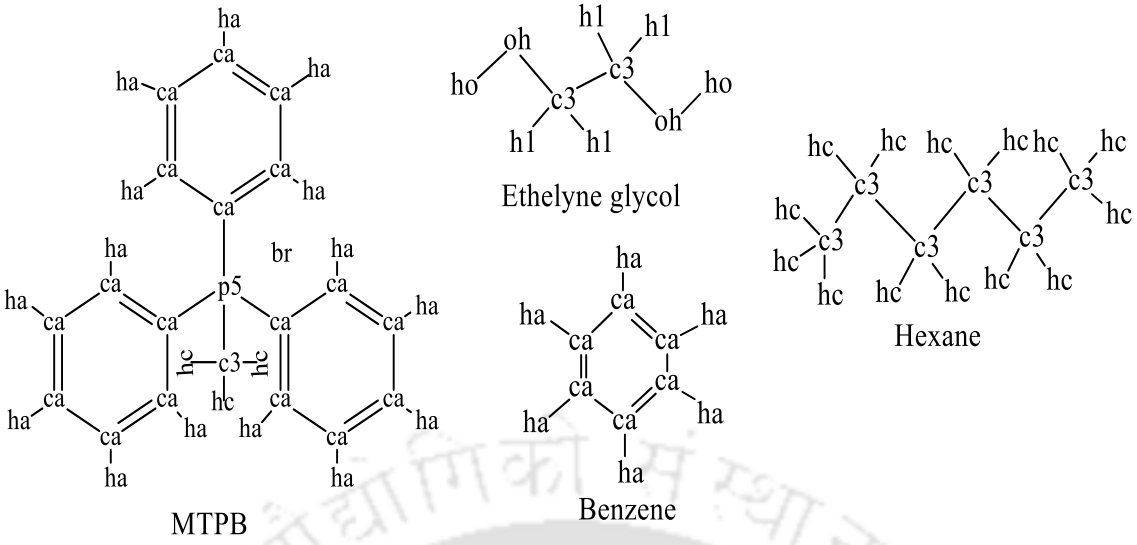

Figure 5.2. Structure with atom types of different molecular species.

The initial arrangement of different systems consisting of DES, benzene, and hexane molecules was made using PACKMOL [45] in a box size of 120 Å × 60 Å × 60 Å. Initially, DES molecules and hexane molecules were inserted into two separate boxes. After that, the boxes were made to come close to each other to create or mimic a two-phase interphase system, i.e., DES-rich and hexane-rich phases. After that, the benzene molecules were uniformly distributed in both phases. All the MD simulations were simulated by NAMD 2.10 package [46] using a Langevin thermostat and Nosé−Hoover Langevin barostat [47,48]. All simulations were run for a time integration step of 1fs. Initially, all the simulated systems were energy-minimized for 1 ns, which was then steadily heated from 0 to 318.15 K for 0.5 ns. After that, the NPT ensemble at 318.15 K and 1 atm pressure was used to equilibrate the systems for 10 ns. For maintaining the static temperature, the Langevin dynamics method [49] with a collision frequency of $1ps^{-1}$ was used. Nosé−Hoover Langevin barostat was used for controlling the pressure with an oscillation period of 100 fs and a damping factor of 50 fs [50].

Table 5.1. Partial charges of different atoms in the molecules species.

MTPB		Ethylene Glycol		Benzene		Hexane	
Atom Type	**Partial Charge**	**Atom Type**	**Partial Charge**	**Atom Type**	**Partial Charge**	**Atom Type**	**Partial Charge**
P1	0.5260	C7	0.2541	C1	-0.1329	C9	-0.3047
C15	-0.0382	H7	0.0059	H1	0.1329	H13	0.0663
C16	-0.1265	H8	0.0059	C2	-0.1329	H14	0.0663
C17	-0.1444	O2	-0.6761	H2	0.1329	H15	0.0663
C18	-0.0643	H9	0.4102	C3	-0.1329	C10	0.2371
C19	-0.1444	C8	0.2541	H3	0.1329	H16	-0.0432
C20	-0.1265	H10	0.0059	C4	-0.1329	H17	-0.0432
H27	0.1460	H11	0.0059	H4	0.1329	C11	-0.0484
H28	0.1663	O1	-0.6761	C5	-0.1329	H18	0.0017
H29	0.1594	H12	0.4102	H5	0.1329	H19	0.0017
H30	0.1663	--	--	C6	-0.1329	C12	-0.0484
H31	0.1460	--	--	H6	0.1329	H20	0.0017
C21	-0.0382	--	--	C1	-0.1329	H21	0.0017
C22	-0.1265	--	--	H1	0.1329	C13	0.2371
C23	-0.1444	--	--	C2	-0.1329	H22	-0.0432
C24	-0.0643	--	--	H2	0.1329	H23	-0.0432
C25	-0.1444	--	--	C3	-0.1329	C14	-0.3047
C26	-0.1265	--	--	--	--	H24	0.0663
H32	0.1460	--	--	--	--	H25	0.0663
H33	0.1663	--	--	--	--	--	--
H34	0.1594	--	--	--	--	--	--
H35	0.1663	--	--	--	--	--	--
H36	0.1460	--	--	--	--	--	--
C27	-0.5744	--	--	--	--	--	--
H37	0.2098	--	--	--	--	--	--
H38	0.2098	--	--	--	--	--	--
H39	0.2098	--	--	--	--	--	--
C28	-0.0382	--	--	--	--	--	--
C29	-0.1265	--	--	--	--	--	--
C30	-0.1444	--	--	--	--	--	--
H40	0.1663	--	--	--	--	--	--
H41	0.1460	--	--	--	--	--	--
C31	-0.1265	--	--	--	--	--	--
H42	0.1460	--	--	--	--	--	--
C32	-0.1444	--	--	--	--	--	--
H43	0.1663	--	--	--	--	--	--
C33	-0.0643	--	--	--	--	--	--
H44	0.1594	--	--	--	--	--	--
Br1	-1.0000	--	--	--	--	--	--

Thereafter, the production run continued for 100 ns for each of the systems with NVT ensemble. The SHAKE algorithm was used to restrain the bonds involving hydrogen atoms [51]. The particle mesh Ewald (PME) method was used to calculate the long-range intermolecular electrostatic interactions [52], and for treating short-ranged intermolecular interactions, a cut-off distance of 12 Å was used. To remove the edge effect, periodic boundary conditions were applied in all three directions. We have not used any charge scaling in the current work as the current system is devoid of any polarizability effect, unlike the water model [53,54]. At every 5 ps, the trajectory data were saved for analysing the different structural and dynamical properties. For the analysis, visual molecular dynamics (VMD) package was used [49].

Table 5.2. Lennard-Jones parameters used for DES, benzene, and hexane.

Atom Type	ε (kcal/mol)	R^* (Å)	Atom Type	ε (kcal/mol)	R^* (Å)
MTPB			Ethylene glycol		
p5	0.2000	2.1000	c3	0.1094	1.9080
ca	0.0860	1.9080	h1	0.0157	1.3870
ha	0.0150	1.4590	oh	1.7210	0.2104
c3	0.1094	1.9080	ho	0.0000	0.0000
hc	0.0157	1.4870	Benzene		
br	0.3200	2.2200	ca	0.0860	1.9080
Hexane			ha	0.0150	1.4590
c3	0.1094	1.9080			
hc	0.0157	1.4870			

Table 5.3. The number of molecules in MD simulations for different system configurations.

System No.	Mole fraction			Total	Number of molecules			Total
	DES	Benzene	Hexane		DES	Benzene	Hexane	
1	0.5	0.025	0.475	1	500	25	475	1000
2	0.5	0.105	0.395	1	500	105	395	1000
3	0.5	0.205	0.295	1	500	205	295	1000

Three different LLE tie-lines data points of ternary experimental systems consisting of DES+ benzene + hexane were selected to understand their behaviour and phase separation using classical molecular dynamics. These experimental tie data points were taken from a previously reported work [26]. MD simulations were then carried out for three such systems of feed, where the number of molecules is given in Table 5.3. Based on MD simulation and comparison with the experimental results, we found that system number 2 gave the closest value of distribution coefficient and selectivity [26]. Thus, we have analysed system number 2 for a detailed MD insight. It should be noted that the DES as a solvent comprises a mixture of two components at a 1:4 molar ratio. Therefore, for MD simulations involving DES (1:4 molar ratio), 500 molecules of MTPB are mixed with 2000 molecules of ETG.

Table 5.4. Experimental and MD simulated liquid-liquid equilibrium data for DES (x_1) +benzene (x_2) +hexane (x_3) ternary system at T= 318.15 K and 1 atm pressure[a].

System No.	Type of data	DES rich phase			Hexane rich phase			Distribution coefficient (β)	Selectivity (S)
		x_1	x_2	x_3	x_1	x_2	x_3		
System 1	Exp.	0.879	0.096	0.024	0.000	0.043	0.957	2.227	87.362
	Comp.	0.911	0.039	0.012	0.000	0.038	0.962	1.026	82.276
System 2	Exp.	0.599	0.378	0.022	0.000	0.236	0.764	1.604	61.292
	Comp.	0.650	0.325	0.025	0.000	0.195	0.805	1.505	57.500
System 3	Exp.	0.416	0.564	0.020	0.000	0.480	0.519	1.174	38.630
	Comp.	0.469	0.522	0.009	0.000	0.519	0.48	1.005	53.753

[a]Experimental value are taken from Kareem et al. [26], RMSD = 0.05%

Table 5.5. Comparison of experimental and simulated data for sulfolane (x_1) + benzene (x_2) + hexane (x_3) at T=318.15 K[a].

Temperature	Type of data	DES rich phase			Hexane rich phase			Distribution coefficient (β)	Selectivity (S)
		x_1	x_2	x_3	x_1	x_2	x_3		
27°C	Exp.	0.929	0.069	0.002	0.000	0.524	0.476	0.131	22.105
25°C	Comp.	0.947	0.051	0.002	0.000	0.544	.0456	0.094	21.375

[a]Experimental values are taken from Mahmoudi *et al.* [25] RMSD = 0.05%

5.3 Results and Discussion

The available experimental results have shown that DES (MTPB: ETG) of molar ratio 1:4 gives the most promising result for the extraction of benzene from hexane. In the first approach, the non-bonded interaction energy studies of DES-benzene-hexane were used to accurately depict the intermolecular forces responsible for the transfer of solute components (benzene) within the bulk liquid phases(*n*-hexane). We first consider the three MD simulated tie-line data for the system DES (1) +benzene (2) +hexane (3), which are shown in Table 5.4. Here we vary the benzene-hexane concentration while keeping a constant solvent-to-feed ratio. In this way, the entire heterogeneity of the benzene in the DES (1) +benzene (2) +hexane (3) system is captured, and the different solvent-to-feed ratio is also studied (Table 5.4).

To validate the simulation procedure, we calculated the mole fraction in both the extract and raffinate phases and then compared the same to the existing experimental results by Kareem et al.[26] We have investigated all three LLE tie-lines mole fractions (as per Table 5.4). The distribution coefficient and selectivity of all systems closely resemble the experimental result (Table 5.4). The concentration of the molecules also agrees reasonably well with the MD results. The deviation in concentration is mainly observed in the hexane-rich phase owing to an absence of a sharp interface, which is challenging to match experimentally (Figure 5.4). We have conducted a detailed analysis of only one single tie line data (system 2) as they all show similar trends. Initially, the simulation was performed at 45°C because a maximum average selectivity was achieved. Even though at 27°C, relatively good selectivity was achieved, distribution coefficients were small. Further, we have performed the same simulation with similar initial configurations and experimental conditions at 25°C (Figure 5.4). This confirms us to recheck the reliability of the simulation process along with the effect of temperature on benzene extraction. The result confirms that the extraction efficiency at 45°C was higher than at lower temperatures. The comparison of experimental (27°C) and simulation results (25°C) are shown in Table 5.5 of the supporting information.

We have again performed a similar simulation run using a conventional organic solvent to benchmark the MD simulation process for benzene extraction using DES by considering a sulfolane+benzene+hexane mixture for the study. We have taken one tie-line data from the reported literature studied by Mahmoudi et al. [25] and carried out the simulation study at 318.15 K.

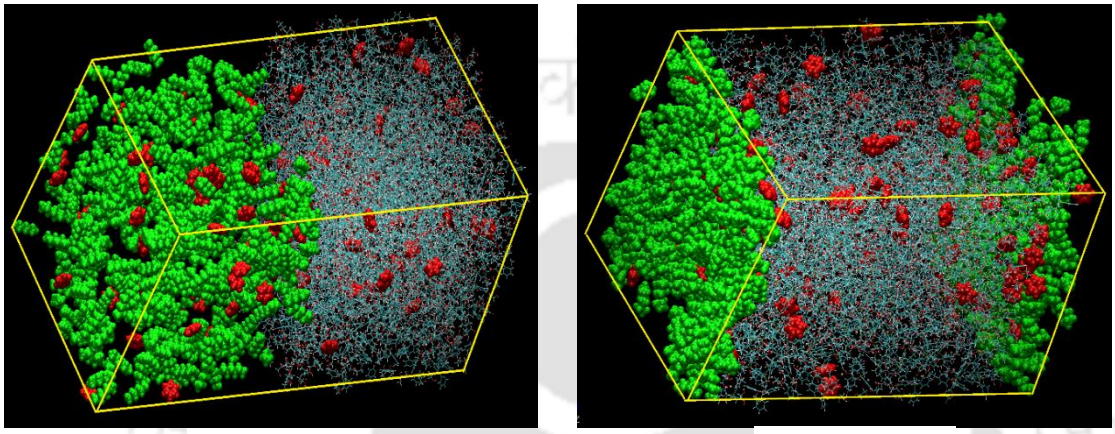

(a) 0 ns (b) 100 ns

Figure 5.3. The system snapshots of benzene in the DES throughout the system at different simulation times: (a) 0 ns, (b) 100 ns, respectively (red: Benzene, green: Hexane, grey: DES (1:4) molecules).

Here, the ternary system consisting of sulfolane (500), benzene (105), and hexane (395) molecule were packed using PACKMOL [45] in a box size of 100 Å × 50 Å × 50 Å with periodic boundary conditions. Then, calculate the respective numbers of molecules present in each phase after 100 ns of the production run. After that, the system's corresponding mole fraction, distribution coefficient, and selectivity were calculated to benchmark the experimental result. A comparison of the experimental and predicted tie line is given below in Table 5.5, and the snapshot is shown in Figure 5.4. This result indicates that the MD simulation method for analysing the extraction methodology consistently agreed with the LLE experiment. Therefore, we confirmed that the simulation procedure adopted in our study was benchmarked correctly.

5.3.1 Non-bonded Interaction Energy

Total non-bonded interaction energies (IE) are calculated using various component pairings of moieties to comprehend the interaction behaviour. Therefore, the total non-bonded interaction energies consist of two contributions, namely electrostatic and van der Waals (vdW) interaction, as shown in Table 5.6. For this, we consider the LLE tie-line data point of a given system 2. Table 5.6 shows that the non-bonded interaction for DES-benzene is more substantial than that of the DES-hexane and benzene-hexane pair.

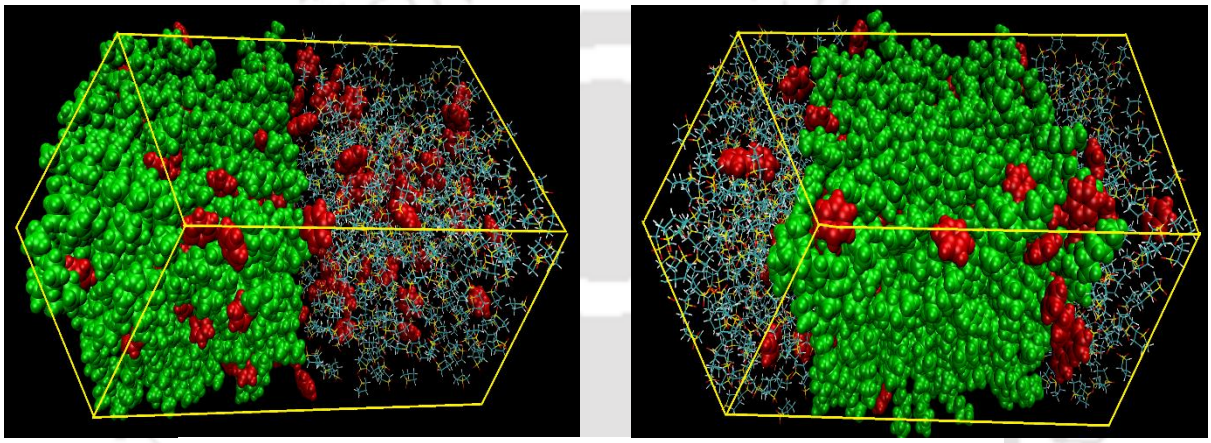

(a) 0 ns (b) 100 ns

Figure 5.4. The system snapshots of benzene in the sulfolane as the solvent system at different simulation times: (a) 0 ns, (b) 100 ns, respectively (red: Benzene, green: Hexane, grey: sulfolane).

A further close investigation reveals that the interaction energy of DES-benzene is four times (-41.970 kJ/mol) higher than the DES-hexane (-11.599 kJ/mol). It provides corroborative evidence for the higher extraction efficiency of benzene using the DES experimentally. It implies that the vdW energy is more prominent than the electrostatic energy within the total non-bonded interaction energies. The van der Waals (vdW) interactions type contributes significantly more to the overall DES-benzene interaction energy, with values of -33.079 kJ/mol, whilst the electrostatic energy component contributes merely -8.892 kJ/mol.

Table 5.6. Interaction energies (kJ/mol) between the different interacting components of DES−benzene−hexane calculated at 318.15 K and 1 atm Pressure.

Interacting moiety	Electrostatic interactions (E_{elec})	vdW interactions (E_{vdW})	Total non-bonded interactions (E_{total})
MTP −BEN	1.328	-17.215	-15.887
MTP−HEX	0.222	-5.737	-5.515
Br−BEN	-8.080	-1.049	-9.129
Br−HEX	-0.254	-0.254	-0.508
ETG−BEN	-2.140	-14.815	-16.955
ETG−HEX	-0.023	-5.553	-5.576
BEN−HEX	-0.012	-3.940	-3.953
DES−BEN	-8.892	-33.079	-41.970
DES−HEX	-0.055	-11.544	-11.599

$\mathbf{E_{total} = E_{elec} + E_{vdW}}$

Total non-bonded interaction between DES-benzene pair can be further decomposed into MTP−benzene, ETG−benzene, and bromide anion−benzene interaction pairs (Figure 5.1). It indicates that the DES-benzene interaction is most favourable among all other interaction pairs and is followed by the ETG-benzene interaction. The least favourable interaction among these is bromide−hexane interaction due to the non-polar nature of aliphatic carbon. Similarly, the disintegration of the DES−hexane pair and total non-bonded interaction suggests that MTP−hexane and ETG−hexane interactions were of the same order. Furthermore, it could be noted that the solubility is less because of the lower interaction energy between the molecules, resulting in higher phase separations. The order of IE is found to be in the following order: DES−Benzene>DES−Hexane>Benzene−Hexane.

5.3.2 Hydrogen Bond Analysis

For the formation of a hydrogen bond, a donor atom with a hydrogen atom bonded to it and an acceptor atom that is not bonded to the donor atom are required. Further, the absolute distance between donor and acceptor atoms should be less than or equal to the cut-off distance, and the

angle between the donor-hydrogen-acceptor pair or angle *D-H-A* should be greater or equal to the cut-off angle, where the angle and distance are user-defined. Figure 5.5 represents the average number of hydrogen bonds between the DES-benzene pair per benzene molecule as a function of simulation time. We have used geometric criteria of hydrogen bond calculation as used in our previous studies [55], and the last 10 ns production run trajectory is considered for this computation of H-bonds.

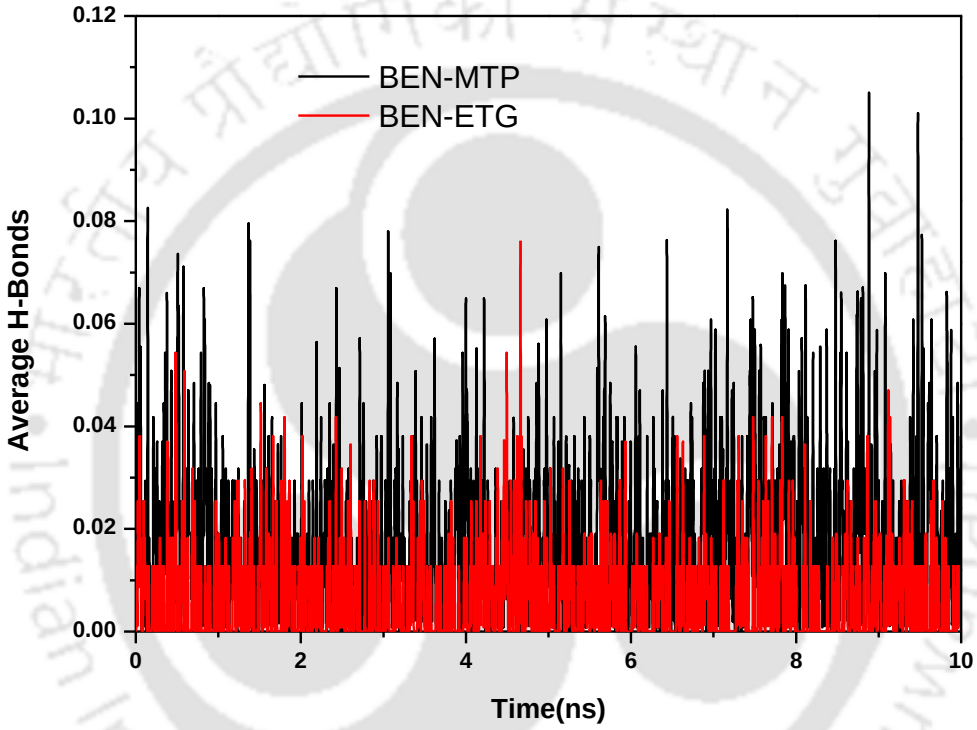

Figure 5.5. The average number of MTP−benzene and ETG−benzene hydrogen bonds per benzene molecule.

It should be noted that benzene forms a C−H···P1 bond with MTP at an average distance of ~3.0 Å. The same can be revealed from RDF (Figure 5.6), while the cut-off angle is taken from 10° to 180° for both the systems (MTP− benzene and ETG−benzene). Figure 5.5 shows that the HBD of DES (i.e., ETG) has a slightly higher number of H bonds with benzene molecules than its hydrogen bond acceptor (HBA) part, namely MTP. The presence of more hydroxyl groups in ETG acts as an active site for forming hydrogen bonds with the π electron cloud of benzene. Again, in between MTP−benzene and bromide−benzene molecules, MTP

forms a higher number of H bonds with benzene than bromide. The average number of H-bonds for bromide-benzene is significantly less than benzene-MTP and benzene-ETG due to the strong interaction of bromide with MTP cation. There are no significant hydrogen bonding interactions found between DES−hexane and hexane–benzene pairs. This also corroborated the lower solubility of hexane in DES, resulting in lower extraction efficiency.

5.3.3 Radial and Combined Distribution Function

The radial distribution functions (RDFs) give evidence about the entire assembly about the interactions between the different moieties of the system. These RDFs are shown in Figure 5.6. The atomic sites that are considered for calculating these pair correlation functions are C15 and P1 atom of MTP, Bromide ion (Br1), O1 and C7 atoms of ETG, C1 atomic site of benzene, and C9 atom of hexane (Figure 5.1). Figure 5.6a shows a strong first solvation peak for MTP-benzene, which refers to the interaction between HBA and benzene. Figure 5.8 for SDF indicates the fact that the bromide ion is uniformly distributed around the benzene molecule as compared to hexane. This is also observed from SDF, which is given in Figure 5.8a-f and later discussed in the spatial distribution function. The interaction between the benzene and hexane needs to be overcome by the DES moiety to extract benzene from hexane. Both RDF and SDF indicate a strong H-bond as the interacting moieties of the DES attract more significantly towards benzene than hexane. This is because benzene gave a more significant first g(r) peak with bromide than hexane, implying that the bromide ion also helps the extraction process along with the MTP cation. The BEN-HEX pair also does not show a very sharp peak because of the higher selectivity of DES towards benzene as compared to hexane.

It should be noted that the RDF of BEN-HEX would differ amid the DES solvent molecule, which is why we do not observe a sharp peak for the benzene-hexane system. The first solvation shell coordination number for the DES components with benzene, such as MTP-BEN, ETG-BEN, and BEN-Br, are 1.54, 1.04, and 2.9, respectively. The corresponding peaks

are in a range of 4-5 Å. However, for the BEN-HEX, the coordination number is 1.3, with a prominent peak at 7 Å.

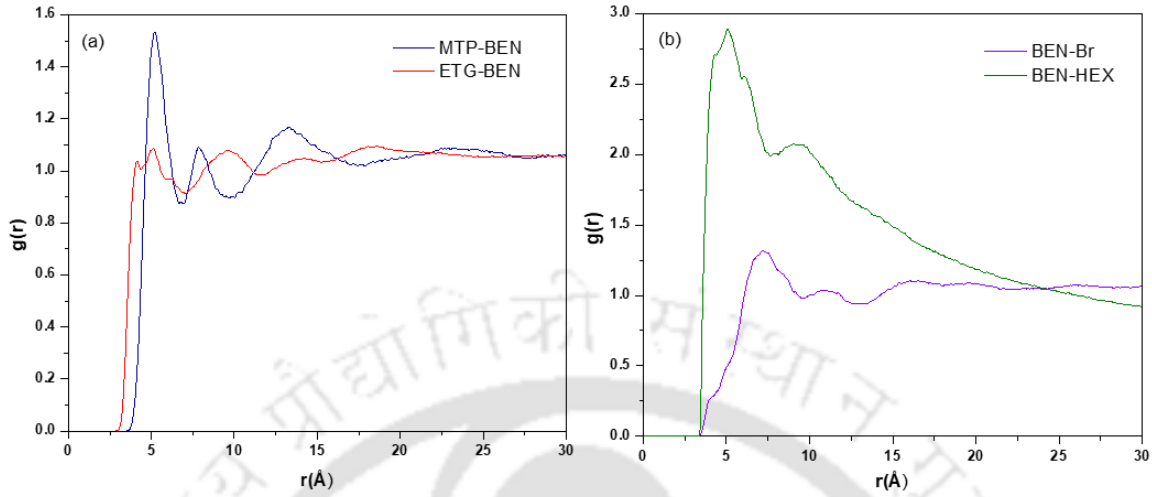

Figure 5.6. Atom−atom RDF plots between the different molecules present in the ternary system (a) MTP − benzene and ETG − benzene, (b) benzene − bromide and benzene – hexane.

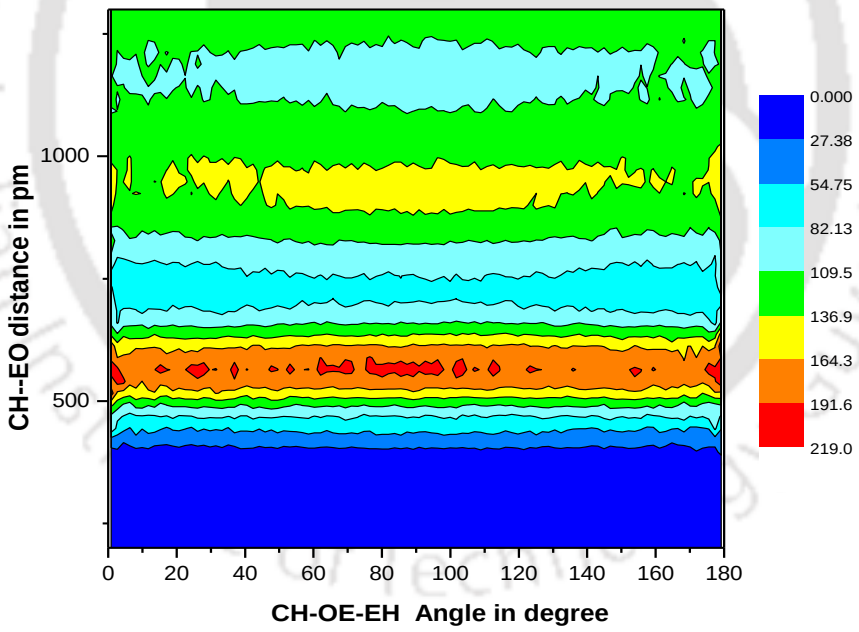

Figure 5.7. CDFs formed between the DES and benzene by plotting the hydrogen bond distance vs. hydrogen bond angle for C1−O1···H7 angle against the corresponding C1···O1 distance (BEN−ETG).

Further, the combined distribution functions (CDFs) were assessed to confirm the attraction of the DES-benzene pair. We have plotted the CDF in Figure 5.7, where the CDF

was plotted between the angular and radial function of benzene–ETG. The TRAVIS package was used for obtaining the SDF & CDF.

A detailed procedure is reported elsewhere [56]. From figure 5.7, we notice that the CH−EO⋯ EH bond was formed for both benzene-ETG pairs. These H bonds are formed in the range of ~3.0-5.0 Å (donor⋯acceptor) for the CH−OE⋯ EH throughout the system. Thus, it agrees with previous RDF peaks (figure 5.6), which are obtained at 4.15 Å for the ETG-benzene ionic pair of the systems.

5.3.4 Spatial Distribution Function

The spatial Distribution Function (SDF) details the average density distribution of different species around a reference centre molecule. Figure 5.8 shows the reference MTP and benzene molecules in the DES solution. These figures are obtained by using the TRAVIS package [56]. The uniform isovalues were used to plot the SDFs in all cases. The values of DES−benzene (1.5 Å) and MTP−hexane are 0.64 Å.

The SDF plots suggest that the phenyl group of MTP acts as an electron-withdrawing group and attracts a benzene electron cloud enabling it to form CH–π type with MTP. Benzene is also set to form a CH-OH or π–OH type hydrogen bond with ETG. The 2D NMR by cross-peaks and active benzene sites with DES components confirms this non-covalent interaction. Figure 5.8a-b shows that all the interactive moieties are highly distributed around the MTP molecule compared to other species.

Therefore, the interaction energy between the bromide−benzene pair is lower than that of MTP−benzene and ETG−benzene. Moreover, the appearance of the distribution of the ETG molecule around the benzene is closer than that of MTP. The positions of the first peaks of these RDFs appear for benzene-MTP and benzene-ETG at 4.95 and 5.15 Å, respectively. Furthermore, the densities of the bromide ion and hexane molecules are also distributed around the MTP (Figure 5.8a−e). The hexane molecules are distributed very far from the MTP

molecule (Figure 5.8d), which can also be confirmed from the RDF plot. Figure 5.8 f suggests that the ETG lies very close to the benzene moiety, initiating a higher interaction than hexane. Hence, it is evident that the isosurface of benzene is distributed around the active sites of DES, which implies that DES more effectively extracts the benzene molecules from the mixture. This SDF very much agrees with our previous sections, 5.4, where it supports the H-bonding and RDF calculation.

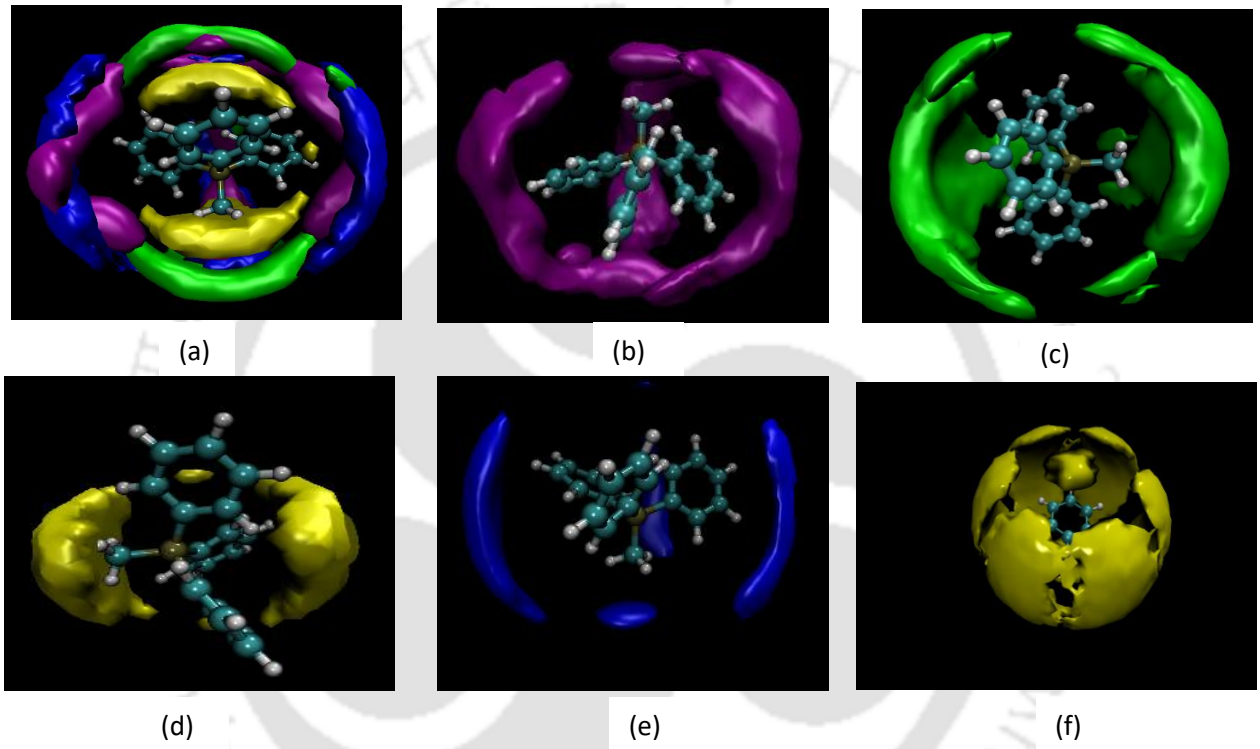

Figure 5.8. SDFs of the DES−benzene−hexane system. (a) Benzene, hexane, Br, and ETG around MTP, (b) Benzene around MTP, (c) Br around MTP, (d) ETG around the MTP molecule, (e) Hexane around the MTP molecule, (f) ETG around the benzene molecule. The violet, green, blue, and yellow surfaces refer to benzene, Br, hexane, and ETG, respectively.

5.3.5 Self-diffusion Coefficient and Mean Square Displacement

The self-diffusion coefficients in the system for the components are calculated by using the Einstein equation:

$$D = \frac{1}{6}\lim_{t\to\infty}\frac{d}{dt}\left\langle \sum_{i=1}^{N} \left|\mathrm{r}_i(t) - \mathrm{r}_i(0)\right|^2 \right\rangle \qquad (5.1)$$

Here, r_i(t) and r_i(0) represent the positions of the i^{th} atom at time t and 0, respectively. The slope of the system's mean square displacement (MSD) plot gives the self-diffusivity value. Figure 5.9 shows the MSD curves of the different species of the ternary system, and it shows that all MSD plots propagate linearly with time. The diffusion coefficient values for different types of molecules are calculated by averaging over time bounds of 10 ns (Table 5.7). This highlights the overall mass transfer process of benzene molecules from the hexane-rich phase to the DES-rich phase.

Table 5.7. Self-Diffusivity value of various moiety of the ternary systems at 318.15 K*

Molecule species	Diffusion coefficient × 10^{-9} m^2 s^{-1}	
	0−10 ns	90−100 ns
Bromide ion	0.464	0.197
MTP cation	0.350	0.135
Ethylene Glycol	0.491	0.190
Benzene	0.666	0.559
Hexane	0.809	1.000

*Values are reported for 10 ns time interval

The self-diffusion coefficient (D) values of all species of the system were comparatively close in the initial simulation stage of the production run at 0-10 ns. By the end of the simulation of the production run (90-100 ns), the values are lower for both benzene and DES components. The smaller diffusivity value of DES and benzene implies stability for extracted benzene within the DES phase, implying they move together.

The high diffusion coefficient value of hexane is nearly the same throughout the simulation, and it is separated from the DES phase with simulation time. The strong interactions between a benzene−MTP cation, benzene−bromide anion, and benzene−ETG (Table 5.7) cause a decrease in benzene diffusivity alone, or in other words, as discussed, gets itself attracted to DES. Due to weak interactions between benzene and hexane, the DES can extract the benzene effectively.

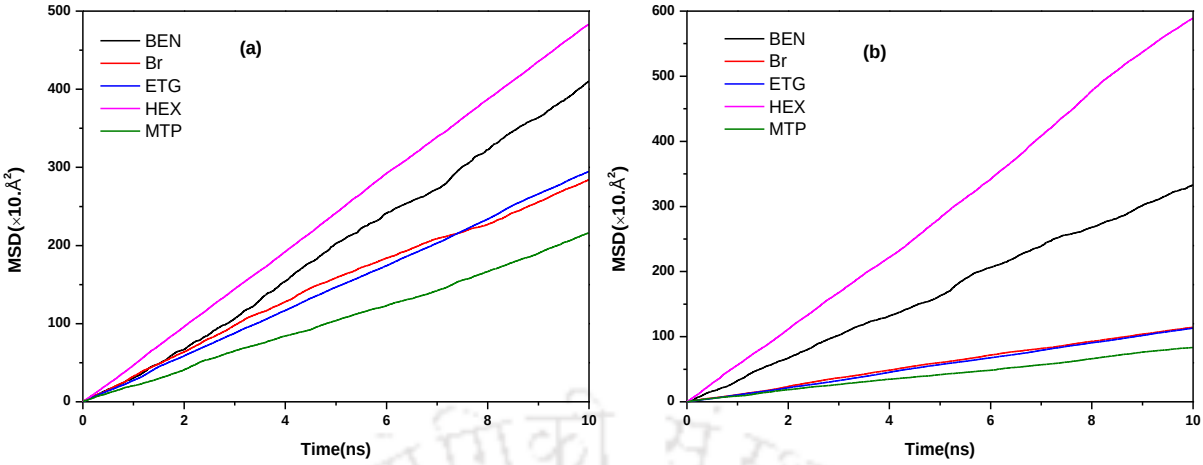

Figure 5.9. MSD curve of the system (a) 0-10 ns and (b) 90-100 ns.

5.3.6 2D-NMR Analysis

The 2D ^{1}H-^{13}C HMBC NMR was performed in order to investigate the hydrogen bonding interactions among components of DES and benzene (Figure 5.10). In the DES-benzene system, a stronger hydrogen bond exists among benzene, MTP, and ETG, confirmed by our MD simulation. In particular, a hydrogen bond of XH−π (X = C, O) type exists between benzene and DES. Further studies disclose that XH−π (BEN) systems such as benzene containing π-electrons can also contribute simply to the formation of XH−π bonds. The strength of such bonds depends on the nature of X attached to hydrogen. 4.10 shows the ^{1}H–^{13}C HMBC spectrum of DES-benzene in DMSO-d_6 at 318.15 K. From the figure, it is found that there exists a hydrogen-bond interaction between the ETG (OH)–π and MTP (CH)–π of benzene. The ^{1}H-^{13}C HMBC NMR provides long-range information for protons and carbons that are connected via one and multiple (up to four) bonds, respectively. From Figure 5.10, the ETG (CH), which resonates at 3.20 ppm, shows cross-peaks with BEN(C) at 120.15 ppm, and MTP (CH) at 7.75-ppm shows cross-peaks with BEN(C) at 120.5 ppm. These cross-peaks indicate that a strong multiple-bond correlation exists between the benzene and the interactive moiety of DES.

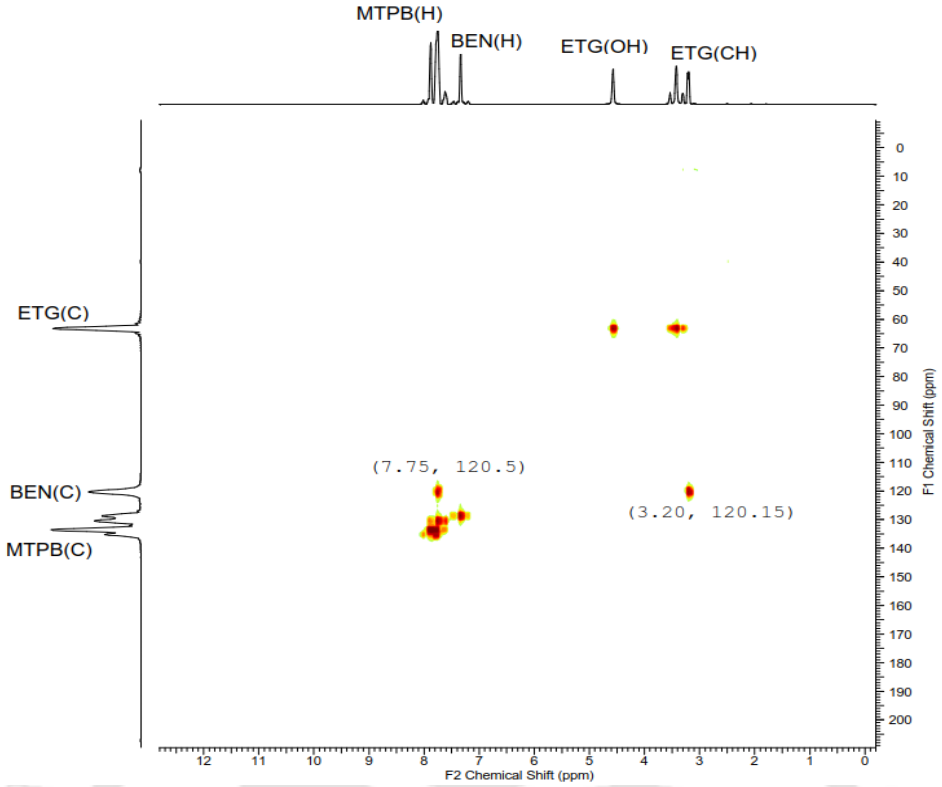

Figure 5.10. ^{1}H-^{13}C HMBC NMR spectra of DES-benzene.

Further, cross-peaks of benzene with ETG and MTP in 2D ^{1}H-^{13}C HMBC is also confirmed from figure 5.10 as it shows the presence of benzene in close vicinity of MTP, ETG, and bromine, so they are capable of forming hydrogen bonding. This is in line with the findings for RDF and CDF, as discussed in section 3.3, giving evidence of close interaction between DES and benzene. The individual ^{1}H and ^{13}C NMR spectra of the DES are provided in the chapter 3. The next chapter shall concentrated on the dispersion of asphtalene based component in crude oil. Here we shall observe the dispersion behvior of asphatelene structure in DES through QC and experiments.

5.4 Summary

The molecular dynamics simulation study was carried out to comprehend the phase equilibria of the DES−benzene−hexane ternary system employing their non-bonded interaction energy and structural properties. According to the interaction energy analysis, it was found that vdW energy plays a significant role compared to electrostatic interactions. Thus, the van der Waal interactions ensured the extraction of benzene from the DES−benzene-hexane mixture. In the ternary system, the DES-benzene pair possessed higher interaction energy than DES-hexane, and the RDF plots corroborated similar results. ETG-benzene gave a higher hydrogen bonding than MTP-benzene because of a higher number of hydroxyl groups present in ethylene glycol. The SDF results suggest that the surfaces of benzene are very closely distributed around the more active sites of HBA and HBD. The self-diffusivity value also suggests higher solubility of benzene in DES than hydrocarbon chain. 2D NMR spectra also confirmed the long-range interaction between the DES-benzene pair. In summary, the cation MTP of HBA and the HBD both play a predominant role in benzene extraction from the aliphatic hydrocarbon mixture. Consequently, this study offers new findings for the computational MD simulation of benzene extraction from hexane, which becomes helpful in the case of the absence of experimental data.

References

1. E. Newson, T. Truong, Low-temperature catalytic partial oxidation of hydrocarbons (C1–C10) for hydrogen production, International Journal of Hydrogen Energy 28 (2003) 1379-1386.
2. B.S. Rawat, I.B. Gulati, Liquid-liquid equilibrium studies for separation of aromatics, Journal of Applied Chemistry and Biotechnology 26 (1976) 425-435.
3. G.W. Meindersma, A. Podt, M.B. Klaren, AB De Haan, Separation of aromatic and aliphatic hydrocarbons with ionic liquids, Chemical engineering communications 193 (2006) 1384-1396.
4. M. Hossain, J.-S. Lee, D.-H. Kim, D.Q. Nguyen, M.-S. Cheong, H.-S. Kim, Ionic liquids as benign solvents for the extraction of aromatics, Bulletin of the Korean Chemical Society 33 (2012) 3241-3247.
5. A. Arce, M.J. Earle, H. Rodríguez, K.R. Seddon, Separation of benzene and hexane by solvent extraction with 1-alkyl-3-methylimidazolium bis {(trifluoromethyl) sulfonyl} amide ionic liquids: effect of the alkyl-substituent length, The Journal of Physical Chemistry B 111 (2007) 4732-4736.
6. C. Manohar, D. Rabari, A.A.P. Kumar, T. Banerjee, K. Mohanty, Liquid–liquid equilibria studies on ammonium and phosphonium based ionic liquid–aromatic–aliphatic component at T= 298.15 K and p= 1 bar: correlations and a-priori predictions, Fluid Phase Equilibria 360 (2013) 392-400.
7. P.K. Naik, P. Dehury, S. Paul, T. Banerjee, Evaluation of Deep Eutectic Solvent for the selective extraction of toluene and quinoline at T= 308.15 K and p= 1 bar, Fluid Phase Equilibria 423 (2016) 146-155.
8. H.F. Hizaddin, M.K. Hadj-Kali, A. Ramalingam, M. Ali Hashim, Extractive denitrogenation of diesel fuel using ammonium- and phosphonium-based deep eutectic solvents, The Journal of Chemical Thermodynamics 95 (2016) 164-173.
9. P.K. Naik, S. Paul, T. Banerjee, Physiochemical Properties and Molecular Dynamics Simulations of Phosphonium and Ammonium Based Deep Eutectic Solvents, Journal of Solution Chemistry 48 (2019) 1046-1065.
10. E.L. Smith, A.P. Abbott, K.S. Ryder, Deep eutectic solvents (DESs) and their applications, Chemical reviews 114 (2014) 11060-11082.
11. M.K. Hadj-Kali, S. Mulyono, H.F. Hizaddin, I. Wazeer, L. El-Blidi, E. Ali, M.A. Hashim, I.M. AlNashef, Removal of Thiophene from Mixtures with n-Heptane by Selective Extraction Using Deep Eutectic Solvents, Industrial & Engineering Chemistry Research 55 (2016) 8415-8423.
12. H.F. Hizaddin, M.K. Hadj-Kali, A. Ramalingam, M.A. Hashim, Extractive denitrogenation of diesel fuel using ammonium-and phosphonium-based deep eutectic solvents, The Journal of Chemical Thermodynamics 95 (2016) 164-173.
13. S. Mulyono, H.F. Hizaddin, I.M. Alnashef, M.A. Hashim, A.H. Fakeeha, M.K. Hadj-Kali, Separation of BTEX aromatics from n-octane using a (tetrabutylammonium bromide+ sulfolane) deep eutectic solvent–experiments and COSMO-RS prediction, RSC Advances 4 (2014) 17597-17606.

14. R. Verma, T. Banerjee, Liquid–liquid extraction of lower alcohols using menthol-based hydrophobic deep eutectic solvent: experiments and COSMO-SAC predictions, Industrial & Engineering Chemistry Research 57 (2018) 3371-3381.
15. R. Anantharaj, T. Banerjee, Liquid–liquid equilibria for quaternary systems of imidazolium based ionic liquid+ thiophene+ pyridine+ iso-octane at 298.15 K: experiments and quantum chemical predictions, Fluid Phase Equilibria 312 (2011) 20-30.
16. L. Gu, W. Huang, S. Tang, S. Tian, X. Zhang, A novel deep eutectic solvent for biodiesel preparation using a homogeneous base catalyst, Chemical Engineering Journal 259 (2015) 647-652.
17. H.-P. Steinrueck, P. Wasserscheid, Ionic liquids in catalysis, Catalysis Letters 145 (2015) 380-397.
18. H. Ohno, Electrochemical aspects of ionic liquids, John Wiley & Sons, 2005.
19. P.M. Fernandes, J.M. Campiña, N.M. Pereira, C.M. Pereira, F. Silva, Biodegradable deep-eutectic mixtures as electrolytes for the electrochemical synthesis of conducting polymers, Journal of Applied Electrochemistry 42 (2012) 997-1003.
20. NM. Pereira, C.M. Pereira, J.P. Araujo, A.F. Silva, Zinc electrodeposition from deep eutectic solvent containing organic additives, Journal of Electroanalytical Chemistry 801 (2017) 545-551.
21. C. Florindo, L.G. Celia-Silva, L.F. Martins, L.C. Branco, I.M. Marrucho, Supramolecular hydrogel based on a sodium deep eutectic solvent, Chemical communications 54 (2018) 7527-7530.
22. E. Durand, J. Lecomte, B. Baréa, G. Piombo, E. Dubreucq, P. Villeneuve, Evaluation of deep eutectic solvents as new media for Candida antarctica B lipase catalyzed reactions, Process biochemistry 47 (2012) 2081-2089.
23. P.K. Naik, M. Mohan, T. Banerjee, S. Paul, V.V. Goud, Molecular Dynamic Simulations for the Extraction of Quinoline from Heptane in the Presence of a Low-Cost Phosphonium-Based Deep Eutectic Solvent, The Journal of Physical Chemistry B 122 (2018) 4006-4015.
24. P.K. Naik, S. Paul, T. Banerjee, Liquid Liquid Equilibria measurements for the extraction of poly aromatic nitrogen hydrocarbons with a low cost Deep Eutectic Solvent: Experimental and theoretical insights, Journal of Molecular Liquids 243 (2017) 542-552.
25. J. Mahmoudi, M.N. Lotfollahi, (Liquid+ liquid) equilibria of (sulfolane+ benzene+ n-hexane),(N-formylmorpholine+ benzene+ n-hexane), and (sulfolane+ N-formylmorpholine+ benzene+ n-hexane) at temperatures ranging from (298.15 to 318.15) K: Experimental results and correlation, The Journal of Chemical Thermodynamics 42 (2010) 466-471.
26. M.A. Kareem, F.S. Mjalli, M.A. Hashim, I.M. AlNashef, Liquid–liquid equilibria for the ternary system (phosphonium based deep eutectic solvent–benzene–hexane) at different temperatures: A new solvent introduced, Fluid Phase Equilibria 314 (2012) 52-59.

27. N.R. Rodriguez, P.F. Requejo, M.C. Kroon, Aliphatic–Aromatic Separation Using Deep Eutectic Solvents as Extracting Agents, Industrial & Engineering Chemistry Research 54 (2015) 11404-11412.
28. U.K. Ravilla, T. Banerjee, Liquid liquid equilibria of imidazolium based ionic liquid+ pyridine+ hydrocarbon at 298.15 K: Experiments and correlations, Fluid Phase Equilibria 324 (2012) 17-27.
29. F.S. Oliveira, AB Pereiro, L.P. Rebelo, I.M. Marrucho, Deep eutectic solvents as extraction media for azeotropic mixtures, Green Chemistry 15 (2013) 1326-1330.
30. P. Dehury, U. Mahanta, T. Banerjee, Partitioning of butanol between a hydrophobic ionic liquid and aqueous phase: Insights from Liquid Liquid Equilibria measurements and Molecular Dynamics simulations, Fluid Phase Equilibria 425 (2016) 421-431.
31. R. Verma, M. Mohan, V.V. Goud, T. Banerjee, Operational Strategies and Comprehensive Evaluation of Menthol Based Deep Eutectic Solvent for the Extraction of Lower Alcohols from Aqueous Media, ACS Sustainable Chemistry & Engineering 6 (2018) 16920-16932.
32. S.L. Perkins, P. Painter, C.M. Colina, Experimental and computational studies of choline chloride-based deep eutectic solvents, Journal of Chemical & Engineering Data 59 (2014) 3652-3662.
33. M. Mohan, P.K. Naik, T. Banerjee, V.V. Goud, S. Paul, Solubility of glucose in tetrabutylammonium bromide based deep eutectic solvents: Experimental and molecular dynamic simulations, Fluid Phase Equilibria 448 (2017) 168-177.
34. S. Jayaraman, Computing thermodynamic and transport properties of room temperature ionic liquids and molten salts from atomistic simulations, University of Notre Dame2010.
35. P.K. Naik, S. Paul, T. Banerjee, Thermal Hydrogenation and Degradation of Quinoline from Reactive Force Field Simulations, ChemistrySelect 4 (2019) 12996-13005.
36. AT Celebi, T.J. Vlugt, O.A. Moultos, Structural, Thermodynamic and Transport Properties of Aqueous Reline and Ethaline Solutions from Molecular Dynamics Simulations, The Journal of Physical Chemistry B DOI (2019).
37. S. Stephenson, R. Offeman, G. Robertson, W. Orts, Ethanol and water capacities of alcohols: a molecular dynamics study, Chemical engineering science 61 (2006) 5834-5840.
38. M. Taha, M.-J. Lee, TES buffer-induced phase separation of aqueous solutions of several water-miscible organic solvents at 298.15 K: Phase diagrams and molecular dynamic simulations, The Journal of chemical physics 138 (2013) 244501.
39. M. Frisch, G. Trucks, H. Schlegel, G. Scuseria, M. Robb, J. Cheeseman, G. Scalmani, V. Barone, B. Mennucci, G. Petersson, Gaussian 09 Program; Gaussian, Inc, Wallingford, CT DOI (2009).
40. W. Kohn, A.D. Becke, R.G. Parr, Density functional theory of electronic structure, The Journal of Physical Chemistry 100 (1996) 12974-12980.
41. C.I. Bayly, P. Cieplak, W. Cornell, P.A. Kollman, A well-behaved electrostatic potential based method using charge restraints for deriving atomic charges: the RESP model, The Journal of Physical Chemistry 97 (1993) 10269-10280.

42. D. Case, T. Darden, T. Cheatham, C. Simmerling, J. Wang, R. Duke, R. Luo, R. Walker, W. Zhang, K. Merz, Amber 12 reference manual, University of California, San Francisco DOI (2012).
43. J. Wang, R.M. Wolf, J.W. Caldwell, P.A. Kollman, DA Case, Development and testing of a general amber force field, Journal of computational chemistry 25 (2004) 1157-1174.
44. J. Wang, W. Wang, P.A. Kollman, DA Case, Automatic atom type and bond type perception in molecular mechanical calculations, Journal of molecular graphics and modelling 25 (2006) 247-260.
45. L. Martínez, R. Andrade, E.G. Birgin, J.M. Martínez, PACKMOL: a package for building initial configurations for molecular dynamics simulations, Journal of computational chemistry 30 (2009) 2157-2164.
46. J.C. Phillips, R. Braun, W. Wang, J. Gumbart, E. Tajkhorshid, E. Villa, C. Chipot, R.D. Skeel, L. Kale, K. Schulten, Scalable molecular dynamics with NAMD, Journal of computational chemistry 26 (2005) 1781-1802.
47. S. Nosé, A unified formulation of the constant temperature molecular dynamics methods, The Journal of chemical physics 81 (1984) 511-519.
48. W.G. Hoover, Canonical dynamics: equilibrium phase-space distributions, Physical review A 31 (1985) 1695.
49. P.H. Hünenberger, Thermostat algorithms for molecular dynamics simulations, Advanced computer simulation, Springer2005, pp. 105-149.
50. S.E. Feller, Y. Zhang, R.W. Pastor, B.R. Brooks, Constant pressure molecular dynamics simulation: the Langevin piston method, The Journal of chemical physics 103 (1995) 4613-4621.
51. H.C. Andersen, Rattle: A "velocity" version of the shake algorithm for molecular dynamics calculations, Journal of Computational Physics 52 (1983) 24-34.
52. U. Essmann, L. Perera, M.L. Berkowitz, T. Darden, H. Lee, L.G. Pedersen, A smooth particle mesh Ewald method, The Journal of chemical physics 103 (1995) 8577-8593.
53. I. Zeron, J. Abascal, C. Vega, A force field of Li+, Na+, K+, Mg2+, Ca2+, Cl−, and SO 4 2− in aqueous solution based on the TIP4P/2005 water model and scaled charges for the ions, The Journal of chemical physics 151 (2019) 134504.
54. M.F. Döpke, O.A. Moultos, R. Hartkamp, On the transferability of ion parameters to the TIP4P/2005 water model using molecular dynamics simulations, The Journal of Chemical Physics 152 (2020) 024501.
55. G. Borgohain, S. Paul, Temperature-mediated switching of protectant-denaturant behavior of trimethylamine-N-oxide and consequences on protein stability from a replica exchange molecular dynamics simulation study, Molecular Simulation 43 (2017) 52-64.
56. M. Brehm, B. Kirchner, TRAVIS-a free analyzer and visualizer for Monte Carlo and molecular dynamics trajectories, Journal of Chemical Information and Modeling 51 (2011) 2007–2023.

CHAPTER 6

Asphaltene Dispersion using the Novel Deep Eutectic Solvents

Dispersion of asphaltene in crude oil is considered a viable solution and significantly changes their viscosity throughout the operation, transportation, and refinement. The present study aims to investigate the mechanism of inhibition of petroleum asphaltene aggregation using a novel combination of deep eutectic solvents (DESs). Deep eutectic solvents have recently gained increasing interest as green solvents to address the issue of asphaltene aggregation. The selection of the molecular model structure of the asphaltene is a crucial step in the molecular simulations to screen potential solvents for asphaltene dispersion. The reliable chemical structure of asphaltene was identified by performing quantum chemical calculations. Further, the COSMO-RS (Conductor-like Screening Model for Real Solvents) model was performed to screen the hundreds of DESs for asphaltene and found that the DES composed of thymol and phenyl rings based were the most promising solvents. After successful DES screening, the COSMO-RS predictions were further validated by performing the experiments. Among the studied DES, thymol-diphenyl ether DES showed higher solubility of asphaltene, and the agreement between experimental and the COSMO-RS predicted thermodynamic properties are excellent. In addition, the Fourier transform infrared (FT-IR) spectroscopy and Nuclear Magnetic Resonance (NMR) techniques were used to characterize the structural interactions between asphaltene and DESs and observed the strong interaction between asphaltene and DES are responsible for the higher asphaltene dispersion. The present study approach paved the way forward to rationally design and understand the impact of structural variation of DESs on their interaction with asphaltene. The penultimate part of this chapter discusses the quantum chemical calculations between the solvents and asphaltene, which reveals that dispersion and van der Waals force interaction are mainly responsible for the higher dispersion.

6.1 Introduction

In the previous chapters, we have primarily seen the extraction of aromatic solutes with and without heteroatom through LLE experiments and atomistic MD insights. The penultimate chapter discusses a relevant topic related to petroleum asphaltene dispersion in DESs. Crude oil is composed of a variety of hydrocarbons, of which the main constituents include saturates, asphaltene, resins, and aromatics (SARA components). Among the SARA components, the heaviest component, asphaltene, is problematic in terms of processing and transportation in the energy sector [1]. Asphaltene precipitates during transportation, plugging the downstream pressure vessels and blocking the reservoir porosity. The different natures of the composition of asphaltene, despite their origin, share a common structural attribute, i.e., strong aromaticity, high polarity, a low H/C ratio, and the inclusion of heteroatoms (e.g., S, N, and O) and porphyrins (a complex ring system). Asphaltene contains a higher number of alky chains attached to their aromatic rings and possess a more substantial intramolecular van der Waals interaction, hydrogen bonds [2], π—π stacking [3, 4], acid-base interactions, electrostatic interactions, and repulsive steric interactions [5-8].

These stronger intramolecular interactions within the asphaltene molecule are responsible for agglomeration and are the least understood of asphaltene structure, which causes additional complications. The polycyclic aromatics, heteroatoms, and polar functional groups have a role in asphaltene bulk flow characteristics. It starts to agglomerate during crude oil recovery and transportation when pressure, temperature, and chemical variations alter the crude oil thermodynamic stability [9, 10]. As a result, it creates a problem during crude oil production by precipitation of asphaltene [11]. In an attempt to avoid the agglomeration that occurs in crude oil production, lots of research have been undertaken to investigate the chemical nature of asphaltene. Mutelet et al. [12] reported that petroleum asphaltene could act as a strong hydrogen-bond acceptor but a weak hydrogen bond donor. Furthermore, Wu et

al.[13] studied the interaction between asphaltene resin and crude oil by considering resins and asphaltene as solutes dispersed in crude oil with the effect of varying temperature and pressure. Transporting, aggregation, and refining process of asphaltene crude oil as feedstock is the critical challenge in the global oil and gas sector. Asphaltene crude oil as feedstock is the critical challenge in the global oil and gas sector.

Stability and aggregation inhibition of asphaltene in crude oil can be achieved by using a variety of organic solvents such as toluene and xylene. However, these aromatic solvents are volatile and harmful to the environment. In addition, the mixing of alternative solvents such as amines and alkyl benzene sulfonic acid, significantly enhanced the asphaltene precipitation inhibition *via* acid-base interactions. However, the asphaltene-amphiphilic interactions are the electrophilic addition reaction which makes the irreversible bond formation between acid-bases and precipitates in a non-polar medium. Recently, ionic liquids (ILs) have been proven to be potential solvents for asphaltene inhibition aggregation, however, the cost of ILs is higher, and multiple steps are involved in the synthesis process. Therefore, there is no economical technique to prevent asphaltene agglomeration in different crude oil operations. Their efficacy and usefulness have been questioned, but they are oil-soluble.

Ionic liquids (ILs), salts with melting temperatures below 100 °C, have a range of desirable features, including high thermal stability, chemical stability, and the capacity to tune the solubility of complex compounds by varying the cation and anion as per requirement. Asphaltene dissolution often necessitates a substantial concentration of ILs for instance, a recent work by Zheng et al. [14] found an asphaltene to ILs ratio of 1:200 demonstrated a dissolution capacity of a phosphonium-based ILs. Even though they are ideal solvents, still it is challenging to synthesize and relatively costlier than conventional solvents. In this context, a sustainable green, and eco-friendly approach for asphaltene dissolution relies on deploying a class of novel solvents known as natural deep eutectic solvents (NADESs) or eutectic solvents.

Abbott et al. [15] initially proposed deep eutectic solvents(DESs), which are formed through two or more compounds capable of forming strong hydrogen bond interactions and allowing a considerable negative deviation in the melting temperature of the mixture from their individual melting points[16]. Several DESs combinations form a clear transparent liquid at ambient conditions and can be employed as solvents in various applications. Generally, DESs are composed of two components: hydrogen bond acceptor (HBA) and hydrogen bond donor (HBD), which contrasts with conventional solvents. These emerging solvents offer low cost, low toxicity, biodegradability, low vapour pressure, and ease of synthesis. When it comes to asphaltene precipitation inhibition, Kashefi et al. [17, 18] studied the choline chloride: phenylacetic acid-based deep eutectic solvents for asphaltene dispersion. Further, the delay in asphaltene precipitation was also found using the choline chloride-based DESs. Jahangiri and coworkers[18] reported similar results using choline chloride: mono ethylene glycol-based DESs, known as ethaline.

Recently, despite many efforts by the scientific community, the most precise and accurate molecular structure of the most known complex asphaltene remains unresolved. The research on asphaltene turned to depend on the model compounds that resemble asphaltene structure based on their source and composition of crude. It should be noted that the composition of asphaltene changes with the source of crude oil. They used model structure to understand the aggregation behaviour and involved molecular-level interaction chemistry. The fundamentals of asphaltene dissolution mechanisms have been limited to a few studies focusing on asphaltene model structure change with different inhibitors, thereby preventing precipitation.

Therefore, the present study focuses on screening deep eutectic solvents for asphaltene precipitation inhibition using the COSMO-RS model. In addition, the current study also aims to evaluate an accurate molecular model structures for computational calculations. First, the

chemical structure of asphaltene was confirmed by performing Fourier transform infrared (FT-IR) spectroscopy and quantum chemical calculations. Further, several combinations of HBAs and HBDs of DESs were screened using the COSMO-RS model by calculating the thermodynamic properties and rank the solvents based on their capability of interaction. Thereafter, the experimental solubility measurement was performed to verify the COSMO-RS results, and the recovered asphaltene was further characterized using FTIR and nuclear magnetic resonance (NMR) techniques to understand the molecular interactions and solubility mechanism of asphaltene in DES. The penultimate part of this chapter discusses the (Density Functional Theory) DFT, (Non-covalent Interaction) NCI, and (Quantum Theory of Atom in Molecule) QTAIM analysis to understand the interaction mechanism between the asphaltene and DESs.

6.2 Experimental Section

6.2.1 Materials

The list of chemicals used in this study are reported in Table 1. Chemicals are used without further purification as received from the supplier.

Table 6.1. The List of chemicals used in the solubility of asphaltene experiments.

Compound Name	Purity (mass fraction %)	CAS No.	Supplier	Product from
Thymol	≥99.5 %	89-83-8	Sigma Aldrich	India
Biphenyl	≥95	92-52-4	Sigma-Aldrich	India
Diphenyl ether	≥95	101-84-1	Sigma-Aldrich	India
Camphor	≥95	464-49-3	Sigma-Aldrich	India
Decanoic acid	≥95	334-48-5	TCI India	India
Toluene	99%	108-88-3	TCI India	India
Hexane	99%	110-54-3	TCI India	India

Dimethyl sulfoxide (DMSO)	≥99.8%	2206-27-1	Sigma Aldrich	India
Chloroform ($CdCl_3$)	99.9 %	865-49-6	Sigma Aldrich	India

6.2.2 Preparation of DESs

The DESs were prepared by mixing the hydrogen bond acceptor (HBA: thymol) and hydrogen bond donors (HBDs: diphenyl ether, biphenyl, and camphor) at specific molar ratios from 1:1 to 7:3. The HBA and HBD mixture were placed in the flat bottom flask and heated in an oil bath at 333.15 ± 0.01 K with a constant stirring speed of 350 rpm until a transparent liquid was formed [20]. The detailed procedure to prepare the DESs is given elsewhere [21]. The obtained DESs were vacuum dried at 510 mbar and 335.15 K overnight to remove any moisture content.

6.2.3 Extraction of Asphaltene from Crude Oil

Asphaltene was extracted with the addition of heptane to crude oil in a 40:1 v/v volumetric ratio under ambient conditions by following the ASTM-D6560-17R standard procedure [22]. The mixture was then filtered under vacuum using 0.2 µm pore size Whatman filter paper. Further, the filter cake was repeatedly washed with *n*-heptane to remove any resins until the effluent from the filter became colourless. Finally, the asphaltene was recovered from the filter cake by dissolution in toluene and then dried through evaporation at 35°C overnight to remove all solvents and impurities, including water. The resulting asphaltene sample was then placed in an airtight vial and stored in a dry place at ambient conditions for further experimental use. The resulting asphaltene sample was then placed in an airtight vial and stored in a dry place at ambient conditions for further experimental use.

6.2.4 Asphaltene Solubility Assays

Solubility was determined by taking an excess amount of asphaltene and adding it to 1 ml of NADESs at 298.15 K and atmospheric pressure. The vials were sealed and placed in an

aluminium block holder. This was transferred to a heating plate temperature control (PT100) with a magnetic stirrer (series H03D from LBX Instruments). The mixtures were magnetically stirred at a constant rpm for at least 12 hr. at 298.15 K and 1 atm pressure. After saturation, the stirring was stopped, and the excess solid was allowed to settle at the bottom. The samples were kept under agitation until reaching a saturation state and then filtered using polytetrafluoroethylene filters (0.2 μm pore size) to remove the undissolved fraction of asphaltene. All solubility tests were performed in duplicate to confirm the accuracy.

The asphaltene solubility was calculated by equation 1, where m_{ASP} and m_{NADESs} represent the weight of asphaltene and NADESs, respectively.

$$\text{Asphaltene wt.\%} = \frac{m_{ASP}}{m_{NADESs}} \times 100 \qquad (6.1)$$

6.3 Analysis and Characterisation Methods

6.3.1 Nuclear Magnetic Resonance (NMR)

The NMR analysis (Bruker Advance-600 MHz instrument, Germany) was used to confirm the purity and presence of various constituents in the synthesized neat NADESs after mixing the asphaltene in NADESs. The DMSO-d_6 and $CdCl_3$ were used as the deuterated solvents in NMR tubes that were adequately sealed with a cap for the ^{1}H and ^{13}C 1D-NMR and 2D-NMR analysis. The purity of NADESs was quantified by integrating the ^{1}H NMR spectra and comparing it with the initial molar ratio composition of its constituents. The chemical shifts for pure deuterated solvents DMSO-d_6 peak (H = 2.50 ppm) and $CdCl_3$ peak (H = 7.27 ppm) are assigned a priori. The experiments were performed at 298.15 K, using different amounts of asphaltene samples diluted in 0.6 mL of deuterated solvents.

6.3.2 FTIR-ATR

The Fourier Transform Infrared (FTIR) spectra of pure asphaltene and asphaltene+NADESs samples were obtained using the Perkin Elmer Spectrum 6700 with a horizontal Golden Gate attenuated total reflection (ATR) with diamond crystals installed. With a resolution of 4 cm^{-1}

for each sample, 32 scans were taken in absorbance units. The wavenumber ranged from 4000 to 400 cm^{-1} for the studied samples.

6.4 Computational Details

6.4.1 Molecular Quantum Chemistry Computation

The initial geometries of different compounds, i.e., thymol, biphenyl, diphenyl ether, decanoic acid, camphor, and different model asphaltene structures, were drawn using gauss view 5.0 [23]. The initial geometries of molecules were optimised at B3LYP (Becke 3-parameter hybrid functional combined with the Lee-Yang–Parr correlation) theory with functional incorporating the dispersion correction 3-D basis set 6-311+G (d, p). The frequency calculations were also carried out to ensure that the optimised structures and energy minima did not possess any negative frequency.

6.4.2 COSMO-RS Model

The quantum chemical calculations were used to optimise the geometries of all compounds, as given in the earlier section. The BVP86/TZVP/DGA1 level of theory was used to generate the COSMO file after the geometry optimization was completed using the DFT calculation. The combination of TZVP and DGA1 basis sets allows the electron density to adjust spatially to the extent appropriate to the particular molecular environment. Finally, using the same BVP86 theory, the ideal screening charges were calculated using the keyword "scrf = COSMORS" on the molecular surface [24, 25] using COSMO logic (version 19.0.1, Leverkusen, Germany) [26]. For the sigma profiles and sigma potentials of the isolated molecules, BP TZVP parametrization was used to calculate excess enthalpy (H^E) and logarithmic activity coefficients ln (γ) of mixtures. The model asphaltene and the NADES compounds were assigned 0.2 and 0.8-mole fractions, respectively, within the COSMO-RS calculations for screening calculations. Accordingly, the logarithmic activity coefficients and excess enthalpy

values were calculated for the given respective systems. The heat of mixing or the excess enthalpy was also calculated using equation 2 [27].

$$H_M^E = \sum x_i H_i^E = \sum x_i \left[H_{i,mixture} - H_{i,pure}\right] \quad (6.2)$$

The difference in enthalpy between components of the pure state and that of the mixture, H_M^E used is used to denote the excess enthalpy of the mixture. The excess enthalpy of a mixture is a summation of different types of interaction energies, such as electrostatic misfit, hydrogen bonding, and van der Waals forces, as given in equation 3.

$$H_M^E = H_M^E(misfit) + H_M^E(Hydrogen\ bond) + H_M^E(vdW) \quad (6.3)$$

In addition, the activity coefficient of component *i* is related to the chemical potential μ_i as given in equation 4 [28]:

$$\ln(\gamma_i) = \left(\frac{\mu_i - \mu_i^{\circ}}{RT}\right) \quad (6.4)$$

Where μ_i^0 is the chemical potential of the pure component *i*, *R* is the real gas constant, and *T* is the absolute temperature. More details of COSMO-RS calculation in predicting the excess enthalpies and activity coefficients are provided in the COSMOtherm's user manual [29].

6.5 Result and Analysis

6.5.1 Asphaltene Structure Validation using the Density Functional Theory

The density functional theory (DFT) calculation is a potential tool in computational chemistry for predicting the complex structures of unknown compounds such as asphaltene. In the last decade, significant progress has been achieved in developing novel DFT techniques that can be used in existing quantum-chemical computing systems. The spectroscopic DFT theory aids in predicting the most accurate molecular structure by comparing the wavelength or intensity of the different functional groups present in the experimentally obtained FT-IR spectra. As a

tool to provide significant insights into the structure of asphaltene, infrared spectroscopy is the most effective technique as it reveals the compositional features of compounds in terms of different functional groups present in the sample.

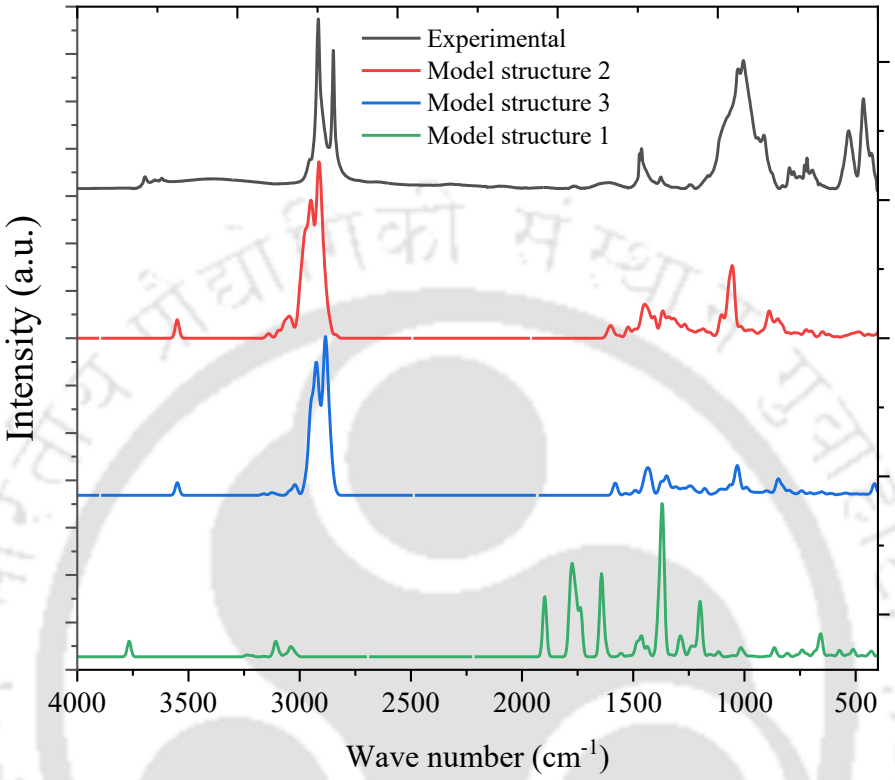

Figure 6.1. The Correlation between quantum chemical calculated and experimental IR spectra of asphaltene with different starting model structures of asphaltene. DFT calculations were calculated at B3LYP theory and 6-311+G (d, p) basis set.

COSMO-RS model-based screening of NADESs requires the most accurate molecular structure to predict the thermodynamic physical properties, which can be verified by benchmarking results by comparing conventional solvents. Therefore, selecting the model structure of asphaltene is critical for screening NADESs that can efficiently dissolve the heavy complex fraction found in crude oil. The various forms of asphaltene structure models have been presented and employed in molecular modeling via instrumental detection in recent decades [30-32]. There is no fixed molecular structure for asphaltene as it changes with the source of crude oil. Still, different structures with similar elemental compositions are currently being used for different applications[14].

(a) Model structure 1

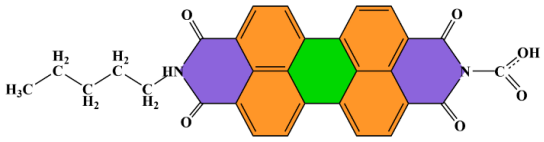

(b) Model structure 2

(c) Model structure 3

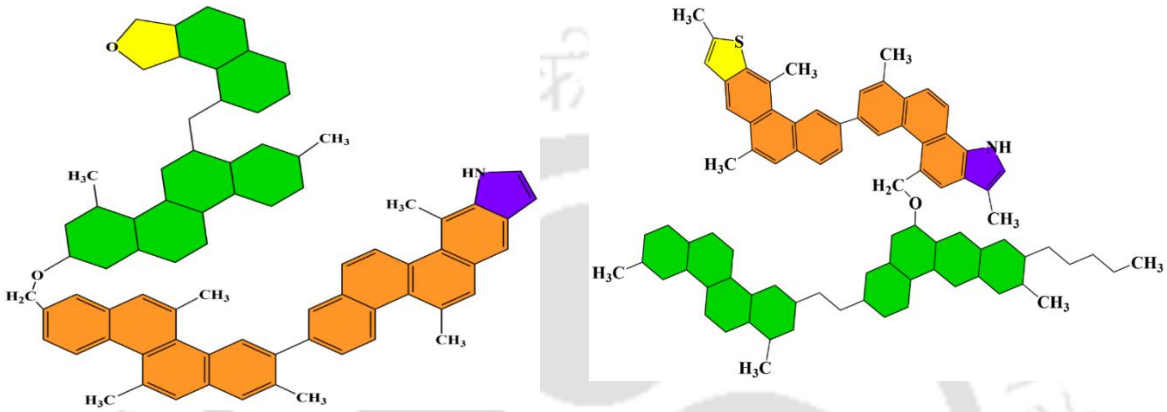

Figure 6.2. The different model structures of asphaltene are used for screening potential NADESs.

Here, we predicted the most suitable structure from the proposed model structure based on the archipelago model as proposed by Mullins [32]. Thereafter, the spectroscopic investigation of asphaltene extracted from crude oil was compared with the available island structure from the literature[19]. The theoretically calculated IR spectra were compared with experimentally obtained FTIR spectra of the asphaltene compound. The different stretching for the groups, i.e., O─H, C─H, N=H, C=O, C─C, C─H_3, and C─H_2 vibrations, can be observed in figure 6.1. It can be confirmed that the IR spectra of model structure 3 closely resemble the FT-IR spectra of extracted asphaltene sample. The hydroxyl group here is either free or non-hydrogen bonded as the O─H group vibrations have a characteristic range of 3000–3600 cm^{-1} [33]. The O─H stretching vibration was found to be 3582 cm^{-1} for the model structure of asphaltene. Thus, an excellent agreement was obtained between the theoretically predicted frequencies for the O─H vibration and experimentally obtained FTIR spectra[34] [35].

Vibration modes in the C=O bond we have theoretically calculated at 1355 cm^{-1} are in close agreement with those found empirically at 1371 cm^{-1}. Overall, the calculation of theoretical vibrational frequencies and their comparison with experimental IR spectra helps us to assign and interpret infrared spectra, which is especially important in complex molecules such as asphaltene.

The fingerprint region peak at $2920 \pm 10\ cm^{-1}$ corresponds to CH_2 stretching in aliphatic bonds (C─H asymmetric). It is the most intensive peak in the spectrum and corresponds to the methylene functional group. The peak at $2850 \pm 10\ cm^{-1}$ represents the CH_2 stretching in aliphatic (C─H symmetric) bonds that correspond to the methylene group. Both peaks exactly match in both experimental spectra as well as with simulated IR spectra. Therefore based on the theoretical prediction model structure, 3 was selected to screen NADESs for dispersion of Asphaltene.

6.5.2 Thermodynamic Screening of DESs

The excess enthalpy (H^E) and logarithmic activity coefficients ln (γ) are two thermodynamic parameters that may be useful in predicting asphaltene solubility for the designed neoteric solvents. The H^E is a valuable thermodynamic parameter for examining the strength of interactions between asphaltene and moieties of NADESs, such as hydrogen bond acceptor (HBA) and hydrogen bond donor (HBD). In contrast, ln (γ) values are frequently used to indicate the dissolving power of NADESs for asphaltene quantitatively. In previous investigations, ln (γ) and H^E were effectively used to predict the solubility of lignin in molecular solvents and were described as the most critical parameter in determining a solvent's capacity for delignification[36, 37]. Therefore, after the prediction of the most relevant model structure of asphaltene, as shown in figure 6.1, the COSMO-RS screening was performed on different structures using different pairs of HBA and HBD with different molar ratios. This aided us in quantifying the dissolution of asphaltene extracted from the crude oil.

The screening results directly correlate with the more negative values of both H^E and ln (γ). The thymol-based solvents were selected for further experimental investigation, and a list of different pairs of NADESs is given in table 6.2. Overall, the screening data suggest that a general rule can be postulated that solvents that enable high asphaltene solubility with cut-off values in the range of $H^E \leq 0.26$ and ln (γ) lies lower than (negative value) -0.51. These cut-off values were selected by benchmarking the excess enthalpy and activity coefficient values for the asphaltene model structures with conventional solvents such as toluene and xylene. These conventional solvents were chosen for benchmarking as asphaltene was found to be soluble and used industrially to dissolve the heavy fraction of crude oil. The potential solvents were selected based on cut-off values for conventional solvents in terms of predicted values of H^E and ln (γ) parameters. From the screening results, the hydrophobic DESs such as thymol: diphenyl ether (1:1), thymol: biphenyl (1.6:1), biphenyl: cadaverine (1:5.66), 2-methylquinoline: cadaverine (1:3.34), thymol: decanoic acid (3:2 and 1:1), and thymol: camphor (7:3) were seen to be potential solvents for asphaltene dissolution than other DESs. Therefore, as in experiments, all the selected NADESs gave a better solubility parameter. The COSMO-RS screening reveals that the relationship between NADESs and asphaltene dissolving power does not show any fixed pattern in asphaltene dissolution. The non-linear relationships are more suited to describe experimental results when mass transport and viscosity of solvents play a crucial role in solubility. However, these developed asphaltene solubilities with non-linear models could be applicable for thymol-based solvents only when $H^E \leq 0.26$ and ln (γ) ≤ -0.51. This value compares with conventional solvents such as toluene and xylene. After the screening, the probable solvents were selected for the experimental study, as depicted in table 6.2, to demonstrate the molecular level chemistry for asphaltene dispersion at higher concentrations. Figure 6.3 displays the thymol-based NADESs, including thymol as the HBA and camphor, decanoic acid, biphenyl, and diphenyl ether as the

HBD, respectively. Table 6.2 shows the composition of NADESs synthesised and the experimental analysis of solvation.

Table 6.2. Potential Solvents of Asphaltene dissolution after COSMO-RS Screening used in experimental analysis.

Abbreviation	HBA	HBD	Molar Ratio	Before Stirring	After Stirring
DES1	Thymol	Diphenyl ether	1:1		
DES2	Thymol	Biphenyl	0.62:0.38		
DES3	Thymol	Camphor	7:3		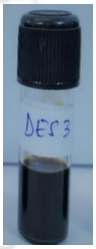
DES4	Thymol	Decanoic acid	3:2		

6.5.3 Asphaltene Solubility in NADESs

The solubility values of asphaltene in NADESs are presented in figure 6. 4. The DES1 gives the best performance for asphaltene solubility, reaching a value of 42.10 ± 0.58 mg/ml asphaltene solubility at 298.15 K and atmospheric pressure compared to the rest of the solvents. The asphaltene solubility was found to be significant in the influence of hydroxyl groups

present in HBD of NADESs interactions with asphaltene have been extensively studied through FT-IR and 2D-NMR. The aromatic ring compounds contribute to the solvent interaction with asphaltene through conjugation to inhibit intramolecular π–π interactions within the asphaltene moiety. It is to be noted that the intramolecular interaction among different asphaltene active sites leads to agglomeration in crude oil.

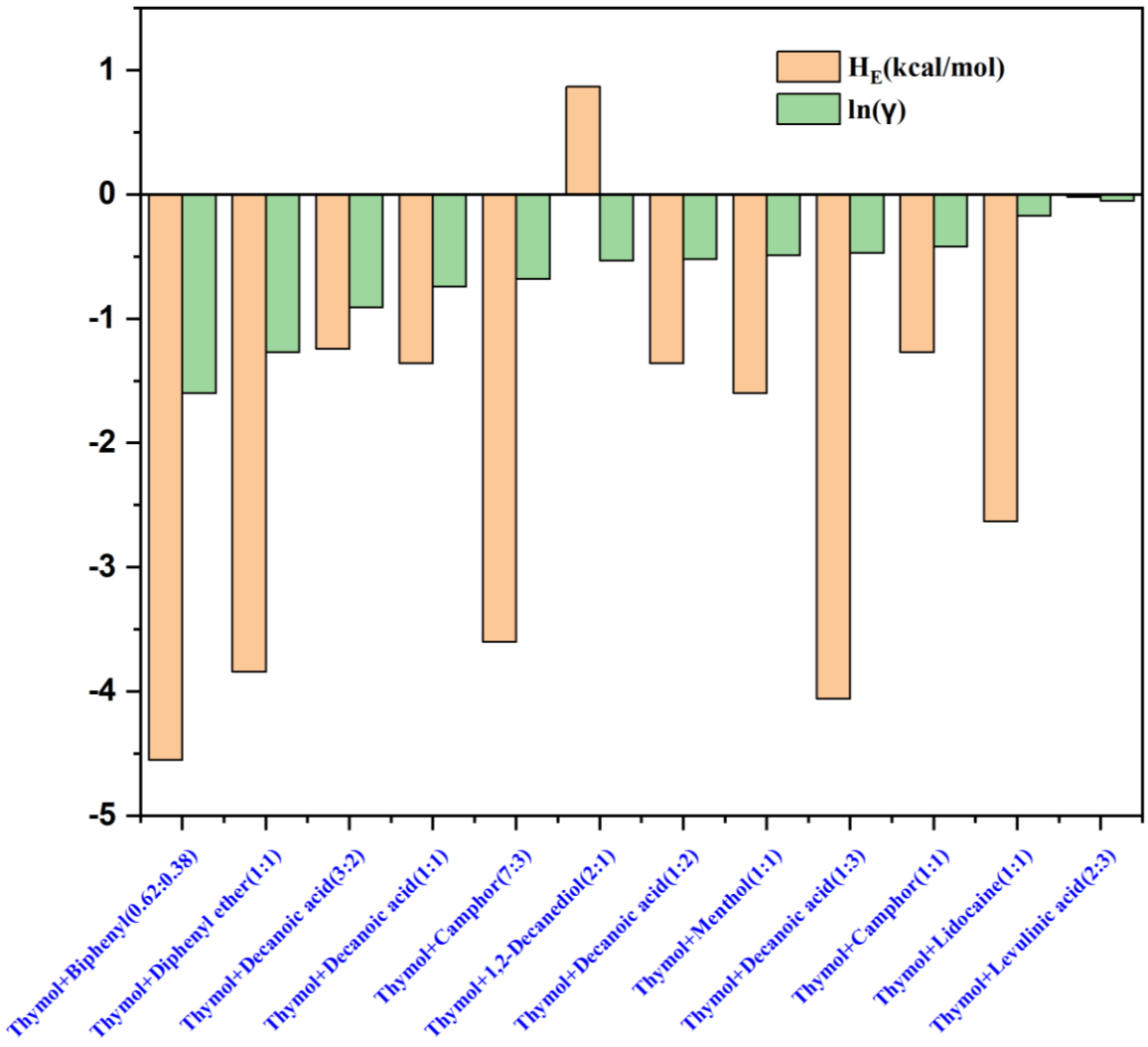

Figure 6.3. COSMO-RS predicted excess enthalpy and logarithmic activity coefficients of asphaltene for model structure 2.

For validation, we compared the asphaltene solubility in toluene, where the true asphaltene solubility in toluene has been reported as 30 μg/L[38], asphaltene starts to make dimers at 50 mg/L[39], and asphaltene aggregates at ~150 mg/L [40, 41]. According to the obtained

results, the ability of DESs to dissolve asphaltene can be ordered as follows: DES1 > DES2 > DES3 > DES4, which follows the results obtained during the screening of solvents. Thus, it is clear that functional groups in HBD contribute significantly to the dissolution of asphaltene.

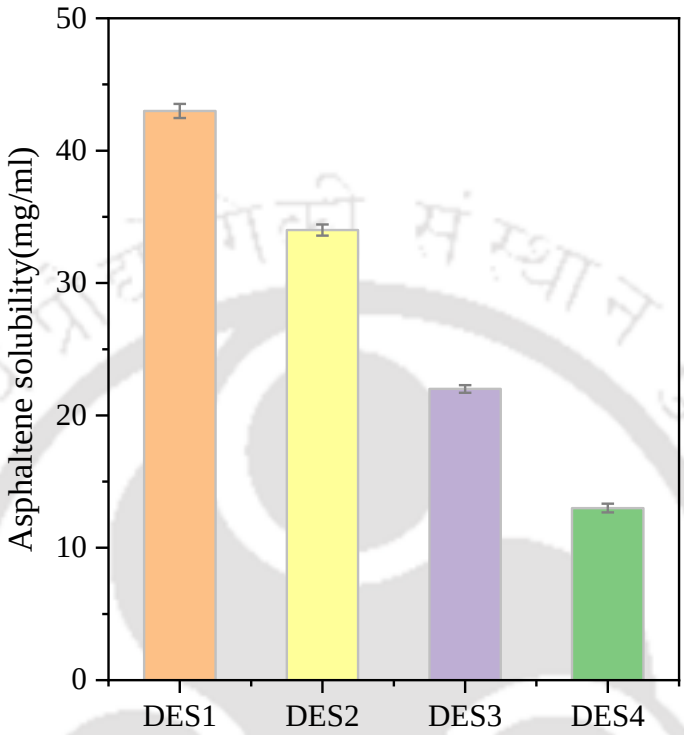

Figure 6.4. Solubility of asphaltene in different NADESs at 298.15 K and ambient pressure. Error bars represent the standard deviation calculated from two independent experiments (p = 0.05). Significant differences between groups (p < 0.05) are indicated with lowercase letters.

6.6 Aggregation Characterisation through FTIR

6.6.1 Asphaltene Structure Characterisation

The FTIR spectra of the asphaltene extracted from crude oil were characterised to identify the chemical compositions in terms of major functional groups. It was divided into polar, diagnostic, and fingerprint regions. It was based on different active functional groups, as shown in figure 6.5. In the peaks of the polar region, the broad bands at 3600–3000 cm^{-1} were assigned to the stretching band of −OH or –NH. The peak relating to the sulfoxide functional group was assigned at 1030 ± 5 cm^{-1}. These polar region peaks in asphaltene spectra can be corroborated by the relevant literature as elaborated by Zojaji et al. [42]. The O─H stretching peak in pure

asphaltene is substantial and more intense than N─H stretching since oxygen, with its higher reduced mass, is more electronegative than nitrogen. The asphaltene sample possess elements such as C, H, O, N, and S and has high aromaticity. Each peak in the absorption region of 3000-3600 cm^{-1} is assigned to an individual hydrogen bond formed by different hydrogen-bonding descriptors, such as N−H· · ·O−H, π· · ·O−H· · ·O−H, and O−H−O. Further, the carboxylic acid group is depicted as a peak at 1600 cm^{-1}, which corresponds to a C=O carbonyl bond. In the case of a hydrogen-bonded molecule, this peak is overlapped by an adjacent peak at 1590 cm^{-1} (C=C double bond) [43], as shown in figure 6.5.

In the IR spectra of the pure asphaltene, two peaks are typically observed at the 2800–3000 cm^{-1} region, similar to the earlier reported work by Silverstein [44]. The peak at 2920 ± 10 cm^{-1} corresponds to CH_2 stretching in aliphatic bonds (C─H asymmetric). It is the most intense peak in the spectrum and corresponds to the methylene functional group. The peak at 2850 ± 10 cm^{-1} represents the CH_2 stretching in aliphatic (C─H symmetric) bonds that correspond to the methylene group. In the third region, the fingerprint region, the following two peaks are observed in the asphaltene spectra[45]. The peak at a wavelength of 1450 ± 10 cm^{-1} is related to the CH_2 scissoring mode, derived from the resonance of the C─H bond in the methyl structure, while the peak at 1370 ± 10 cm^{-1} is related to the CH_3 umbrella mode and is the only peak corresponding to the methyl group in the asphaltene. The molecular structure characterisation of asphaltene here depends on the source of crude, as studied by Zojaji et al. [42].

The fingerprint regions are between 1000 and 1370 cm^{-1}. A peak corresponding to S···O sulfoxide attachment is detected at 1035 cm^{-1}. The asphaltene spectra displayed two distinct medium-intensity peaks, such as C–O–C stretching, prevalent in asphaltene with an ether functional group [46], at 1100 cm^{-1}. Further, the C···O stretching is referred to at 1215 cm^{-1}. Overall, the higher asphaltene dissolution was attributed to the hydrogen bonding and

C–H···π interaction between solvents and asphaltene, allowing DES to prevent the agglomeration successfully. This was confirmed by FTIR and NMR spectroscopic techniques.

6.6.2 FTIR Mesurement of DESs with Asphaltene

In the polar region (figure 6. 5), the hydroxyl and amine group show peaks typically observed in the range of 3000 cm^{-1}-3580 cm^{-1}, corresponding to free pyrrolic N-H or bonded hydroxyl O-H stretching. The raw asphaltene shows two characteristic overlapping absorption peaks in the region at 2920 cm^{-1} and 2854 cm^{-1} for asymmetric and symmetric alkyl chain stretches, respectively. Polar interactions occur between 3000 cm^{-1} and 3600 cm^{-1}. This is because hydrogen bonds are initiated between hydrogen bond acceptors or donors of NADESs and the free active sites in raw asphaltene. These polar region interactions dominate the dispersion of asphaltene in NADESs. The detailed analysis of FT-IR spectra of pure NADESs and after adding the different mass fractions of asphaltene are given in figure 6.6-6.10. The characteristics and frequency range of each free and bonded stretch peak for asphaltene dispersion in different solvents are given in table 6.3. The type of interaction and the asphaltene mass fraction dissolved in solvents are two factors that can affect the peak height and area of the hydroxyl functional group. The polar region is crucial to asphaltene's solubility in NADESs because these solvents can establish hydrogen bonds with asphaltene functional group descriptors and active sites. This region can be divided into the following non-covalent interactions, which elaborate the solvation interaction descriptors of asphaltene.

- N─H·····O─H (OH available in HBA of NADESs forming a hydrogen bond with the NH group present in asphaltene).
- π─O─H·····O─H (Hydrogen bonds are formed between OH and other OH groups in nearby molecules only when two asphaltene molecules are also linked by a π -bond)
- OH─O (one of the asphaltene molecules has a primary group, and the other has an acid group in which the proton exchange takes place).

The FT-IR of different mass fractions of asphaltene in four solvents shows an effect on specific polar region interaction. The distinct types of free and bonded OH stretches are observed at the following frequencies, namely 3600 cm^{-1} and 3400 $cm^{-1,}$ as given in table 6.3. This is similar to the observation of Chang and coworkers, who reported the stabilization of asphaltenes in aliphatic solvents using alkylbenzene-derived amphiphiles. Further, they studied the asphaltene-amphiphile interactions and structures using Fourier transform infrared spectroscopy and small-angle X-ray scattering techniques. In another similar study, Athokpam et al. studied the effect of hydrogen bonding on the infrared absorption intensity of OH stretch vibrations[47, 48]. They concluded that the intermolecular interaction between the asphaltene and solvents results in lower absorption intensity. The higher aggregation results due to significant intramolecular interaction give higher absorption intensity.

Increasing the mass fraction of asphaltene in solvents decreases intensity due to intermolecular hydrogen bonding between NADESs and asphaltene. Thus, if asphaltene aggregation occurs or is present in solvents, it demonstrates a higher intensity due to intramolecular interactions as the mass fraction increases. A higher intensity implies significant aggregation of asphaltene, and a reduction in intensity represents the dispersion in solvents, as shown with DES1. If the aggregation of asphaltene molecules is higher due to strong intramolecular interaction, the peak of the OH/NH group depicts the highest intensity.

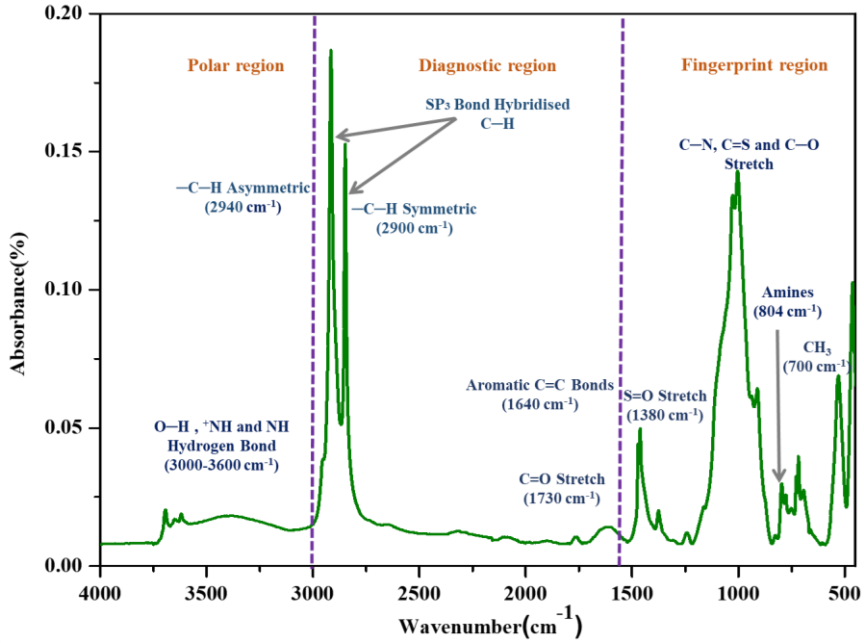

Figure 6.5. The characterisation of asphaltene compound extracted from the crude oil using the FT-IR spectra.

The intensity of the polar stretch peak decreases when the mass fraction of asphaltene increases due to the formation of an intermolecular type of non-covalent interaction. As a result, mainly hydrogen bonds and dispersion interactions were established between the functional group descriptors of DESs and asphaltene, as indicated in figures 6.6-6.10. Thus, we conclude that as asphaltene starts to disperse in NADESs, its peak intensity decreases, as evident from figures 6-7 in the case of DES1. Chang and co-workers have noted that the addition of asphaltene causes a decrease in the intensity caused by the bonded OH functional group. This is because of the creation of strong intermolecular hydrogen bonds [47]. Table 6.3 also displays NADESs aggregation behaviour relative to the amount of free and bonded polar groups. The bonded stretch is a measure of intermolecular interaction replicated by lowering wavelength intensity. The observed interactions between the investigated NADESs and asphaltene can be classified through highest to lowest peak height and area in the order of DES1>DES2>DES3>DES4.

Table 6.3. Characteristics and frequency range of each of the free and bonded OH peaks.

Peak	Wavenumber (cm^{-1})	Characterisation
Nonbonded ─OH Stretch	3600 ± 20	An intense sharp peak indicates Aggregation in NADESs
Bonded pyrrolic ─NH	3400, 3480−3470	─OH, ─NH forms a hydrogen bond with the functional group of NADESs
OH─N	3170	Hydroxyl group forms hydrogen bonds with the ─NH group
Bonded OH Stretch	3600 to 3100	A very broad peak with higher intermolecular interaction indicates higher dispersion Peak intensity depends on concentration and intermolecular hydrogen bonding strength

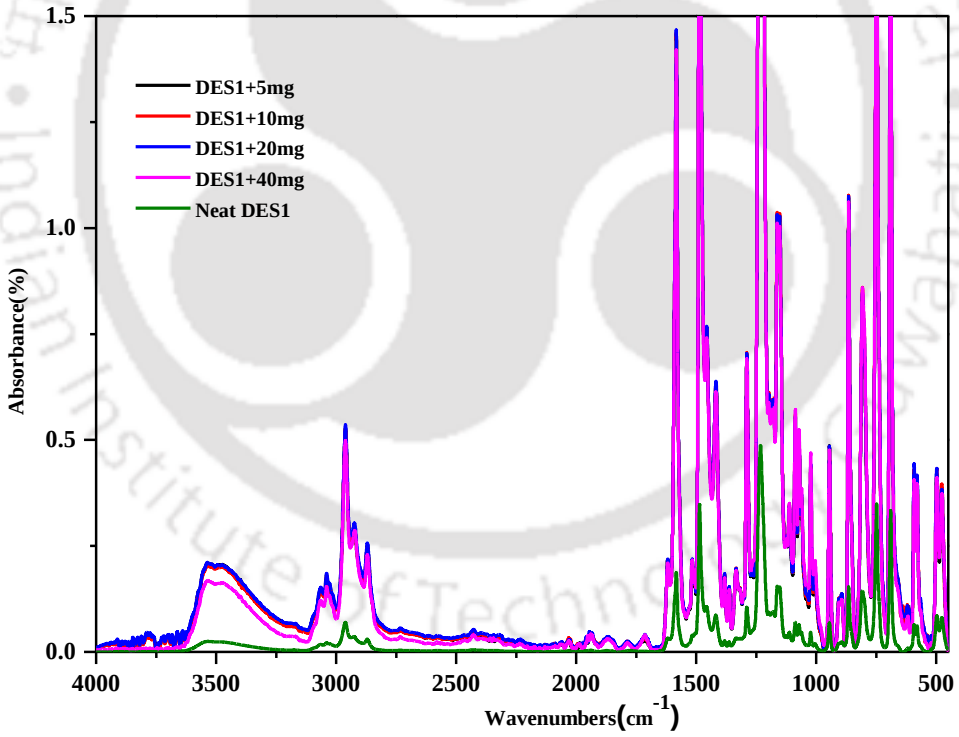

Figure 6.6. FTIR spectra of DES1+ *x* asphaltene in different mixture compositions, where *x* represents the different weight fractions of asphaltene in particular deep eutectic solvents.

A stronger intramolecular hydrogen bonding in asphaltene molecules results in lower dispersion in NADESs. Therefore, it implies that the higher peak height and peak area in the 3000-3600 cm^{-1} exist for absorption peaks that correspond to the intramolecular hydrogen-

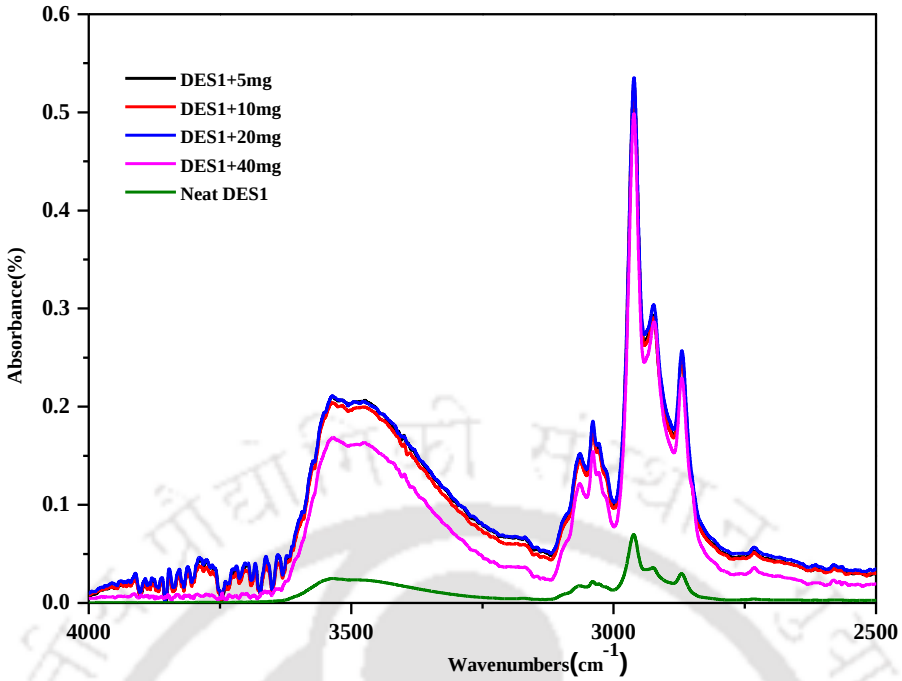

Figure 6.7. Comparison of the FTIR spectra of the asphaltene sample at four different mass fractions in the presence of DES1 with neat DES1 focuses on the OH stretching band.

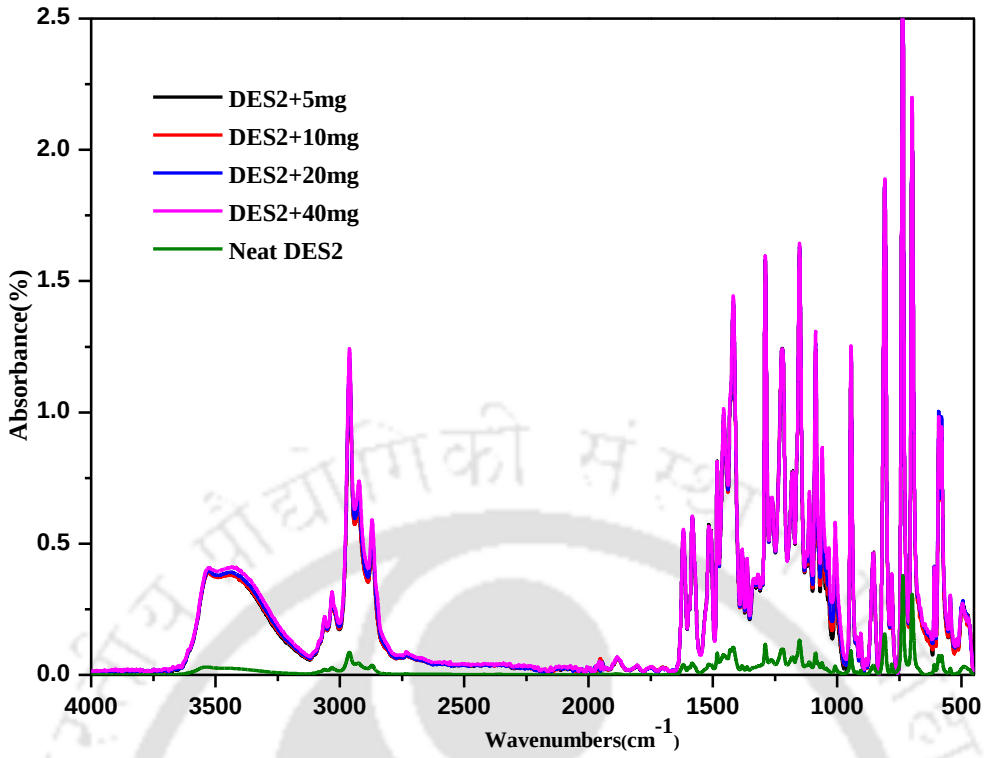

Figure 6.8. The FT–IR spectra of DES2+ *x* asphaltene in different mixture compositions, where *x* represents the different weight fractions of asphaltene in particular deep eutectic solvents.

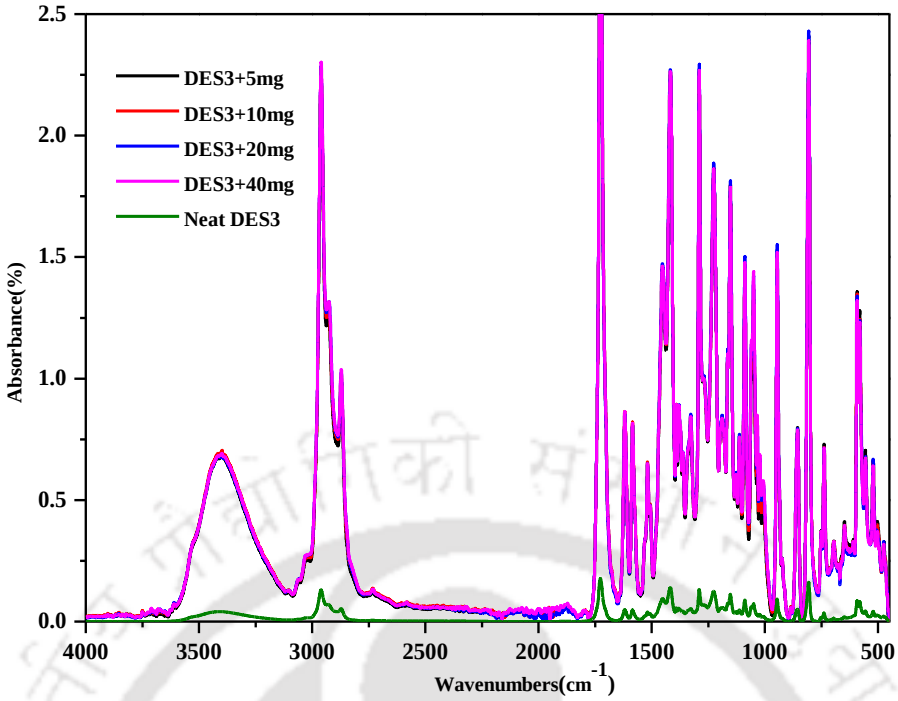

Figure 6.9. FT–IR spectra of DES3+ *x* asphaltene in different mixture compositions, where *x* represents the different weight fractions of asphaltene in particular deep eutectic solvents.

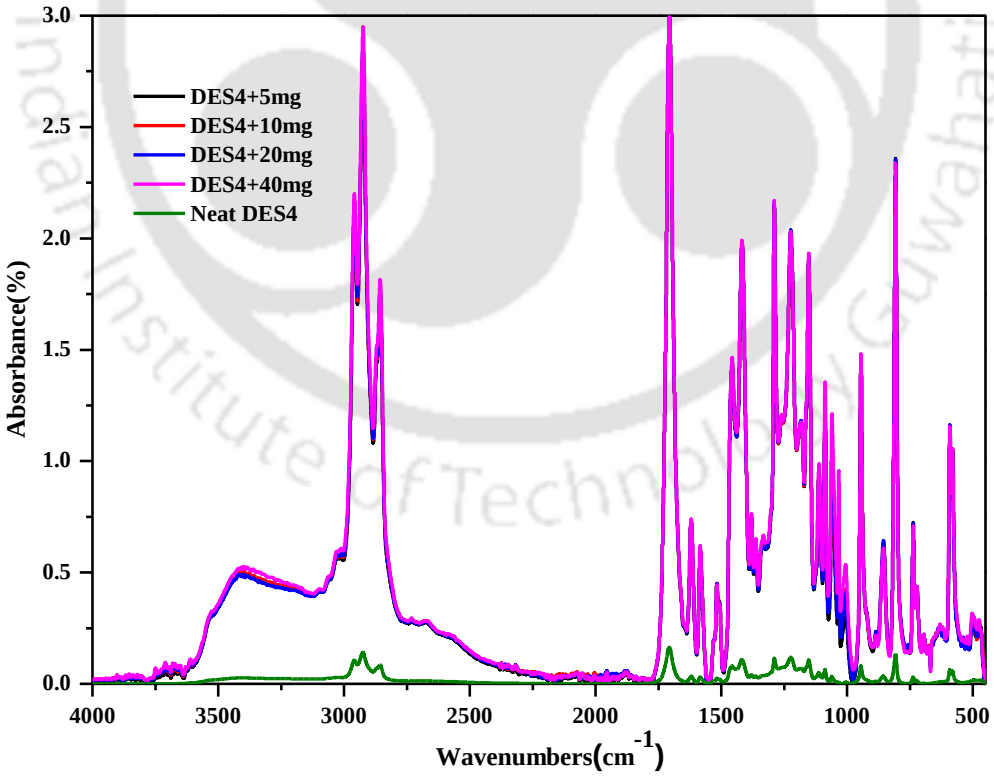

Figure 6.10. The FTIR spectra of DES4+ *x* asphaltene in different mixture compositions, where *x* represents the different weight fractions of asphaltene in natural deep eutectic solvents.

-bonded between the OH or NH group of asphaltene [49]. When DESs as solvents are added with asphaltene at different mass fractions, hydrogen bonding is revealed by comparing the intensity of the free OH stretch peak and the bonded OH stretch peak. The peak area and height decrease as the intermolecular interactions distributes between the asphaltene and functional group of NADESs with higher weight fractions. The spectra of asphaltene in the presence of different DESs and varying mass fractions are shown schematically in Figures 6.6-6.10.

6.7 Structural Characterisation of Asphaltene by NMR

The characterization of pure asphaltene and the isotropic chemical shifts of ^{1}H NMR spectra are shown in figure 6.11. The chemical shifts of ^{1}H NMR spectra were divided into multiple types of proton peak regions based on the hydrogen atom attached as per the previous protocol [21, 22]. Table 6.4 mentions the different types of hydrogen-atom assignments, classified as H_A, H_α, H_β, H_γ, and H_N, based on the respective proton attached to different aliphatic and aromatic ring compounds in their immediate vicinity. The most complex heavy fraction of crude oil is made up of aliphatic, polycyclic aromatics, paraffinic, and olefinic chemicals. At the same time, naphthenic compounds can also be detected by NMR spectroscopy.

The aromatic protons (H_A) are directly attached to the aromatic ring, aliphatic hydrogen in position to the aromatic ring (H_α), aliphatic hydrogen in position or further from aromatic and methylene/methyne hydrogen in alkane (H_β). Furthermore, methyl hydrogen in position or further from the aromatic ring and methyl hydrogen in alkane (H_γ) are mainly calculated for the asphaltene sample to understand the structure of asphaltene as given in figure 6.11. The contents of an aromatic proton (H_A) in the asphaltene are about 20%, which is the second highest of methylene/methyne type hydrogen in alkane (H_β), i.e. (64.53%). The number of distinct hydrogen atoms in asphaltene mainly depends upon the source and location of crude oil.

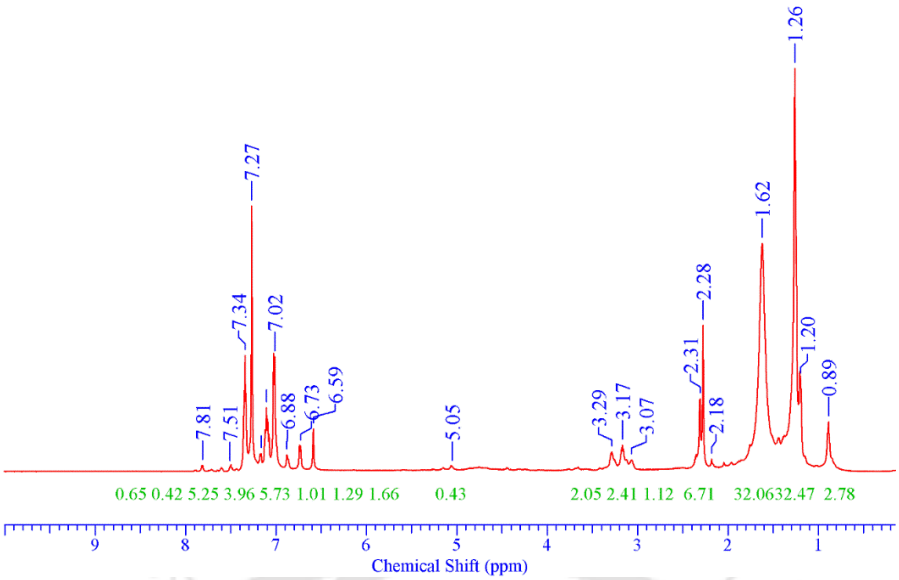

Figure 6.11. ^{1}H NMR of pure Asphaltene compound used in this study with integral values.

Peak areas of each specific type of proton in ^{1}H NMR spectra were used to calculate the relative abundance of each species, as illustrated in Figure 6.11. The distributions were used to compute the number of hydrogens per 100 carbons with the help of equation 5. The obtained H/C ratio for the particular compound was then compared to the theoretically calculated H/C ratio of the proposed model structures.

$$\boldsymbol{H\ per\ 100\ C} = (\mathbf{3} \times \%\boldsymbol{CH_3}) + (\mathbf{2} \times \%\boldsymbol{CH_2}) + (\%\ \mathbf{CH}) \qquad (6.5)$$

Here % CH_3, % CH_2, and % CH are the percentages of methyl, methylene, and methyne (including aromatic =C−H)) carbons present, respectively. The calculated H/C ratio (1.33) was compared to the H/C ratio obtained from elemental analysis (1.30) to validate the asphaltene composition obtained using the integration of ^{1}H NMR. A 97.7% agreement between their H/C ratios suggests that the peak-fitting model and the assignments of the ^{13}C resonances are accurate.

Table 6.4. Classification of ^{1}H NMR spectra based on the different types of significant proton types attached to the asphaltene compound.

Chemical Shift Ranges (ppm)	Symbol	Type of Hydrogen
6.0-9.0	H_A	aromatic protons
6.0-4.0	H_N	naphthenic and porpyrinic CH/CH_2 groups
2.1-4.0	H_α	aliphatic hydrogen in α position to an aromatic ring
1.0-2.1	H_β	aliphatic hydrogen in β position or further from aromatic; methylene/methyne hydrogen in alkane
0.5-1.0	H_γ	methyl hydrogen in γ or further from the aromatic ring; methyl hydrogen in alkane

Table 6.5. ^{1}H NMR spectra analysis for the composition of pure asphaltene sample.

Sample Name	H_A	H_α	H_β	H_γ	H_N
Asphaltene	19.97	12.29	64.53	2.78	0.43

The dissolving mechanism of asphaltene was determined by observing the upfield or downfield shift of peaks in ^{1}H NMR spectra of asphaltene at different concentrations. The molar ratio of NADESs was also quantified by integrating the ^{1}H NMR peaks to assess the purity of synthesized NADESs. The resonance peaks at 0.920 ppm (H_α) and 1.31 ppm (H_β) in the ^{1}H spectra show the presence of terminal –CH_3– and –CH_2– groups of the asphaltene compound (Figure 6.11).

6.7.1 Asphaltene–Solvent Interaction using NMR

The site-site specific interaction environment between the active sites present in designed solvents and asphaltene was examined using ^{1}H NMR, 2D{^{1}H–^{1}H} NOESY (nuclear overhauser effect spectroscopy), and 2D {^{1}H-^{13}C} HMBC (Hetero-nuclear Multiple-Bond Correlations) spectra. The 2D-NMR is a valuable tool to determine which signals arise from

asphaltene protons close to NADESs in space but may not be covalently bonded. The phase-sensitive cross-peak signals can result from physically close protons, chemically and kinetically exchanging protons, or J-coupled protons displaying artifacts [50].

In the present work, we confirmed the molar ratio of HBA to HBD in NADESs after mixing various mass fractions of asphaltene in solvents by integrating all peaks in the ^{1}H NMR spectrum, as shown in figures S1 through S4. The ^{1}H NMR of DES+ *x* (asphaltene) was performed to obtain the chemical shift after adding asphaltene to green solvents. The 2D {^{1}H–^{1}H}-NOESY spectra of asphaltene dispersion in different solvents were performed to reveal the main interaction sites responsible for the higher dispersion. The potential asphaltene structures interact with the solvents based on region-by-region assignments of the resonances detected in the ^{1}H and ^{13}C dimensions of the 2D NMR spectra. Figure 6.12a-6.12d displays the results of a structural analysis of the narrow correlations found in the NOESY spectra of the asphaltene sample with the NADESs.

In figure 6.12a, the positive proton NOEs were observed between the active sites of asphaltene with the primary functional group of DES1. The active protons of asphaltene H_{β}, $H\alpha$, and H_N proton attached to asphaltene, indicate that these protons were merged with the alkyl group of thymol. The diagonal NOEs cross-peaks indicate NADESs and (H_{β}, $H\alpha$) alkyl protons interacting with each other. However, an exact distinction between the DES1 compounds attached to CH_3, CH_2, and asphaltene protons attached groups is not possible. The active functional group NOEs cross peaks in asphaltene show high-intensity interaction with the OH/NH functional group of thymol and ether functional group of diphenyl ether, and weaker NOEs cross-peaks methyl protons attached to themselves. The hydrogen whose signal (H_{γ}) is at 1.28 ppm, associated with the proton $H\alpha$ (3.23 ppm) and H_A (6.82 ppm), is designated as strong interaction. In addition, protons of porphyrins with an H_N (1.9 ppm) resonance and

Hα (3.23 ppm) and H_A (6.82 ppm) resonance are associated with protons at 7.61, and 7.08 ppm are classified as π–π type interaction between the asphaltene and DES1. The DES1 shows a strong interaction with asphaltene, which was also evident through strong interaction in the FT-IR spectrum, as shown in figure 6.3. The interaction between the solvents and asphaltene was confirmed through NOESY, as shown in figure 6.12a-12d. The number of cross peaks apart from the diagonal also confirms a similar trend as given in solubility. This trend is also seen in figure 6.12d, where lesser interaction is observed due to the long alkyl chain of aliphatic compounds.

The diphenyl ether and thymol protons show a weak negative cross peak with the methyl protons of thymol, which is attributed to an exchange of negative NOEs. In addition, an exchange between both HBA and HBD with the different types of protons of asphaltene was seen. These observations indicate that hydrogen bonds were formed between the DES1 and interactive sites of asphaltene molecules. Further, in figure 6.12 broadening of peaks was reduced substantially, confirming the cross-peaks between the different solvents and asphaltene. Furthermore, it shows that the individual components maintained their structure in the NADESs, which agrees with previous studies in other DESs [21].

Such strong hydrogen-bonding interactions between carboxylic and amide groups are present in asphaltene with the NADESs. It also shows the non-covalent interaction due to the delocalization of aromatic π-electron between the asphaltene with solvents that are mainly of π–π and π–σ interactions, van der Waals forces, and electrostatic attractions.

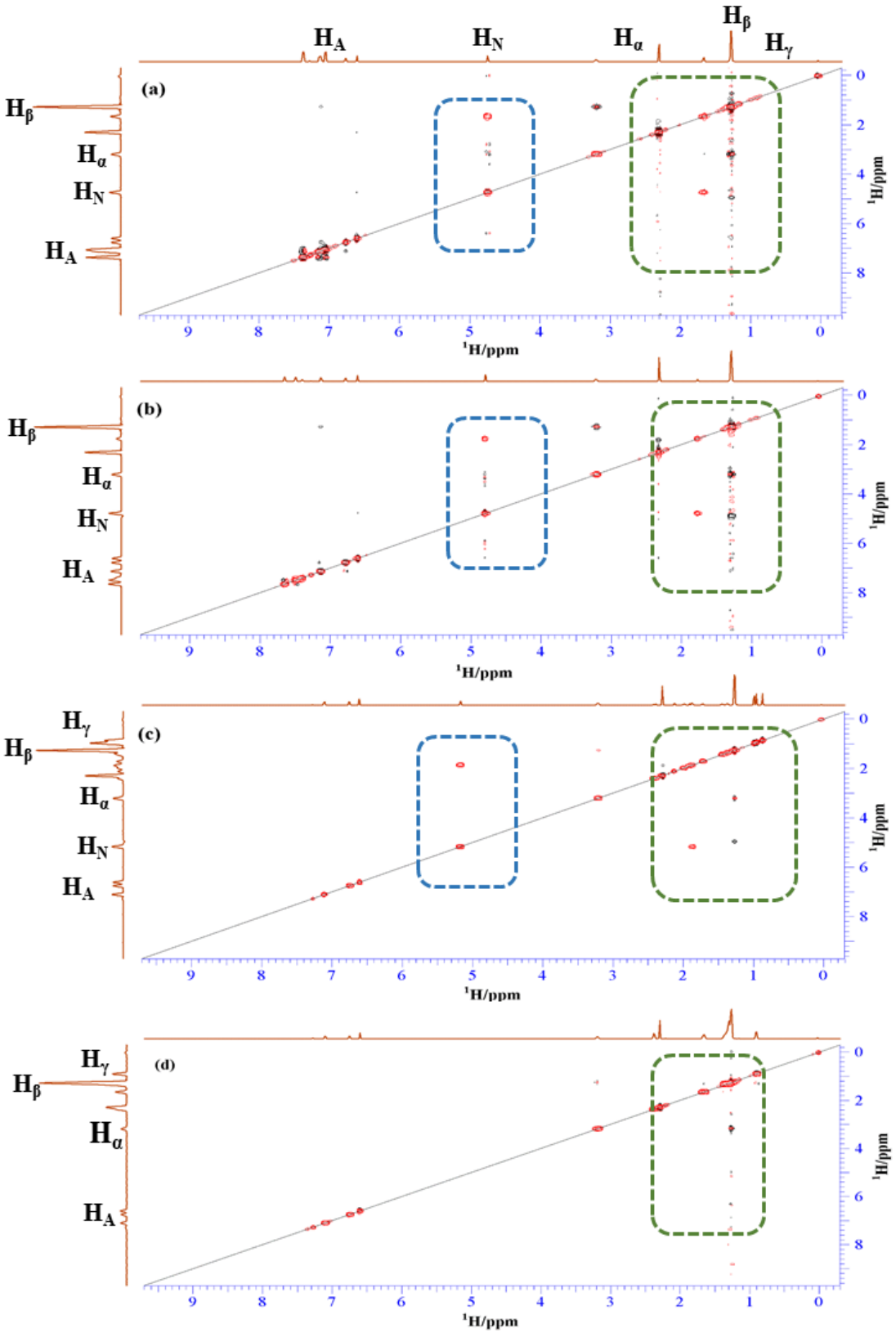

Figure 6.12. Representative NOESY (^{1}H-^{1}H) NMR spectra of asphaltene dissolve in DESs (a) DES1+ASP (b) DES2+ASP (c) DES3+ASP (d) DES4+ASP.

6.7.2 Hetero-nuclear Multiple Bond Correlations (HMBC) for NADESs and Asphaltene

The detailed long-range interaction prevailing between the asphaltene in NADESs was interpreted using the HMBC spectra, as shown in figure 6.13a-6.13d. The HMBC spectra reveal three bond couplings between the active carbonyl carbon and neighboring methylene and methane protons. Therefore, in the HMBC spectrum, more than one set of cross-peaks might appear due to the interaction between methane and methylene protons in different configurations with carbonyl carbon. The evidence of correlations between non-protonated aromatic carbons and the protons at further distances (at least two or three bonds) are seen in the HMBC spectra, as shown in figure 6.13a.

Figure 6.13a has the highest number of correlations in the HMBC spectrum among all the reported asphaltene and solvents interactions. A higher correlation between the NADESs and asphaltene molecules indicates higher interaction, as evident from figure 6.13a, while less interaction is shown in figure 6.13d. In figure 6.13a, the proton resonance at 1.39 ppm (CH_3 attached to aromatic rings) has correlations with ^{13}C frequencies at 129.38 ppm (an aromatic carbon) and 138.10 ppm (quaternary aromatic carbon in the α position to sulfur or nitrogen atom). The proton peak at 1.39 ppm (aliphatic CH) has two correlations: aliphatic CH_2 (attached to asphaltene), whose ^{13}C signals are at 35.25 and 30.33 ppm, and one correlation with an aromatic carbon at 139.40 ppm. Most of the protons have two correlations with ^{13}C peaks. Aliphatic CH_2, namely α or β attached to the aromatic ring, has four correlations: two with CH_2 at 34.86 and 31.69 ppm, one with CH_3 group at 14.15 ppm, and one with carbon at 147.32 ppm. Most of the aliphatic groups whose ^{1}H peaks are between 1.29 and 0.78 ppm have correlations either between each other's carbons or with the –C(═O), whose ^{13}C resonances appear around 60.00 and 75.00 ppm.

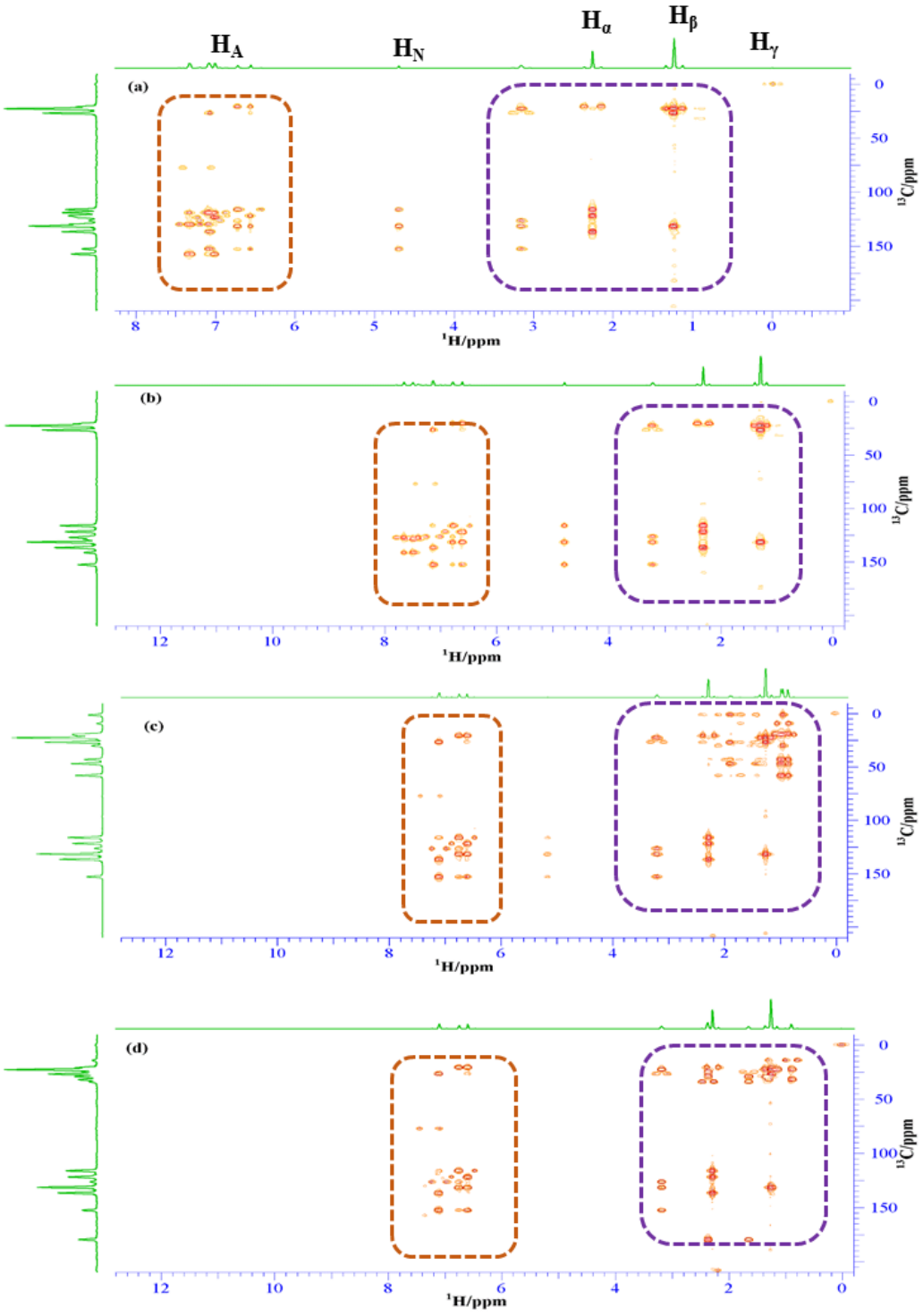

Figure 6.13. Representative HMBC NMR spectra of asphaltene dissolve in DESs (a) DES1+ASP (b) DES2+ASP (c) DES3+ASP (d) DES4+ASP.

The majority of these aliphatic protons do not show a significant number of correlations with aromatic carbons in the HMBC spectrum (figure 6.13d). Most of these aliphatic protons

are further away, at least four bonds away from aromatic cores. The other possibility is that some of these aliphatic groups, particularly those correlated with –C(═O), belong to the porphyrin derivatives.

Referring to the HMBC spectrum of asphaltene solubility analysis, we focus on the significant differences in the HMBC spectra of four solvents, as given in figures 6.13a-6.13d. After analysis, it was observed that figure 6.13a has a higher number of correlations in the HMBC spectrum than other solvents. This justifies the higher solubility as predicted by the COSMO-RS model. DES1+ASP has a large number of correlations between aromatic protons and aromatic carbons. There are correlations between protons with resonances of 8.14 and 1.38 ppm and carbons with frequencies of 134.46 and 138.45 ppm. These two HMBC correlations are attributed to the existence of the sulfur-based cyclic group. The correlations between carbon resonances around 168.00 ppm and corresponding protons with the signals around 7.75 or 4.33 ppm belong to porphyrin derivatives. The aromatic protons, with frequencies between 7.40 and 7.75 ppm, have correlations with the non-protonated aromatic carbons, whose resonances are between 131.05 and 128.75 ppm. The correlations for asphaltene with DES4 are shown in figure14d, and they are less than other solvents. Combining the results summarized and analyzing the single- and multiple-bond correlations allow us to propose a higher solubility of asphaltene in NADESs.

6.8 Quantum Chemical Insights

Quantum chemical (QC) calculations were performed to better understand the asphaltene dispersion mechanism on a molecular level. The systems chosen for this quantum chemical calculation study were asphaltene (ASP) dispersion by DES1 and DES2 since the experimental dissolution was highest for these solvents compared to DES3 and DES4. The investigation was intended to understand the atomistic chemistry of the HBA and the HBD with the developed

asphaltene model structure. The intrinsic molecular and atomic-level insights can be highlighted by having a comprehensive understanding of the structural properties, charge transfer behaviour, molecular level energies, thermochemistry, and molecular orbitals. The interactions between DES's main components and the asphaltene model structure may shed light on the improved molecular rearrangement, which could explain the promising dispersion results found in the experimental section that were previously discussed. A valid and efficient method for validating experimental results is QC analysis, which operates at an atomistic level at which each molecular entity may be expressed separately, and the resulting interactions can be evaluated without the expense of the experiments.

6.8.1 Computational Methodology

In order to construct the first three distinct cluster structures of DES and DES+ASP conformers, we placed each component through all of the distinct orientations it may take around the system's constituent components. Among them, the lowest energy was chosen for further study with no negative frequency. To save time during the computation calculations, the resolution-of-identity approximation was used by combining the atom-pair-wise correction schemes developed by Grimme et al.[51] with Becke-Johnson damping correction (D3BJ)[52], we were able to consider dispersion effects in large cluster structures. Using harmonic vibrational frequencies at the same level, the resulting stationary points were defined as energy minima on the potential energy hypersurface[52]. The geometries were optimized using the B3LYP/6-311+G (d, p) density functional[51], which was deemed appropriate for evaluating thermochemical parameters for complex clusters. Quantum chemistry calculations were used to determine the interaction energies of the initial individual structures and the newly formed DES clusters; the counterpoise correction approach was used to account for the basis set superposition error (BSSE)[53]. The software of Gaussian16 quantum chemistry software was

used to optimize different structures[54]. The molecular reactivity and accessible active sites were investigated with the help of a frontier molecular orbital (FMO) analysis. To learn more about the bonding and molecular structure of HBA, HBD, and their interactions with asphaltene, the Multiwfn (multiwave function) code was used to perform the QTAIM [55] and NCI (or RDG) [56] techniques. For the investigation of intermolecular interactions between pure DES and DES-ASP clusters, QTAIM is an effective method. It is possible to assess the intensity of intermolecular interaction by measuring the electron density at the bond critical points (BCPs), denoted by (ρ_{BCP}).

In addition, the Laplacian ($\nabla\rho_{BCP}^2$) of the electron density at BCP indicates charge concentration (negative sign) and charge depletion (positive sign) for a chemical bond. NCI analysis has been used to investigate the complex cluster structures, providing more evidence for intermolecular interactions between the solvents and asphaltene structure. In molecular systems with low electron density and low gradient values, NCI analysis provides insight into the partitioning of electron density. The term "RDG analysis" is often used to describe this NCI.

6.8.2 Cluster Chemistry

The geometries of pure DES and DES-ASP clusters were optimized at the M06-2X/6-311+G(d,p)[51] level of theory for comparative analysis, as shown in Figures 6.15 and 6.16. D3BJ dispersion correction was introduced for the level of theory to incorporate the dispersion forces that might be present in the DES and DES-ASP clusters rearrangement. The individual structures of DES (i.e., HBA and HBD) and model structure of asphaltene were built in the Gauss view 06 package, and the structures were optimized with the levels mentioned above of theory using Gaussian 16. The DES structures were optimized by arranging the components (HBA and HBD) in different orientations to obtain the minimum energy. The frequency

analysis at the same theoretical level was carried out using the '*freq'* keyword in Gaussian to confirm the no negative frequency.

6.8.3. Interaction Energy Analysis

The term "interaction energy" describes the reduction in complex system energy caused by interactions between two or more molecules. Calculating the difference between the energy of the system or clusters generated and the total energy of the individual molecules participating in the interaction corresponds to computing the interaction energy. This calculation will consider the counterpoise method-corrected basis set superposition error (BSSE)[57]. To calculate the interaction energy of the HBA-HBD pair in the DES, one must subtract the sum of the complex DES's energy from the sum of the energy of HBA and HBD separately, as shown in the following eqn.

$$\Delta E_{DES} = E_{DES} - (E_{HBA} + E_{HBD}) + E_{BSSE} \quad (6.6)$$

Where E_{BSSE} is the basis set superposition error (BSSE) corrected by the counterpoise method, E_{HBA} and E_{HBD} are the total energies of the HBA and HBD, respectively E_{DES} is the total energy of the DES. Each energy is quantifiable in terms of kilojoule per mole(kJ/mol). Thus, the following formula is used to determine the interaction energy between asphaltene and DES:

$$\Delta E_{CLUSTER} = E_{CLUSTER} - (E_{DES} + E_{ASP}) + E_{BSSE} \quad (6.7)$$

E_{DES} and E_{ASP} are the energies of DES and asphaltene, respectively, while $E_{CLUSTER}$ is the overall energy of the complex structure. Table 6.6 displays every estimated value of distance of pure DES with cut off <3.5 Å.

Insights on the compactness of the interacting molecules and the distance between the interacting atoms in the molecules are revealed by interaction energy. The decrease in overall energies of the final entities created from the beginning components in the development of both DES and DES-ASP clusters is indicated by the negative values of the interaction energies. This reduction in energy is attributed to the formation of non-bonded interactions, such as

hydrogen bonding and van der Waals interaction between the active sites of the interacting components. The formation of the OH (thymol)...hydrogen attached to phenyl rings in both DES with a bond distance less then<3.5Å, as illustrated in figure 6.14, is what causes the drop in interaction energy in the case of DES. This was in agreement with the DES's higher stability. In the DES-ASP clusters, the numerous weak non-covalent interactions, such as hydrogen bonding and van der Waals (vdW) formed as depicted in figure 6.15, can be used to explain the negative value of the interaction energy. The hydrogen bond strength increases when the compactness, or the distance between interacting atoms, decreases. As a result, the overall interaction energy or binding energy is reduced. The DES-ASP clusters may be significantly more stable and less polarisable as they possess a higher interaction energy (negative). The fact that there is better compactness of the DES-asphaltene complex due to favourable interactions between interaction components is further supported by the shorter hydrogen bonding distance between the active moieties of asphaltene with DES, which is shown in table 6.7.

Table 6.6. Intermolecular Distances (Å) Calculated at the B3LYP-D3BJ/6-311+G** Theoretical Level for the Significant Intermolecular Interactions in Various DES Clusters (figures 6.14 a–d)

Distance (in Å)	Pure DES 1	Pure DES 2	Pure DES 3	Pure DES 4
d_1	2.97	2.70	2.55	2.83
d_2	2.54	2.72	2.63	2.60
d_3	3.08	3.15	1.95	2.68
d_4	3.04	3.17	2.48	2.56
d_5	3.20	2.64	1.88	2.71
d_6	-	3.16	2.59	2.69
d_7	-	-	1.99	2.65
d_8	-	-	-	2.78

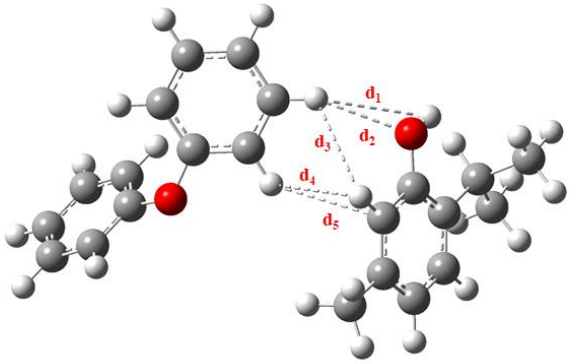

(a) DES1

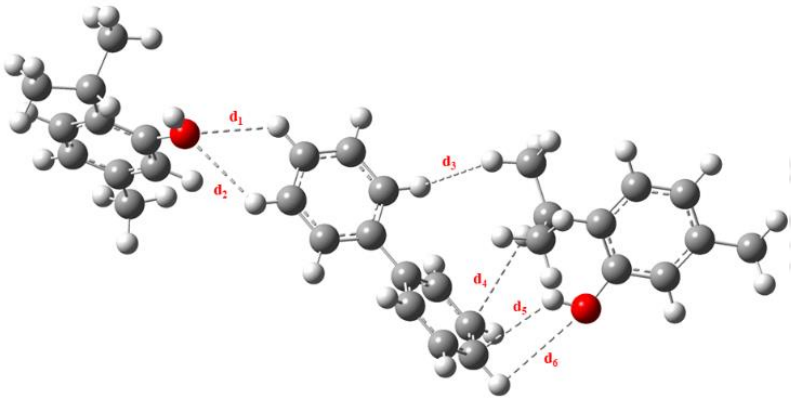

(b) DES2

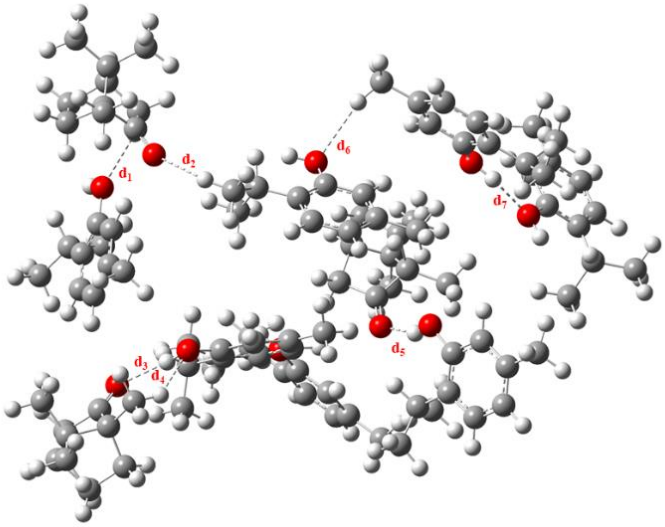

(c) DES3

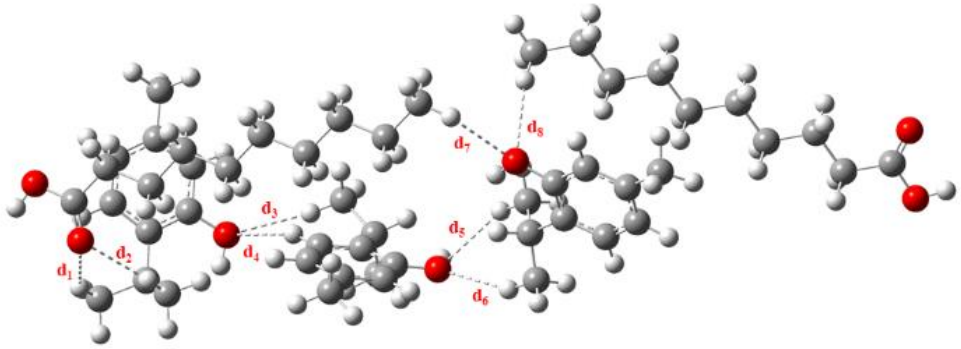

(d) DES4

Figure 6.14. Optimized Structures of (a) DES 1, (b) DES 2, (c) DES 3, and (d) DES 4 at the B3LYP/6-311+G (d, p) level of theory with D3BJ dispersion correction.

Table 6.7. Intermolecular distances (Å) calculated at the B3LYP-D3/6-311+G** theoretical level for the significant intermolecular interactions in various DES clusters (figure 6.15a–d)

Distance (Å)	DES1+Model structure-1	DES2+Model structure-1	DES1+Model structure-2	DES2+Model structure-2
d_1	2.37	2.52	3.26	2.49
d_2	2.41	2.38	2.75	3.04
d_3	2.61	3.30	3.09	3.07
d_4	2.87	2.9	2.21	3.32
d_5	2.28	2.89	2.84	2.86
d_6	1.92	3.17	-	2.88
d_7	3.26	2.61	-	3.11
d_8	2.49	2.65	-	2.78
d_9	3.39	2.73	-	2.72
d_{10}	-	-	-	2.76

Short to medium-range interactions ranging from 1.730 to 2.07 Å are observed between the −OH (thymol) and other active sites indicating the occurrence of a network of non-bonded interactions such as hydrogen bonds and van der Waals or dispersion interactions between the HBA and the HBD to achieve stable DES formation. The compactness of the DESs follows

the order as such: DES1> DES2, and solvents with model asphaltene structure also follow a similar order. The model structure of asphaltene with DES1 shows a more stable cluster, which confirms by the higher interaction/binding energy.

6.8.4 Orbital Energies

The chemical stability of a system can be analysed or estimated by studying the energies of the highest occupied molecular orbital (HOMO) and the lowest unoccupied molecular orbital (LUMO). According to Fukui et al.[58] the HOMO-LUMO energy gap is a primary feature that helps determine the molecular electronic transport characteristics. A big HOMO-LUMO gap suggests a stable material that is resistant to polarizability and changes in the number and distribution of electrons. Therefore, the difference between the HOMO and LUMO energies is significantly more significant in hard molecules. On the contrary, a small HOMO-LUMO gap indicates high polarizability since the energy barrier to reach the excited states is minimal. In this context, the existence of soft molecules is indicated by a small HOMO-LUMO gap. When considering single molecules (such ILs and DESs), the HOMO-LUMO gap indicates stability through the lowest electronic excitation energy.

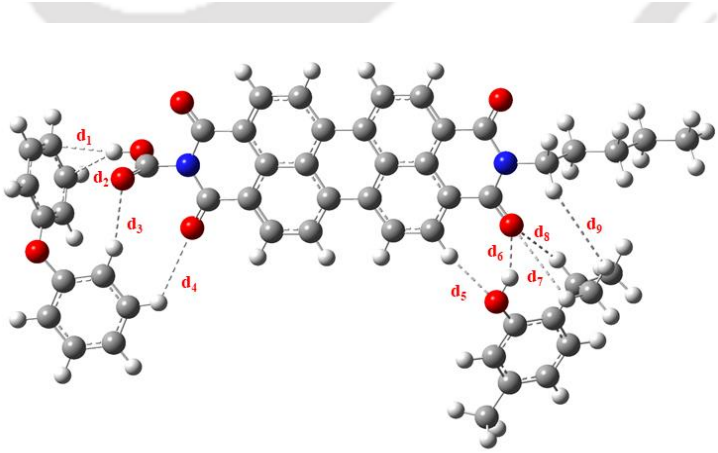

(a) DES1+Model Structure 1

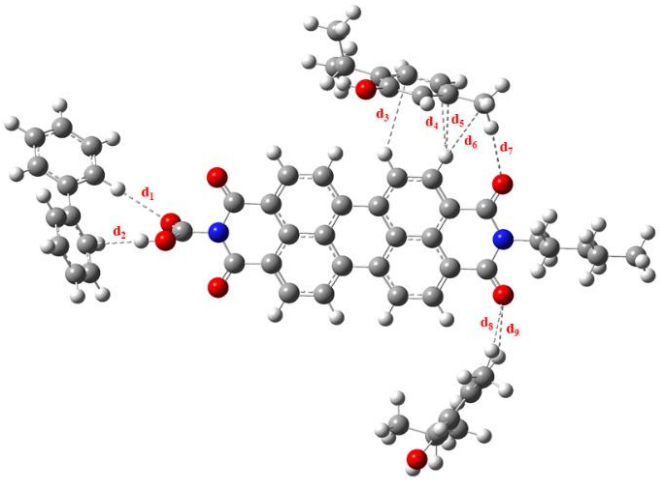

(b) DES2+Model Structure 1

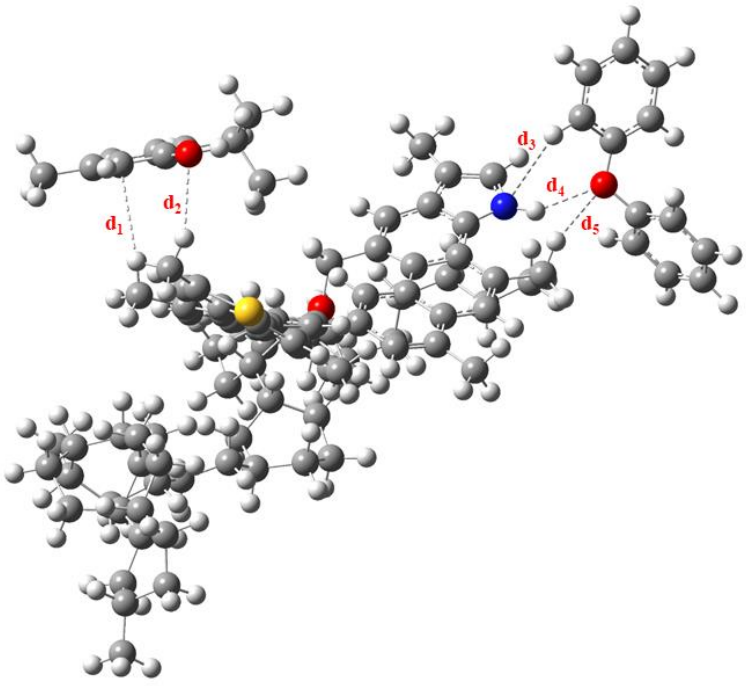

(c) DES1+Model Structure 2

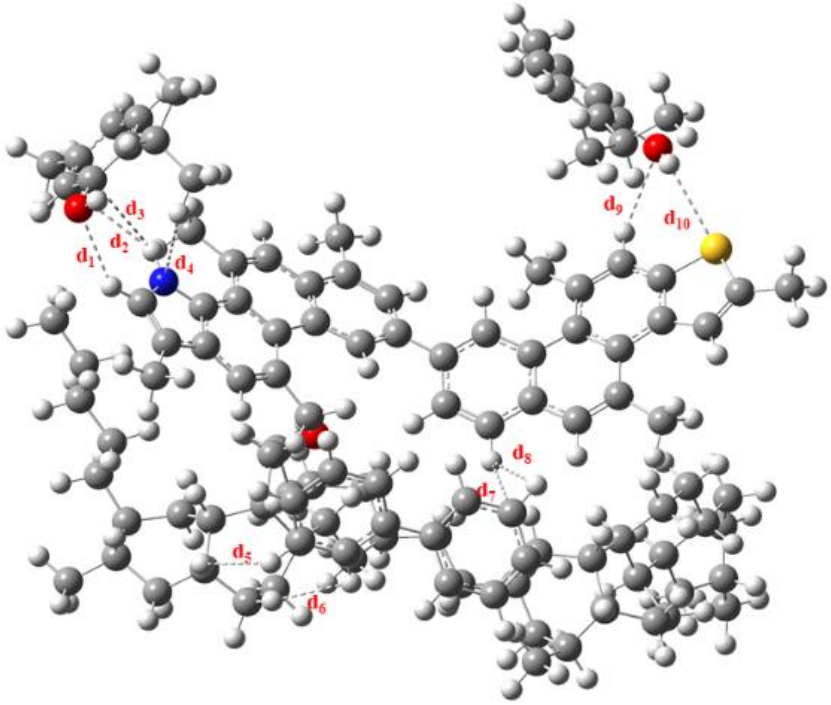

(d) DES1+Model Structure 2

Figure 6.15. Optimized structures of (a) DES1+ASP, (b) DES2+ASP, (c) DES3+ASP, and (d) DES4+ASP at the B3LYP/6-311+G (d, p) level of theory with D3BJ dispersion correction.

Still, the HOMO-LUMO gap indicates reactivity through electronic hopping energy between the species when considering pairs of molecules. DES1 (13.425 eV) has a more energy gap than DES 2 (12.267 eV), indicating that DES1 is more stable and less reactive. Since LUMO is an electron acceptor, its shape and orientation suggest a likely favourable for bond formation. On the other hand, HOMO provides the potential for external interactions in terms of energy. By contrast, a low LUMO energy denotes high electron affinity and superior electron acceptor properties, while a high HOMO energy signifies a high ionization potential and better electron donor properties. That is why having both a high HOMO energy and a low LUMO energy helps make a DES more stable. After optimization of DES with both types of model structure, it was found that the archipelago model structure complex is more stable than the island type structure. Therefore, it can be signified that higher stability means higher dispersion, as shown in the experimental study.

Table 6.8. Theoretically obtained HOMO, LUMO (Ground and Excited State), energy gap, chemical hardness (η), and chemical potential (μ) computed in the DFT-B3LYP method (All the units are in a.u.)

System Name	E_{HOMO} (a.u)	E_{LUMO} (a.u)	Global Hardness (η) (a.u)	Global Softness (σ) (a.u)	Chemical Potential (μ) (a.u)	Energy Gap (eV)
DES1	-0.235	0.259	0.247	4.054	0.012	-13.425
DES2	-0.230	0.221	0.225	4.436	-0.004	-12.267
DES1+Model 1 Structure	-0.199	0.083	0.141	7.068	-0.058	-7.700
DES2+Model 1 Structure	-0.195	0.088	0.142	7.060	-0.054	-7.709
DES1+Model 3 Structure	-0.174	0.182	0.178	5.622	0.004	-9.681
DES1+Model 3 Structure	-0.176	0.180	0.177	5.623	0.002	-9.679

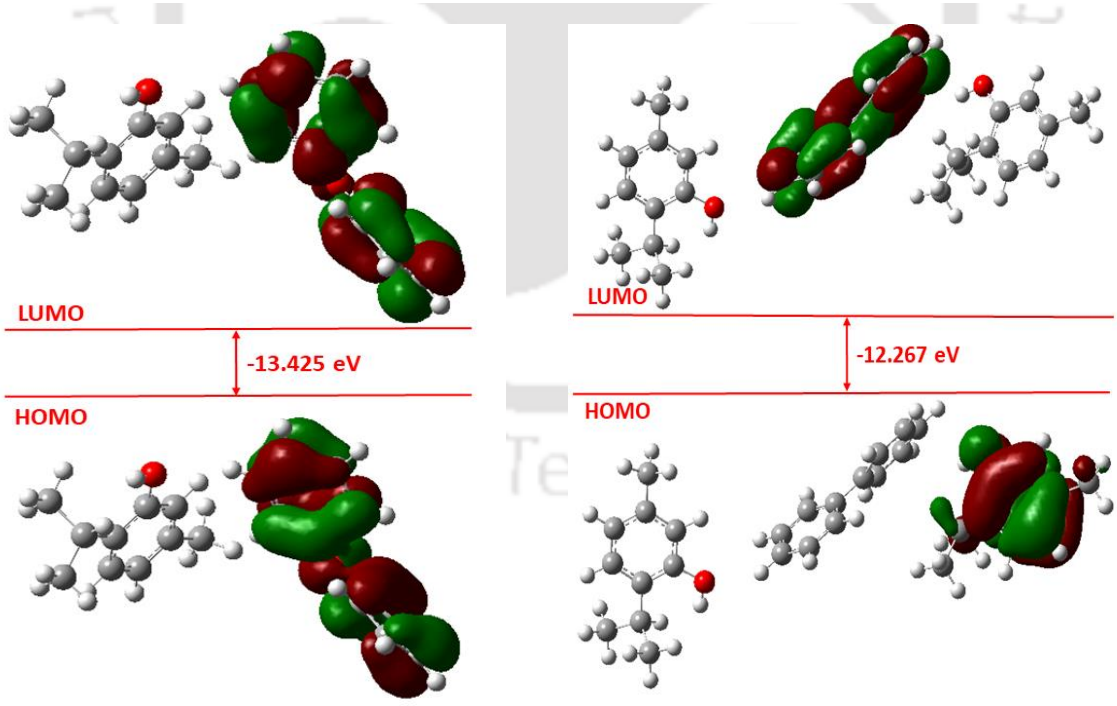

(a) DES 1 **(b) DES 2**

Figure 6.16. HOMO–LUMO iso-surfaces of different DESs studied for the dispersion of asphaltene.

The energy gap between the HOMO and the LUMO is directly related to a molecule's global hardness and softness. The global hardness can recognize the charge transfer and stability of a specific molecule or complex, where a higher η value suggests more excellent stability and resistance to charge transfer, and vice versa.

$$\text{Global Hardness } (\eta) = (E_{LUMO} - E_{HOMO})/2 \qquad (6.8)$$

The high hardness value of DES1 (0.24669a.u.) compared to DES2(0.22541a.u.) in table 6.16 suggests its high resistance to charge transfer which further shows its tendency to react less and thus exists as a stable solvent. Similarly, DES1-model structure 3 (0.17788 a.u.) has a high hardness compared to DES1-model structure 2 (0.14149a.u.), indicating more stability and less polarisability.

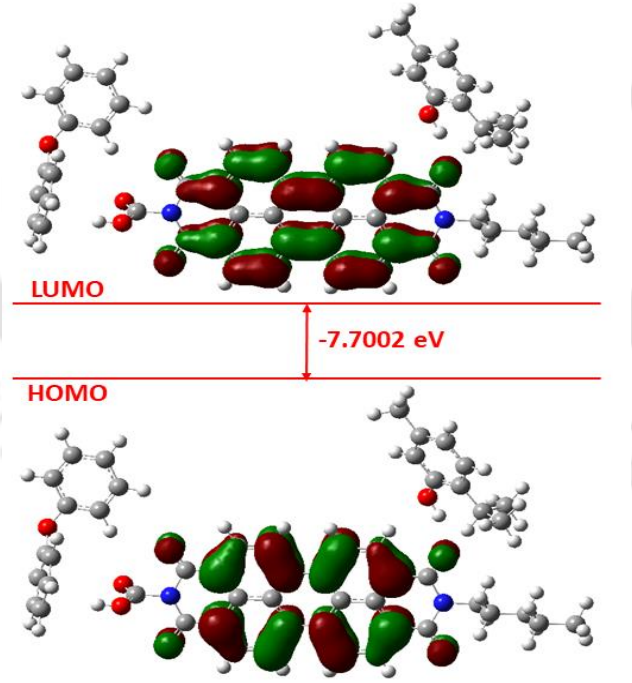

(a) DES1+ Model structure 1

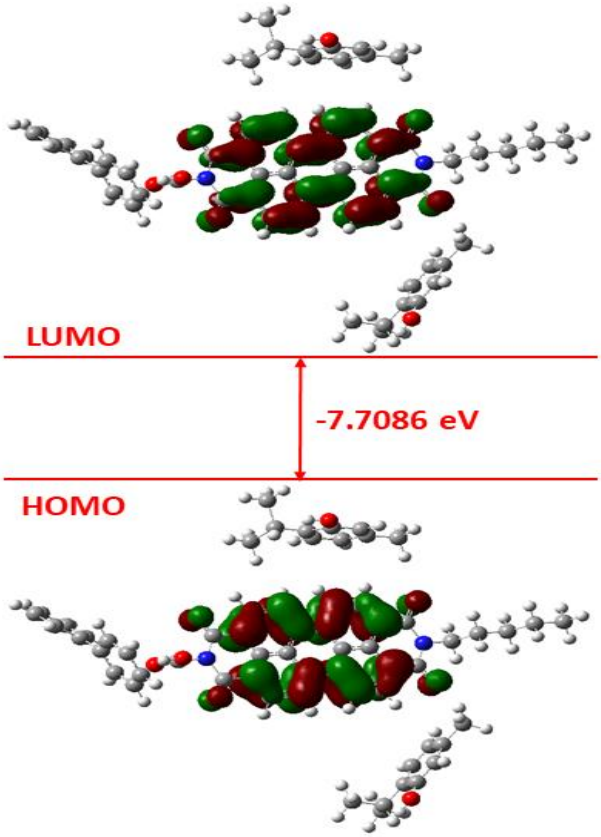

(b) DES2+ Model structure 1

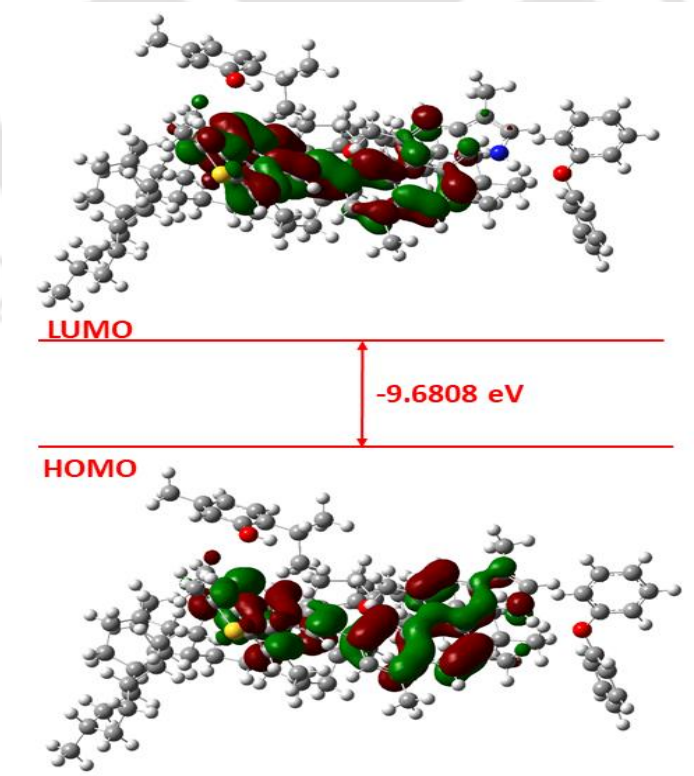

(c) DES1+Model structure 2

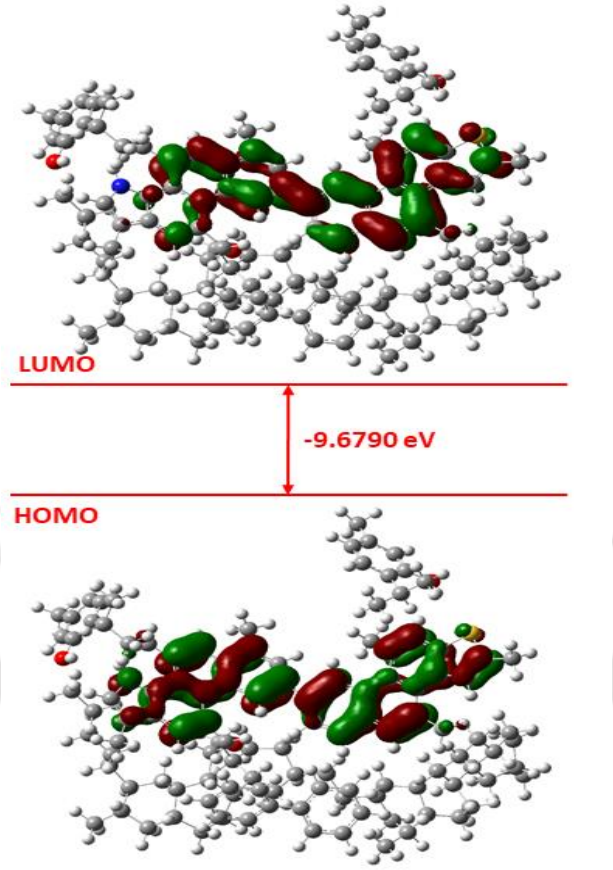

(d) DES 2+Model structure 2

Figure 6.17. HOMO–LUMO iso-surfaces of the DES-ASP complex (DES intermolecular) moiety.

The relatively higher value of η for DES-model structure 3 compare to DES-model structure 1 suggests higher stability and less polarisability. This higher stability can be the reason for the higher dispersion of asphaltene in DES1. The chemical potential (μ) also suggests a similar understanding. Overall, it can be concluded that the DES-asphaltene complex is relatively stable in its formation. The HOMO–LUMO energy gap is more for DES+ Model structure 3 (~9.68 eV) than for DES+ Model structure-1 (~7.70 eV), indicating a stable DES system with a model structure 3.

6.8.5 Quantum Theory of Atoms in Molecules (QTAIM) Analysis

The "Quantum Theory of Atoms in Molecules" (QTAIM) analysis was incorporated as an effective technique for deciphering complex interactions due to the existence of multiple donor

and acceptor pairs in the DES-asphaltene system. The partitioning of electron density distribution at the so-called bond critical points (BCPs) (3,−1) based on Bader's QTAIM scheme[55] allows one to interpret the numerous non-covalent interactions between molecules or atoms.

Table 6.9. Electron density (ρ_{BCP}), the laplacian of electron density ($\nabla\rho_{BCP}^2$), and the energetic components at the relevant BCPs in the DES and DES-ASP complex.

Component Pair	BCP interaction	ρ_{BCP}(a.u.)	$\nabla\rho_{BCP}^2$(a.u.)
DES 1 (THY + DPE)	BCP1 : O_{46} - H_{19}	8.67E-03	2.68E-02
DES 2 (THY + BP)	BCP 1 : H_{20} - O_{70}	6.06E-03	2.30E-02
	BCP 2 : H_{46} - C_5	8.28E-03	2.72E-02
Model structure 1 + DES 1	BCP 1 : O_{82} - H_{34}	6.37E-03	2.20E-02
	BCP 2 : O_{87} - H_{33}	3.65E-03	1.53E-02
	BCP 3 : O_{86} - H_{24}	2.48E-02	7.67E-02
	BCP 4 : H_{71} - O_{23}	1.35E-02	3.83E-02
Model structure 1 + DES 2	BCP 1 : O_{106} - H_{18}	8.18E-03	2.62E-02
	BCP 2 : H_{42} - O_{109}	6.27E-03	2.19E-02
	BCP 3 : O_{110} - H_{68}	6.75E-03	2.28E-02
Model structure 3 + DES 1	BCP 1 : H_{193} - O_{220}	1.48E-02	4.54E-02
	BCP 2 : N_{189} - H_{207}	3.46E-03	1.22E-02
	BCP 3 : H_{107} - O_{243}	5.68E-03	2.07E-02
Model structure 3 + DES 2	BCP 1 : H_{194} - O_{242}	9.54E-03	3.07E-02
	BCP 2 : H_{102} - O_{267}	6.24E-03	2.26E-02
	BCP 3 : S_{33} - H_{268}	7.96E-03	3.00E-02

The bond critical points (BCPs) seem to be the sites where the electron density is maximal in two directions and minimal in another third direction perpendicular to the first two. The electron density (ρ_{BCP}) corresponds to the strength of the interaction and the sign of ($\nabla\rho_{BCP}^2$)

specifies the characteristic of the interaction. If the BCP electron density is high, the bonding affinity is likely to be strong, while a low value indicates weak bonds and a significant distance between atoms. A negative Laplacian of electron density ($\nabla\rho_{BCP}^2$) designates a covalent bond, whereas a positive value suggests closed-shell interactive properties such as ionic, van der Waals, or hydrogen bonds. An extensive closed-shell interactive network was found using QTAIM analysis of pure DESs, as shown in 6.19a-b. Multiple greens and blue spikes between 0 and −0.05 a.u. They revealed non-covalent interactions such as hydrogen bonding and dispersion interactions crucial for stable DES production. The AIM analysis revealed that all the values of ρ_{BCP} and the $\nabla\rho_{BCP}^2$ at different BCPs of the studied DESs were positive, confirming the closed-shell noncovalent interactions. In each of the DES systems, two types of BCPs were observed, as presented in figure 6.18, which signified the interactive involvement of the active chemical groups present in the HBAs and the HBDs, i.e., −OH, ether, and hydrogen attached to phenyl ring groups, respectively. Table 6.9 provides the results of these calculations for the DES-asphaltene molecular system. All the electron densities (BCP) fall between 0.002 and 0.034 a.u., and the Laplacian of electron densities (BCP2) varies between 0.02 and 0.139 a.u. Therefore, the analysis agrees with the proposed requirements of weak interactions.

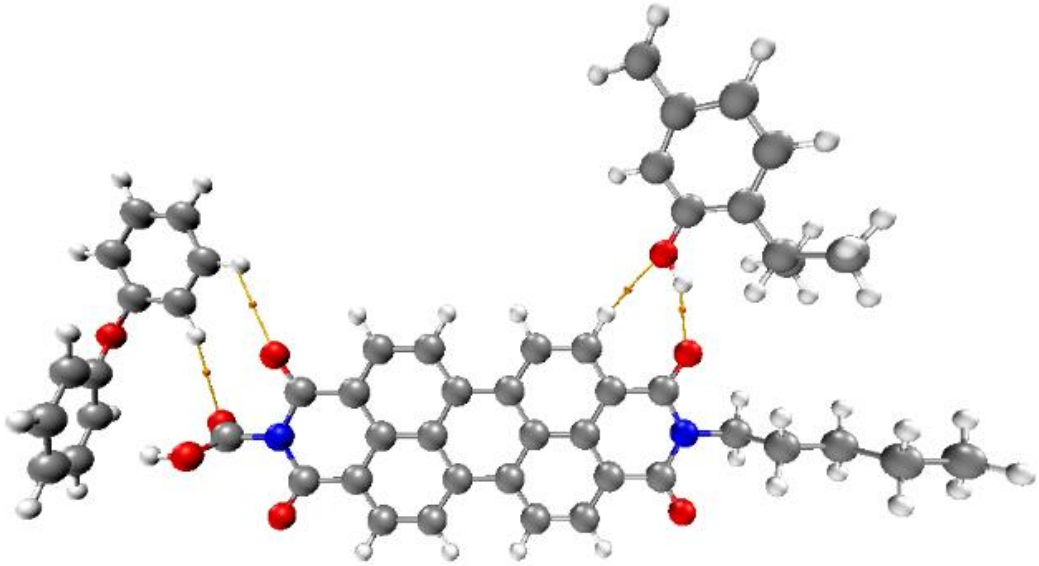

(a) DES1+Model Structure 1

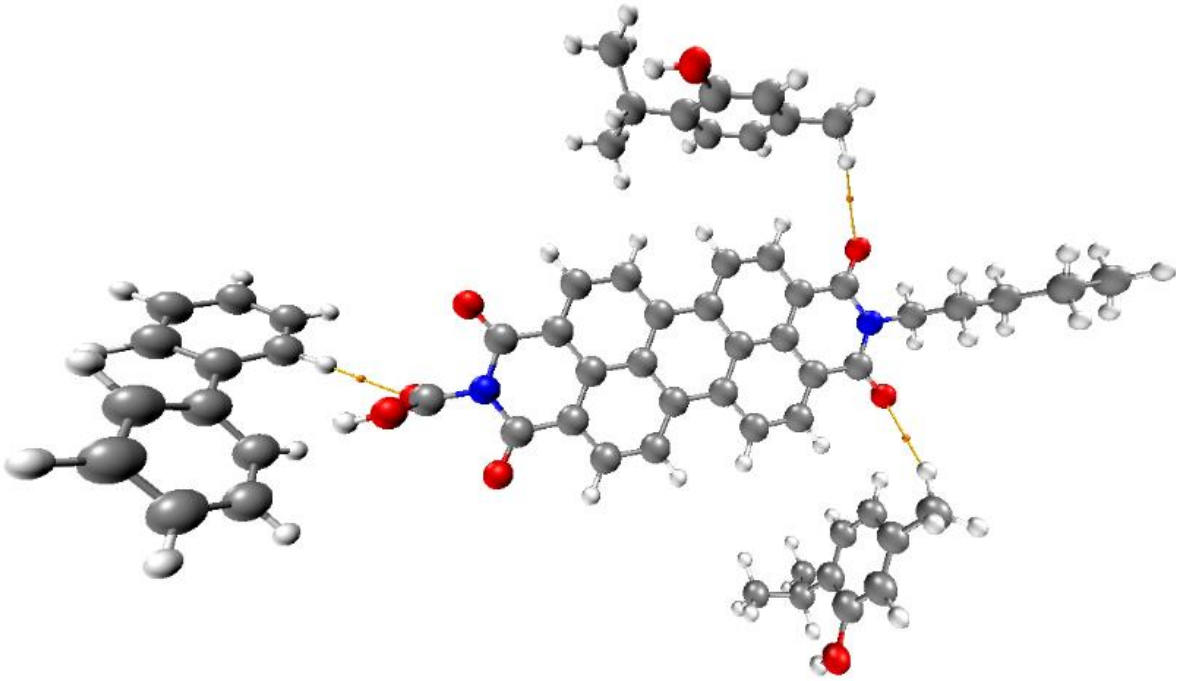

(b) DES2+Model Structure 1

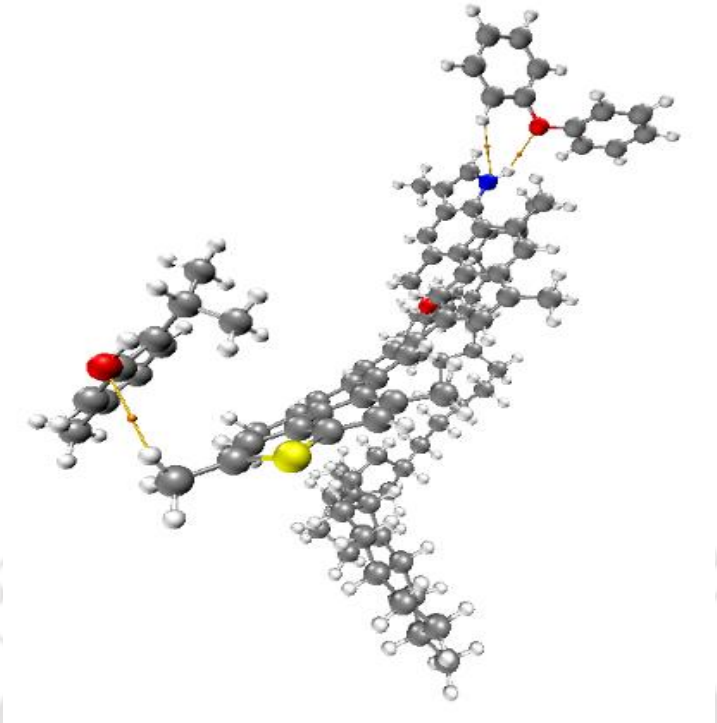

(c) DES1+Model Structure 2

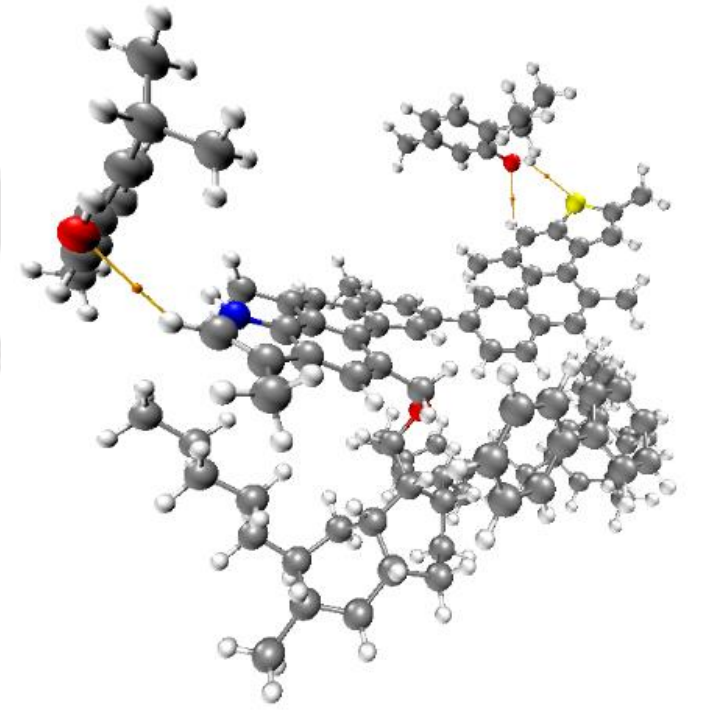

(d) DES2+Model Structure 2

Figure 6.18. The complex clusters of DES-ASP at the M06-2X/6-311+G (d, p) level reveal bond critical points (BCPs) and their corresponding paths.

6.8.6. Noncovalent Interaction

Noncovalent Interactions (NCI) study as an alternative approach to understanding the weaker interactions. NCI focuses on analyzing the electron density distribution in molecular systems in regions of low electron density and low gradient values. This method is often referred to as RDG analysis. This method was first developed to determine the presence of noncovalent bonds in a system (water and methane dimer) by Contreras-Garci´a and Johnson [59]. Spikes in (reduced density gradient) RDG graphs at low densities can be interpreted with the help of NCI [59]. The mathematically RDG can be interpreted as given in Eqn.

$$\text{RDG} = \frac{1}{2(3\pi^2)^{1/3}} \frac{|\nabla\rho|}{\rho^{4/3}} \qquad (6.9)$$

The insightful NCI analysis is based on the interpretation of RDG spikes. Hydrogen-bonding, van der Waals, and dispersion interactions are just a few examples of weak interactions that can be discovered and measured by an NCI study employing the RDG approach. The RDG scatter graph is plotted as a function of electron density multiplied by the sign of the electron density Hessian second eigenvalue. The RDG isosurfaces and RDG scatter plot for the DES-ASP complex at the M06-2X/6-311+G (d, p) level of theory demonstrate a wide range of weak interactions, from positive to negative values (see Figure 6.19). Different coloured spikes indicate a specific kind of interaction (blue: H-bonds or halogen bonds ($\lambda_2 < 0$); green: van der Waals or dispersion interaction ($\lambda_2 \cong 0$); and red: steric effect due to ring or cage formation ($\lambda_2 > 0$)). The presence of asphaltene in DESs has weakened the HBA-HBD interaction. A marginally small blue flake can be spotted in Figure 6.19c, whereas no green flakes were observed in the NCI diagram's intermolecular region of HBA and HBD (Figure 6.19 a-b). This suggested that along with the hydrogen-bonding network, the dispersion interactions were also affected in the presence of asphaltene dispersion in DES1.

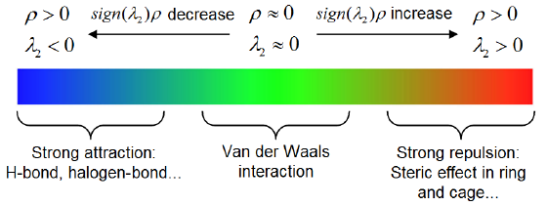

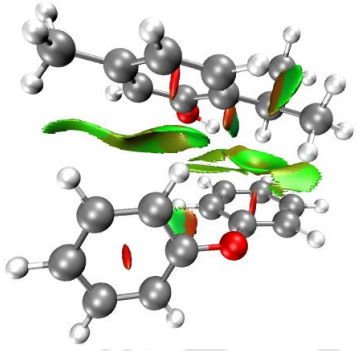

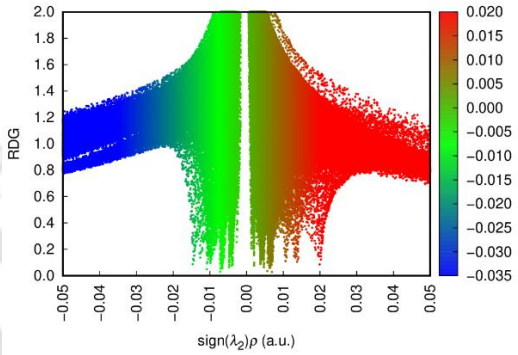

(a) DES 1

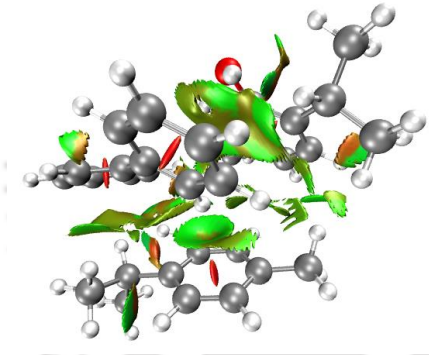

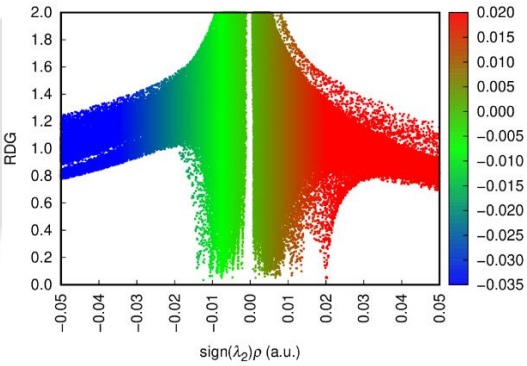

(b) DES 2

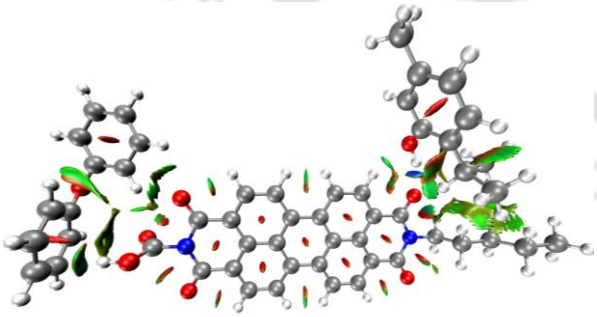

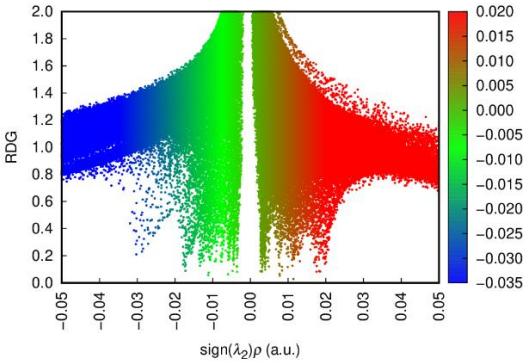

(c) Model structure-1 + DES 1

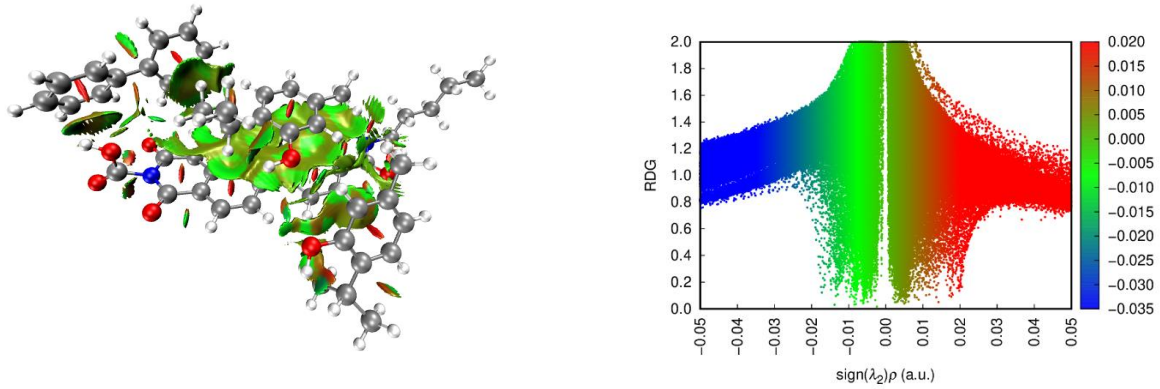

(d) Model structure-1 + DES 2

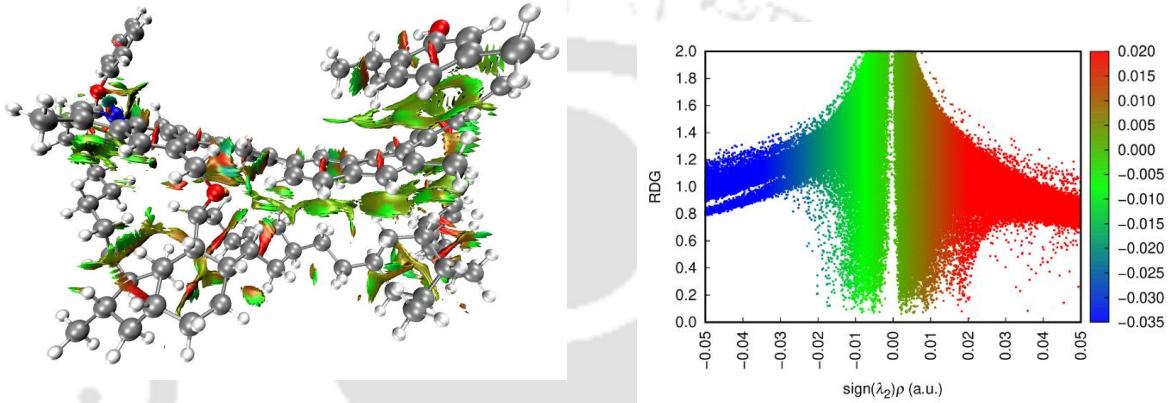

(e) Model Structure-2 + DES 1

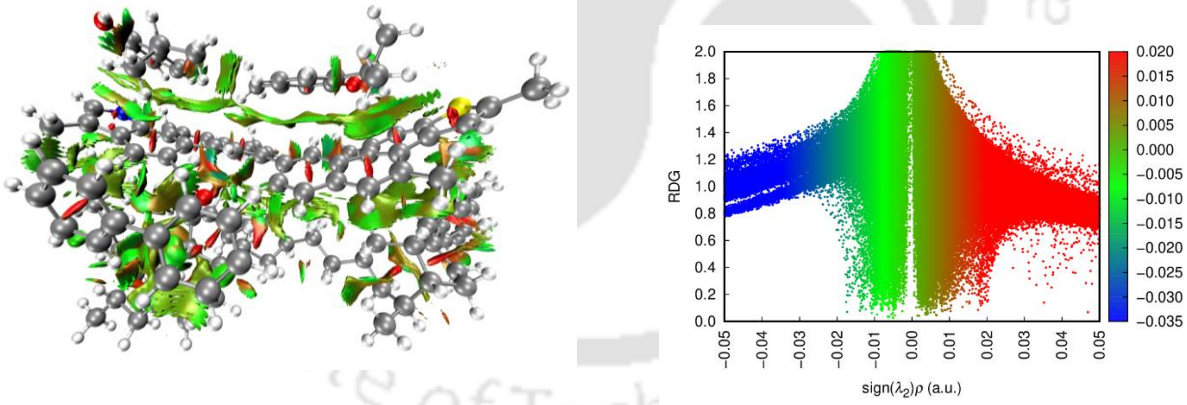

(f) Model structure-2 + DES 2

Figure 6.19. RDG iso-surfaces and scatter graphs of RDG for neat DES and DES-ASP clusters at the M06-2X/6-311+G(d,p) level.

Multiple low-density RDG peaks between 0 and 0.02 a.u. are seen, which the present RDG investigation interprets as evidence of the combination of hydrogen bonding and dispersion interactions (vdW). Hydrogen bonding at a lower level and the presence of this vdW interaction

are both evident in the iso-surfaces obtained from the RDG analysis. The DFT analysis phase of the quantum chemical analysis presents and confirms these interactions. RDG peaks in the range > 0.005 a.u. are evidence of steric repulsive hindrance caused by the presence of bulky aromatic rings in the molecular system. Dispersion interactions are more prevalent in the molecular system, which is consistent with the idea that DES components interact with asphaltene molecules in a way that is not reliant on covalent bonds and does not involve considerable electrostatic interaction.

6.9 Summary

The present study aims to understand the complex molecular level structure and solubility mechanism of asphaltene in green natural deep eutectic solvents. The theoretical DFT calculations were employed to predict the structure of a model asphaltene compound based on the chemical composition revealed by the FTIR spectra of the asphaltene compound extracted from crude oil. The model structure-2, based on the archipelago model, was found to be the most significant structure, as the IR spectra highly resemble the FT-IR spectra of extracted asphaltene. After that, excess enthalpy and activity coefficient values for thymol-based solvents were calculated using the COSMO-RS model. They were superior after benchmarking with conventional solvents such as toluene and xylene. The FT-IR and 2D-NMR suggest that the solvation capacity of the NADESs for the asphaltene is based on hydrogen bonding and van der Waals dispersion energy. The solubility of asphaltene is primarily due to the van der Waals dispersion energies of the solvents and the donor-acceptor energies of the hydrogen bonds between the asphaltene molecule and the green solvents. The lower solubility of Thymol: decanoic acid (3:2) is due to weaker van der Waals energies and reduced hydrogen bond forming capacity. The asphaltene solubility was found to be lowest in DES4 because of the additional length of the alkane chain in decanoic acid. It reduces its ability to prevent the π–π interaction in asphaltene molecules in contrast to other HBD, which consists of polar aromatic

rings. The outcome of the current approach helps us to understand the mechanism of asphaltene solubility and hence to develop targeted NADESs for asphaltene dispersion in crude oil.

The quantum chemical study on the DES-asphaltene complex suggests a stable formation of the DES-asphaltene complex in the DES phase. All the DESs are generally relatively stable regarding their respective HOMO-LUMO energy gap and interaction energy. The solvents with archipelago model structure 2 possess a stable structural arrangement with multiple interactions with the thymol and diphenyl ether and biphenyl Non-bonded interactions such as hydrogen bonding and dispersion interactions were present in the formation of both the DES and the DES-ASP clusters. Higher compactness can be witnessed in terms of significantly lowering the interaction energy for the DES and the DES-ASP formation. Overall, the result obtained with the quantum chemical calculation aligns with the experimental results. The QTAIM analysis suggests the formation of the DES-ASP complex via a combined effect of hydrogen bonding linkage with van der Waals dispersion interaction as supported by the electron density at BCP (ρ_{BCP}) and the Laplacian of electron density ($\nabla\rho_{BCP}^2$). The NCI plot with RDG analysis was performed to highlight the regions of weak interaction. Hydrogen bonding and dispersion interactions (vdW) were witnessed between 0 to −0.02 a.u. They confirmed the presence of weak non-bonded interactions in DES and the DES-ASP complex formation.

References

1. *Silva, F., et al., Extraction and Characterization (compositional and thermal) of Asphaltenes from Brazilian Vacuum Residues. Brazilian Journal of Petroleum and Gas, 2013. **7**(3).*
2. *Da Costa, L.M., et al., Density functional theory investigation of the contributions of π–π stacking and hydrogen-bonding interactions to the aggregation of model asphaltene compounds.* Energy & fuels, 2012. **26**(5): p. 2727-2735.
3. Painter, P., M. Sobkowiak, and J. Youtcheff, *FT-IR study of hydrogen bonding in coal.* Fuel, 1987. **66**(7): p. 973-978.
4. Zhao, R. and R.-Q. Zhang, *A new insight into π–π stacking involving remarkable orbital interactions.* Physical Chemistry Chemical Physics, 2016. **18**(36): p. 25452-25457.
5. Anisimov, M., et al., *Asphaltene aggregation in hydrocarbon solutions studied by photon correlation spectroscopy.* The Journal of Physical Chemistry, 1995. **99**(23): p. 9576-9580.
6. Wilt, B.K., W.T. Welch, and J.G. Rankin, *Determination of asphaltenes in petroleum crude oils by Fourier transform infrared spectroscopy.* Energy & fuels, 1998. **12**(5): p. 1008-1012.
7. Wang, H., et al., *Revealing the intermolecular interactions of asphaltene dimers by quantum chemical calculations.* Energy & Fuels, 2017. **31**(3): p. 2488-2495.
8. Scott, D.E., et al., *Deciphering structure and aggregation in asphaltenes: hypothesis-driven design and development of synthetic model compounds.* Chemical Society Reviews, 2021.
9. Hirschberg, A., et al., *Influence of temperature and pressure on asphaltene flocculation.* Society of Petroleum Engineers Journal, 1984. **24**(03): p. 283-293.
10. García, M.d.C., *Crude oil wax crystallization. The effect of heavy n-paraffins and flocculated asphaltenes.* Energy & fuels, 2000. **14**(5): p. 1043-1048.
11. Chen, C., et al., *Study of asphaltene deposition from Tahe crude oil.* Petroleum Science, 2013. **10**(1): p. 134-138.
12. Mutelet, F., et al., *Solubility parameters of crude oils and asphaltenes.* Energy & fuels, 2004. **18**(3): p. 667-673.
13. Buenrostro-Gonzalez, E., et al., *Asphaltene precipitation in crude oils: Theory and experiments.* AIChE Journal, 2004. **50**(10): p. 2552-2570.
14. Zheng, C., et al., *Dissolution and suspension of asphaltenes with ionic liquids.* Fuel, 2019. **238**: p. 129-138.
15. Abbott, A.P., et al., *Novel solvent properties of choline chloride/urea mixtures.* Chemical communications, 2003(1): p. 70-71.
16. Martins, M.A., S.P. Pinho, and J.A. Coutinho, *Insights into the nature of eutectic and deep eutectic mixtures.* Journal of Solution Chemistry, 2019. **48**(7): p. 962-982.
17. Kashefi, S., et al., *Investigation of the performance of several chemical additives on inhibition of asphaltene precipitation.* Energy Sources, Part A: Recovery, Utilization, and Environmental Effects, 2016. **38**(24): p. 3647-3652.

18. Jahangiri, S., et al., *Choline chloride/monoethylene glycol deep eutectic solvent as a new asphaltene precipitation inhibitor.* Petroleum Science and Technology, 2017. **35**(19): p. 1896-1902.
19. Rashid, Z., et al., *Investigating the solubility of petroleum asphaltene in ionic liquids and their interaction using COSMO-RS.* Journal of industrial and engineering chemistry, 2019. **79**: p. 194-203.
20. Abbott, A.P., et al., *Deep eutectic solvents formed between choline chloride and carboxylic acids: versatile alternatives to ionic liquids.* Journal of the American Chemical Society, 2004. **126**(29): p. 9142-9147.
21. Kumar, N. and T. Banerjee, *Dearomatization insights with phosphonium-based deep eutectic solvent: Liquid–liquid equilibria experiments and predictions.* Journal of Chemical & Engineering Data, 2021. **66**(9): p. 3432-3442.
22. Testing, A.S.f. and Materials, *ASTM D6560, Standard Test Method for Determination of Asphaltenes (Heptane Insolubles) in Crude Petroleum and Petroleum Products*. 2005, ASTM International West Conshohocken, PA.
23. Dennington, R., T. Keith, and J. Millam, *GaussView, version 5.* 2009.
24. Mohan, M., V.V. Goud, and T. Banerjee, *Solubility of glucose, xylose, fructose and galactose in ionic liquids: Experimental and theoretical studies using a continuum solvation model.* Fluid Phase Equilibria, 2015. **395**: p. 33-43.
25. Anantharaj, R. and T. Banerjee, *COSMO-RS-based screening of ionic liquids as green solvents in denitrification studies.* Industrial & engineering chemistry research, 2010. **49**(18): p. 8705-8725.
26. Eckert, F. and A. Klamt, *Fast solvent screening via quantum chemistry: COSMO-RS approach.* AIChE Journal, 2002. **48**(2): p. 369-385.
27. Li, Y. and Y. Jin, *Effects of thermal pretreatment on acidification phase during two-phase batch anaerobic digestion of kitchen waste.* Renewable Energy, 2015. **77**: p. 550-557.
28. Kurnia, K.A., S.o.P. Pinho, and J.o.A. Coutinho, *Evaluation of the conductor-like screening model for real solvents for the prediction of the water activity coefficient at infinite dilution in ionic liquids.* Industrial & Engineering Chemistry Research, 2014. **53**(31): p. 12466-12475.
29. COSMOtherm, V., *C3. 0, Release 1501; COSMOlogic GmbH & Co KG, Leverkusen, Germany, 2014*.
30. Groenzin, H. and O.C. Mullins, *Molecular size and structure of asphaltenes from various sources.* Energy & Fuels, 2000. **14**(3): p. 677-684.
31. Sabbah, H., et al., *Evidence for island structures as the dominant architecture of asphaltenes.* Energy & Fuels, 2011. **25**(4): p. 1597-1604.
32. Mullins, O.C., *The modified Yen model.* Energy & Fuels, 2010. **24**(4): p. 2179-2207.
33. Larkin, P., *Infrared and Raman spectroscopy: principles and spectral interpretation*. 2017: Elsevier.
34. Chukanov, N.V. and A.D. Chervonnyi, *Infrared spectroscopy of minerals and related compounds*. 2016: Springer.

35. Baldrich, C., B. Murcia, and A. Bueno, *Development of a methodology to determine the aromatic structural distribution in light and medium petroleum fractions by HPLC.* CT&F-Ciencia, Tecnología y Futuro, 2006. **3**(2): p. 149-162.
36. Huang, K., et al., *Integration of acetic acid catalysis with one-pot protic ionic liquid configuration to achieve high-efficient biorefinery of poplar biomass.* Green Chemistry, 2021. **23**(16): p. 6036-6049.
37. Achinivu, E.C., et al., *A predictive toolset for the identification of effective lignocellulosic pretreatment solvents: a case study of solvents tailored for lignin extraction.* Green Chemistry, 2021. **23**(18): p. 7269-7289.
38. Andrews, A.B., et al., *Diffusivity of asphaltene molecules by fluorescence correlation spectroscopy.* The Journal of Physical Chemistry A, 2006. **110**(26): p. 8093-8097.
39. Goncalves, S., et al., *Absorbance and fluorescence spectroscopy on the aggregation behavior of asphaltene–toluene solutions.* Fuel, 2004. **83**(13): p. 1823-1828.
40. Andreatta, G., N. Bostrom, and O.C. Mullins, *High-Q ultrasonic determination of the critical nanoaggregate concentration of asphaltenes and the critical micelle concentration of standard surfactants.* Langmuir, 2005. **21**(7): p. 2728-2736.
41. Andreatta, G., et al., *Nanoaggregates and structure− function relations in asphaltenes.* Energy & Fuels, 2005. **19**(4): p. 1282-1289.
42. Zojaji, I., A. Esfandiarian, and J. Taheri-Shakib, *Toward molecular characterization of asphaltene from different origins under different conditions by means of FT-IR spectroscopy.* Advances in Colloid and Interface Science, 2021. **289**: p. 102314.
43. Zhao, Y., M.R. Gray, and K.H. Chung, *Molar kinetics and selectivity in cracking of Athabasca asphaltenes.* Energy & fuels, 2001. **15**(3): p. 751-755.
44. Silverstein, R.M. and G.C. Bassler, *Spectrometric identification of organic compounds.* Journal of Chemical Education, 1962. **39**(11): p. 546.
45. Smith, B., *Infrared spectral interpretation: a systematic approach*. 2018: CRC press.
46. Siminovitch, D., P. Wong, and H. Mantsch, *High-pressure infrared spectroscopy of ether-and ester-linked phosphatidylcholine aqueous dispersions.* Biophysical journal, 1987. **51**(3): p. 465-473.
47. Chang, C.-L. and H.S. Fogler, *Stabilization of asphaltenes in aliphatic solvents using alkylbenzene-derived amphiphiles. 2. Study of the asphaltene-amphiphile interactions and structures using Fourier transform infrared spectroscopy and small-angle X-ray scattering techniques.* Langmuir, 1994. **10**(6): p. 1758-1766.
48. Athokpam, B., S.G. Ramesh, and R.H. McKenzie, *Effect of hydrogen bonding on the infrared absorption intensity of OH stretch vibrations.* Chemical Physics, 2017. **488**: p. 43-54.
49. Sheng, X., et al., *FTIR study of hydrogen bonding interaction between fluorinated alcohol and unsaturated esters.* Spectrochimica Acta Part A: Molecular and Biomolecular Spectroscopy, 2018. **198**: p. 239-247.
50. Claridge, T.D., *High-resolution NMR techniques in organic chemistry*. Vol. 27. 2016: Elsevier.
51. Zhao, Y. and D.G. Truhlar, *The M06 suite of density functionals for main group thermochemistry, thermochemical kinetics, noncovalent interactions, excited states, and transition elements: two new functionals and systematic testing of four M06-class*

functionals and 12 other functionals. Theoretical chemistry accounts, 2008. **120**(1): p. 215-241.

52. Grimme, S., S. Ehrlich, and L. Goerigk, *Effect of the damping function in dispersion corrected density functional theory*. Journal of computational chemistry, 2011. **32**(7): p. 1456-1465.
53. Boys, S.F. and F. Bernardi, *The calculation of small molecular interactions by the differences of separate total energies. Some procedures with reduced errors*. Molecular Physics, 1970. **19**(4): p. 553-566.
54. Frisch, M.e., et al., *Gaussian 16*. 2016, Gaussian, Inc. Wallingford, CT.
55. Bader, R.F., *Atoms in molecules.* Accounts of Chemical Research, 1985. **18**(1): p. 9-15.
56. Marekha, B.A., O.N. Kalugin, and A. Idrissi, *Non-covalent interactions in ionic liquid ion pairs and ion pair dimers: a quantum chemical calculation analysis.* Physical Chemistry Chemical Physics, 2015. **17**(26): p. 16846-16857.
57. Simon i Rabasseda, S., M. Duran i Portas, and J. Dannenberg, *How does basis set superposition error change the potential surfaces for hydrogen-bonded dimers? ©* Journal of Chemical Physics, 1996, vol. 105, núm. 24, p. 11024-11031, 1996.
58. Fukui, K., *Theory of orientation and stereoselection*, in *Orientation and Stereoselection*. 1970, Springer. p. 1-85.
59. Johnson, E.R., et al., *Revealing noncovalent interactions.* Journal of the American Chemical Society, 2010. **132**(18): p. 6498-6506.

Chapter 7

Research Conclusions and Future Scope

7.1. Research Conclusions

The primary conclusions of the thesis are summarized below:

The thesis begins by discussing the liquid structure of DESs and solvent-solute interaction in Chapter 2. Atomistic MD simulations were then performed to investigate the solvation structure of benzene, thiophene, and *n*-hexane in monoethanolamine-based DESs. This study reveals that the solvation of thiophene in the studied DES is higher than benzene due to the electron delocalization effect of sulphur atom attached to the aromatic ring of thiophene. The monoethanolamine (MEA), which acts as the hydrogen bond donor (HBD), exhibits a stronger hydrogen bond than the choline cation. Benzene was found to interact with the choline cation and HBD (MEA) components of the deep eutectic solvent through multiple weak non-covalent interactions (e.g., C–H$\cdots\pi$, O–H$\cdots\pi$, and N–H$\cdots\pi$).

Similarly, thiophene's electron-withdrawing property improves its solubility in DES through non-covalent interactions (e.g., C–H$\cdots\pi$, O–H$\cdots\pi$, and N–H$\cdots\pi$). The solvation environment is dynamic and is dominated by different hydrogen bonding interactions along with dynamic heterogeneities resulting from hydrogen bonding interactions. Moreover, the DFT study reveals that Cl^- acts as a charge transfer bridge between the choline cation and monoethanolamine, which further confirms the rigid nature of DES after the solvation of organic solutes. Further, the ^{1}H and 2D NOESY spectroscopy revealed that the choline chloride and HBD were the primary interaction sites between aromatic compounds with DES.

The thesis then proceeds to utilise the understanding of DES liquid structure and specific solute-solvent interaction to a process that meets the criteria of being "green" in the extraction of the light aromatic compound. Chapter 3 reports a phosphonium-based DES for the dearomatisation of model diesel components at 298K and *p*=1 bar. The DES comprising of Hydrogen Bond Acceptor (HBA), namely methyltriphenylphosphonium bromide (MTPB),

along with ethylene glycol as hydrogen bond donor (HBD), was formulated with a molar ratio of 1:4. The DES was then used to extract benzene from representative diesel fuel components namely a mixture of *n*-decane, *n*-dodecane, and *n*-hexadecane. The experimental results revealed an increase in distribution ratio, selectivity, and extraction efficiency for aromatic extraction from model diesel components in the following order: *n*-hexadecane > *n*-dodecane > *n*-decane. The extraction efficiency achieved for benzene using the (MTPB+EG) was 83% for a single stage and more than 98% for three stages or more. The three systems presented RMSD (%) values of ~1%, which specifies definitive agreement amid the experimental and COSMO-SAC model predictions. An absence of DES was found in the *n*-alkane-rich phase, indicating this would decrease the operational cost of the extraction process, as it will reduce the extra cost of solvent recovery systems. Further, COSMO-SAC-based sigma profile studies also signify a high interaction between DES and benzene, especially in the hydrogen bond acceptor regions. It revealed the benzene extraction mechanism using FTIR and NMR, where the non-covalent interaction between DES and benzene accounts for the higher dearomatisation efficiencies.

The following chapter 4 in the thesis has demonstrated the extraction of ultra-low benzothiophene(BT) from *n*-decane(DC) as representative model diesel fuel using phosphonium-based deep eutectic solvents (DESs) at 308.15 K and 1 bar pressure. The Liquid-Liquid Equilibria studies of DES comprising Methyltriphenylphosphonium bromide (MTPB) and Ethylene glycol (EG) in the specific molar ratio of 1:4 was analysed in the extraction of benzothiophene from *n*-decane as representative model diesel. The LLE experimental data was then validated with the quantum chemical-based COSMO-SAC predictions with deviations within 1.07% in average RMSDs. The extraction efficiency achieved for benzothiophene from *n*-decane as representative model diesel was 78% for the single stage and more than 98% for the 3 stages.

The higher extraction of benzothiophene is due to the higher contribution of hydrogen bonding and dispersion-type interactions. Within the DFT calculation, the BT interacts with the MTP cation and EG of the deep eutectic solvent through multiple non-covalent interactions (e.g., C–H···π, Br^{-}···O–H, Br^{-}···C–H and O–H···π). However, they were not found to interact directly with the bromide (Br^{-}) ion. The charge transfer analysis using the CHELPG and Mulliken population charge analysis reveals substantial charge transfer from the aromatic sulphur compound to the DES, indicating strong non-bonded interaction compared to the aliphatic model diesel compound. The absence of benzothiophene and bromide (Br^{-}) ion interactions results from the retention of multiple, strong hydrogen bonds between the ethylene glycol as HBD, MTP cation, and bromide (Br^{-}) ion species upon formation of the DES clusters. Notably, all the intermolecular interactions within the DES cluster are preserved after a complex cluster formation, confirming DES stability during the liquid-liquid extraction studies.

Further, this thesis provides insights into the extraction of benzene from hydrocarbon stream using atomistic MD simulations in Chapter 5. The classical molecular dynamic (MD) simulation technique was employed to investigate the equilibrium interphase behaviour of the DES + benzene + *n*-hexane ternary system concerning DES-rich and hydrocarbon-rich phases. In the ternary system, the DES-benzene pair possessed higher interaction energy than DES-hexane, and the RDF plots corroborated similar results. ETG (ethylene glycol)-benzene gave a higher hydrogen bonding than MTP (methyl triphenyl phosphonium bromide)-benzene because of a higher number of hydroxyl groups present in ethylene glycol. The SDF results suggest that the localised iso-surface density of benzene is very closely distributed around the more active sites of MTP and ETG. The self-diffusivity value also suggests higher solubility of benzene in DES than *n*-hexane based on the mean square displacement. The 2D NMR spectra also confirmed the long-range interaction between the DES-benzene pair. In summary,

the cation MTP of HBA and the HBD both play a predominant role in benzene extraction from *n*-hexane. Consequently, this study offers new findings for the computational MD simulation of benzene extraction from hexane, which becomes helpful in the case of the absence of experimental data.

In the penultimate chapter of the thesis, we have focussed on the screening of DES for asphaltene precipitation inhibition using the COSMO-RS model. In addition, an accurate molecular model structure was also predicted and used for computational calculations. Initially, the chemical structure of asphaltene was confirmed by performing FTIR and quantum chemical calculations. Further, several combinations of HBAs and HBDs of DESs were screened using the COSMO-RS model by calculating the thermodynamic properties. A rank of the solvents based on their capability of interaction was presented. From the screening results, the hydrophobic DESs such as thymol: diphenyl ether (1:1), thymol: biphenyl (1.6:1), biphenyl: cadaverine (1:5.66), 2-methylquinoline:cadaverine (1:3.34), thymol: decanoic acid (3:2 and 1:1), and thymol: camphor (7:3) were seen to be potential solvents for asphaltene dissolution than other DESs. Thereafter, the experimental solubility measurement was performed to verify the COSMO-RS results. DES composed of thymol-diphenyl ether gives the best performance for asphaltene solubility, reaching a value of 43 ± 0.58 mg/ml asphaltene solubility at 298.15 K compared to other investigated DESs. The asphaltene and solvents were further characterized using FTIR and NMR techniques to understand the molecular interactions and solubility mechanism of asphaltene in DES. The dispersion mechanism of the asphaltene in DES was found to proceed via intramolecular and intermolecular interactions, as demonstrated experimentally and computationally.

7.2. Future Scope

The scope of DES as an extracting agent in the application of dearomatisation adds a new class

of solvent that has the potential to improve extraction efficiency for hard-to-separate systems. The lingering concerns about the recovery and recyclability of DESs provide us with some perspective that can be addressed in future work. The following describes the future scope.

a) Detailed research can be conducted on DESs and ILs-based DESs solvents by tuning up their physical and chemical properties using machine learning for complex system applications. The large set of HBA and HBD can help us to tune the solvents more accurately with the help of artificial intelligence.
b) The regeneration of DES is a significant impediment to its use as an extracting agent for simultaneous desulfurization and dearomatisation. We performed the regeneration for the benzene-DES system, but still, there is scope to improve the regeneration of DESs in concurrent systems. This problem needs to be formulated and solved so that these solvents can be explored in industry, which can be possible through technology transfer.
c) The recyclability of these environmentally friendly solvents is a further key issue that might be addressed in future studies. Antisolvents and cosolvents could be explored to recover solvents in complex simultaneous dearomatisation, desulfurization, and denitrification processes.
d) Development of force field parameters for the predicted asphaltene compounds can be undertaken. Thereafter, their aggregation behavior studies in model crude oil can be carried through classical molecular dynamics simulation. The MD study can give more insights into the aggregation behavior of asphaltene in model crude oil and their inhibition mechanisms.
e) Another avenue of future research could be using green solvents such as DES as dispersing and extracting agents for different applications such as biological and pharmaceutical compounds.

APPENDIX

8.1 Sample Calculation for Mole Fraction from NMR Spectra

A sample calculation has been illustrated below to quantify the mixture's known composition of DES (MTPB+EG), benzene, and hexane (Chapter 3). The peak position and its components are located in Figure A1 is given below.

Stoichiometric Ratio Calculation of pure DES from ^{1}H NMR data

Figure A1 shows the ^{1}H NMR spectra of the prepared DES solvent (Methyltriphenylphosphonium bromide (MTPB): Ethylene glycol; molar ratio 1:4) in the supporting information. The peak of $CdCl_3$-d_6 was observed at 7.27 ppm and is used as a reference peak. The equation given below is used to calculate the concentration of other components as given below.

$$x_i = \frac{H_i}{\sum_{i=1}^{3} H_i} \qquad 8.1$$

So, from figure A1, the peak position and its area are calculated as given below.

Peak area equivalent to 1 Hydrogen of DES (Peaks of MTBP)= (7.52+30.36)/15 = 2.52 (peak assigned to hydrogen atoms of Phenyl rings of MTPB)

Similarly for CH_3 of MTPB = (3.82+3.81)/3 = 2.542 (peak assigned to CH_3 of MTPB)

Peak area equivalent to 1 Hydrogen of DES(Peaks of ETG)= (38.21)/4= 9.55

It is interesting to observe that the peak area of $–CH_2$ in Ethylene glycol contributes an area of 38.21 or 38.21/4=9.55. This is approximately four times the contribution of the hydrogen atom of MTBP i.e, 2.52. This proves the fact that the mixture of MTBP and Ethylene Glycol are in the stoichiometric ratio of 1:4 and remains as a single phase entity in DES form. This similar calculation was also repeated for the extract and raffinate phase of the LLE experiment.

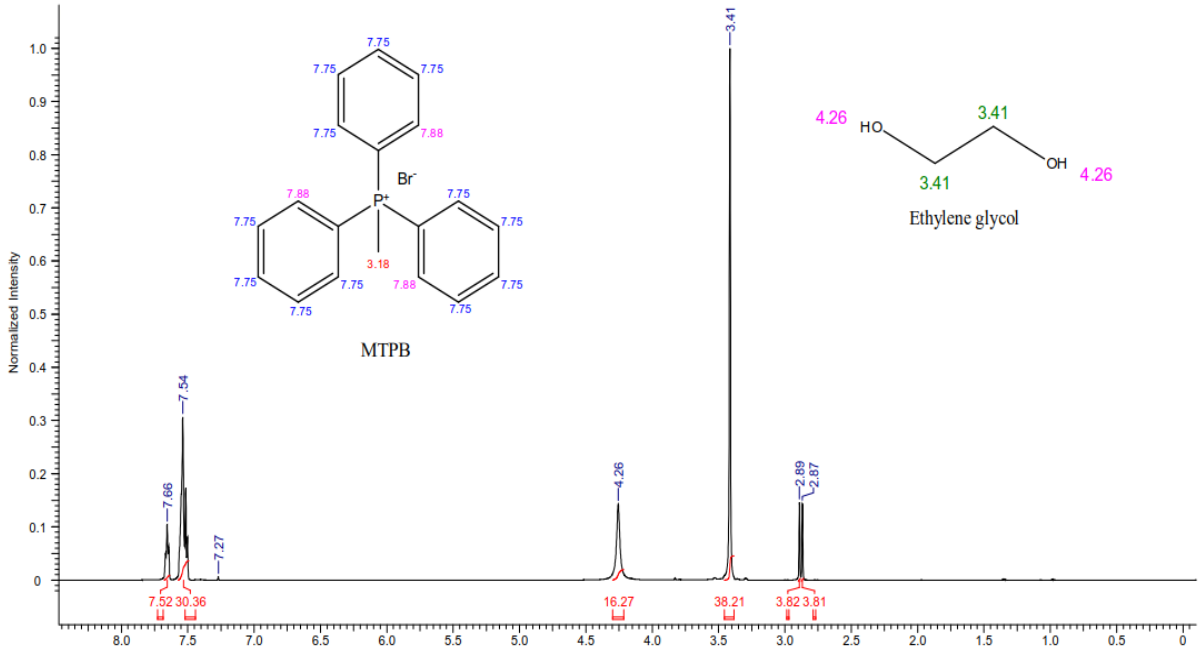

Figure A1. ^{1}H NMR spectra of DES (7.27 ppm belongs to NMR solvent ($CdCl_3$-d_6)).

8.2 COSMO-SAC Model and Solubility Thermodynamics of DES

The activity coefficient $\gamma_{i/s}$ of solute *i* in the solution *s* is derived from the following equation 1.

$$\ln \gamma_{i/s} = \frac{\Delta G_{i/s}^{*res} - \Delta G_{i/s}^{*res}}{RT} + \ln \gamma_{i/s}^{SG} \qquad 8.2$$

Here ΔG^{*res} is the restoring solvation free energy, superscript *SG* denotes the Staverman-Guggenheim combinatorial term (Table A.2). Finally, the activity coefficient is calculated and given as equation 2.

$$\ln\gamma_{i/s} = n_i \sum_{\sigma} P_i(\sigma_m)\left[\ln\Gamma_s(\sigma_m) - \Gamma_i(\sigma_m)\right] + \ln\gamma_{i/s}^{SG} \qquad 8.3$$

Here $\Gamma_s(\sigma_m)$ and $\Gamma_i(\sigma_m)$ are the activity coefficient of the segment in the mixture and in the component *i*, respectively. σ_m is the surface charge density of segment mixture. The three-dimensional screening charge density distribution $p_i(\sigma_m)$ is quantified using the σ-profile, which is the probability of finding a surface segment with screening charge density σ, i.e., $p(\sigma) = \{A_i(\sigma)\}/A_i$, where $A_i(\sigma)$ is the surface area with a charge density of value σ and A_i is total surface area of species *i*. The term, $n_i = A_i/a_{eff}$, here, a_{eff} is the effective area of the standard surface segment. The interactions, both electrostatic and hydrogen bonding, are taken into account through a ΔW term (equation 3).

$$\Delta W(\sigma_m, \sigma_n) = \left(\frac{\alpha'}{2}\right)(\sigma_m + \sigma_n)^2 + c_{hb} \max[0, \sigma_{acc} - \sigma_{hb}] \min[0, \sigma_{don} + \sigma_{hb}] \qquad 8.4$$

Where σ_m and σ_n are charge densities of the paired segments m and n in mixture. $\alpha'/2$ is a constant for the misfit energy, c_{hb} the hydrogen bonding parameter, and σ_{hb} a cutoff value for the hydrogen bonding interactions. Hydrogen bonds can occur between two segments. To express them, the segments are divided into two categories: acceptor and donor. In fact, segments can be either neutral segments, acceptor segments (σ_{acc}), or donor segments (σ_{don}). The global adjustable parameters for generating the activity coefficient via a statistical mechanical framework were the effective area of the standard surface segment (a_{eff} = 6.32 Å^2), the misfit energy interaction constant [α' = 8419 kcal Å^4/(mol e^2)], the cutoff for hydrogen-bonding interaction (σ_{hb} = 0.0084 e/Å^2), and the hydrogen-bonding interaction constant [c_{hb} = 75,006 kcal Å^4/(mol e^2)].

COSMO-SAC applies the concept of mutual solubility as a function of temperature and hence predicts the eutectic composition and temperature employing solid−liquid equilibrium (SLE) theory [3]. The procedure starts with the geometry optimization followed by COSMO-SAC predictions. The geometry optimization on all the structures was carried out using the density functional theory (DFT). Thereafter the COSMO file was generated. Thereafter, the mole fraction was predicted for both HBD and HBA by the activity coefficient in either phase at different temperatures (T) with the following equation 4.

$$\ln\left(\gamma_{solute} x_{solute}\right) = \frac{-\Delta H_f}{RT_m}\left(\frac{1}{T} - \frac{1}{T_m}\right) \qquad 8.5$$

Where γ_{solute}, x_{solute}, ΔH_f, and T_m are the activity coefficient, the mole fraction, the enthalpy of fusion, and the melting point, respectively. For the ideal situation, the activity coefficient of the solute in the liquid phase is unity. i.e., γ_{solute} =1. Then the ideal solubility equation is (equation 5).

$$\ln x_{solute} = \frac{-\Delta H_f}{RT_m}\left(\frac{1}{T} - \frac{1}{T_m}\right) \qquad 8.6$$

For the prediction of experimental mole fraction, mole fraction at ideal solvation from equation (5) is predicted. This value is then used to obtain the activity coefficient of the component in the mixture using COSMO-SAC model in equation (2). Thereafter the desired mole ratio for HBA: HDB can be found for the eutectic formation.

Table A.1: Equations used in the NRTL and UNIQUAC model

NRTL Model

$$\ln \gamma_i = \frac{\sum_{j=1}^{c} \tau_{ji} G_{ji} x_j}{\sum_{k=1}^{c} G_{ki} x_k} + \sum_{j=1}^{c} \left[\frac{G_{ij} x_j}{\sum_{k=1}^{c} G_{kj} x_k} \left(\tau_{ij} - \frac{\sum_{i=1}^{c} \tau_{ij} G_{ij} x_i}{\sum_{k=1}^{c} G_{kj} x_k} \right) \right]$$

$$G_{ij} = \exp\left(-\alpha_{ji}\tau_{ji}\right),\ \tau_{ji} = \left[\left(g_{ji} - g_{ii}\right)/RT\right] \text{ and } \alpha_{ji} = \alpha_{ij} = \alpha$$

UNIQUAC Model

$$\ln \gamma_i = \ln\left(\frac{\Phi_i}{x_i}\right) + \frac{z}{2} q_i \ln\left(\frac{\theta_i}{\Phi_i}\right) + l_i - \frac{\Phi_i}{x_i}\sum_{j=1}^{c} x_j l_j + q_i \left(1 - \ln \sum_{j=1}^{c} \theta_j \tau_{ji} - \sum_{j=1}^{c} \frac{\theta_j \tau_{ij}}{\sum_{k=1}^{c} \theta_k \tau_{kj}}\right)$$

$$\tau_{ji} = \frac{g_{ji} - g_{ii}}{RT} = \frac{A_{ji}}{T};\ \theta_i = \frac{q_i x_i}{q_T};\ q_T = \sum_k q_k x_k;\ \Phi_i = \frac{r_i x_i}{r_T}$$

$$r_T = \sum_k r_k x_k;\ l_i = \frac{z}{2}(r_k - q_k) + 1 - r_k$$

Table A.2: Equations used in the COSMO-RS calculations

Sigma profile of component and mixture	$P_s(\sigma) = \sum_{i \in S} x_i p^{x_i}(\sigma)$	
Sigma profile averaging	$\sigma_m = \frac{\sum_n \sigma_n^* \frac{r_n^2 r_{eff}^2}{r_n^2 + r_{eff}^2} \exp\left(-\frac{d_{mn}^2}{r_n^2 + r_{eff}^2}\right)}{\sum_n \frac{r_n^2 r_{eff}^2}{r_n^2 + r_{eff}^2} \exp\left(-\frac{d_{mn}^2}{r_n^2 + r_{eff}^2}\right)},\ r_{eff} = \sqrt{a_{eff}/\pi},\ r_n = \sqrt{a_n/\pi}$	
Sigma potential (Chemical potential of segment)	$\mu_s(\sigma) = -kT \ln\left\{\sum_{\sigma'} \exp\left[\frac{-E_{pair}(\sigma,\sigma') + \mu_s(\sigma')}{kT}\right]\right\} + kT \ln p_s(\sigma)$	(a)
	$p_s(\sigma)\Gamma_s(\sigma) = \exp\left(\frac{\mu_s(\sigma)}{kT}\right)$	(b)

Activity coefficient of Segment	$\ln \Gamma_s(\sigma) = -\ln\left\{\sum_{\sigma'} p_s(\sigma)\Gamma_s(\sigma)\exp\left[\frac{-E(\sigma,\sigma')}{kT}\right]\right\}$
Solubility equation	$\ln(\gamma^L_{solute}\, x^L_{solute}) = \frac{-\Delta h_f}{R}\left(\frac{1}{T}-\frac{1}{T_m}\right)-\frac{\Delta c_p}{R}\left(\frac{T_m-T}{T}\right)+\frac{\Delta c_p}{R}\ln\left(\frac{T_m}{T}\right)$
Activity coefficient in mixture	$\ln\gamma_{i/s} = n_i \sum_{\sigma} P_i(\sigma)\left[\ln\Gamma_s(\sigma) - \Gamma_i(\sigma)\right] + \ln\gamma^{SG}_{i/s}$ (a)
	$\ln\gamma^{SG}_{i/s} = \ln\frac{\phi_i}{x_i} + \frac{z}{2} q_i \ln\frac{\theta_i}{\phi_i} + li - \frac{\phi_i}{x_i}\sum_j x_j l_j$ (b)
Staverman-Guggenheim term	Where $\theta_i = \frac{x_i q_i}{\sum_j x_j q_j}$, $\phi_i = \frac{x_i r_i}{\sum_j x_j r_j}$, $l_i = \frac{z}{2}\left((r_i - q_i) - (r_i - 1)\right)$ (c)

8.3 Molecular Dynamic Simulation: Setup and Running

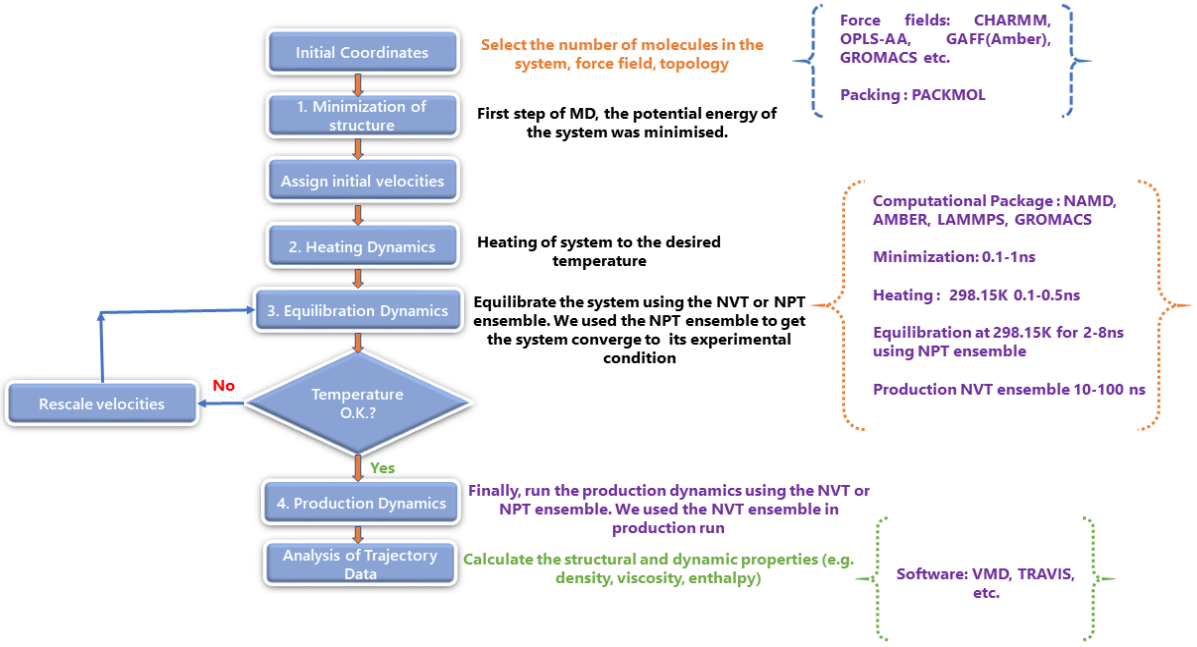

8.4 Description of AMBER Force Field

$$E_{Total} = E_{Bonded} + E_{Nonbonded}$$

$$E_{Total} = \left(E_{Bond} + E_{Angle} + E_{Dihedral} \right) + \left(E_{vdW} + E_{Electrostatic} \right)$$

$$E_{Total} = \sum_{Bonds} K_b (r - r_0)^2 + \sum_{Angles} K_\theta (\theta - \theta_0)^2 + \sum_{Dihedrals} \frac{V_n}{2} [1 + \cos(n\phi - \gamma)]$$
$$+ \sum_{i=j}^{N-1} \sum_{i<j}^{N} \left\{ 4\varepsilon_{ij} \left[\left(\frac{\sigma_{ij}}{r_{ij}} \right)^{12} - \left(\frac{\sigma_{ij}}{r_{ij}} \right)^{6} \right] + \frac{q_i q_j}{4\pi\varepsilon_0 r_{ij}} \right\}$$

8.5 A Sample NAMD Configuration File

```
#############################################################
## JOB DESCRIPTION                                         ##
#############################################################
# Minimization of 400 DES, 400 heptane and 200 molecules of quinoline
#############################################################
## ADJUSTABLE PARAMETERS                                   ##
#############################################################
ambercoor           ../common/ER4.inpcrd
set temperature     0
set outputname      ER4_min
set restart         0
# Continuing a job from the restart files
if {$restart} {
set inputname         $outputname
Coordinates           ../$inputname.restart.coor
Velocities            ../$inputname.restart.vel
extendedSystem        ../$inputname.xsc
}
firsttimestep     0
#############################################################
## SIMULATION PARAMETERS                                   ##
#############################################################
```

```
# Input
amber                   on
parmfile                ../common/ER4.prmtop
if {$restart-1} {
temperature             $temperature
}
# Force-Field Parameters
dielectric              1.0             ;# Value of the dielectric constant
exclude                 scaled1-4
nonbondedScaling        1.0
1-4scaling              1.0
cutoff                  12.0            ;#Angstorm
switching               on
switchdist              10.0            ;#Angstorm
pairlistdist            14.0            ;#Angstorm

# Integrator Parameters
timestep                1.0             ;# 1fs/step
rigidBonds              all
rigidTolerance          0.00001
rigidIterations         100             ;# Maximum number of SHAKE iterations
nonbondedFreq           1
vdwGeometricSigma       yes
fullElectFrequency      2
stepspercycle           20
pairlistsperCycle       2

# Periodic Boundary Conditions
if {$restart-1} {
set X       150.00
set Y       75.00
set Z       75.00
set C       0.00
set C1      0.00
```

```
cellBasisVector1   $X      0.0      0.0      ;#Angstorm
cellBasisVector2   0.0      $Y      0.0      ;#Angstorm
cellBasisVector3   0.0      0.0      $Z      ;#Angstorm
cellOrigin         $C       $C1      $C1      ;#Angstorm

# PME (for full-system periodic electrostatics)
PME                    yes
PMEGridSpacing         1.0
PMETolerance           0.000001



#manual grid definition
#PMEGridSizeX          150
#PMEGridSizeY          75
#PMEGridSizeZ          75
}
wrapAll                on

# Constant Temperature Control
if {0} {
langevin               on              ;# do langevin dynamics
langevinDamping        1               ;# damping coefficient (gamma) of 1/ps
langevinTemp           $temperature
langevinHydrogen       off             ;# don't couple langevin bath to hydrogens
}

# Constant Pressure Control (variable volume)
if {0} {
useGroupPressure       yes             ;# needed for rigidBonds
useFlexibleCell        no
useConstantArea        no
langevinPiston         on
langevinPistonTarget   1.01325         ;#  in bar -> 1 atm
langevinPistonPeriod   100.0
```

```
langevinPistonDecay     50.0
langevinPistonTemp      $temperature
}

# Fixed Atoms Constraint (set PDB beta-column to 1)
if {0} {
fixedAtoms              on
fixedAtomsForces        on
fixedAtomsFile          myfixedatoms.pdb
fixedAtomsCol           B
}
# IMD Settings (can view sim in VMD)
if {0} {
IMDon                   on
IMDport                 3000        ;# port number (enter it in VMD)
IMDfreq                 1           ;# send every 1 frame
IMDwait                 no          ;# wait for VMD to connect before running?
}
# Output
outputName              $outputname
XSTfile                 $outputname.xst

restartfreq             500         ;# 500steps = every 1ps
dcdfreq                 2000
outputEnergies          100
outputPressure          100
binaryoutput            no
binaryrestart           no
#############################################################
## EXTRA PARAMETERS                                        ##
#############################################################

#############################################################
## EXECUTION SCRIPT                                        ##
```

```
#####################################################################
# Minimization
minimization        on
seed                1536        ;# Random number
minimize            500000      ;# Number of integration steps
```

References

1. Lin, S.-T. and S.I. Sandler, *A priori phase equilibrium prediction from a segment contribution solvation model.* Industrial & engineering chemistry research, 2002. **41**(5): p. 899-913.
2. Klamt, A., *Conductor-like screening model for real solvents: a new approach to the quantitative calculation of solvation phenomena.* The Journal of Physical Chemistry, 1995. **99**(7): p. 2224-2235.
3. Alkhatib, I.I., et al., *Perspectives and guidelines on thermodynamic modelling of deep eutectic solvents.* Journal of Molecular Liquids, 2019: p. 112183.

List of Publications

Books

1. Papu Kumar Naik, **Nikhil Kumar,** Nabendu Paul, and Tamal Banerjee. Deep Eutectic Solvents in Liquid-Liquid Extraction: Correlation and Molecular Dynamics Simulation (1st ed. 2022). CRC Press. https://doi.org/10.1201/9781003231158

Published Articles

1. **Nikhil Kumar,** Papu Kumar Naik, and Tamal Banerjee. "Molecular modeling insights in the extraction of benzene from hydrocarbon stream using deep eutectic solvent." Journal of Molecular Liquids 317 (2020): 113909. https://doi.org/10.1016/j.molliq.2020.113909
2. **Nikhil Kumar** and Tamal Banerjee. "Dearomatization insights with phosphonium-based deep eutectic solvent: Liquid–liquid equilibria experiments and predictions." Journal of Chemical & Engineering Data 66.9 (2021): 3432-3442. https://pubs.acs.org/doi/full/10.1021/acs.jced.1c00241
3. **Nikhil Kumar** and Tamal Banerjee. "Molecular Mechanism and Solubility Performance Evaluation for Separation of Benzothiophene and Model Diesel Compounds through Deep Eutectic Solvents as Extractants." Industrial & Engineering Chemistry Research 61.3 (2022): 1464-1474. https://pubs.acs.org/doi/full/10.1021/acs.iecr.1c04083
4. **Nikhil Kumar,** Papu Kumar Naik, and Tamal Banerjee. "Molecular Dynamic Insights into the Distinct Solvation Structures of Aromatic and Aliphatic Compounds in Monoethanolamine-Based Deep Eutectic Solvents." The Journal of Physical Chemistry B (2022). https://pubs.acs.org/doi/full/10.1021/acs.jpcb.2c01735
5. **Nikhil Kumar,** Mohan Mood, Blake A. Simmons, Jereme Smith, Seema Singh, and Tamal Banerjee. "Deciphering Structure and Aggregation in Asphaltene: COSMO-RS Driven Design and Development of Novel Natural Deep Eutectic Solvents." Submitted to Environmental Science & Technology (Under Review)
6. **Nikhil Kumar,** Mohan Mood, Blake A. Simmons, Jereme Smith, Seema Singh, and Tamal Banerjee. “Study of Aggregation of asphaltene behaviour Using Thymol-Based Hydrophobic Eutectic Solvents: Multiscale Modeling Insights." (Under Review)

Other Publications

1. Mohan Mood*, **Nikhil Kumar*,** Vaibhav V. Goud, Blake A. Simmons, Kenneth Sale, John M. Gladden, Seema Singh, and Tamal Banerjee. "Effect of Cosolvent on the Solubility of Glucose in Ionic Liquids: Experimental and Molecular Dynamics Simulations." Fluid Phase Equilibria (2022): 113559. ***Equal Contribution** https://doi.org/10.1016/j.fluid.2022.113559
2. **Nikhil Kumar** and Tamal Banerjee. "Study of Phenolic Compounds Extraction using the Hydrophobic Deep Eutectic Solvents using Quantum Chemical and Molecular Dynamic" (Manuscript under preparation)

International Conferences and Workshops

1. **Nikhil Kumar,** and Tamal Banerjee. "Molecular Modeling Insights in the Extraction of Benzene from Hexane using Deep Eutectic Solvent.", (Oral presentation), DAE-CCS 2019, Bhabha Atomic Research Center Mumbai, November 7-9, 2019, India
2. **Nikhil Kumar,** and Tamal Banerjee. "Investigating the solubility of asphaltene in deep eutectic solvents and their interaction using COSMO-RS." (Poster presentation), ASIL 9, 9th Australasian Symposium on Ionic Liquids. Melbourne, Australia
3. **Nikhil Kumar,** and Tamal Banerjee. "De-aromatization of diesel fuel using Phosphonium based deep eutectic solvents." (Oral presentation). 2nd International Conference on FUTURE ASPECTS OF SUSTAINABLE TECHNOLOGIES.
4. **Nikhil Kumar,** and Tamal Banerjee. "Investigating the solubility of petroleum asphaltene in Ionic liquids" (Poster presentation), Complex Fluids Symposium 2020.
5. **Nikhil Kumar,** and Tamal Banerjee. "The solubility of Benzene, Thiophene and hexane in choline chloride-based deep eutectic solvents: Quantum and Molecular Dynamics Simulations" (Oral presentation), 6th edition of the Iberoamerican Meeting on Ionic Liquids (IMIL 2021).
6. A short-term GIAN course on **"Density Functional Theory for Heterogeneous Catalysis"** was organized Department of Chemical Engineering during 7-10 August 2018 at India Institute of Technology Guwahati, Guwahati, Assam, India.
7. A short-term course on "**Gaussian16: theory and Practice workshop**" organized by Gaussian and SCUBE Scientific software solutions India was held at Hotel Hindustan International, Kolkata, India, during 14-18 January 2019.
8. **Machine Learning for Chemistry and Drug Design "learning by doing,"** 12 Weeks Course, IHUB-DATA, IIIT Hyderabad.

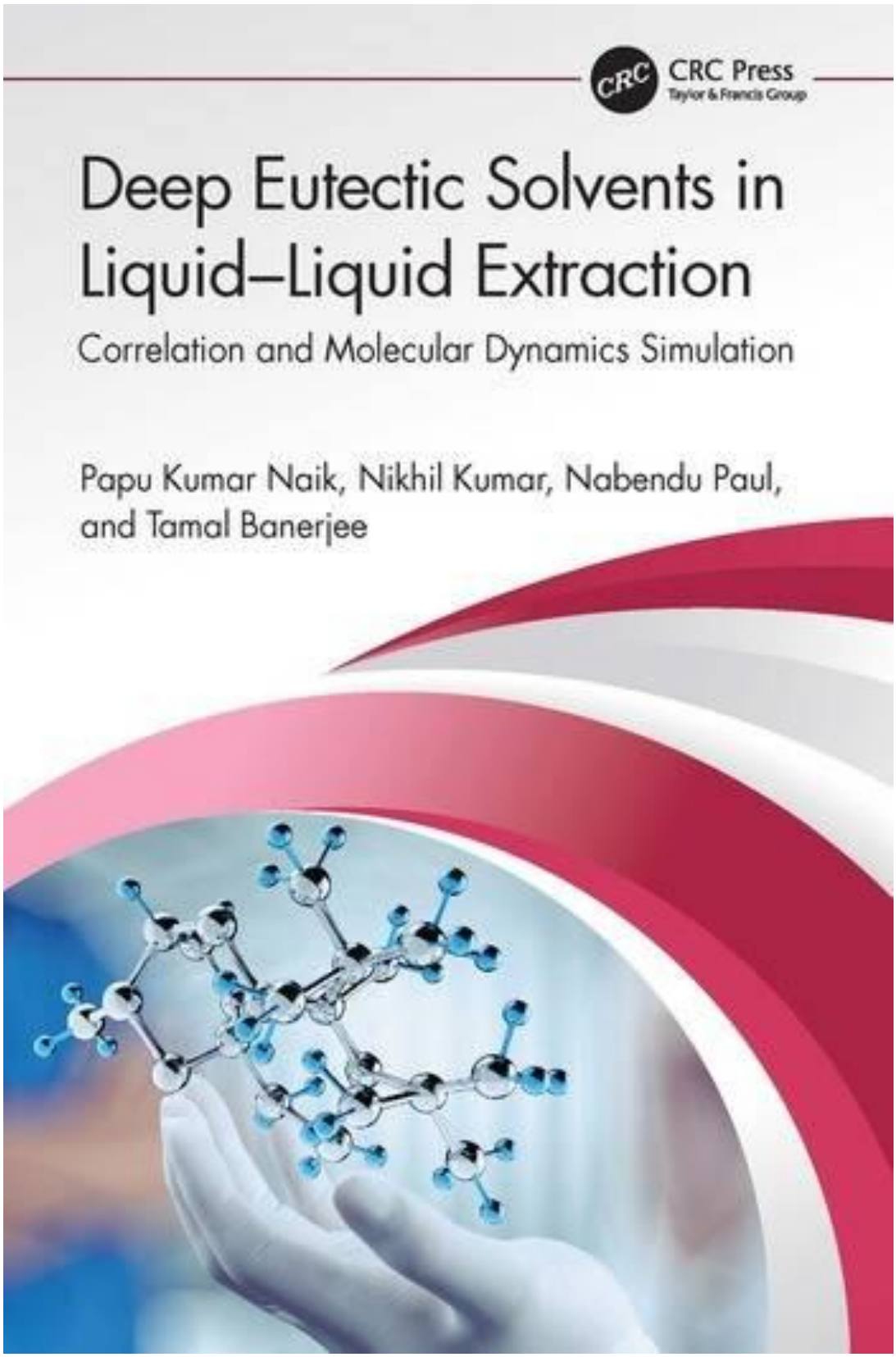

THE JOURNAL OF PHYSICAL CHEMISTRY B
A JOURNAL OF THE AMERICAN CHEMICAL SOCIETY

pubs.acs.org/JPCB Article

Molecular Dynamic Insights into the Distinct Solvation Structures of Aromatic and Aliphatic Compounds in Monoethanolamine-Based Deep Eutectic Solvents

Nikhil Kumar, Papu Kumar Naik, and Tamal Banerjee*

Cite This: J. Phys. Chem. B 2022, 126, 4925−4938 Read Online

ACCESS | Metrics & More | Article Recommendations | Supporting Information

ABSTRACT: Deep eutectic solvents (DESs) are developing as an alternate medium for aromatic extraction, especially benzene and thiophene from aliphatic hydrocarbon mixtures. In this work, molecular dynamics (MD) simulations were first used to investigate the solvation structure of benzene, thiophene, and *n*-hexane in monoethanolamine-based DESs. It reveals the liquid structures in the adjacent neighbor shells, which is a function of electron-withdrawing sulfur attached to thiophene and the π-electron cloud of benzene. The intermolecular forces between aromatic, aliphatic, and DES components are analyzed in van der Waals and hydrogen bond interactions. The chloride ions serve as a charge carrier bridge between choline and monoethanolamine precursors. The solvation of benzene, thiophene, and *n*-hexane in the DESs depends on volume expansion and minor solvent structural changes. Density functional theory results provided information on the mechanism of short-range interactions between organic solutes and studied DES.

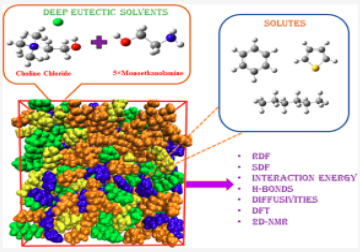

It aids in understanding the structural orientations of a DES with the addition of solutes, essential to the formation of DES. The solvation shell structure and characteristics were investigated in tandem with the possibility of benzene and thiophene clustering. The ^{1}H NMR and 2D ^{1}H−^{1}H-NOESY were used to investigate the intermolecular interactions between benzene, thiophene, and *n*-hexane with monoethanolamine-based solvents. It concludes that high-ordered DES1 is more inclined to higher solubility than lower-ordered ones with a higher molar ratio of monoethanolamine. The solvation was reduced because the entropy gain was not maximized in the lower ordered DESs.

I&EC research
Industrial & Engineering Chemistry Research

pubs.acs.org/IECR Article

Molecular Mechanism and Solubility Performance Evaluation for Separation of Benzothiophene and Model Diesel Compounds through Deep Eutectic Solvents as Extractants

Nikhil Kumar and Tamal Banerjee*

Cite This: Ind. Eng. Chem. Res. 2022, 61, 1464−1474 Read Online

ACCESS | Metrics & More | Article Recommendations | Supporting Information

ABSTRACT: During combustion, sulfur compounds in fuels are oxidized to SO_x, poisoning automatic catalytic converters and posing severe environmental risks (e.g., acid rain). As an outcome, effective liquid fuel desulphurization is a vital step in reducing SO_x emissions and their inherent ecological impacts. The extraction of ultralow benzothiophene from *n*-decane as representative model diesel fuel was analyzed using phosphonium-based deep eutectic solvents (DESs) at 308.15 K and 1 bar pressure. Liquid−liquid equilibrium (LLE) studies were conducted on a ternary system of DES−benzothiophene−*n*-decane for all six feed point concentrations. ^{1}H NMR analysis was used to determine the molar composition of each raffinate and extract phase. The LLE experimental findings were examined using a conductor-like screening model for segment activity coefficient (COSMO-SAC) based on quantum calculations. The average root-mean-square deviation (RMSD) of the studied LLE ternary system was 1.07%, which was suitable considering the prior nature of the approach. The σ-profile calculations using the COSMO-SAC model and Hansen solubility parameters (HSPs) using different predicted models were used to provide insights into the molecular mechanism of benzothiophene extraction efficacy using DES. We observed higher extraction of benzothiophene due to the higher proportion of hydrogen-bonding and dispersion-type interactions. Charge transfer analysis using the density functional theory (DFT) calculation of the DES cluster suggested that bromide (Br^-) ions can act as a charge transfer bridge between the methyltriphenylphosphonium (MTP) cation and the hydrogen bond donor. The MTP cation and ethylene glycol also aided in the extraction of benzothiophene by dislocating charge from the aromatic sulfur compound. The bromide (Br^-) ion is essentially noninteractive with benzothiophene due to retention of the conventional hydrogen bond network existing within the initial components of DES, mainly hydrogen bond donors and hydrogen bond acceptors.

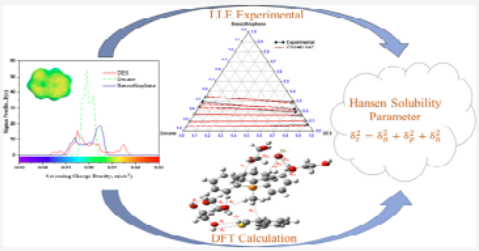

Journal of Chemical&Engineering Data

pubs.acs.org/jced Article

Dearomatization Insights with Phosphonium-Based Deep Eutectic Solvent: Liquid−Liquid Equilibria Experiments and Predictions

Nikhil Kumar and Tamal Banerjee*

Cite This: J. Chem. Eng. Data 2021, 66, 3432−3442 Read Online

ACCESS | Metrics & More | Article Recommendations | Supporting Information

ABSTRACT: In a challenge to develop a process that meets the criteria of being "green" in the extraction of aromatics, deep eutectic solvents (DESs) are currently gaining importance as separation media. This work reports a phosphonium-based DES for the dearomatization of model diesel components at 25 °C and p = 1 bar. The DES comprising a hydrogen bond acceptor, namely, methyltriphenylphosphonium bromide, along with ethylene glycol as a hydrogen bond donor, was formulated with a molar ratio of 1:4. The DES was then used to extract benzene from representative diesel fuel components, a mixture of n-decane, n-dodecane, and n-hexadecane. Ternary liquid−liquid equilibrium experiments were then performed at ambient conditions with different benzene concentrations with the feed varying from 2 to 20 wt %. An absence of the solvent in the raffinate phase was found in all the tie lines, suggesting limited solvent recovery costs. Besides, it was also found that all three ternary systems show type I phase activity with positive slopes, indicating that the desired removal of benzene requires a small amount of solvent. The quantum chemical-based COSMO-SAC model was then used to predict the tie lines giving an average root mean square deviation value of 1.2%. The mechanism of the extraction process was also extensively studied with the help of quantitative ^{1}H NMR and Fourier transform infrared spectroscopy. Higher benzene extraction efficiencies were observed due to the strong noncovalent interaction between the DES and benzene.

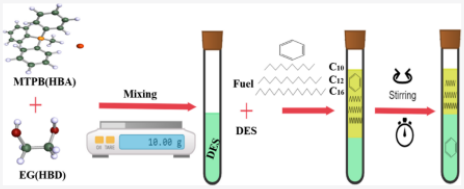

Contents lists available at ScienceDirect

Journal of Molecular Liquids

journal homepage: www.elsevier.com/locate/molliq

Molecular modeling insights in the extraction of benzene from hydrocarbon stream using deep eutectic solvent

Nikhil Kumar [a], Papu Kumar Naik [b], Tamal Banerjee [a,b,*]

[a] Department of Chemical Engineering, Indian Institute of Technology Guwahati, Guwahati 781039, Assam, India
[b] Centre for the Environment, Indian Institute of Technology Guwahati, Guwahati 781039, Assam, India

ARTICLE INFO

Article history:
Received 5 March 2020
Received in revised form 18 June 2020
Accepted 22 July 2020
Available online 29 July 2020

Keywords:
Benzene
Deep eutectic solvent
MD simulation
Interaction energy
2D NMR

ABSTRACT

The present study aims to elucidate the molecular insights into the extraction of benzene from hydrocarbon mixture using a phosphonium based deep eutectic solvent (DES). The prepared DES consists of the hydrogen bond acceptor (HBA; methyltriphenylphosphonium bromide, MTPB) and hydrogen bond donor (HBD; ethylene glycol) at a molar ratio of 1:4. The atomic-level classical molecular dynamic (MD) simulation technique is then employed to investigate the equilibrium phase behaviour of the DES + benzene + hexane ternary system with respect to solvent rich and hydrocarbon-rich phases. To observe the effect of feed concentration, three different concentrations were considered from the reported experimental runs, which gave high selectivity and distribution coefficient values. The non-bonded interaction energies of different species and the structural properties such as radial distribution functions, spatial distribution functions (SDFs), and the average number of hydrogen bonds are then computed. It is found that the cation within the HBA, namely, MTP, initiates interactions with benzene when compared to HBD or its anion (Br). MTP and ethylene glycol both are seen to contribute to the hydrogen bonding with benzene, which results in a higher experimental solubility value. The calculations of SDFs further reveal the fact that the benzene molecules are evenly distributed around the active sites of the MTP molecule, whereas hexane molecules are found to be distributed around the non-active sites of the DES. In order to validate the simulation procedure, the concentration in both the phases was compared with the existing LLE experimental results. In the penultimate part, 2D ^{1}H-^{13}C Heteronuclear Multiple Bond Correlation (HMBC) NMR is performed for investigating and confirming the hydrogen bonding interactions among components of DES and benzene.

Contents lists available at ScienceDirect

Fluid Phase Equilibria

journal homepage: www.journals.elsevier.com/fluid-phase-equilibria

Effect of cosolvent on the solubility of glucose in ionic liquids: Experimental and molecular dynamics simulations

Mood Mohan [a,b,c,1,*], Nikhil Kumar [c,1], Vaibhav V Goud [c], Blake A. Simmons [a,d], Kenneth L. Sale [a,e], John M. Gladden [a,b], Seema Singh [a,b], Tamal Banerjee [c,**]

[a] Deconstruction Division, Joint Bioenergy Institute, 5885 Hollis Street, Emeryville, California 94608, United States
[b] Bioresource and Environmental Security Department, Sandia National Laboratories, 7011 East Avenue, Livermore, California 94551, United States
[c] Department of Chemical Engineering, Indian Institute of Technology Guwahati, Guwahati, Assam, 781039, India
[d] Biological Systems and Engineering Division, Lawrence Berkeley National Laboratory, 1 Cyclotron Road, Berkeley, California 94720, United States
[e] Department of Computational Biology and Biophysics, Sandia National Laboratories, 7011 East Avenue, Livermore, California 94551, United States

ARTICLE INFO

Keywords:
Ionic liquids
Cosolvent
Glucose
Molecular dynamics
Solubility
Thermodynamic models

ABSTRACT

The present study attempts to measure the solubility of glucose in three neat ionic liquids (ILs), namely 1-ethyl-3-methylimidazolium methylsulfonate [Emim][$MeSO_3$], 1-ethyl-3-methylimidazolium ethyl sulfate [Emim][$EtSO_4$], 1-ethyl-3-methylimidazolium thiocyanate [Emim][SCN] and IL/cosolvent mixtures as a function of temperature. The IL [Emim][$MeSO_3$] has shown higher solubility of glucose than other ILs. The experimental glucose solubility data was further correlated with Apelblat empirical equation along with regression using a local thermodynamic model such as NRTL (non-random two-liquid). The thermodynamic functions of dissolution, such as enthalpy $\Delta^{*}_{diss,sol}H$, Gibbs energy $\Delta^{*}_{diss,sol}G$ and entropy $\Delta^{*}_{diss,sol}S$ were also determined using the modified van't Hoff equation. The dissolution functions for all the systems studied were positive, indicating that the process is endothermic, non-spontaneous, and entropically viable. Dimethyl sulfoxide (DMSO) was added as a cosolvent to enhance the solubility of glucose in ILs by reducing viscosity, which leads to a higher mass transfer rate of solute in solvent even at low temperatures. Furthermore, we performed molecular dynamics (MD) simulations to understand the microscopic interactions of glucose-IL and glucose-IL/DMSO systems. From the MD simulations, it was observed that anions of IL dominate the solvation of glucose, whereas the cation plays a secondary role. The addition of DMSO to ILs, weakens the stronger interactions between anion and cation of IL, thereby enhancing the solvation of glucose by increasing the interaction energies and contact probabilities between glucose and anion of ILs.